Thermally and Acoustically Driven Transport in Supercritical Fluids

A Thesis

Submitted to the Faculty

of

Drexel University

by

Nusair Mohammed Ibn Hasan

in partial fulfilment of the

requirements for the degree

of

Doctor of Philosophy

July 2014

DEDICATIONS

I dedicate this thesis to my wife Farin who has done more than her share during the past four years when I was busy working for my Ph.D. I would also like to dedicate this thesis to the people of Bangladesh; the taxpayers whose contributions helped provide for my education (from kindergarten to university) and that of so many others.

ACKNOWLEDGEMENTS

I would like to convey my gratitude to my adviser Prof. Bakhtier Farouk whose help, support and guidance were appreciated throughout my graduate studies. His constant drive to do great research and publish has always inspired me to push myself a bit harder and a bit further. I also would like to thank my committee members – Prof. Yossef Elabd, Prof. Nicholas Cernansky, Prof. Matthew McCarthy and Prof. Ying Sun for their participation, time and useful suggestions that helped improve my dissertation research.

I am grateful for the financial support that I received during my graduate study especially from the NSF grant (CBET-0853959), the teaching assistantship from the department of Mechanical Engineering and Mechanics (MEM) and the George Hill Jr. Fellowship. I am thankful to the Department of Mechanical Engineering and Mechanics at Drexel University for providing an excellent graduate education and an invaluable learning experience. I would like to thank my colleagues and friends in the MEM department and the Combustion and Energy group, especially Dion S. Antao and Ersin Sayar for their camaraderie and always being there to discuss new ideas.

Finally, my eternal gratitude goes to my family for their prayers, their love, their patience and their support.

TABLE OF CONTENTS

LIST OF TABLES

LIST OF FIGURES

ABSTRACT

Thermally and Acoustically Driven Transport in Supercritical Fluids
Nusair Mohammed Ibn Hasan
Bakhtier Farouk, Ph. D.

Supercritical fluids are fluids at temperature and pressure above their respective critical values. Such fluids are increasingly being used in power generation, refrigeration and chemical process industry. The objectives of the current research were to develop a fundamental understanding of the transport phenomena in near-critical supercritical fluids via high-resolution numerical simulations and careful experiments for improved design of industrial processes and applications that employ supercritical fluids. A set of synergistic experimental and numerical studies were proposed in this research. Four main focus areas under the broad spectrum of supercritical fluid transport were chosen – (a) characterization of thermoacoustic transport, (b) interaction of thermoacoustic transport with natural convection, (c) characterization of acoustically augmented transport and (d) enhancement of mass transport using acoustic waves.

A numerical model to simulate thermoacoustic convection in near-critical fluids was developed. In the computational model, the conservation equations were solved along with a real-fluid equation of state for supercritical fluid and variable thermo-physical properties. Thermoacoustic waves in near-critical carbon dioxide were also investigated experimentally on acoustic time scales using a fast response measurement system. The predicted results from the calculation and the measurements provide interesting details regarding the thermal transport mechanisms at near-critical states. The numerical model was applied to investigate the interaction of buoyancy driven flows with thermoacoustic convection in near-critical supercritical fluids. This model can be extensively used for studying the steady-state thermal transport and stability behavior of near-critical fluids.

Mechanically driven acoustic waves in supercritical fluid generated by a vibrating wall in a cylindrical resonator were studied both numerically and experimentally. The simulations revealed interesting steady-periodic flow patterns in the resonator filled with near-critical fluid due to the fluctuations caused by the vibrating wall. High-fidelity computational fluid dynamics models of mass transport processes in supercritical fluid extraction systems were also developed. A novel application of acoustically driven transport in supercritical fluid was demonstrated numerically for the supercritical fluid extraction process. The numerical predictions indicated major improvements in the extraction yield due to the application of acoustic waves and can be utilized in the design and optimization of supercritical fluid extraction systems.

CHAPTER 1: INTRODUCTION

1.1 Background

This thesis reports the interactions between thermal and acoustic energy, and the effect of induced acoustic waves on the transport in near-critical supercritical fluids. The focus of this dissertation is placed on how these interactions are harnessed to the purpose of energy transport and process enhancement, specifically in solvent extraction. The information contained within this chapter will put into context the motivations and objectives of the current research and will provide a better understanding of the results presented in the following chapters.

1.1.1 Critical point and supercritical fluids

In thermodynamics, a critical point specifies the conditions (temperature, T_c and pressure, p_c) at which a phase boundary ceases to exist and above which distinct liquid and gas phases do not exist. For pure substances, there is an inflection point in the critical isotherm on a p-v diagram [1]. This means that at the critical point:

$$\left(\frac{\partial p}{\partial v}\right)_T = \left(\frac{\partial^2 p}{\partial v^2}\right)_T = 0 \tag{1.1}$$

The supercritical state of a fluid is defined as the state of a compound, mixture or element above its critical pressure (p_c) and critical temperature (T_c) but below the pressure required to condense it into a solid [2]. In that sense, the critical point corresponds to the highest temperature and pressure at which the substance can exist as a vapor and liquid in equilibrium. Figure 1.1 shows a p-T (pressure - temperature) phase diagram for carbon dioxide in gas, liquid, solid and supercritical states. The critical pressure (p_c) for carbon dioxide is 7.377 MPa and the critical temperature (T_c) is 304.13 K [3]. If both pressure and temperature are beyond each critical point, the carbon dioxide is in a supercritical state.

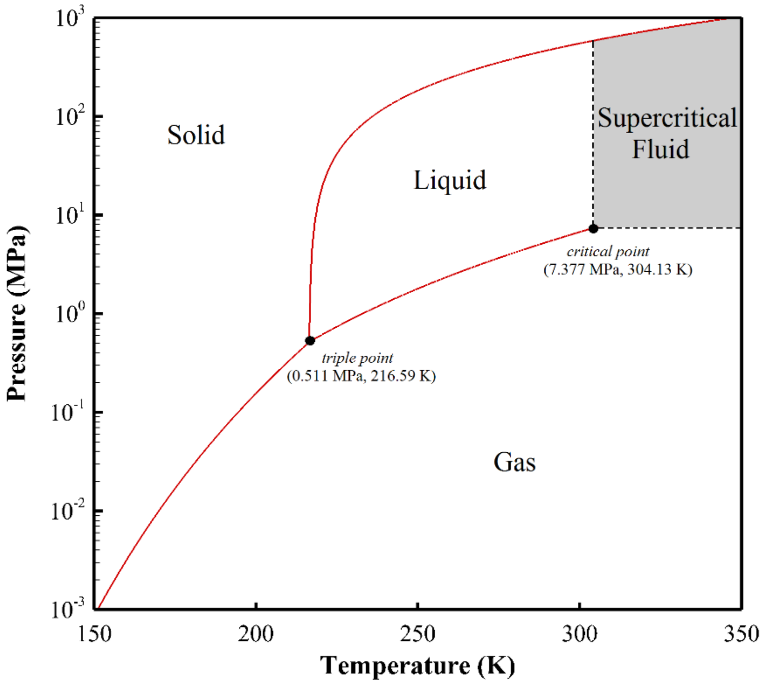

Figure 1.1: *p*-*T* phase diagram for carbon dioxide.

The thermo-physical properties of a supercritical fluid vary over a wide range depending on the temperature and the pressure, but generally are intermediate between those of liquids and gases. However, these properties are highly sensitive to small changes in temperature and pressure near the critical point. Supercritical fluids has been considered very useful as reaction, extraction and thermal transport media because of their high compressibility, specific heat and solubility as well as their tunability, which allows one to control the thermo-physical properties to cater specific applications. In addition, supercritical fluids has the ability to dissolve gases such as H_2, O_2 and CO [4].

1.1.2 Thermoacoustics

Pressure waves in fluids can be generated by either mechanical or thermal effects. Pressure waves travelling in a medium at the speed of sound of that medium are known as acoustic waves. In fluids, pressure waves that are generated due to a rapid expansion or compression of the fluid due to thermal effects are characterized as thermally generated acoustic waves or *thermoacoustic* waves. The study of this phenomenon (involving both thermodynamics and acoustics) is broadly classified as thermoacoustics. The term ‘thermoacoustics’ includes all effects in acoustics in which heat conduction and entropy variations of the gaseous medium play a significant role [5]. All acoustics in fluids in which diffusive effects are considered belong within the field of thermoacoustics.

Thermoacoustic waves are generated due to the rapid heating or cooling of a gas [6]. When a gas is subjected to a rapid temperature increase at a solid surface, the fluid in the immediate vicinity of the boundary is heated by conduction and tends to expand. However, the sudden expansion of the gas due to the energy input is constrained by the inertia of the unperturbed media and induces a pressure wave called a thermoacoustic wave. The pressure wave that is generated from the hot wall travels at approximately the speed of sound within the fluid and impinges on the opposite wall and is reflected back. The wave repeatedly traverses between the walls, and its amplitude eventually damps out due to the viscous and thermal losses within the gas. Thermal transport by thermoacoustic waves can be significant when the fluid is close to the critical point or when other modes of convection are weak or absent [7].

1.1.3 Acoustic streaming

Acoustic streaming can be defined as steady convection which is driven by oscillatory phenomenon in bounded channels [8]. It is well-known that acoustic sources may generate a convective field in which the particle velocities are not simply sinusoidal, and a pattern of time-independent vortical flows or steady circulations is often found in the body of compressible media. These second-order steady flow patterns are known as *acoustic streaming*, which always have rotational character. Figure 1.2a below shows the streaming patterns that appear near the external surface of a cylinder oscillating in a quiescent medium (here glycerin-water mixture). Figure 1.2b shows similar streaming patterns on the inside of an acoustic resonator tube that is excited by a loudspeaker.

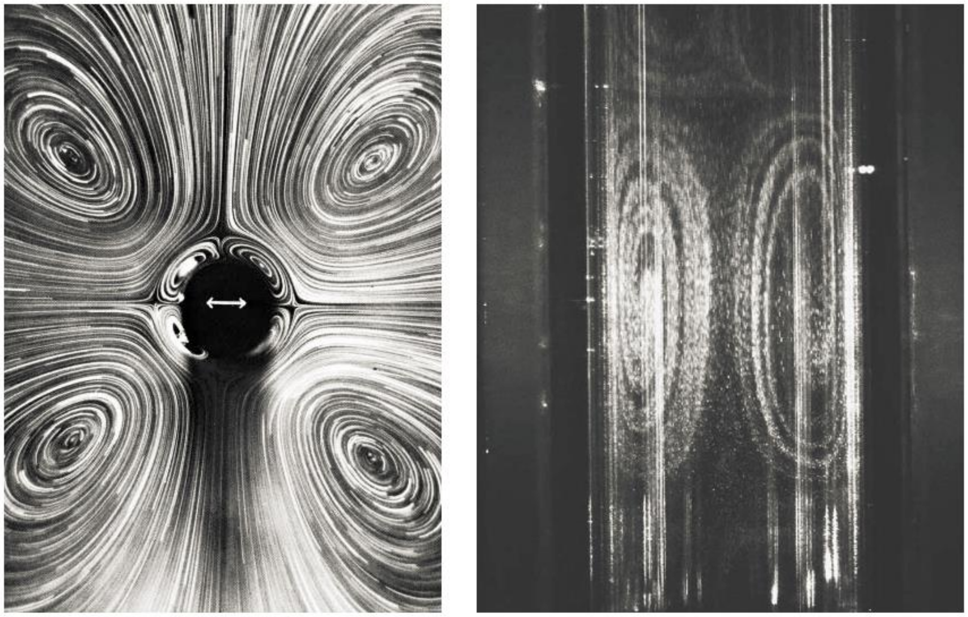

(a) (b)

Figure 1.2: Acoustic streaming patterns (a) external: outside a cylinder oscillating in a quiescent medium [9] and (b) internal: inside a cylinder that has oscillatory flow within it generated by a loudspeaker [10].

Typical acoustic streaming velocities are more than an order of magnitude smaller than the instantaneous oscillatory velocity flow field in the resonator [11]. Acoustic streaming flows are mostly uni-directional in nature as compared to the alternating nature of the oscillatory flow. Acoustic streaming has applications in mixing channels and enhanced convective transport.

1.1.4 Supercritical fluid extraction

Supercritical fluid extraction (*SFE*) covers the application of fluids at supercritical or near-critical conditions in separation processes or extractive operations [12]. The supercritical fluid extraction (SFE) process has attracted increasing interest over the past few years [13, 14]. Conventional separation techniques such as solvent extraction, partitioning (also known as *liquid–liquid extraction*; a method to separate compounds based on their relative solubility in two different immiscible liquids) and distillation usually have the drawback of leaving trace amounts of inorganic (potentially toxic) solvents or to cause thermal degradation [15]. Some supercritical fluids have the potential to replace these toxic industrial solvents. Due to its unique characteristics and physic-chemical properties such as being less toxic, nonflammable, and having the extraction power tuned by temperature and pressure, supercritical carbon dioxide is generally used as a green solvent for extraction of substances especially from solid or liquid substrates. Such extraction has been carried out on commercial scale for more than two decades and applications like decaffeination of coffee beans and black tea leaves and hops extraction are involved in large-scale processes [16].

1.2 Motivation of the dissertation research

Although supercritical fluids have been used in various industrial applications for the past 60 years, it is only in the early ‘90s that their peculiar thermo-physical properties have been identified, following the works of Widom, Kadanoff and Wilson [17-19]. The understanding of the hydrodynamics and transport phenomena in these fluids is thus a relatively recent result. However, the knowledge regarding the thermal and chemical (species) transport phenomena in supercritical fluids is not complete and many open questions exist. An important area is the detailed understanding of transport behavior of supercritical fluids near the critical point. The typical characteristics of supercritical fluids near the critical point can be summarized by the following points –

- Near the critical point, supercritical fluids are dense and compressible at the same time.
- Thermal diffusion coefficient of near-critical fluids is generally very small compared to gases while the mass diffusion coefficients are much larger than in most liquids.
- Near the critical point, minor adjustments in temperature and pressure can provide significant variations of the thermo-physical properties.
- The divergence of the thermo-physical properties at the critical point can also be felt around the pseudo-critical states (*i.e.* where $\rho = \rho_c$).

Due to the above characteristics, near-critical thermal transport exhibits features that are not observed in supercritical fluids far from their critical point and also in gas/liquid phases [20-22]. A significant amount of research on heat transfer to supercritical fluids has been carried out over the past years [23-29]. The existing studies in the literature regarding thermal transport in supercritical fluids mainly focus on two working fluids - carbon dioxide [30-34] and water [35-38]. This is due to their widespread practical applications in the refrigeration and nuclear industries. However, there is a lack of understanding and ability to predict the transport behavior of supercritical fluids in the near-critical region. Also, it is well known that, acoustic phenomena (*thermoacoustic* waves) are responsible for the fast thermal homogenization in supercritical fluids (near the critical point) which occurs on a much shorter time scale than in a purely diffusive medium [39-43]. These aspects are of practical importance in space engineering purposes like the storage and utilization of rocket fuel at supercritical conditions. Also, supercritical fluids have been considered for reclaiming potable water from the biological waste in long range space flights [44]. The low heat diffusivity character of near-critical conditions makes the thermoacoustic convection mode of heat transport significant for supercritical fluid storage systems which involve rather weak diffusive and convective transport of heat, especially in a reduced-gravity environment. Because of the high density and compressibility values of fluids in these systems, strong thermoacoustic waves are produced and heat transfer effects of these waves become critical due to the possibility of a sudden phase change in the storage system. Detailed numerical simulations are needed to clearly understand the physics of convection, thermal and chemical transport in supercritical fluids with and without the effects of thermally induced acoustic waves.

Solvent extraction processes using supercritical fluids have attracted increasing interest over the past few years [13, 14, 45]. This is particularly motivated by concerns about environmental aspects, given the capability of some supercritical fluids for replacing toxic industrial solvents and the possibility to tune the solvent characteristics for highly specific reactions or separations. Supercritical fluids are now being used in several applications (lab-scale or industrial) associated with the development of sustainable chemistry and engineering. However, chemical (species) transport processes in supercritical fluids has a very slow dynamics near the critical point and hence the operating parameters are set relatively far from the critical point. The use of acoustic excitation represents a potential efficient way of enhancing mass transfer processes in the near critical region by increasing localized convection [13, 46-49]. Also, acoustic streaming has the potential to accelerate certain kinds of rate processes and has applications in localized micro-mixing and convective transport processes [50-53].

A detailed study of thermally and acoustically driven flows in supercritical fluids near the critical point is important for understanding the hydrodynamics and transport behavior and for extending the range of process parameter space (pressure and temperature). Although extensive investigations of transport characteristics in supercritical fluids have been reported [34, 54, 55], experimental or numerical studies near the critical point are limited. The response to any thermal disturbance to near-critical fluids is complex and not fully understood. The difficulties mostly arise from the divergence of the thermo-physical properties near the critical point. Detailed numerical modeling (accompanied by experimentations) of the thermally and acoustically driven flows in near-critical supercritical fluids can provide important insight into the interplaying thermo-fluid/acoustic-fluid interactions and transport behavior that would be difficult to obtain via experiments only. This would provide better understanding of the regime of operation and would also provide guidelines for optimizing different process operating parameters.

1.3 Objectives of the dissertation research

The objectives of the current research were to develop comprehensive computational models to accurately predict and study the thermally and acoustically induced flow and transport in near-critical supercritical fluids and to validate the numerical modes with detailed experiments. The objective was to perform the research based on a set of synergistic experiments and numerical simulations that can be used to understand the thermal and chemical (species) transport behavior in near-critical supercritical fluids. The developed models were used to study thermally and acoustically driven flows in simplified geometries (one dimensional slot, two dimensional enclosure, cylindrical tube etc.) as well as in complex systems (fixed bed extractor, membrane contactors etc.)[1] and to investigate the effects of a variety of operating conditions (mainly thermodynamic state) on the transport. Based on the overall goal, the specific objectives for the current project are listed below –

a. Develop real-fluid computational fluid dynamic models considering all of the relevant fluid property variations to accurately predict thermally driven convective flows (thermoacoustic and natural convection) and related transport phenomena in supercritical fluids.
b. Generate and measure thermally induced acoustic waves in an experimental test cylinder filled with supercritical fluid.
c. Numerically simulate the generation, propagation and dissipation of thermally induced acoustic waves in supercritical fluids and validate the numerical calculations with the results obtained from the experimentation.

---

[1] Fixed bed extractors and membrane contactors will be discussed in detail in the following chapter.

d. Investigate the physical mechanisms of thermoacoustic convection and transport in near-critical supercritical fluids.
e. Design, build, instrument and test a lab-scale experimental setup to generate and measure mechanically driven acoustic waves in near-critical supercritical fluids.
f. Numerically investigate mechanically driven acoustic waves and *acoustic streaming* phenomena in near-critical supercritical fluids.
g. Develop computational fluid dynamics (CFD) models to predict the chemical (species) transport characteristics in supercritical fluid extraction systems (fixed bed extractor and membrane contactor).
h. Numerically investigate the effect of acoustically augmented flow in supercritical fluid extraction systems.

To a significant extent, the objectives set at the onset were met by the present research study. The completed research and how it meets the objectives listed above is discussed in the following chapters.

1.4 Overview of the dissertation

The organization of this dissertation is as follows. Chapter 1 introduces the thesis topic and discusses the motivations and objectives of the research. Chapter 2 provides introductory information and background to familiarize the reader with the thermo-physical properties variation in near-critical supercritical fluids and supercritical fluid extraction systems in context of the current research. Chapter 2 also includes a detailed literature review of the past research performed on convective and thermoacoustic transport in supercritical fluids and modeling of supercritical fluid extraction processes.

The presentation of results begins in chapter 3. For the most part, the chapters are self-contained with introductions, experimental setup/numerical model and simulation conditions, results and discussion and a brief set of conclusions corresponding to each study. Chapter 4 is devoted to the numerical investigation of thermally induced acoustic waves in supercritical fluids, and the effect of near-critical property variations on the thermoacoustic transport. This includes a detailed description of the numerical model developed and the validation of the numerical model with previously published data. Experimental studies of thermally induced acoustic waves in near-critical fluids are presented in chapter 4. The experimental study details the procedure followed to design, fabricate and instrument the test setup for measuring thermoacoustic waves in supercritical fluids. The experimental results are then compared with the calculations presented in chapter 3. Numerical investigation of the interaction between thermoacoustic convection and buoyancy induced convective transport in near-critical fluids are presented in chapter 5. A correlation to predict the buoyancy-driven thermal transport is also proposed in this chapter. Chapter 6 describes the fundamental investigation for characterizing mechanically driven acoustic waves in supercritical fluids. Both experimental and numerical investigation of the mechanically driven acoustic waves and acoustic streaming formation in supercritical fluids are presented in this chapter. In chapter 7, computational fluid dynamic models to predict transport processes in supercritical fluid extraction systems, namely – fixed bed reactors and membrane contactors are introduced. The developed CFD models are applied to study acoustic wave induced enhancement of the transport processes in these systems which are typical in solvent extraction industry. Finally Chapter 8 summarizes and concludes the research presented in this dissertation with a proposal and discussion of research tasks that may be undertaken in the future to improve and better understand the near-critical transport phenomena and its applications in energy and solvent extraction systems.

CHAPTER 2: BACKGROUND AND LITERATURE REVIEW

2.1 Critical point phenomena

The transition between the vapor and liquid phases of a pure fluid is one of the most fundamental in nature. Critical point is considered as the reference point, from which all of the transition properties of such a fluid can be derived. This is the point, characterized by a fixed temperature, pressure and density, at which the distinction between the gas and the liquid phase simply disappears. For a better understanding of the phenomena, the phase equilibrium of carbon dioxide at a supercritical pressure is shown in figure 2.1. In the first image (Figure 2.1a), the temperature is sub-critical ($T < T_c$) the separated phases (liquid and vapor) of carbon dioxide are easily observed. With a slight increase in temperature, the meniscus (the line between the two phases) begins to diminish (Figure 2.2b). Increasing the temperature further causes the gas and liquid densities to become more similar. The meniscus is less easily observed but still evident (Figure 2.2c). Once the critical temperature and have been reached the two distinct phases of liquid and gas are no longer visible. The meniscus can no longer be seen. One homogenous phase (*i.e.* supercritical fluid phase) occurs which shows properties of both liquids and gases (Figure 2.2d). Similar phenomena is observed for all others fluids approaching critical point.

In a wide domain around the critical point, thermo-physical properties such as isothermal compressibility, the density of the gas and liquid phases, and the surface tension, can be set in the form of scaled, universal functions (power laws) with respect to the critical-point parameters [56]. This has the very important consequence that any results obtained with one fluid can be immediately re-scaled to describe any member of a whole class of systems, called a '*class of universality*' [57].

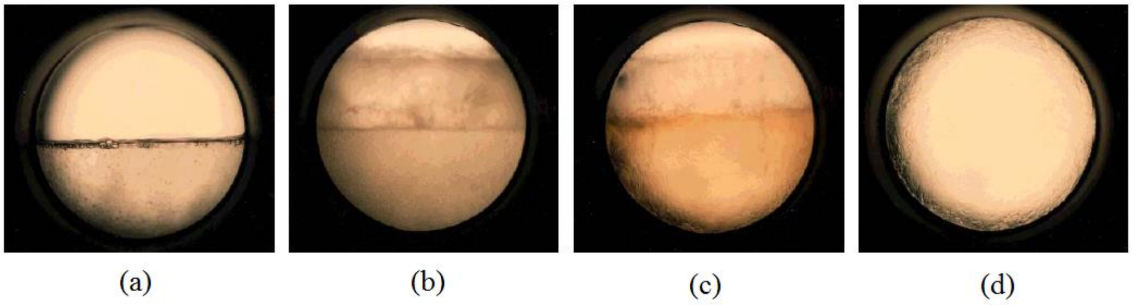
(a) (b) (c) (d)

Figure 2.1: Carbon dioxide transition from (a)-(c) vapor-liquid equilibrium to (d) a supercritical fluid phase [58].

The thermo-physical properties of a near-critical fluid can easily be varied by using small changes in the temperature. The highly variable properties of near-critical fluids make them very appealing for studying many interesting phenomena that, because of the universality of the power laws, are valid for all fluids. Above the critical temperature and pressure (*i.e.* in the supercritical state) the fluids exhibit a number of specific properties (high density, low viscosity, large diffusivity), which make them intermediate between liquids and gases. In addition, the isothermal compressibility of near-critical fluids become extremely large. As the critical point is approached, the fluids become extremely compressible much more so than ideal gases. Excited by the thermal fluctuations and enhanced by the large compressibility of the fluid, the density fluctuates more strongly as the critical point is approached. A supercritical fluid may be considered macroscopically homogeneous but microscopically, it is inhomogeneous – consisting of clusters of atoms/molecules and free volumes. The vicinity of the critical point is thus characterized by the presence of very-large-scale density fluctuations (or more generally, order parameter fluctuations), which develop throughout the fluid. These order parameter fluctuations are correlated with the correlations having a spatial extent that can be characterized by a correlation length ξ [56, 59, 60]. The specific nature of the critical region therefore involves the appearance of this new characteristic distance, which can become much larger than the inter-particle distance. The correlation length then becomes the natural length scale of critical-point phenomena. Figure 2.2 shows the shadowgram of near-critical SF_6 in a thermostated cell ($p = p_c$, $T = T_c + 10$ μK) under zero gravity (taken during STS-91 at Mir Space Station) [61]. The density inhomogeneity and the correlation length of the near-critical fluid can be clearly observed from this shadowgram.

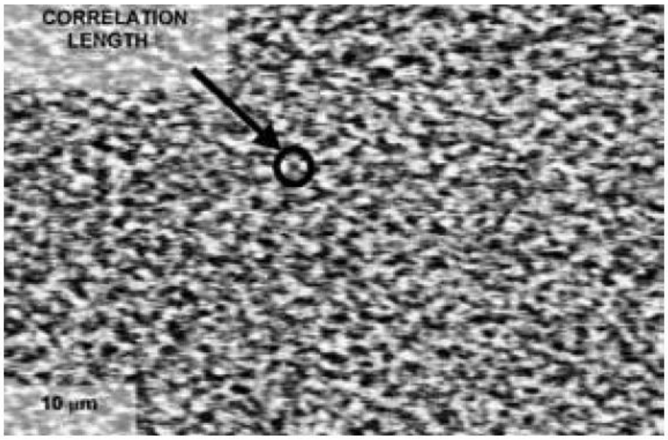

Figure 2.2: Shadowgram of near-critical SF_6 ($T - T_c = 10$ μK) showing large density fluctuations [61].

Apart from the strong dependency on state variables, transport properties of a near-critical fluid undergoing acoustic perturbation can also show dependence on the frequency (f) of the perturbation [62-64]. Normally, the fluctuations in a fluid relax on a time scale much shorter than the period of the perturbation; the fluid remains in equilibrium despite the macroscopic motions within and frequency effects are not detected. On the other hand, when a fluid approaches the critical point, the decay time of the fluctuations (τ_{fluc}) becomes very large. Hence a fluid sufficiently close to the critical point can no longer equilibrate within the time scale of the acoustic process and frequency effects become significant. Variation of the thermo-physical properties of near-critical supercritical fluids are discussed in the following sub-sections in context of the work presented in this dissertation.

2.1.1. Variation of transport and thermo-physical properties near the critical point

Near the critical and pseudo-critical states of a pure fluid, the thermo-physical properties exhibit unusual behaviors; showing large gradients for a small change in the state variables (pressure and temperature). Figure 2.3 shows a pressure vs. specific volume (p-v) diagram [22] for carbon dioxide in gas, liquid, gas-liquid mixture and supercritical states. The critical pressure (p_c) for carbon dioxide is 7.3773 MPa, the critical temperature (T_c) is 304.1282 K and the critical density (ρ_c) is 467.6 kg/m^3 [3].

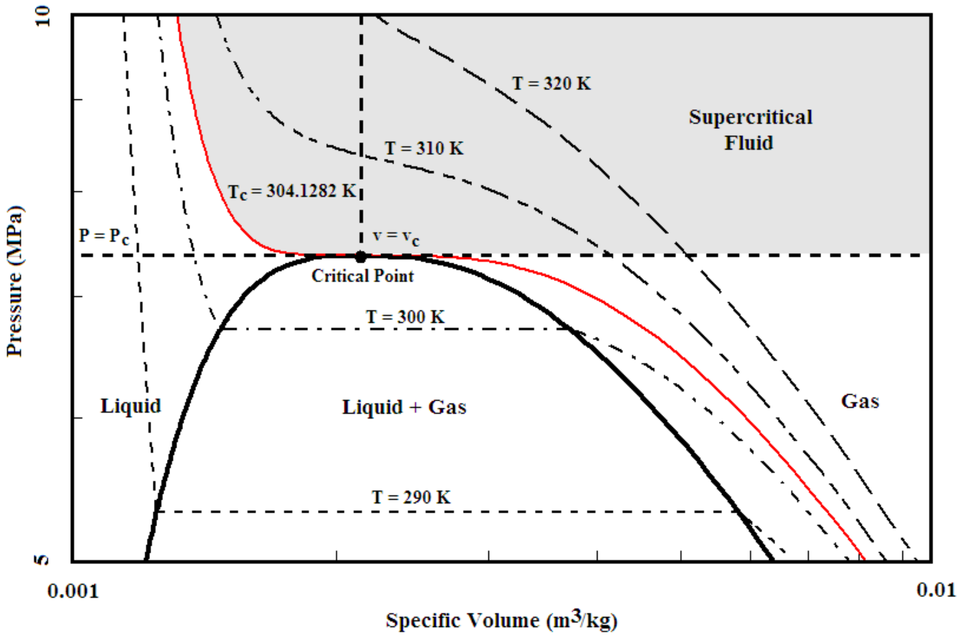

Figure 2.3: The p-v diagram for carbon dioxide [3].

The equation of state describing the *ρ-p-T* relation of supercritical fluids is complicated. It has been shown earlier [39, 56] that the van der Waals equation of state does not represent the properties of supercritical carbon dioxide accurately near the critical point. In this dissertation research, the NIST Standard Reference Database 23 [3] is used for evaluating the *ρ = f(p, T)* relations and most other thermodynamic and transport properties of supercritical fluids. The NIST23 [3] equation of state describing the *ρ-p-T* relation for carbon dioxide is based on the equation of state proposed by Span and Wagner [65], which is mainly empirical in nature and includes special non-analytic terms to predict the correct behavior of the fluid to the immediate vicinity of the critical point.

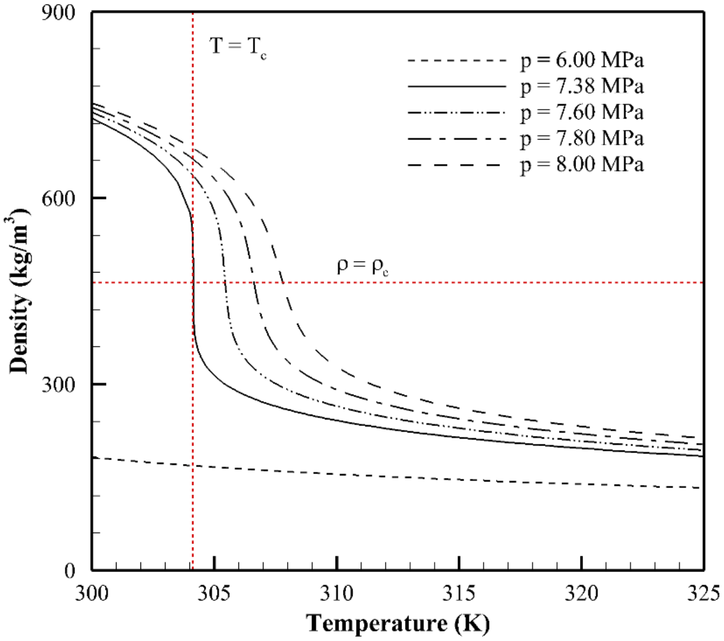

Figure 2.4: Variation of density as a function of pressure and temperature for near-critical CO_2 [3].

Figure 2.4 shows the density vs. temperature (*ρ-T*) relationship of carbon dioxide at different pressures ranging from sub-critical to supercritical states. The density of carbon dioxide at a sub-critical pressure (say, 6.0 MPa) varies slightly with temperature, while the density in the near-critical pressure condition (~ 7.38 MPa) varies widely across the phase interface from the liquid or vapor to the supercritical fluid phase. Above the critical point, the thermo-physical property variations are mainly characterized by the *pseudo-critical* states. The pseudo critical state of a pure fluid can be defined as the state in near-critical supercritical region at which the density of the fluid is equal to its critical density (*i.e.* where $\rho = \rho_c$) and the thermodynamic and transport properties have their maximum rate of change with temperature, at a given supercritical pressure [66]. Its significance is that, below the temperature corresponding to the pseudo-critical state (where $\rho / \rho_c > 1$), the fluid has liquid-like properties while above (where $\rho / \rho_c < 1$); it more closely resembles a vapor.

Figures 2.5(a) and 2.5(b) show the variation of thermal diffusivity (α) and thermal conductivity (k) of carbon dioxide with temperature respectively at different pressures and also along the critical isochor ($\rho = \rho_c$). It is observed that along the pseudo-critical states, thermo-physical properties of pure fluids experience significant changes. In particular, the thermal diffusivity (α) and acoustic speed (c_s) approaches very small values while the thermal conductivity (k), specific heat (c_p) and isothermal compressibility (β) tends to very high values. Hence, even around 10 K above the critical temperature (304.13 K), carbon dioxide is found to be compressible but the density remains high. The specific heat also shows a strong divergence around the critical point. Due to these divergences of thermo-physicals properties at the critical point, thermal diffusion at 10 K above the critical point is about 170 times slower than that at the ambient conditions (and about 3000 times slower at T_c + 0.1 K).

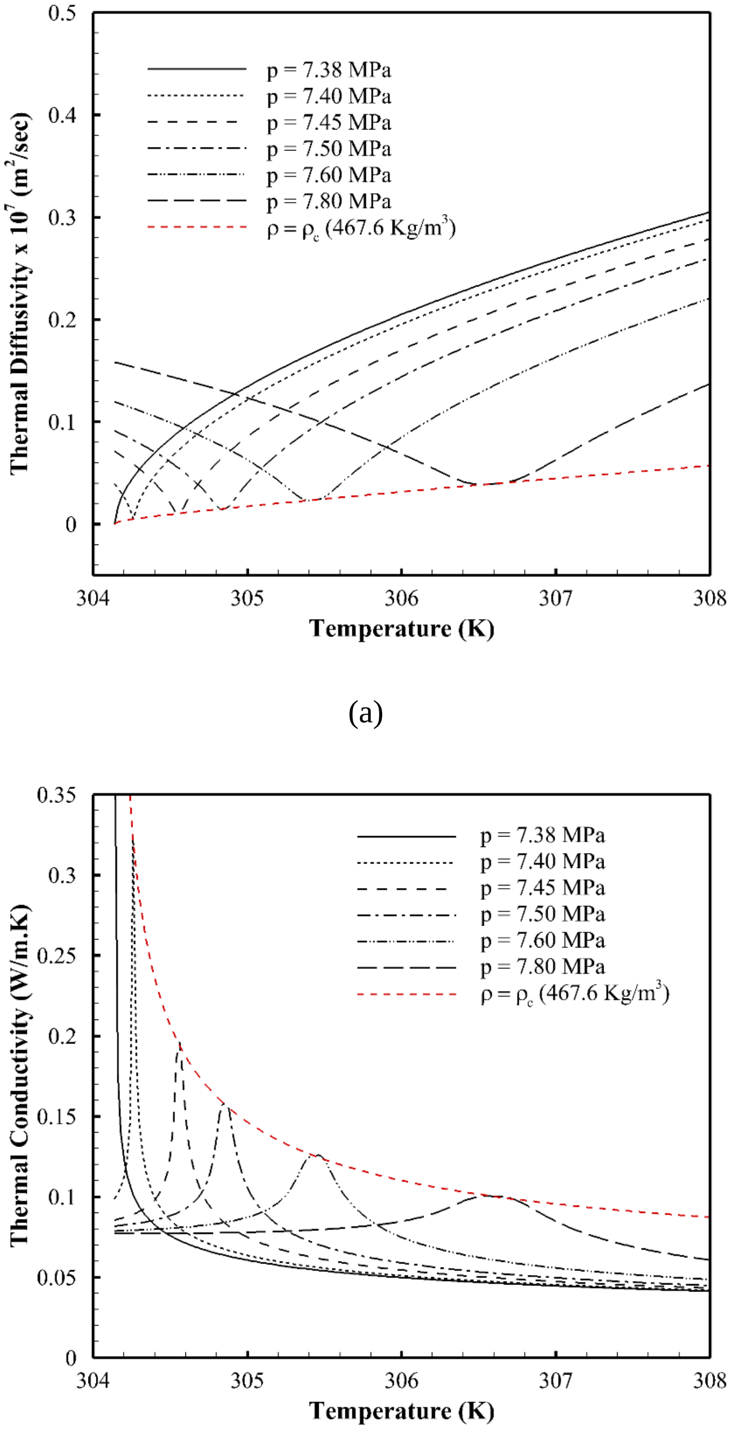

(a)

(b)

Figure 2.5: Variation of (a) thermal diffusivity and (b) thermal conductivity as a function of temperatures at different pressure for near-critical carbon dioxide [3].

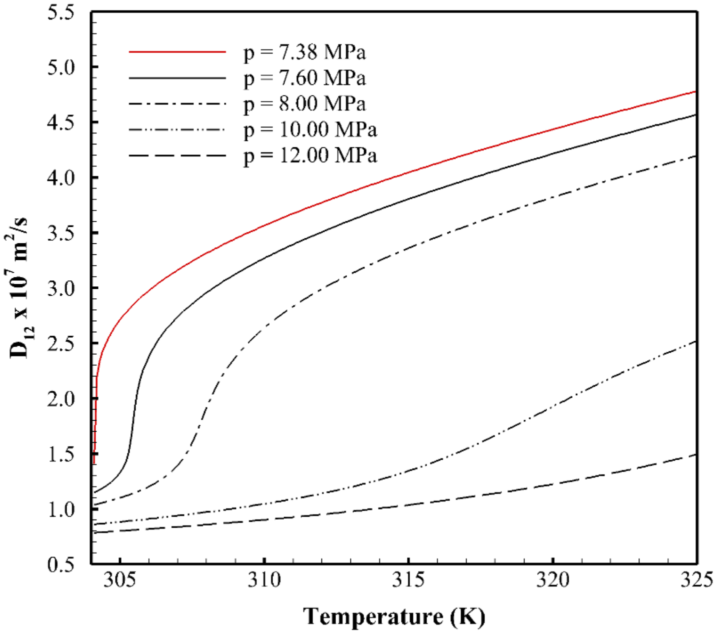

Figure 2.6: Variation of the calculated binary diffusion coefficient (D_{12}) of caffeine in supercritical carbon dioxide as a function of temperature at different pressures near the critical point of carbon dioxide.

The binary diffusion coefficients of different species in a supercritical solvent can be calculated using the correlation developed by Catchpole and King [67, 68]. The correlation can be used to estimate both self and binary diffusion coefficients in a range of near critical solvents (including supercritical carbon dioxide) with an average error of 10%. The binary diffusion coefficient of caffeine ($C_8H_{10}N_4O_2$) in supercritical carbon dioxide as obtained from Catchpole and King [67] correlation is shown in figure 2.6. It is observed that the binary diffusion coefficient of caffeine in supercritical carbon dioxide is a strong function of pressure and temperature and it closely follows the density variation of supercritical carbon dioxide in the near critical region with very small coefficient of diffusivity near the critical point. Correlation developed by Gurdial *et al.* [69] is used to calculate the solubility of a solute in supercritical solvents. The variation of equilibrium mole fraction of caffeine in supercritical carbon dioxide is shown in figure. 2.7.

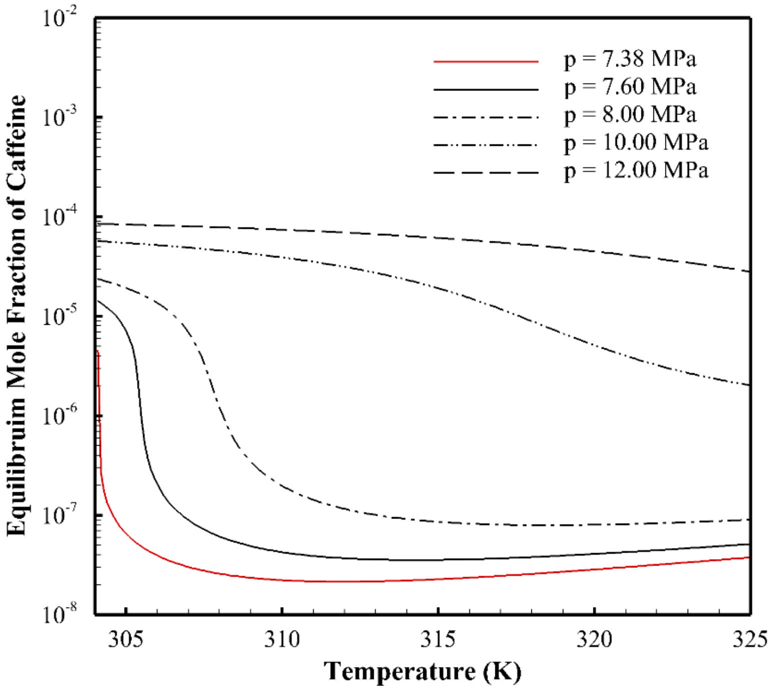

Figure 2.7: Variation of the calculated equilibrium mole fraction of caffeine in supercritical carbon dioxide as a function of temperature at different pressures near the critical point of carbon dioxide.

Another thermo-physical property, the bulk viscosity (μ') also shows significant variations near the critical point of a fluid. Bulk viscosity is a measure of the resistance of a fluid which is being deformed by a normal stress [70]. Mathematically, bulk viscosity is given by:

$$\mu' = \lambda + \frac{2}{3}\mu \tag{2.1}$$

Here λ is the second coefficient of viscosity and μ is the shear viscosity. Bulk viscosity becomes important only for such effects where fluid compressibility is essential. For most gases and incompressible fluids, the Stokes hypothesis [70] is valid and the bulk viscosity is considered to be negligible. However, for supercritical fluids, near the liquid-vapor critical point, the bulk viscosity is significant and the value diverges at the critical point and along the pseudo-critical states in the near-critical zone. In the present work, Onuki's equation [56, 71] is used for calculating the zero frequency bulk viscosity (μ') of carbon dioxide:

$$\mu' = \left(\frac{R_B \rho {c_S}^2 \tau_{fluc}}{1+Q} \right) \tag{2.2}$$

Here, R_B is a constant (~ 0.03), ρ is the density, c_s is the acoustic speed and for carbon dioxide, Q is given by:

$$Q = -0.9\left(T/T_C - 1\right)^{0.11} \tag{2.3}$$

The fluctuation relaxation time (τ_{fluc}) is given by [56]:

$$\tau_{fluc} = \frac{6\pi\xi^3\mu}{k_B T_C} \tag{2.4}$$

Here, ξ is the correlation length of the critical fluctuations and k_B is the Boltzmann constant. On the critical isochore ($\rho = \rho_C$), Onuki [72] gave:

$$\xi = \xi_0 \left(T/T_C - 1\right)^{-0.63} \tag{2.5}$$

Here, $\xi_0 = 1.5\,\overset{o}{\mathrm{A}}$ for CO_2. However, for thermodynamic states that are not on the critical isochore the above expression for calculating the correlation length is not valid. Moldover *et al.* [73] gave a more generalized expression for calculating the correlation length, ξ :

$$\xi = \xi_0 r^{-0.63}\left(1 + 0.16\theta^2\right) \tag{2.6}$$

Here, the parameters r and θ can be found by simultaneously solving the following non-linear equations:

$$r(1-1.2766\theta^2)-\left(\frac{T-T_C}{T_C}\right)=0 \tag{2.7}$$

$$r^{0.325}(1+0.055\theta^2)\theta-\left(\frac{\rho-\rho_C}{\rho_C}\right)=0 \tag{2.8}$$

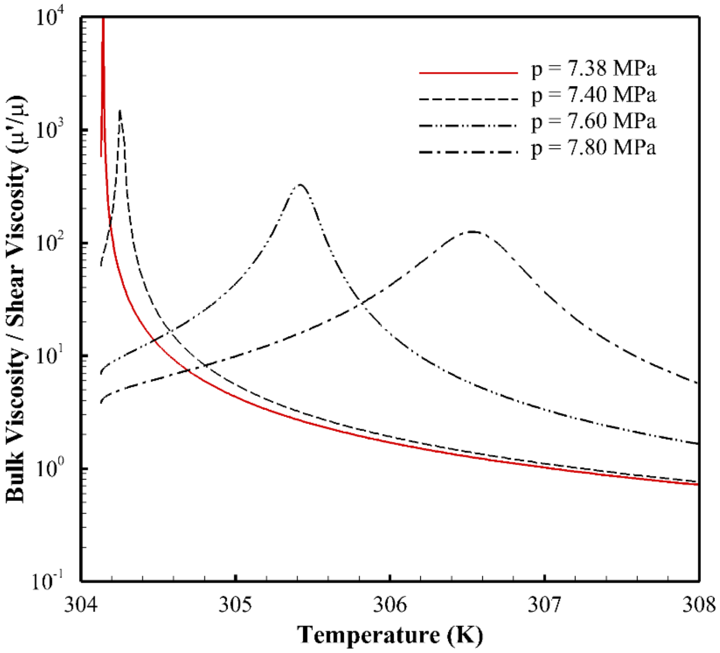

Figure 2.8: Variation of the ratio of bulk viscosity to shear viscosity as a function of temperatures at different pressure for near-critical carbon dioxide.

Figure 2.8 shows the calculated bulk viscosity to shear viscosity (μ'/μ) ratio of supercritical carbon dioxide as a function of pressure and temperature near the critical point. The bulk viscosity tends to infinity when temperature and pressure approach critical values. This divergence of bulk viscosity of pure fluids along the pseudo-critical states plays a major role in the thermal equilibration of near-critical fluids.

2.2 Thermoacoustic transport

There has been a considerable amount of analytical, numerical and experimental studies on thermoacoustic waves [7, 74-77]. The past studies can be divided into two categories: thermally induced acoustic waves in ideal gases and in supercritical fluids. Investigations in both of these categories are reviewed in detail in the following subsections.

2.2.1 Thermally induced acoustic waves in ideal gases

In 1899 Lord Rayleigh [78], starting from the Navier-Stokes equations for compressible fluids, derived an approximate solution in the form of a series for the generation of a pressure wave with a finite amplitude induced by the imposition of a high temperature plane in a gas. Trilling [79] also treated the problem of thermally induced sound fields in a semi-infinite body of a perfect gas, subjected to a step change in temperature at the solid wall. The one-dimensional compressible flow equations were linearized and a closed-form asymptotic solution was obtained using a Laplace transform technique. He also determined how sound intensity depended on wall temperature history by developing analytical solutions. Larkin [80] was the first to develop a finite difference solution to study the thermally induced acoustic waves, in a confined gas, generated by instantly heating one parallel plate with the other maintained at the initial temperature. He employed an explicit finite difference scheme for the continuity and momentum equations, but an implicit one for energy equation. His solution predicted the generation of a thermally induced acoustic wave traveling approximately at the local acoustic speed in helium. Additionally, he found that neglecting the convective and dispersive terms in the momentum equation was not permissible. Kassoy [6] studied the response of a perfect gas confined in a slot to a monotonically varying temperature disturbance at the boundaries, employing a variety of perturbation methods. Kassoy investigated this problem in two time scales: acoustic time scale and conduction time scale. On the acoustic time scale, the solutions were based on a thin expanding conduction boundary layer adjacent to the slot wall and an isentropic core in which a thermally induced acoustic wave propagates. On the conduction time scale, the governing equations were found to include nonlinear convection and pressure work terms. Additionally, a weak acoustic field was found to be propagating in the spatially anisotropic system. Radhwan and Kassoy [81] investigated the behavior of a gas confined between infinite parallel planar walls subjected to significant heat addition. The solutions were developed in terms of asymptotic expansions, which are valid when the ratio of the acoustic time scale to the conduction time scale is small. Ozoe *et al.* [82, 83] numerically studied one- and two-dimensional thermoacoustic convection, due to rapid heating of one of the enclosing walls, in a confined region filled with a compressible fluid. The compressible Navier-Stokes equations with constant viscosity, constant conductivity and negligible viscous dissipation were non-dimensionalized, and numerically solved by a finite-difference method, with the convective terms approximated by a first-order upwind scheme, which is a flip-flop procedure depending on the sign of the velocity. The pressure waves were captured with substantial numerical diffusion in their numerical results. It is also shown that the fluctuating velocity generated by the pressure waves greatly enhance the rate of heat transfer over that for pure transient conduction. They also studied effects of various parameters, such as gravity, viscosity, wall temperature, and fluid properties on the development of convection. The description of thermally induced acoustic waves in a fluid by the Navier-Stokes equations (continuity equation, momentum equation and energy equation) along with an appropriate equation of state was compared, by Churchill and Brown [84], with that provided by the hyperbolic conduction equation. Churchill and Brown found that the Navier-Stokes equations with the equation of state provided a satisfactory model for thermally induce acoustic waves for short, long and intermediate times. However the simplified hyperbolic conduction equation model just provided a crude approximation, due to the postulate of a wave velocity with a constant magnitude, was thereby invalid for the wave generation, propagation and dissipation. Brown and Churchill [77] also numerically investigated, with finite-difference method, thermally induced acoustic waves in a gas by rapid heating of a bounding solid surface. The numerical predictions showed that rapid heating of a solid surface bounding a region of gas generates a slightly supersonic wave with positive amplitude in pressure, temperature, density and mass velocity, which are in good qualitative agreement with prior experimental measurements. Thermally induced acoustic waves in a semi-infinite medium [85] and in a confined medium [86] were theoretically and numerically investigated by Huang and Bau. Huang and Bau solved the linearized wave model with asymptotic methods and a numerically inverted Laplace transform. Farouk *et al.* [7] used a control-volume-based flux-corrected transport algorithm to predict the early time behavior of thermally induced acoustic waves in a compressible-fluid filled cavity. In their numerical model, the temperature dependent fluid properties were used. Aktas and Farouk [87] studied the effect of gravity on the fluid motion generated by the thermally induced acoustic waves in a rectangular enclosure. The gravitational acceleration was found to have a negligible effect on the behavior of thermal induced acoustic wave for early times. A uniformly heated side wall was considered and the flow development of thermally induced acoustic waves under zero-gravity conditions was not studied. Lin *et al.* [88, 89] numerically investigated the flows generated by thermally induced acoustic waves in an enclosure with and without gravity, using a control-volume-based flux corrected transport algorithm. They considered that the left wall of the enclosure was heated rapidly either in a spatially uniform or a non-uniform manner, whereas the right wall was held at the initial temperature of the gas. Their simulations showed that, at zero gravity, the spatially non-uniform heating induced a vortical flow in the enclosure, similar to that found in buoyancy-induced flows in a side-heated enclosure.

The generation of thermally induced acoustic waves in gases has been studied experimentally by only a few investigators. Parang and Salah-Eddine [90] investigated the thermoacoustic convection phenomena in a cylinder containing air in both normal and reduced gravity environments. In their resulting measurements of air temperature, no oscillations was recorded due to the small oscillation amplitude and low sample rate of measurement, but the air temperatures were found to rise much faster than in the computational results for the case of pure conduction. No pressure measurement was reported. Experimental measurements of pressure waves generated by rapid heating of a surface were reported by Brown and Churchill [74]. In their experiments, the rapid heating procedure was achieved by an *R*-*C* circuit. The pressure measurements in the wall of the closed chamber clearly demonstrated the generation of acoustic waves by rapid heating of a wall. Lin and Farouk [75] experimentally investigated the behaviors of thermally induced acoustic waves generated by rapid heating of a bounding solid wall in a closed cylindrical tube. Following Brown and Churchill [74], they used a *R-C* circuit to generate a rapid temperature increase in a thin nickel foil located at one end of the closed cylindrical tube, generating a thermally induced acoustic waves. They measured the characteristics of generation, propagation, and decay of the acoustic waves with two different pressure transducers, and found that the measured decay rate of the acoustic waves was somewhat faster than the numerically predictions.

2.2.2 Thermally induced acoustic waves in near-critical fluids

Thermally induced acoustic waves are much stronger in supercritical fluids than in ideal gases under the same temperature increase and the rate of increase [91]. Because of the specific properties of supercritical fluids, such as the vanishingly small thermal diffusivity near the critical point, thermally induced acoustic waves play a dominant role in temperature equilibration [92, 93]. Due to the vanishingly small thermal diffusivity near the critical point, very long time to reach equilibrium was expected for heat transfer in near-critical fluids. However, thermoacoustic waves in a confined layer of near-critical fluid induce an adiabatic compression of the bulk fluid which results in a homogeneous temperature increase of the bulk. This adiabatic compression known as the '*piston effect*' phenomena in fluids near the gas-liquid critical point, was first explained by Boukari *et al.* [94] using thermodynamic analysis and was later confirmed by Onuki *et al.* [95, 96] using analytical solution of linearized hydrodynamic equations.

Zappoli *et al.* [97, 98] studied the response to a boundary heating of supercritical CO_2 under microgravity by numerically solving the complete one-dimensional Navier-

Stokes equations. The van der Waals equation of state for supercritical CO_2 was used in this study. However, the internal energy of supercritical CO_2 (as it appears in the energy equation) was considered as a function of temperature only, which is correct only for ideal gas. The PISO (Pressure Implicit with Splitting of Operators) method was employed to solve the one-dimensional Navier-Stokes equations. The temperature of one boundary was increased linearly by 13.0 mK in 1.3 ms. Figure 2.9a and 2.9b shows the temperature profiles for short times and for longer times respectively. Both figures show rapid thermal equilibration in the supercritical CO_2. It was concluded that the thermal energy is transformed into kinetic energy in a hot expanding boundary layer, which in turn transformed into thermal energy in the bulk fluid.

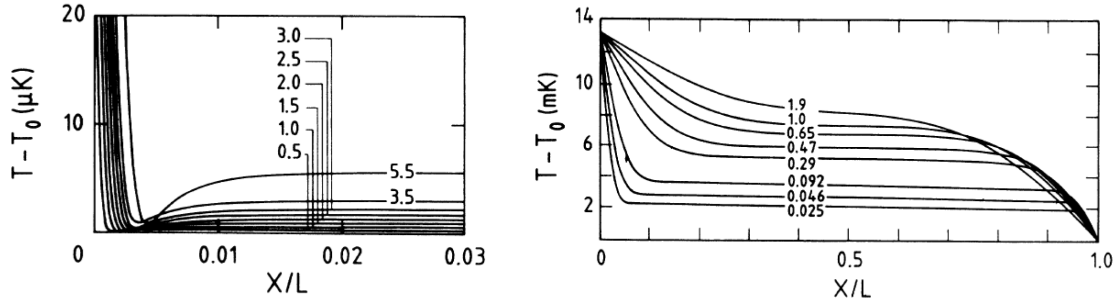

(a) (b)

Figure 2.9: Temperature profiles (a) in the short time scale for different acoustic times (t/t_a: where t_a = 11.5 μs) and (b) in the longer time scale for different diffusion times (t/t_d; where t_d = 157 s) [98].

Klein *et al.* [99] published their experimental results of temperature propagation in near-critical sulfur hexafluoride (SF_6). The SF_6 sample of critical density was housed in a cylindrical copper cell. The sample was rapidly cooled down form a temperature some milli-Kelvins above the critical temperature to a temperature some milli-Kelvins below the critical temperature under reduced gravity in a sounding rocket of the TEXUS

(*Technologische Experiment unter Schwerelosigkeit*) program. At the critical temperature, thermal diffusivity of SF_6 is of the order of $10^{-7}cm^2/s$. This, along with the thermal length of 2.0 mm of Klein's sample cell, leads to a thermal relaxation time of the order of about 100 h. However in Klein's microgravity experiments, temperature changes were found propagating through the sample cell within seconds. Based on their experiment results and the theory of Onuki *et al.*[96], Klein *et al.* [99] pointed out that using thermal diffusivity in relaxation time estimation only qualifies for samples at constant pressure. If the sample volume is fixed and gravity convection is absent, the propagation of temperature changes into the interior region of the fluid near its critical point is mainly proceeding by adiabatic heating, like the temperature rise due to adiabatic compression. Temperature changes somewhere in the fluid cause expansion or contraction of the adjacent fluid. This in turn causes a pressure change throughout the sample volume with the consequence that the sample temperature is changed adiabatically and quickly.

Zappoli and Carles [100] numerically studied the thermo-acoustic nature of piston effect. The problem geometry was a 1-D slab-like container filled with a near-critical fluid, which was submitted to a given heat flux at the boundary. Zappoli's governing equations [100] were non-dimensional 1-D compressible Navier-Stokes equations, in which the internal energy of near-critical fluids was assumed to be a function of temperature only. This assumption does not qualify for supercritical fluids. For other properties in the governing equations, such as thermal conductivity and viscosity, Zappoli and Carles [46] used the formulation:

$$\frac{\lambda'}{\lambda'_0} = 1 + \Lambda[(T' - T_C)/T_C]^{-0.5} \tag{2.9}$$

Here λ' is the dimensional property, λ_0' denotes the property of the ideal gas. T' is temperature and T_C' is the critical temperature. Λ is a constant. Along with the van der Waals equation of state, the 1-D compressible Navier-stokes equations were solved by the matched asymptotic expansion method and multiple-time-scale techniques. Figure 2.10 shows temperature profiles at $t = 0.25$ s and $t = 0.5$ s for a 0.5 s boundary heating at constant flux. The homogeneous heating of the bulk fluid can be seen from this figure.

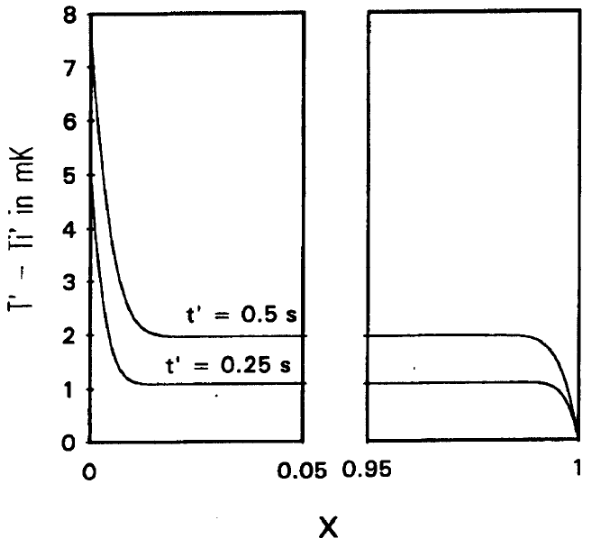

Figure 2.10: Temperature profiles at $t = 0.25$ s and $t = 0.5$ s for a 0.5 s boundary heating at constant flux [100].

The mechanisms of heat and mass transport in a side-heated square cavity filled with a supercritical fluid were explored numerically by Zappoli *et al.* [76] with emphasis on the interplay between buoyancy-driven convection and the thermally induced acoustic waves. The response of a fluid in near-critical conditions to a heat pulse, in the absence of gravity effects was also studied experimentally by Garrabos *et al.* [93]. The study demonstrated that the dynamics of thermal relaxation is governed by two typical time scales, a diffusion time and a time associated to the adiabatic heat transport. They also provided interferometric observations of the piston effect under terrestrial and micro-gravity conditions. Formation of a hot boundary layer around the upper heating thermistor was observed. Also fading out of this boundary layer and the reappearance of distorted fringes was noticed as time proceeds. Time comparison of the relaxation process of the hot boundary layer density inhomogeneities for the two different initial temperatures T_i evidences the diffusive critical slowing down. A striking observation was the simultaneous shift under weightlessness of the whole fringe pattern, with the fringes remaining straight and parallel. This bulk phenomenon, which coincides with the growth of the hot boundary layer, is the signature of the piston effect phenomena [101]. Lei [40] numerically investigated the generation and propagation of thermoacoustic waves in supercritical nitrogen and carbon dioxide by solving a fully compressible form of the Navier-Stokes equations and variable thermo-physical property relations. However, the model failed to predict the piston effect phenomena in supercritical fluids.

Piston effect in a layer of supercritical nitrogen was recently studied numerically by Shen *et al.* [102] by employing a real fluid equation of state based on thermodynamic relations. The results show that, dependent on the rapidity of the heating, inherently different fluid dynamical wave behaviors occur on the acoustic timescale with respect to acoustic emission, propagation, and reflection patterns. Specifically, the sudden ramp of the boundary temperature is capable of triggering a strong thermoacoustic pulse in the fluid, whose reflection at the isothermal boundary introduces complex features. In contrast, linear compressive waves dominate under the gradual heating. On a longer timescale, both types of fast processes lapse into slow thermal diffusion coupled by pronounced density inhomogeneities, via different routes nonetheless.

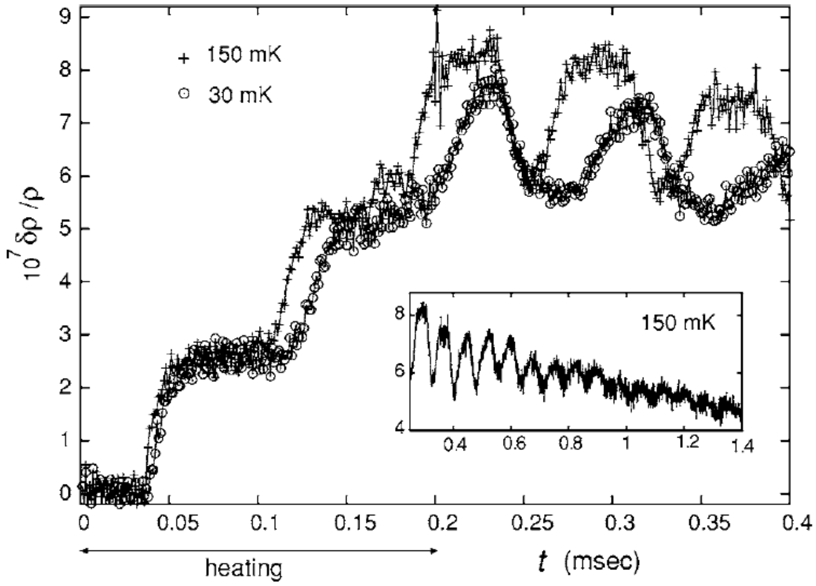

Figure 2.11: Normalized density change at the cell center in the time region 0 ~ 0.4 ms for $T - T_c = 150$ and 30 mK, produced by continuous heating in 0 ~ 0.2 ms in a cell of length 1.03 cm. Inset: Long-time behavior for $T - T_c = 150$ mK in the time region 0.2 ~ 1.4 ms [103].

Due to the difficulty of experimentation near the critical point (hydrodynamic stability, measurement in high pressures), only a few experimental studies are reported in the literature. By means of laser holographic interferometry the long-term evolutions of the piston effect in supercritical nitrogen [104] was measured and compared against theoretical analyses, which yielded good agreement. Lei [40] attempted to measure thermally induced acoustic waves both in supercritical nitrogen and carbon dioxide far from the critical point. However, the pressure field measurements were severely obstructed by the convective flows induced by inhomogeneous heating of the experimental cell. Acoustic emission and propagation caused by rapid boundary heating in near-critical carbon dioxide was first measured by Miura *et al.* [103]. They developed an experimental setup to measure density changes of order 10^{-8} g/cm^3 on a time scale of 1 μs in a cell filled with CO_2 on the critical isochore close to the critical point. Figure 2.11 shows the temporal acoustic density variations $\delta\rho(t)$ at the cell center x=L/2 in a cell of L=1.03 cm at $T - T_c$ = 150 and 30 mK. Continuous heating was applied in the time region 0 - 0.2 ms and the supplied heat to the fluid was 367 erg.

2.3 Convective thermal transport in supercritical fluids

Convective thermal transport has been the subject of research for many years due to its importance in the understanding of phenomena appearing in nature and engineering applications. Numerical studies on buoyancy driven convective flow inside an enclosure have been conducted by several researchers. de Vahl Davis [105] numerically investigated the natural convection of air in a square enclosure. This study has widely been accepted as the benchmark solution for such flows. Kimura and Bejan [106] studied natural convection in a rectangular cavity with uniform heat flux imposed at different sides of the cavity. A review of the developments in understanding and modeling of natural convection studies in enclosures can be found in the review paper by Ostrach [107]. However, the above studies are mainly focused toward atmospheric pressure gases.

Due to the increasing number of applications of supercritical fluids in chemical and thermal process industries, convective transport in near-critical and supercritical fluids has drawn a lot attention to the researchers in the recent decade [28, 108-111]. In spite of the number of applications, the heat transfer mechanisms involved in near-critical supercritical fluids has not been studied in sufficient detail. Large scale variation of the thermo-physical properties of fluids in the near-critical region affects the mechanism of heat transfer and particularly that of natural convection. Also as discussed in the previous sections, fluids near their critical point are subjected to a specific temperature equilibration mechanism called piston effect, which becomes increasingly efficient as the critical point is approached. Early experimental investigations by Knapp and Sabersky [20] reported an increase of heat transfer coefficient for natural convection in supercritical carbon dioxide as the critical point is approached. Since then, similar phenomena have been observed for natural convection from electrically heated wires to supercritical carbon dioxide by Hahne *et al.* [31], Neumann *et al.* [22] and Nishikawa *et al.* [112]. However, most of these studies are performed either relatively far from the critical point or covers only a small part of the near-critical region where the thermo-physical properties show a strong divergence.

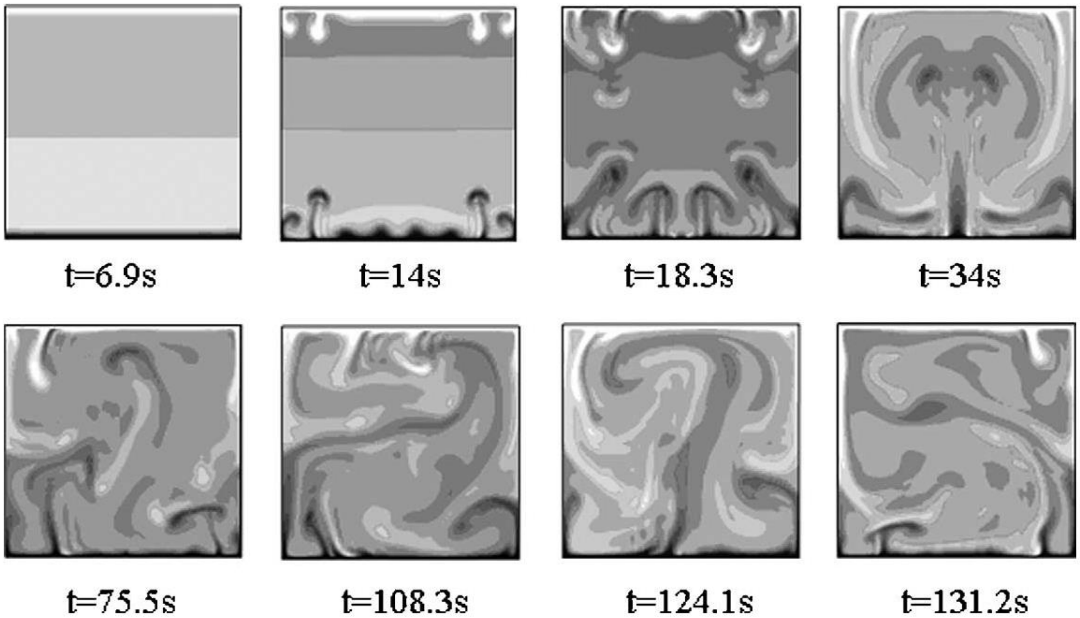

Figure 2.12: Instantaneous temperature fields for $T_i - T_c = 1$ K and temperature difference $\delta T = 2.5$ mK in a bottom heated cavity filled with supercritical CO_2 [113].

A number of numerical studies have also been performed to model the buoyancy driven convective flows and heat transfer in supercritical fluids. Zappoli *et al.* [76] developed a numerical model to predict hyper-compressible, low Mach number and buoyant convection flows for application to a problem involving near-critical fluids subjected under normal gravity conditions to heat addition at a boundary. A three dimensional numerical model for the prediction of supercritical fluid buoyant flows inside heated enclosures was developed by Accary and Raspo [114]. Raspo *et al.* [113] also investigated the buoyancy driven flow of near-critical fluid in a bottom heated cavity. It was observed that, in the convective regime the heat flow which is obtained on long time scales exhibits some characteristics of that observed in turbulent convection in normally compressible fluids: it is composed of plumes in thermal boundary layers, jets on lateral walls and a large-scale flow. The results show that, as it is the case in turbulent convection, this large-scale flow can suddenly change its orientation. Figure 2.12 shows the instantaneous temperature fields for $T_i - T_c = 1$ K and temperature difference $\delta T = 2.5$ mK . Due to the high compressibility and the very small thermal diffusivity of the supercritical fluid, the heating of the bottom wall induces the appearance of three distinct zones in the fluid layer: two very thin thermal boundary layers near the bottom and top walls, in which diffusion realizes heat transfer, and the bulk of the cavity which temperature is homogeneously increased by thermoacoustic effects. Furukawa *et al.* [115] presented a hydrodynamic model of compressible fluids taking into account the piston effect and the adiabatic temperature gradient effect. Several other studies [29, 116, 117] have also been performed to numerically model the buoyancy driven flow in a near-critical fluid.

2.4 Mass transport in supercritical fluids

Mass transport behavior of different species in ideal gases as well as in liquids is a well-studied problem and there have been many fluid-to-solid mass transfer correlations in the literature, such as those of McCune and Wilhelm [118], Williamson *et al.* [119], Wilson and Geankoplis [120] and Upadhyay and Tripathi [121]. Most of these correlations were obtained by applying the solid dissolution technique. Owing to the difference in Schmidt numbers, gases and liquids usually follow different correlations for mass transfer coefficients. The Schmidt numbers for supercritical fluids lie between those for gases and for liquids [122]; hence the correlations obtained for gases and liquids may not be applicable to supercritical fluids. A number of researches have been performed to study transport behavior in supercritical fluids [45, 123-128]. Usually the mass transfer resistance and the binary diffusion coefficients of nonvolatile solutes in supercritical fluids are studied theoretically and experimentally.

Debenedetti *et al.* [129] measured diffusion coefficients of two different solutes (benzoic acid and naphthalene) in supercritical SF_6 and CO_2 experimentally. In a similar study, Knaff *et al.* [130] measured diffusion coefficients of naphthalene and caffeine in supercritical CO_2. The experimental setup consisted of an annular duct with a bar of naphthalene at the center. Catchpole *et al.* [67] also measured the diffusion coefficients of benzoic acid, oleic acid, a-tocopherol, and glycerol tri-oleate over a range of temperatures and pressures in near critical CO_2 and developed a correlation to predict both self and binary diffusion coefficients over a wide density range. The correlation can be applied to nonionic near critical fluids, and does not require additional parameters, such as hard sphere molecular diameters or viscosities. However, most of these studies are based on specific applications (particular solutes) focused towards supercritical fluid extraction systems.

2.4.1 Supercritical fluid extraction (SFE) systems

In recent years supercritical fluid technology has been applied to the extraction of raw materials from both solid matrices and liquid mixtures. Examples of processes in which supercritical fluids are currently used are decaffeination of coffee or tea, removal of pesticides, batch hop extraction, recovery of solvents and the continuous fractionation of beverages and oils [16, 131-134]. Supercritical fluid extraction (SFE) from solid phase is usually carried out in fixed bed extractors (*i.e.* packed extraction columns), while that from fluid phase is carried out using a membrane contactor. Introduction as well as the investigations carried out in both of these systems are provided in detail in the following subsections.

2.4.1.1 Fixed bed extractors

An important application of supercritical fluids is the extraction of one or more components from porous solid matrices. In most cases, this technology constitutes a cleaner alternative to the traditional industrial techniques, which are based on extraction with hydrocarbon solvents. Mass transfer processes take place when a solute is extracted from a fixed bed of a porous material (usually organic components, vegetables, seeds etc.), with a solvent in supercritical or near-critical state. The pressurized solvent flows continuously through the porous bed. After extraction, pressure is reduced and, consequently, solubility decreases and the solute precipitates in a separator. The process is characterized by an extraction curve, the plot of the cumulated extract versus the extraction time or the amount of solvent required in the extractor. Schematic diagram of a typical fixed bed extractor is shown in figure 2.13.

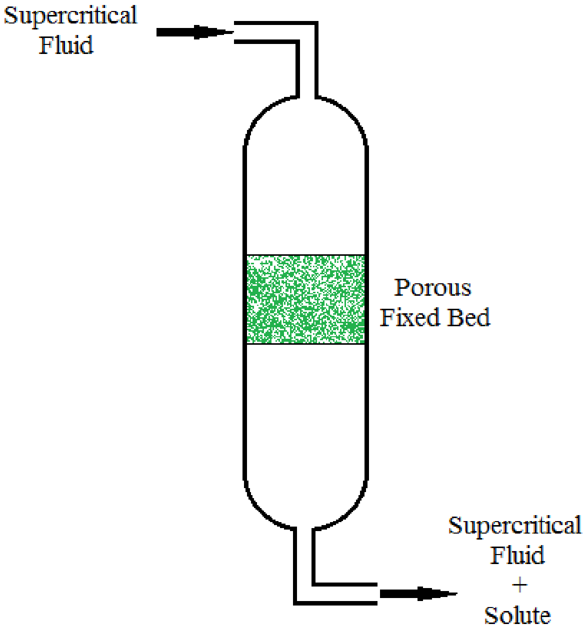

Figure 2.13: Schematic diagram of a typical fixed bed extractor.

Supercritical fluid extraction (SFE) of different organic species in fixed bed extractors has been studied by several authors from the processing point of view and a wide range of seed species has been explored [123, 135-140]. Despite the relatively large number of species processed, only a few numerical models of the SFE of organic solutes have been published [125, 128, 137, 141-144]. Also, the mathematical models proposed are generally based on differential mass balance integration only. Models developed by Bulley *et al.* [123], Lee *et al.* [141] and Fattori *et al.* [135] assumed mass transfer resistances only in the solvent phase. In other models, the authors considered an internal mass transfer resistance.

King and Catchpole [68] used a shrinking core model to describe a variable external mass transfer resistance where the solute balance on the solid phase determines the thickness of the mass transfer layer in the external part of the particles. In a more recent study, Reverchon and Marrone [127] presented a numerical model considering the physical description of organic substrates and it extend the model to all the seed oils obtained by SFE using the data sets available in the literature. Nei *et al.* [145] developed a mathematical model to predict fatty acid extraction from trout powder considering diffusion-controlled regime in the particle and film mass transfer resistance around the particle with axial dispersion of the bulk phase at dynamic conditions. A review of the relevant mathematical models employed for supercritical fluid extraction of solutes from liquids or solids was presented by Oliveira et al [124]. With proper inclusion of the model parameters (solute solubility, diffusion coefficient, packed bed porosity etc.), the mathematical models discussed above can predict the yield of the traditional supercritical extraction process fairly well.

2.4.1.2 Membrane contactors

Separation processes using membrane contactors have been conducted in concentration or purification processes such as solvent extraction, gas absorption, ion exchange and membrane distillation. In membrane contactors, the membrane mainly operates as a physical barrier between two fluids and unlike most membrane operations, the membrane has no selectivity to the separation, *i.e.* it has no impact on the partition coefficients [146, 147]. One of the applications of membrane contactors is supercritical extraction. This process is called porocritical extraction. This process utilizes a hollow fiber membrane contactor to contact two phases for the purpose of separation [147]. A macro-porous membrane provides contact between the aqueous feed (*i.e.* the solute phase) and the supercritical fluid. The aqueous feed solution is passed on one side, while the extraction solvent is flowed on the other side. The aqueous solution is also maintained at a high pressure near the dense solvent to establish interface between solvent and feed. A hydrophobic material is chosen as the membrane, so that the aqueous solution does not penetrate the membrane pores and the supercritical phase can fill the membrane pores. In this process, the driving force is the concentration gradient of the solute between feed and dense solvent. Schematic diagram for a membrane contactor is shown in figure 2.14.

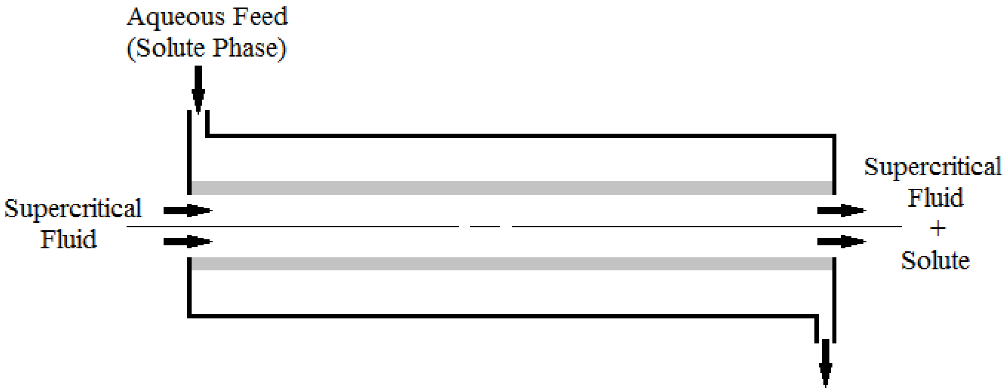

Figure 2.14: Schematic diagram of a typical membrane contactor.

Introducing membrane contactors in supercritical fluid extraction process has been suggested by several authors, main for two different potential applications – solvent recovery after a typical supercritical fluid extraction step and carbon dioxide extraction coupled with cross-flow or countercurrent-flow filtration. Semenova *et al.* [148] studied the separation of supercritical fluid and ethanol mixtures with an asymmetric polyimide membrane and obtained a separation factor (α-ethanol / CO_2) of 8.7. For the separation of supercritical CO_2 / iso-octane mixtures, a separation factor of 12.8 was obtained by Ohya *et al.*[149]. Sartorelli and Brunner [150] used two different inorganic membranes to separate low volatile compounds from supercritical carbon dioxide extracts. Retention factors between 80 and 90% were reported in this study. Regeneration of supercritical carbon dioxide from caffeine loaded gas phases was achieved by commercial nano-filtration membranes, with a ZrO_2–TiO_2 thin layer [151]. Finally, Carlson *et al.* [152] applied reverse osmosis membranes (thin layer supercritical membrane) to separate efficiently limonene (94% retention factor) from supercritical carbon dioxide extracts.

The use of hollow fiber micro-porous membrane contactors in supercritical fluid extraction processes has been reported in the literature in recent years [153-155]. Sarrade *et al.* [156] proposed the coupling of supercritical carbon dioxide extraction with nano-filtration separation to extract and purify low molecular weight compounds. A tubular membrane of nano-filtration resistant enough to endure supercritical conditions was applied to two different processes – the fractionation of triglycerides from fish oil and the purification of β-carotene issued from either carrot oils or carrot seeds. The coupled process lead to good quality extracts.

2.4.2 Enhancement of mass transport using acoustic waves

The conventional process of supercritical fluid extraction (either in a fixed bed extractor or in a membrane contactor) has a very slow dynamics even when solute free solvent is re-circulated and therefore improvements in the extraction process are required [157]. The use of acoustic waves represents a potential efficient way of enhancing mass transfer processes in the supercritical region [13, 46-49]. This is due to the effects produced by compressions and decompressions, as well as by radiation pressure and acoustic streaming. In addition, this is probably the unique practical way to produce agitation in the system because the limitation of use of mechanical stirrers.

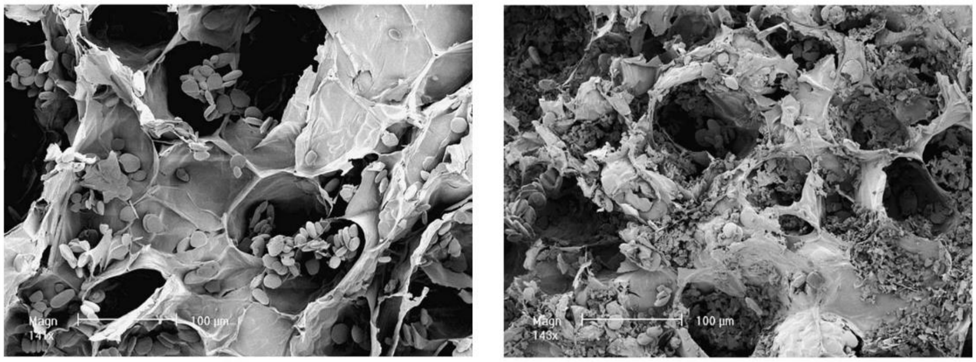

(a) (b)

Figure 2.15: FESEM images of ginger particles. (a) Experiments without the influence of ultrasound and (B) experiments with ultrasound [46].

Balachandran *et al.* [46] studied the influence of ultrasound on supercritical extraction based on extraction from a freeze-dried ginger sample. The study reported a significant increase in the yield of pungent compounds from ginger under the influence of ultrasound, with improvements of up to 30% towards the end of the extraction period. The ginger particles were also analyzed by field emission scanning electron microscopy (FESEM). Figure 2.15 shows the FESEM image of the ginger particles with and without the ultrasonic excitation. The observations suggest that the intensification of mass transport is due to physical effects on the surface of the particles (SEM showed clear evidence of cellular damage).

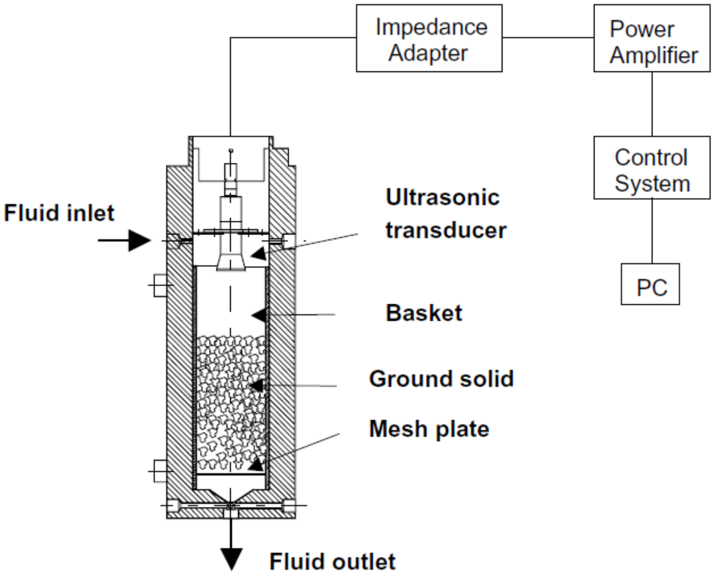

Figure 2.16: Schematic diagram of the extractor used by Riera *et al.* [49].

In a recent experimental study, Riera *et al.* [48, 49] proposed power ultrasound assisted supercritical fluid extraction to enhance the mass transport in almonds oil extraction. The ultrasonic system is composed of a power piezoelectric transducer (Langevin type) with a 100 W power capacity, an impedance matching box and a power generator unit. This unit consists of two parts – a power amplifier and a resonant frequency control system to keep constant the power applied to the transducer during the SFE process. The control system generates a signal which lies within the resonance frequency band of the transducer during operation. A schematic diagram of the extraction system used in these studies is shown in figure 2.16.

Although results from these studies show that power ultrasound significantly accelerates the kinetics of the process and improves the final extraction yield, characteristics of the extraction curve from these two studies are significantly different.

Balachandran *et al.* [46] proposed that the improvement in extraction yield is attributed to an increase in solubility of the solute in the solvent at the early time. While, according to Riera *et al.* [48, 49], this is due to an increase in the mass transfer coefficient in the convective regime.

2.5 Relevance and significance of present research

Supercritical fluids have gained increased importance in thermal transport and chemical process industries in the recent past. However, basic understanding of the transport phenomena in the near-critical states as well as improvements of the transport processes associated with supercritical fluids are needed to increase the efficiency and effectiveness of the current state of the art supercritical fluid systems. These improvements in performance can be achieved by superior design and performance prediction models. There are numerous analytical and numerical models available in the literature to predict supercritical fluid transport. However, most of the published research work is based on some simplified (and sometimes questionable) assumptions about the equation of state and thermo-physical properties in the near-critical region. In general, thermo-physical properties of supercritical fluid are considered to be constants [97, 158] or a function of temperature only [100, 159-163] whereas it is a function of both temperature and pressure (or density).

The research performed in the past on the thermoacoustic convection in near-critical fluids has resulted in numerous models that have been able to predict the generation and propagation of thermoacoustic waves. However, the transitional behavior of the thermoacoustic waves from a subcritical to supercritical phase has not been reported in the literature. While piston effect phenomena in near-critical fluids is reported in literature numerous times [72, 94-97, 100, 159, 161-165], most of these studies are analytical in nature and the piston effect is investigated quite far (Generally, T_c + 1.0K) from the critical point to avoid critical divergence of the thermo-physical properties. Several earlier studies [95, 159] reported that, under the same temperature perturbation at the boundary, stronger acoustic fields can be generated in near-critical fluids as the critical point is approached. But, the different near-critical fluid states considered in these studies were along the critical isochor ($\rho = \rho_c$) only. Thus, a detailed description of the behavior of the piston effect phenomena in the near-critical supercritical region covering the pseudo-critical states is absent in the literature. Additionally, effect of the critically diverging bulk viscosity on the thermoacoutic transport has not been investigated in the past. Experimental studies on the behavior of the thermoacoustic phenomena in the near-critical supercritical region detailing the temperature and pressure measurements are also not reported in the literature. Since, convection of a pure fluid near the critical point is difficult to study both experimentally and theoretically due to the critical divergence of the thermo-physical properties, no satisfactory correlations are currently available to predict the convective heat transfer in near-critical fluids.

Transport processes in supercritical fluid extraction systems are generally modeled using the species (mass) conservation equation with a constant flow-field [124, 141, 142, 145, 166]. However, models solely based on the differential mass balance integration are unable to predict the yield of the extraction process under an oscillating flow field or in complex geometries. Full hydrodynamic description of the solvent fluid along with proper mass balance of the solute and solvent phases are necessary in this regard. Guardo et al. [167, 168] developed a CFD model to predict the particle-to-fluid mass transfer coefficients in supercritical fluid solvents in a packed bed reactor. But, the model does not take into account the actual dynamics of the transport processes associated with supercritical fluid extraction process (solute solubility, particle porosity and finite mass of the solute) and cannot accurately predict the yield too. A reliable and validated CFD model of the supercritical fluid extraction process for understanding the near-critical transport phenomena in supercritical fluid extraction systems is not available in the literature.

A comprehensive research program was undertaken to overcome the shortcomings of the past research in the field of transport in near-critical fluids focused towards thermal and chemical process systems. The goal was to develop robust computational models to design and predict the transport processes in these systems and provide useful design guidelines based on the predictions of the models. To accomplish this, four main focus areas were chosen: (a) studying the thermoacoustic wave induced transport phenomena in near-critical fluids, (b) experimentally investigating thermoacoustic wave generation and propagation in near-critical fluids, (c) computationally studying the transport processes in supercritical fluid extraction systems and (d) investigating transport enhancement in supercritical fluid extraction systems using acoustically augmented flow.

CHAPTER 3: NUMERICAL INVESTIGATION OF THERMOACOUSTIC TRANSPORT IN NEAR-CRITICAL SUPERCRITICAL FLUID[2]

3.1 Introduction

Thermal and mechanical processes in compressible fluids are closely coupled and a local thermal disturbance is always followed by a mechanical response, and vice versa. When a compressible fluid is subjected to a fast temperature increase at a solid surface, the fluid in the immediate vicinity of the boundary is heated by conduction and tends to expand. The sudden expansion of the fluid due to the energy input is constrained by the inertia of the unperturbed media and it induces thermoacoustic waves from the heated wall. the heat transfer effects of such waves may be very significant when the fluid is close to the thermodynamic critical point or when other modes of convection are weak or absent [98, 170]. The diminishing thermal diffusivity and diverging compressibility character of near-critical fluids make the thermoacoustic convection mode of heat transport significant for cryogenic storage systems which involve rather weak diffusive and convective transport of heat, especially in a reduced-gravity environment [76].

In this chapter, the generation and propagation of thermally induced acoustic waves in supercritical carbon dioxide (in near-critical and near-pseudo-critical states) are investigated numerically by considering accurate representation of the thermo-physical properties. A high-order (central difference) numerical scheme is used for the simulations.

---

[2] The results presented in this chapter can be found in, [169] N. Hasan and B. Farouk, "Thermoacoustic Transport in Supercritical Fluids at Near-critical and Near-pseudo-critical States," *The Journal of Supercritical Fluids*, vol. 68, pp. 13-24, 2012.

Thermally quiescent and motion free supercritical carbon dioxide in a one-dimensional layer confined by two rigid walls is considered. The NIST database 23 [3] is used to obtain the *ρ*-*p*-*T* relations for supercritical carbon dioxide, along with the static enthalpy $h_0 = f$ (p, T), thermal conductivity $k = f\,(p, T)$, viscosity $\mu = f\,(p, T)$ and specific heat $c_p = f\,(p, T)$ relations. Equations developed by Onuki [56, 71] and Moldover [73] are used for the determination of the bulk viscosity (μ') of supercritical carbon dioxide. Different features regarding the flow field and thermal transport induced by thermoacoustic waves near the critical and pseudo-critical points are revealed by the simulations. The thermo-mechanical behavior in supercritical carbon dioxide in response to external thermal perturbations in the forms of different types of boundary heating is also observed and a novel thermal transport device utilizing the thermoacoustic convection in near-critical fluids is proposed.

3.2 Mathematical modeling

The thermoacoustic effect in fluids can be modeled by the complete hydrodynamic description for an isotropic, Newtonian, compressible, and dissipative (viscous and heat-conducting) fluid [7, 87, 88]. Although there have been reasonable concerns over the legitimacy of applying continuum physics at the vicinity of the critical point, according to Stanley[57] the hydrodynamic limit is located around $\left(T - T_c\right)/T_c \approx 10^{-5}$ (for CO_2, $T - T_c \approx 3.0\,\text{mK}$) on the critical isochor ($\rho = \rho_c$). But the thermodynamic states we consider here are relatively far from the hydrodynamic limit, and as a result they fall safely into the realm of continuum mechanics. We consider one-dimensional continuity and the compressible form of the Navier-Stokes equations to describe the generation and propagation of thermally induced acoustic waves in supercritical carbon dioxide:

$$\frac{\partial \rho}{\partial t}+\frac{\partial}{\partial x}(\rho u)=0 \tag{3.1}$$

$$\frac{D}{Dt}(\rho u)=-\frac{\partial p}{\partial x}+\frac{\partial}{\partial x}\left(\mu\frac{\partial u}{\partial x}\right)+\frac{\partial}{\partial x}\left[\mu'\frac{\partial u}{\partial x}\right] \tag{3.2}$$

$$\frac{D}{Dt}(\rho h)=\frac{\partial p}{\partial t}+\frac{\partial}{\partial x}\left(k\frac{\partial T}{\partial x}\right)+\frac{4}{3}\mu\left(\frac{\partial u}{\partial x}\right)^2+\mu'\left(\frac{\partial u}{\partial x}\right)^2 \tag{3.3}$$

Here, x is a Cartesian coordinate, t is time, ρ is density, u is the velocity, h is the total enthalpy, T is the temperature and p is pressure. The equation of state describing the ρ-p-T relation of supercritical fluids is complicated. It has been shown earlier [39, 56] that the van der Waals equation of state does not represent the properties of supercritical carbon dioxide accurately near the critical point. In this study, we used the NIST Standard Reference Database 23 [3] for the $\rho = f(p, T)$ relations and for evaluation of other thermodynamic properties of supercritical carbon dioxide. The NIST23 [3] equation of state describing the ρ-p-T relation for carbon dioxide is mainly empirical in nature and includes special non-analytic terms to predict the correct behavior of the fluid to the immediate vicinity of the critical point.

Two-dimensional look-up tables are employed in the present study to represent the $\rho = f(p, T)$, $k = f(p, T)$, $\mu = f(p, T)$, $h_0 = f(p, T)$ and $c_p = f(p, T)$ data provided by the NIST Standard Reference Database 23 and the bulk viscosity $\mu' = f(p, T)$ data provided by analytical functions. Onuki's equation [56, 71] is used for calculating the zero frequency bulk viscosity (μ') of carbon dioxide (as described in chapter 2).

3.2.1 Numerical modeling

The governing equations (3.1 – 3.3) are solved by finite volume method using a central difference scheme for the spatial discretization and a Crank-Nicolson scheme for time discretization. The coupling between the velocity field and the pressure in the Navier–Stokes equations is solved through the *SIMPLEC* algorithm [171]. A 10.0 mm layer of supercritical carbon dioxide, bounded by two rigid walls is considered for the simulations reported here. Throughout the simulations, a uniform grid spacing of $\Delta x = 0.01$ mm is relied on to generate sufficiently high spatial resolution such that the fine structures of the acoustic waves can be resolved. For the early time calculations reported here, a Courant number ($c_s \Delta t / \Delta x$) of 0.4 is set to assure proper numerical convergence of the solutions. Here Δt is the time step, and c_s is the local acoustic speed. All computations were carried out on a Dell OPTIPLEX 755 personal computer.

3.3 Verification of the numerical scheme

The numerical prediction of thermally induced acoustic waves in near-critical carbon dioxide with the present method is compared with a previous numerical study [97] and an experimental measurement [103].

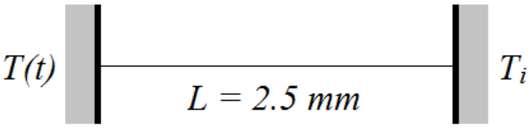

Figure 3.1: Schematic diagram of the problem domain used by Zappoli *et al.* [97].

Zappoli *et al.* [97] presented a model for predicting thermoacoustic wave induced flows in supercritical carbon dioxide. In their numerical model, supercritical carbon dioxide at the critical isobar ($p_i = p_c$) and at a temperature greater than the critical temperature ($T_i = T_c + 1.0$ K) was considered in a one dimensional enclosure of length, $L = 2.5$ mm. Here, the subscript 'i' and 'c' denotes initial and critical values respectively. The schematic diagram of the problem domain used in shown in figure 3.1. The left wall of the enclosure was heated to 13.0 mK with a constant heating rate of 10.0 K/s. The simulations with the present model for the comparison is carried out based on the same initial and boundary conditions as specified in [97].

Figure 3.2a shows the comparison of the predictions of the spatial variations of the rise in pressure at different times by the present method with those obtained by Zappoli *et al.* [97]. The spatial variations of the rise in temperature inside the enclosure are also shown in figure 3.2b. The numbers identifying each line in the figures refer to the ratio t/τ, where $\tau = L/c_s$ is the acoustic time-scale; L is the distance between the two walls, and c_s is the acoustic speed at the initial conditions of the fluid. For the initial condition considered, the acoustic speed used by Zappoli *et al.* [97] is $c_s = 216$ m/s while we obtain $c_s = 187.4$ m/s from the NIST Standard Reference Database 23 [3]. This error propagates to the results obtained in [97]. In order to compare our predictions to those given in ref. [97], we have re-scaled the results by a factor $(216.0/187.4 = 1.15)$ as discussed below. Two values of t/τ are given in identifying the results in figures 3.2a and 3.2b, where the values within the parentheses correspond to the value $c_s = 216$ m/s used by Zappoli *et al.* [97].

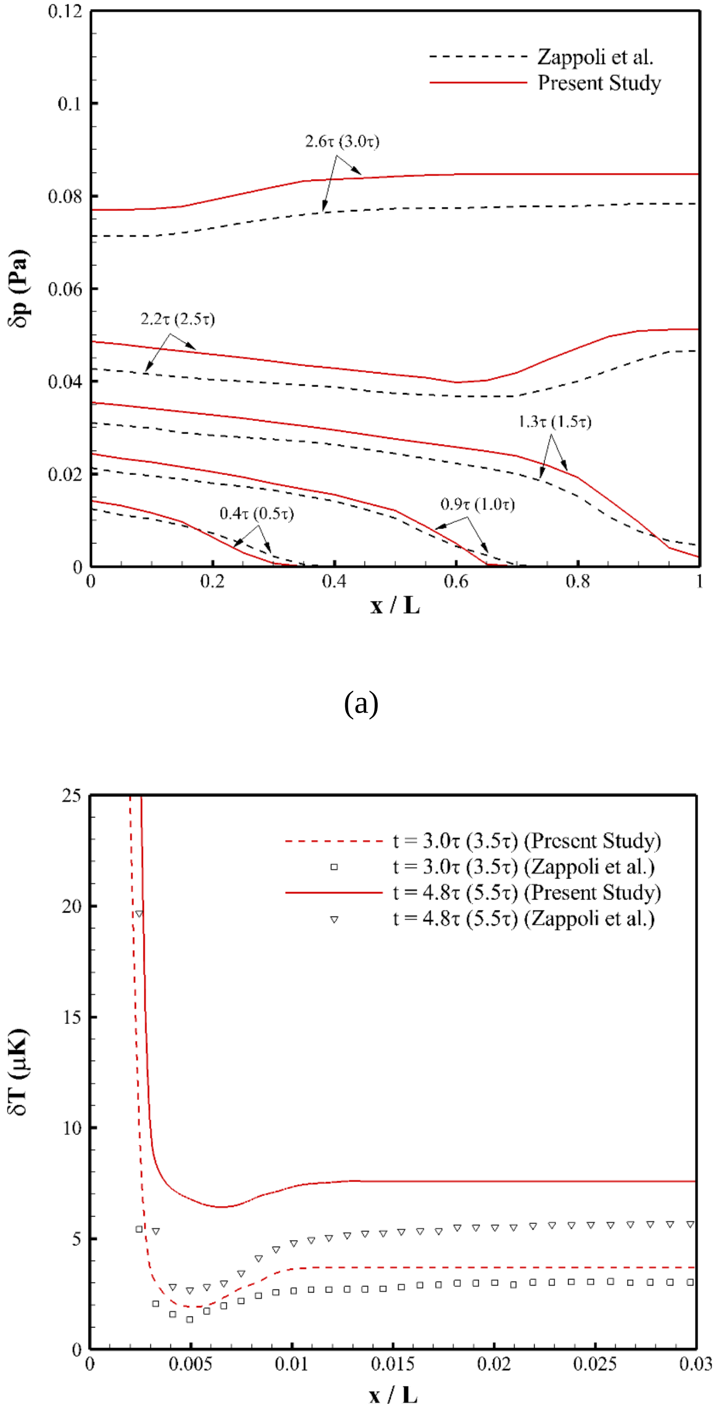

(a)

(b)

Fig. 3.2: Comparison of spatio-temporal variations of calculated (a) pressure and (b) temperature in enclosure filled with near-critical CO_2 with results by Zappoli *et al.* [97].

It can be seen from figure 3.2a that the general shape of the thermoacoustic waves calculated with the present study agrees well with the result obtained from the previous study [97]. Comparing the results quantitatively, it is observed that higher pressure levels are predicted by the present model. In figure 3.2b, piston effect can be clearly observed in the results predicted by both the models, but the change in bulk temperatures (δT) predicted in the present model is higher than those given in Zappoli *et al.* [97]. The difference in magnitudes of the change in pressure (δp) and temperature (δT) inside the computational domain (in figures 3.2a and 3.2b) show an increasing trend within several reflections. The variation in the results predicted by the two studies is clearly due to the use of van der Waals equation of state and constant thermo-physical properties in ref. [97]. The density for the initial condition ($p_i = p_c$, $T_i = T_c + 1.0$ K) predicted by van der Waals equation is 276.2 kg/m^3 [97], whereas it is 307.1 kg/m^3 in the NIST Standard Reference Database 23 [3]. Figures 3.2a and 3.2b indicate that predicted acoustic speed (from the waveforms) is close to the value obtained from the NIST23 Database (i.e. $c_s = 187.4$ m/s) at early time (0 ~ 1τ).

Miura *et al.* [103] measured density changes of order 10^{-8} g/cm^3 on a time scale of 1 μs due to weak continuous heating in a cell ($L = 10.3$ mm) filled with carbon dioxide on the critical isochore close to the critical point ($T_i - T_c = 30$ mK and 150 mK) using an ultrasensitive interferometer. Continuous heating was applied in the time region $0 < t < 0.2$ msec and the supplied heat to the fluid was 367 erg ($q''_{in} \approx 1.83$ kW/m^2). A simulation with the present model considering the same initial and boundary conditions of the experiments is performed.

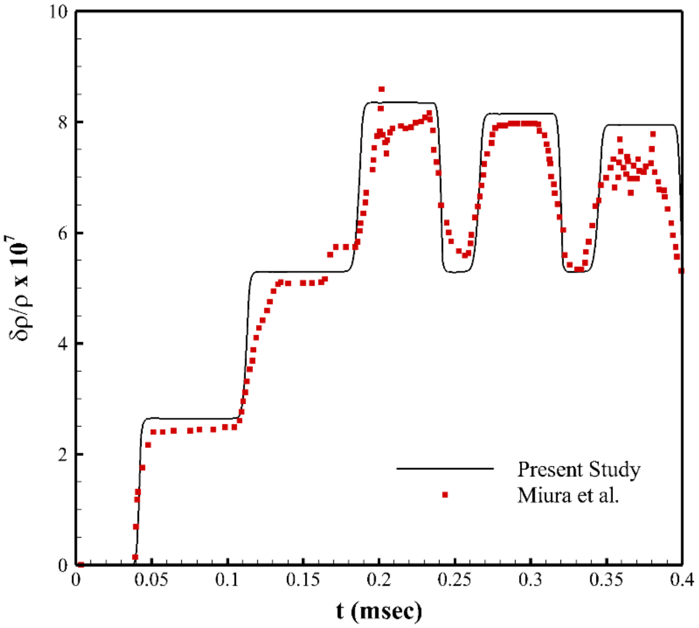

Figure 3.3: Comparison of calculated normalized density change (*δρ/ρ*) at the cell center in the time region $0 < t < 0.4$ msec for $T_i - T_c = 150$ mK, produced by continuous heating in $0 < t < 0.2$ msec in a cell of L=10.3 mm with measurements given by Miura *et al.* [103]

Figure 3.3 shows the numerical results for the continuous heating case with $T_i - T_c = 150$ mK. Although, a generally fair agreement with the experimental measurements is noticed, some inconsistencies are also observed. The predicted amplitudes of the acoustic field (*δρ/ρ* in this case) appear to slightly overshoot from those observed in the measurement. However, numerical prediction of the normalized density changes in the first oscillation ($\delta\rho/\rho = 2.641\times10^{-7}$) is more close to the analytical value of the density change along the critical isochore given by $\frac{\delta\rho}{\rho} = \frac{\left(\partial T/\partial p\right)_S}{c_s T} q''_{in}(t) = 2.591\times10^{-7}$ [103] than the experimentally measured value ($\delta\rho/\rho \approx 2.2\times10^{-7}$). Also, the numerical results show relatively less damping of the acoustic field in the time when heating is turned off (0.2 < *t*

< 0.4 msec). This is possibly due to the viscous losses incurred in the experimentation due to the presence of the side walls, while the numerical model, being one dimensional, do not account for those losses.

3.4 Problem description

For the present study of thermoacoustic transport, a confined layer of thermally quiescent and motion-free supercritical carbon dioxide inside a one dimensional layer (L = 10 mm) is considered. At $t > 0$, a prescribed thermal load is applied at the left boundary in the form of:

$$T_L = f(t) = T_i + \Delta T(1 - e^{-At/\tau}) \tag{3.4}$$

Here, ΔT is the target temperature rise and A is the parameter that controls the rate of boundary heating. In Eq. (3.4), the acoustic time, $\tau = L/c_s$ is defined as the flight time for an acoustic wave to traverse the layer. The right wall is held at the initial temperature. The thermally induced acoustic waves generated are studied as a function of space and time.

3.5 Fundamental studies of thermoacoustic transport: Result and discussion

Numerical simulations for thermally induced acoustic waves in supercritical carbon dioxide as well as in ideal gases (for comparative purpose) are carried out for 20 cases, which are summarized in Table 3.1. The parameter (ρ_i/ρ_c) shown as the last column in Table 3.1 indicates the relative distance of the initial state of the supercritical fluid from the critical/pseudo-critical state. Also $\rho_i/\rho_c = 1$ is a critical/pseudo critical state. For the near-pseudo-critical cases, $\rho_i/\rho_c \approx 1$. The results presented are for the early time behavior of thermally induced acoustic waves in terms of pressure and other variables. Multiple wave reflections and wave damping are observed within a short time for the thin layer of fluid considered.

Table 3.1: List of computational cases for thermoacoustic transport studies

Case No.	Physical State	p_i (MPa)	T_i (K)	ΔT (K)	A	$\frac{\rho_i}{\rho_c}$
01	Gas	0.10	310.00	10.0	10	--
02		1.00	310.00	10.0	10	--
03		2.00	310.00	10.0	10	--
04		4.00	310.00	10.0	10	--
05	Supercritical	7.40	310.00	10.0	10	0.520
06		7.40	305.00	0.1	10	0.687
07		7.40	304.50	0.1	10	0.758
08		7.40	304.30	0.1	10	0.851
09		7.40	304.28	0.1	10	0.8835
10		7.40	304.24	0.1	10	1.131
11		7.40	304.22	0.1	10	1.161
12		7.40	304.20	0.1	10	1.179
13		7.38	305.00	0.1	10	0.671
14		7.38	304.80	0.1	10	0.689
15		7.38	304.60	0.1	10	0.712
16		7.38	304.50	0.1	10	0.727
17		7.38	304.40	0.1	10	0.746
18		7.38	304.30	0.1	10	0.772
19		7.38	304.30	0.1	2	0.772
20		7.38	304.30	0.1	1	0.772

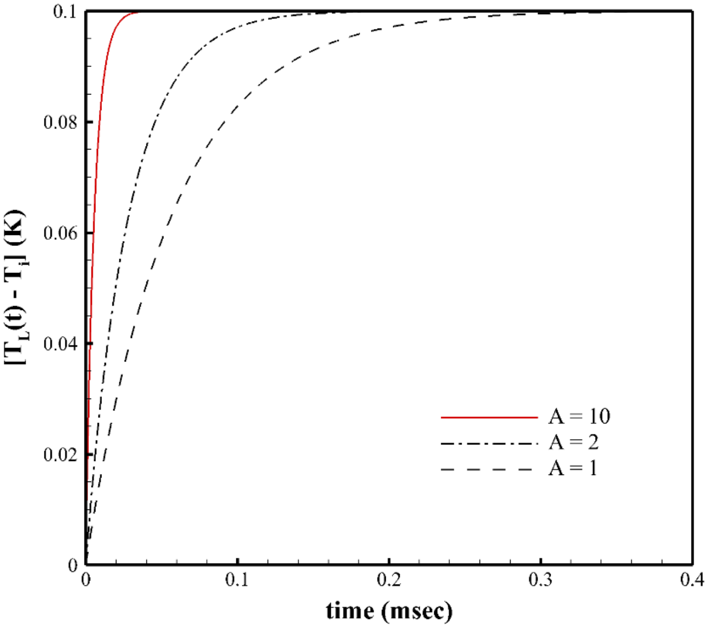

Figure 3.4: Temporal variation of change in left wall temperature [*TL(t)* - *Ti*] for different boundary heating rate parameters (*A*).

To determine the frequency dependency of transport properties for the applied temperature perturbation (equation 3.4) shown in figure 3.4, the most representative frequency of the strongest temperature perturbation (with A = 10) was determined. The time dependent part of the temperature perturbation function is given by

$$\Delta T(t) = T_L(t) - T_i = \Delta T_{\max}\left(1 - e^{-\frac{At}{\tau}}\right), \quad \text{for } t > 0 \tag{3.5}$$

The Fourier approximation of *ΔT*(*t*) can be expressed by the following integral function –

$$\Delta T_\Omega(t) = \Delta T_{\max} - \frac{2\Delta T_{\max} A}{\pi\tau}\int_0^{\Omega=2\pi f}\frac{\cos(\omega t)}{\left(A/\tau\right)^2 + \omega^2}d\omega, \quad \text{for t > 0 and ω > 0} \tag{3.6}$$

Here, $\Delta T_\Omega(t) \to \Delta T(t)$ as $\Omega \to \infty$ (or cyclic frequency, $f \to \infty$). A comparison of the temperature perturbation function (equation 3.5) with the Fourier approximations at different limiting frequency (*f*) values is shown in figure 3.5. From figure 3.5, it is observed that the most representative frequency of the function is around f = 1 MHz.

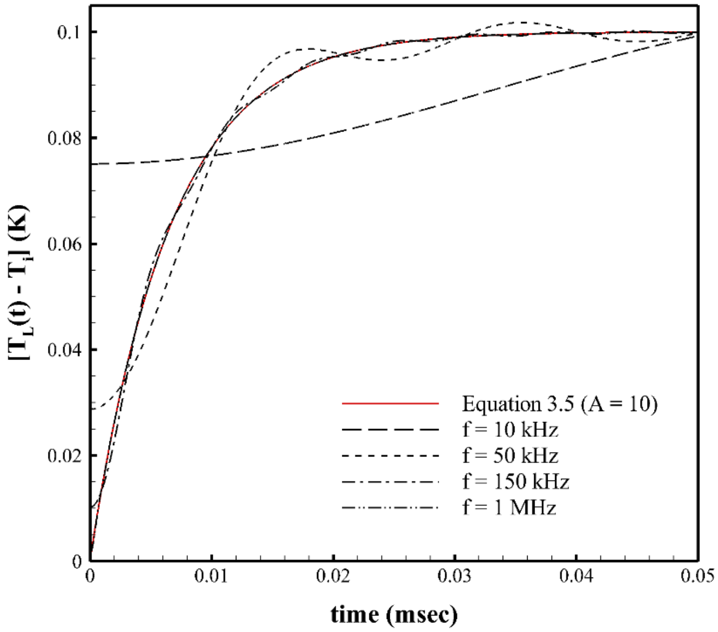

Figure 3.5: Temporal variation of the temperature perturbation function (Eqn. 3.5) and the corresponding Fourier approximations at different limiting frequencies.

The transport properties of a near-critical fluid are independent of the frequency in the low frequency limit. The low frequency limit is given by [56, 62]:

$$\omega\tau_{fluc} < 1 \tag{4.4}$$

Here, $\omega = 2\pi f$ and τ_{fluc} is the fluctuation relaxation time (discussed in chapter 2). For the different cases considered in the present study, the largest fluctuation relaxation time obtained is $\tau_{fluc} = 4.95\times10^{-8}$. Hence, $\omega\tau_{fluc} = 0.311$ (with $f = \omega/2\pi = 10^{-6}$) and all the cases considered in the present study are in the low frequency limit where frequency dependence of the transport properties can be ignored.

3.5.1 Generation and propagation of thermoacoustic waves

Before studying thermally induced acoustic waves in supercritical fluids, we numerically investigate thermally induced acoustic wave shapes in gases (Cases 1 ~ 4). The different characteristic of thermally induced acoustic waves in intermediate states between ideal gases and supercritical fluids are thus explored. A temperature perturbation of 10 K (with boundary heating rate parameter $A = 10$) is applied to the left wall of the enclosure for all of these cases and its effect is investigated.

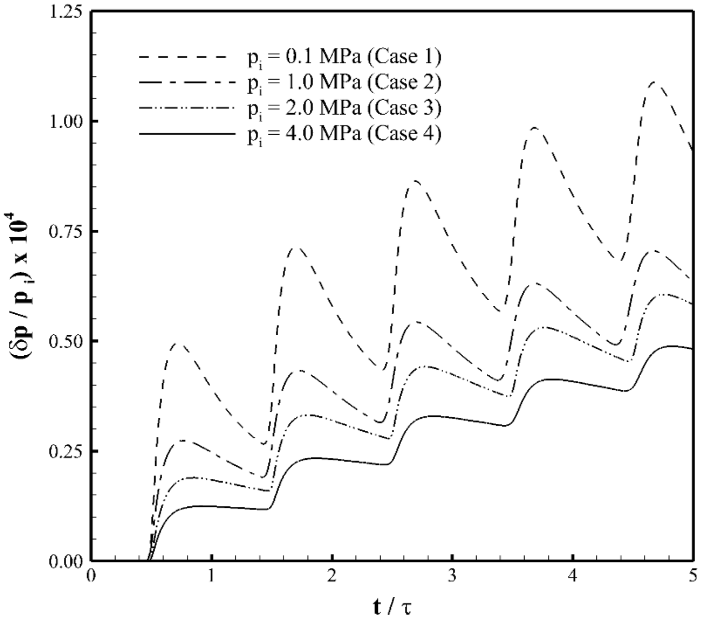

Figure 3.6: Temporal variation of change in pressure ($\delta p/p_i$) at the center of the enclosure with different initial pressures for subcritical CO_2 [Cases 1-4].

Figure 3.6 shows the temporal variations of pressure change ($\delta p/p_i$) at the midpoint of the enclosure for cases 1 ~ 4. It is observed that, as initial pressure increases, the induced thermoacoustic field get stronger and stronger (*i.e.* $\delta p/p_i$ increases), and the acoustic speed also decreases with increasing initial pressure. The spatial variation of the acoustic field at five different times for case 1 is shown in figure 3.7. The rapid heating along the left wall causes a sharp pressure rise in the ideal gas and the generated pressure waves travel towards the right wall with wave speeds of about 274 m/s (figure 3.7). The predicted wave speed is close to the value obtained from the NIST database 23 [3].

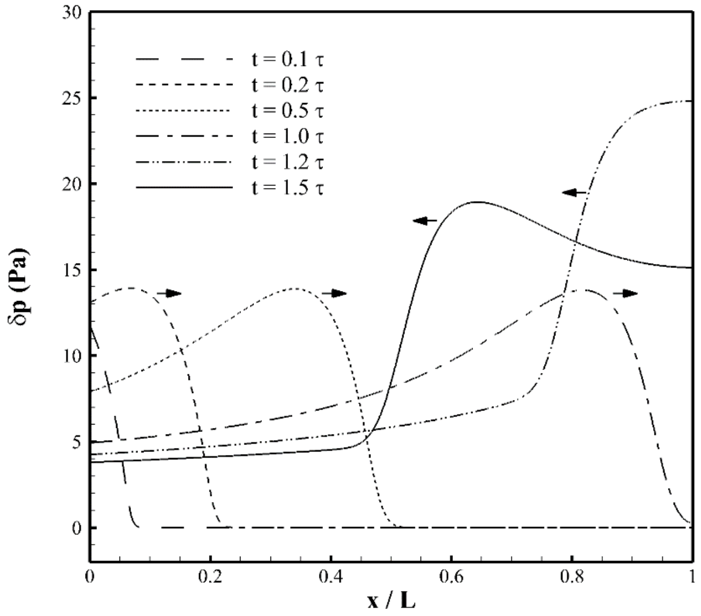

Figure 3.7: Spatial variation of change in pressure ($\delta p/p_i$) inside the enclosure at different times for subcritical CO_2 with p_i = 0.1 MPa and T_i = 310 K [Case 1].

In case 5 (Table 3.1) we consider supercritical CO_2 at the initial pressure of 7.4 MPa and initial temperature of 310.0 K (>> T_c). Temporal variation of pressure change ($\delta p/p_i$) at the midpoint of the enclosure for case 5 (supercritical CO_2) is shown in figure 3.8. The result shows that, for a large temperature perturbation (ΔT = 10 K, A = 10), strong acoustic field is induced in the supercritical fluid. The current numerical model predicts the correct speed of propagation of the acoustic waves generated due to rapid heating in supercritical fluid.

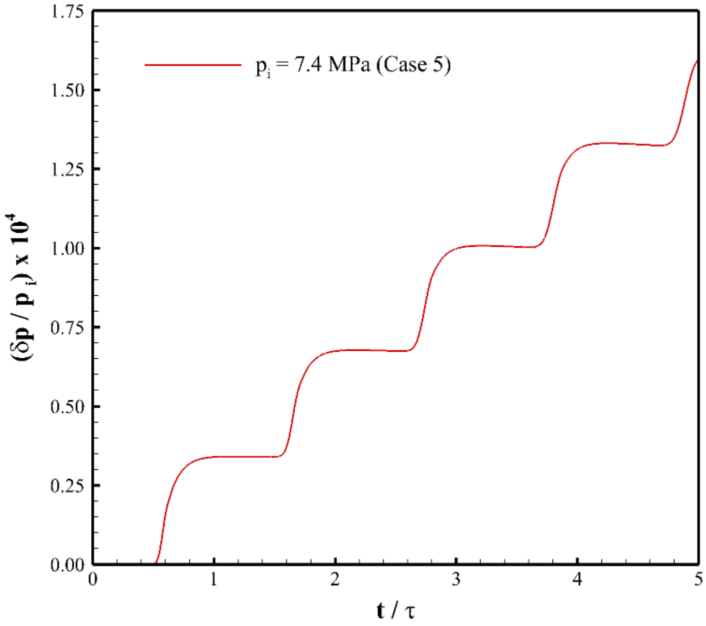

Figure 3.8: Temporal variation of change in pressure ($\delta p/p_i$) at the center of the enclosure for supercritical CO_2 with p_i = 7.40 MPa and T_i = 310 K [Case 5]

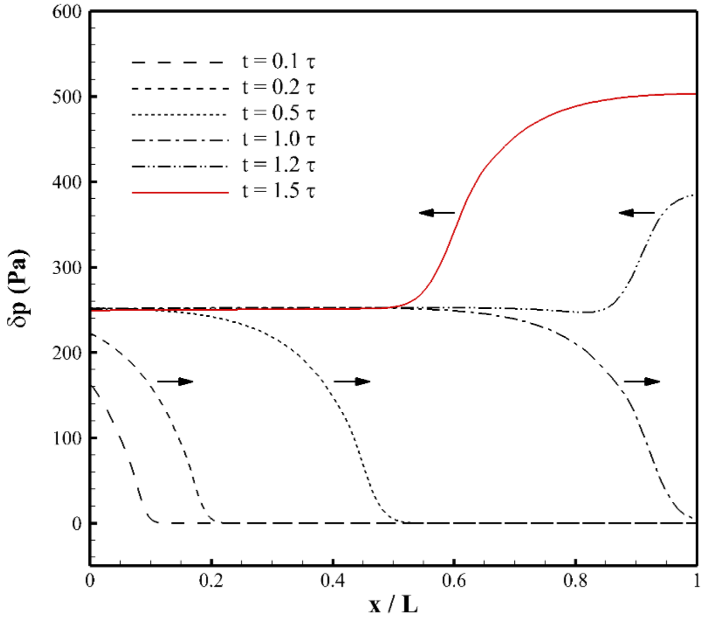

Figure 3.9: Spatial variation of change in pressure (δp) inside the enclosure at different times for supercritical CO_2 with p_i = 7.40 MPa and T_i = 310 K [Case 5].

Figure 3.9 shows the spatial variation of change in pressure (δp) inside the enclosure at five different times for case 5. Comparing figure 3.7 (sub-critical CO_2) and 3.9 (supercritical CO_2), it is observed that, unlike the characteristic long tails of the thermally induced acoustic waves in ideal gas (CO_2), the pressure wave signatures in supercritical fluid show a step-like profile due to the high density and compressibility in the near-critical region.

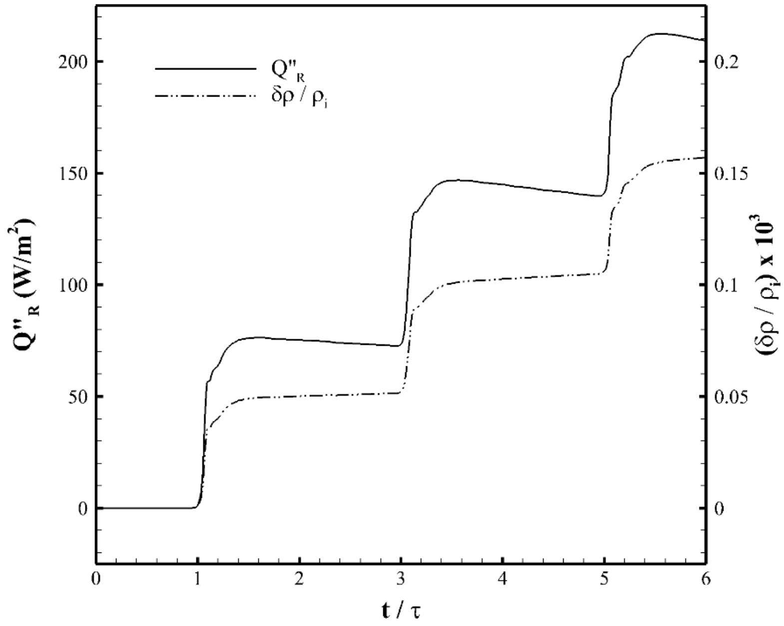

Figure 3.10: Temporal variation of density change ($\delta\rho/\rho_i$) and heat flux (Q''_R) at the right wall of the enclosure for supercritical CO_2 with p_i = 7.40 MPa and T_i = 310 K [Case 5].

Figure 3.10 shows the temporal variation of change in density ($\delta\rho/\rho_i$) and heat flux Q''_R at the right (cold) boundary for case 5 where the undisturbed fluid is supercritical. It is observed from the figure that the compressive waves reflecting from the right boundary acts as carriers of thermal energy delivering energy to the right wall. However, with the vanishingly small thermal diffusivity near the critical point, the energy that the wave carries cannot be efficiently diffused through the boundary via thermal conduction. As a result, a large portion of the energy is reflected back from the boundary, whose superposition with the incoming wave thus increases the temperature and pressure in the bulk fluid. Due to such a reflection pattern, the reflected pressure waves seem to directly gather upon the incoming waves.

3.5.2 Piston effect in near-critical supercritical fluids

Cases 6 ~ 18 represent thirteen cases in the near-critical and near-pseudo-critical regions on two different isobars p = 7.4 MPa and p = 7.38 MPa with the heating rate parameter A =10. The pseudo-critical states at p = 7.40 MPa (cases 6 - 12) and p = 7.38 MPa (cases 13 - 18) are characterized by $\rho = \rho_c$ = 467.6 kg/m^3. The same temperature perturbation (ΔT = 0.1K) is applied to all of these thirteen cases (case 6 ~ 18) under the same boundary heating rate parameter (A = 10). It should be noted that creating a controlled thermal perturbation of such rate and magnitude is experimentally feasible. The experimental study by Miura *et al.* [103] reports measurement of thermoacoustic disturbances in supercritical fluid under the temperature perturbation of only 0.01 mK. For cases 6 - 12 (p_i = 7.4 MPa, Table 3.1), the values of ρ_i/ρ_c range from 0.687 to 1.179. For cases 13 - 18 (and p_i = 7.38 MPa, Table 3.1), the values of ρ_i/ρ_c range from 0.671 to 0.772. As can be seen from the p-v diagram for CO_2 (see chapter 2 – figure 2.3), we reach very close to the critical point when $\rho_i/\rho_c = 0.772$. Two additional cases (19 and 20) are shown in table 3.1 where $\rho_i/\rho_c = 0.772$, albeit for heating rate values of A = 2 and 1 respectively.

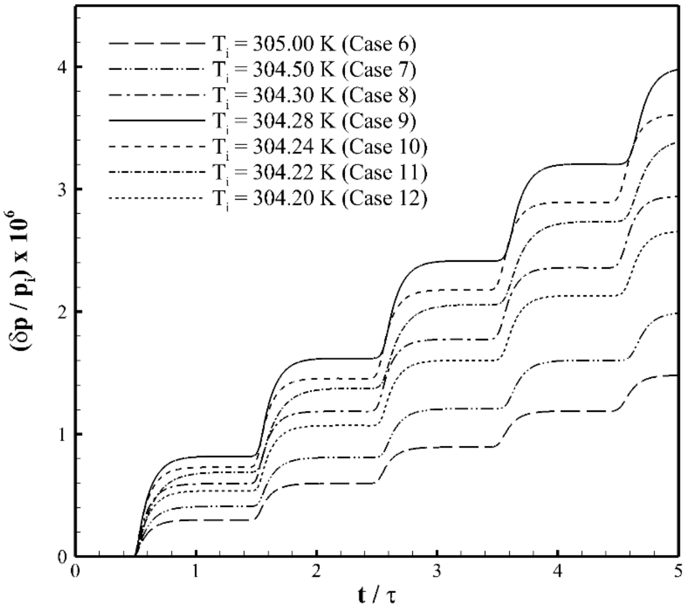

Figure 3.11: Temporal variation of change in pressure ($\delta p/p_i$) at the center of the enclosure with different initial temperatures for supercritical CO_2 (p_i = 7.40 MPa) [Cases 6 ~ 12].

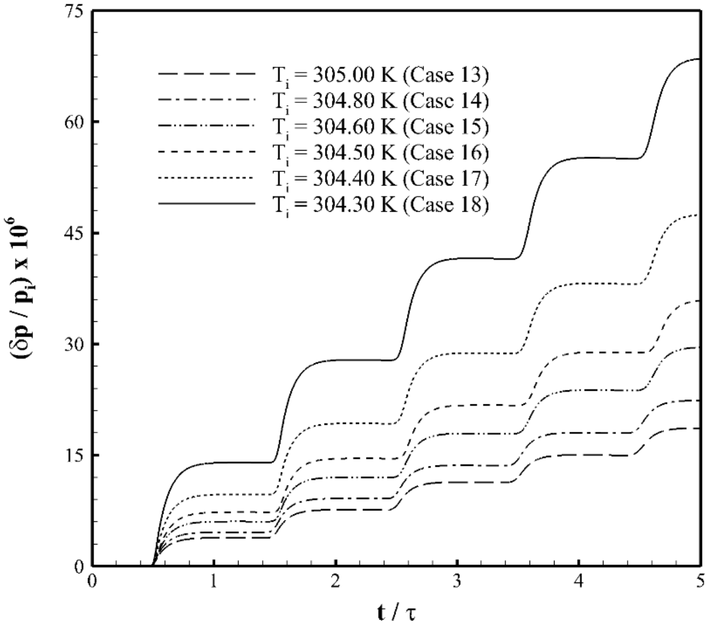

Figure 3.12: Temporal variation of change in pressure ($\delta p/p_i$) at the center of the enclosure with different initial temperatures for supercritical CO_2 (p_i = 7.38 MPa) [Cases 13 ~ 18].

Temporal variation of change in pressure ($\delta p/p_i$) at the center for cases 6 ~ 12 (on the isobar p = 7.40 MPa) is shown in figure 3.11. As the initial state of the fluid approaches the corresponding pseudo-critical state (p = 7.40 MPa, T = 304.26 K, ρ = 467.6 kg/m^3), relatively stronger acoustic waves (*i.e.* greater value of $\delta p/p_i$) are generated for the same boundary heating rate parameter (A) and temperature perturbation (ΔT) in the fluid. Accordingly, the strongest waves are generated (in figure 3.11) for case 9, which has the initial state closest to the corresponding pseudo-critical state. Similar phenomenon is also observed for cases 13 ~ 18 (figure 3.12) which are on the isobar p = 7.38 MPa and even closer to the critical state of carbon dioxide. Here, the strongest waves are generated (in figure 3.12) for case 18, which has the initial state closest to the corresponding pseudo-critical state.

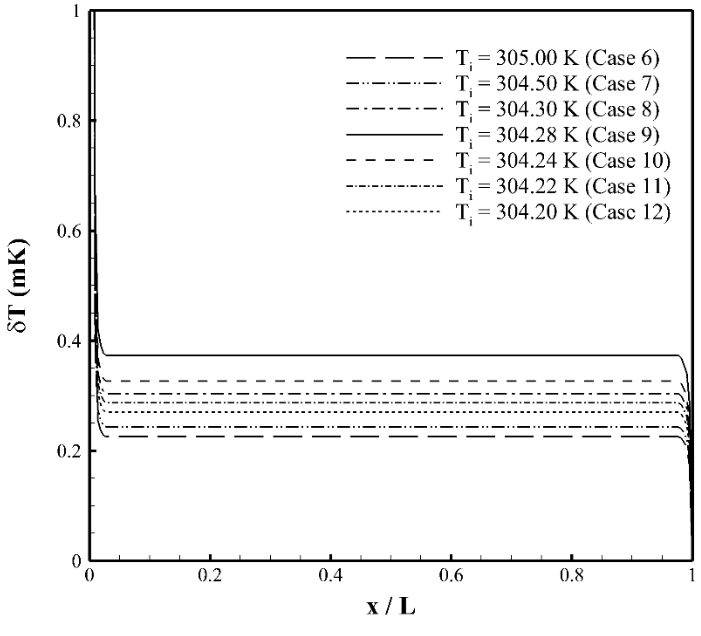

Figure 3.13: Spatial variation of change in bulk temperature (δT) inside the enclosure at t = 5τ with different initial temperatures for supercritical CO_2 (p_i = 7.40 MPa).

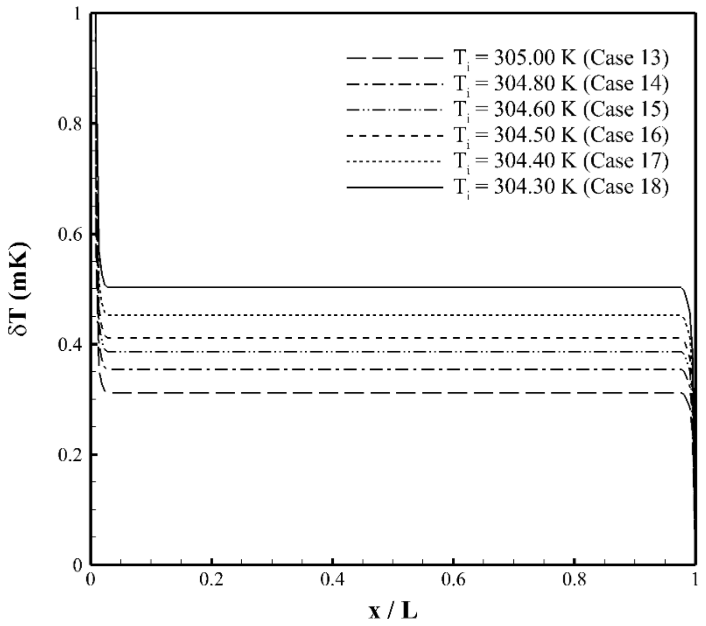

Figure 3.14: Spatial variation of change in bulk temperature (δT) inside the enclosure at $t = 5\tau$ with different initial temperatures for supercritical CO_2 ($p_i = 7.38$ MPa).

Figure 3.13 and 3.14 show the spatial variation of the change in bulk temperature $\left[\delta T = T(t) - T_i\right]$ at $t = 5\tau$ for cases 6 ~ 12 and 13 ~ 18 respectively. It is observed from the figures that the stronger acoustic fields induced in the near-critical fluid (figure 3.11 and 3.12) due to the temperature perturbation at the boundary eventually gives rise to larger change in bulk temperature (δT) as the corresponding pseudo-critical state is approached.

From previous analysis [88], it was found that decreasing the thermal diffusivity (α) weakens the acoustic field, while both increasing $\left(\frac{\partial p}{\partial T}\right)_\rho$ and isothermal compressibility (β) enhances the acoustic field. In the above cases, increase in strength of the acoustic field is observed mainly due to the constructive combination of the increasing isothermal compressibility (β) and decreasing thermal diffusivity (α) near the pseudo-critical state.

The spatial variation of the change in bulk temperature [$\delta T = T(t) - T_i$] at five early times for case 18 is shown in figure 3.15. Within these times, the thermally induced acoustic waves have reverberated within the domain several times and the wave amplitudes have begun to damp out, heating the bulk fluid homogeneously. The homogeneously heated bulk is sandwiched between two thin thermal diffusion layers that have developed on the enclosing walls. This demonstrates the existence of the so called *piston effect* in supercritical fluid due to rapid heating of a side wall.

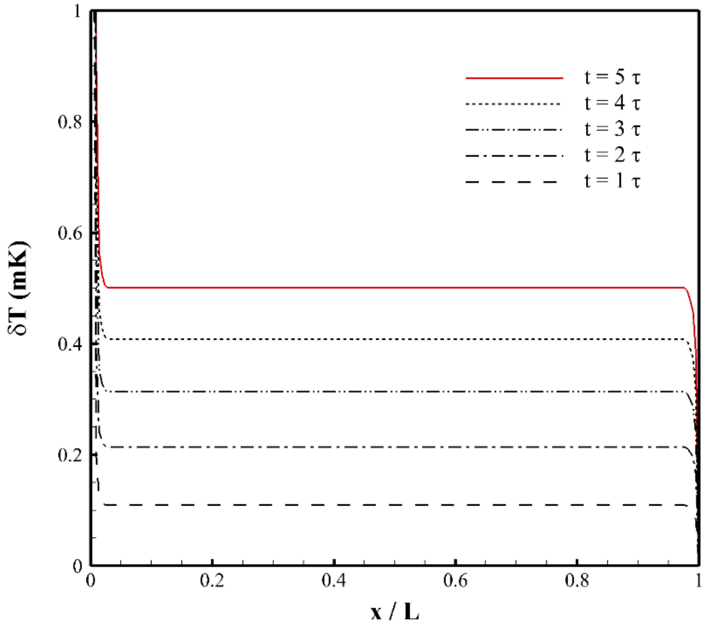

Figure 3.15: Spatial variation of change in bulk temperature (δT) inside the enclosure at different characteristic times (τ) for supercritical CO_2 with p_i = 7.38 MPa and T_i = 304.3 K [Case 18].

The results shown in figures 3.13 and 3.14 are summarized in figure 3.16. It shows the change in bulk temperature [$\delta T = T(t) - T_i$] at the midpoint ($x / L = 0.5$) of the enclosure and at $t = 5\tau$ for the different cases considered (Cases 6 ~ 18). For the seven cases considered on the isobar p = 7.40 MPa (Cases 6 ~ 12), the initial temperature of the fluid varies from 305.0 K to 304.2 K, while the temperature corresponding to the pseudo-critical state is 304.26 K. Hence, the parameter ($\frac{\rho_i}{\rho_c}$) has values both less than (Case 6 ~ 9) and greater than unity (Case 10 ~ 12). It is observed that, the change in bulk temperature (δT) in these cases (Cases 6 ~ 12) show an increasing trend as the parameter ($\frac{\rho_i}{\rho_c}$) approaches unity and the initial state of the fluid approaches the corresponding pseudo-critical state (p = 7.40 MPa, T = 304.26 K, ρ = 467.6 kg/m^3). Thus, the curve for the isobar p = 7.40 MPa shows a sharp peak (extrapolated and shown by the dotted line in figure 3.16) at the corresponding pseudo-critical state.

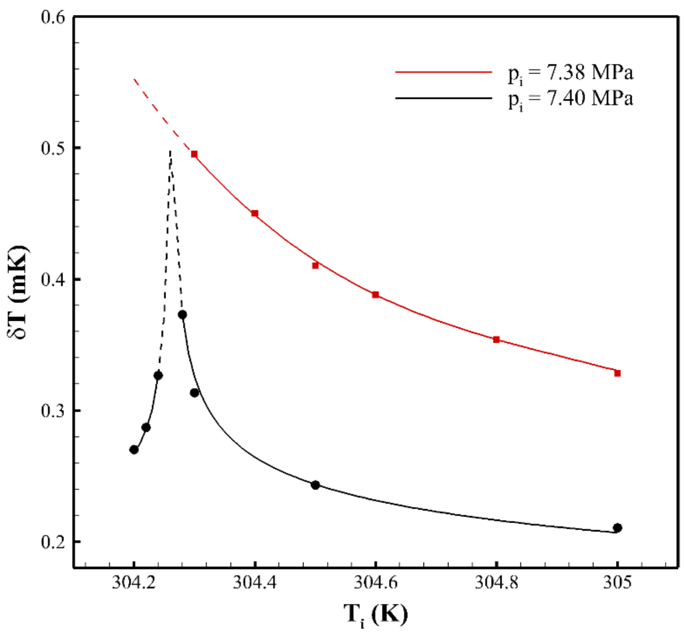

Figure 3.16: Variation of the change in bulk temperature (δT) at the midpoint of the enclosure and at $t = 5\tau$ as a function of initial temperature (T_i) for different initial pressures [Cases 6 ~ 18].

On the other hand, for the cases (Cases 13 ~ 18) considered on isobar p = 7.38 MPa, the initial temperature of the fluid varies from 305.0 K to 304.3 K while the temperature corresponding to the pseudo-critical state is 304.14 K. Hence, the parameter ($\frac{\rho_i}{\rho_c}$) is less than unity and the results show a monotonically increasing trend in change in bulk temperature (δT) as the initial state of the fluid approaches the corresponding pseudo-critical state (p = 7.38 MPa, T = 304.14 K, ρ = 467.6 kg/m^3). It is also observed that, the change in bulk temperature (δT) are much higher in cases on the isobar p = 7.38 MPa (Cases 13 ~ 18) than that for cases on the isobar p = 7.40 MPa (Cases 6 ~ 12). This is explained by the close proximity of cases 13 ~ 18 to the critical point than that for cases 6 ~ 12.

3.5.3 Effect of bulk viscosity on thermoacoustic transport

To investigate the effect of critically diverging bulk viscosity on the thermally induced acoustic waves, an initial condition (case 9) with a relatively high bulk viscosity $\left(\mu' / \mu \approx 800\right)$ is considered. The temporal and spatial variation of the thermally induced acoustic field ($\delta p/p_i$) is shown in figures 3.17 and 3.18 respectively. It is observed that, the effect of bulk viscosity on the thermoacoustic field is twofold. Initially, during the expansion of the hot boundary layer along the left wall, a relatively stronger acoustic field ($\delta p/p_i$) is observed when the bulk viscosity is present in the model. This is mainly due to the viscous resistance imposed on the expanding boundary layer by the high bulk viscosity fluid. Figures 3.17 and 3.18 also reveals that, the acoustic field starts to attenuate slowly after several reflections when bulk viscosity is present in the model.

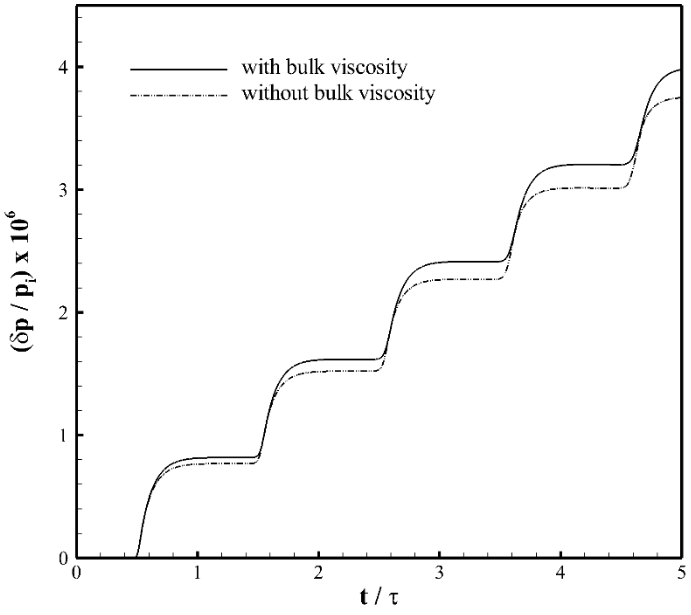

Figure 3.17: Temporal variation of change in pressure ($\delta p/p_i$) at the center of the enclosure for supercritical CO_2 with p_i = 7.40 MPa and T_i = 304.28 K [Case 9] showing the effect of bulk viscosity.

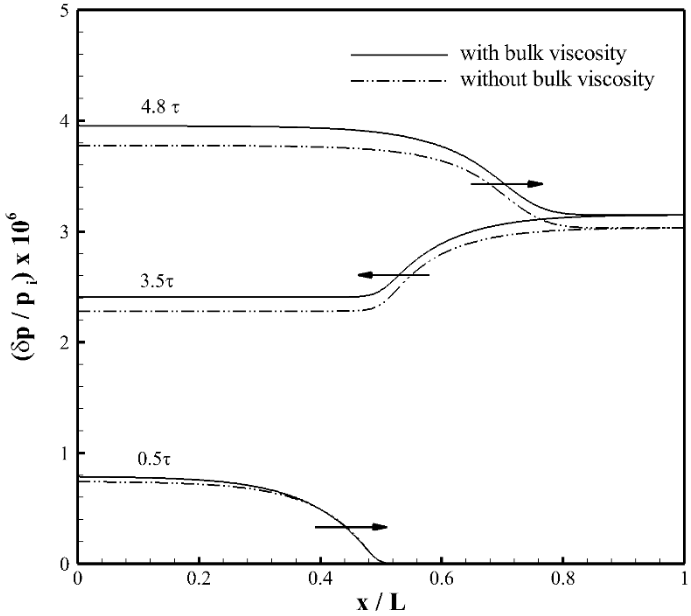

Figure 3.18: Spatial variation of change in pressure ($\delta p/p_i$) inside the enclosure at different times for supercritical CO_2 with p_i = 7.40 MPa and T_i = 304.28 K [Case 9] showing the effect of bulk viscosity.

3.5.4 Effect of boundary heating rate on heat transfer

In cases 18 ~ 20, the initial states of the supercritical fluid are identical. The boundary heating rate decreases gradually from case 18 to case 20. As illustrated in figure 3.4, the fastest heating corresponds to A = 10 (case 18) with decreasing heating rates for case 19 (A = 2) and case 20 (A = 1). For the same initial state, rapid boundary heating generate stronger thermally induced acoustic field ($\delta p/p_i$) and thus larger change in bulk fluid temperature (δT).

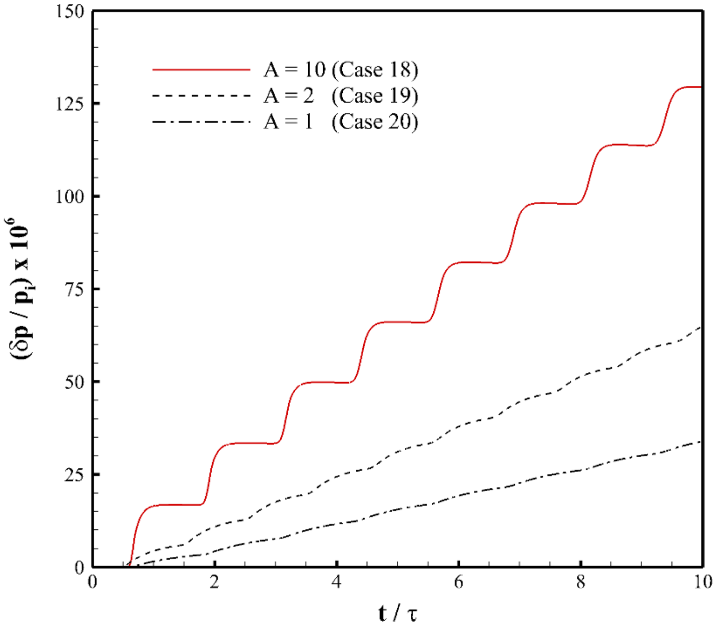

Figure 3.19: Temporal variation of change in pressure at the center of the enclosure for p_i = 7.38 MPa and T_i = 304.3 K with different heating rates [cases 18-20].

Temporal variations of change in pressure at the center point for cases 18 ~ 20 are shown in figure 3.19. For case 20 (A = 1), the generated acoustic field is weak (*i.e.* relatively smaller $\delta p/p_i$) and the reverberations are not as noticeable as for case 18 (A = 10). The computed value of the acoustic speed for cases 18 ~ 20 compare very well with the tabulated value given in the NIST23. The strength of the acoustic field ($\delta p/p_i$) and the overall rate of pressure increase are found to be strongly correlated to the boundary heating rate. The rapid temperature increase at the boundary (A = 10) induces large-scale oscillations into the fluid giving rise to a stronger acoustic field ($\delta p/p_i$) whether the acoustic waves produced are rather weak when the boundary heating rate is slower (A = 1).

3.6 Thermal transport over a long distance using supercritical fluids

Thermal transport over a shorter distance can be achieved by conduction while for a relatively long distance; it is generally performed by heat pipes (latent heat). However, performance of heat pipes is limited by the combination of latent heat, viscosity and surface tension of the working fluid, gravity and design of the wick etc. Piston effect phenomena in near-critical fluids can be utilized to design a simple yet effective thermal transport device for transfer of heat over longer distances. The prospect of thermal transport over a long distance in zero gravity conditions using the adiabatic heat transfer mechanism (piston effect) in supercritical fluids was first demonstrated by Beysens *et al.* [172]. However, the computational model proposed in that study [172] does not consider the hydrodynamics effect of the problem.

Table 3.2: List of computational cases for long distance thermoacoustic transport studies

Case No.	Physical State	p_i (MPa)	T_i (K)	Q_{in} (W/m^2)
21	Gas	0.10	304.4	100.0
22	Supercritical	7.38	304.4	100.0
23		7.38	304.3	100.0

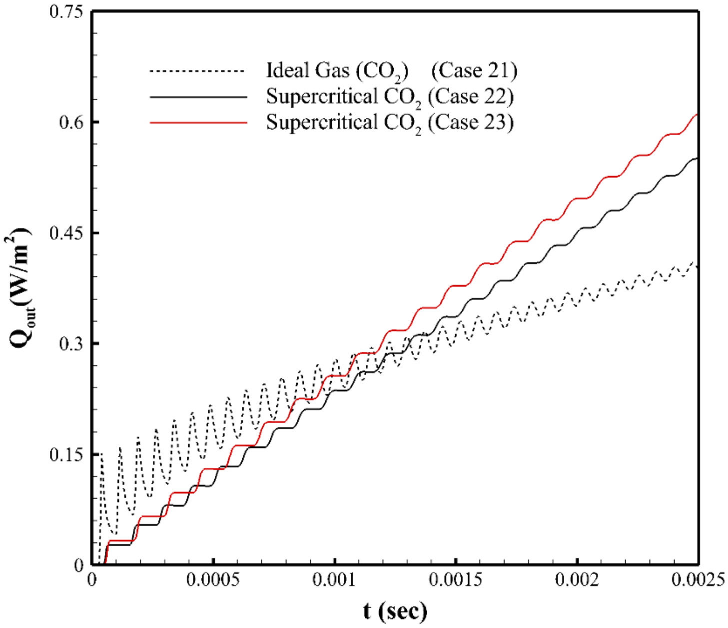

Figure 3.20: Temporal variation (early time) of heat flux (Q_{out}) at the right (cold) wall of the enclosure for carbon dioxide at both ideal and supercritical phases after a constant heat flux (100 W/m^2) is applied at the left wall.

To study the thermal transport behavior in near-critical fluids, three cases are simulated using a constant heat flux boundary condition for the same layer (L = 10.0 mm) of fluid contained between two rigid walls. A constant heat flux boundary condition is applied to the left wall of the enclosure instead of the isothermal boundary condition while the right wall is maintained constant at the initial temperature of the fluid. Gravity is not included in the model. Figure 3.20 shows the predicted temporal evolution (early time) of the heat flux at the right wall (Q_{out}) of the enclosure from 0 to 2.5 msec for cases 21 ~ 23. The fluid (CO_2) in case 21 is low (atmospheric) pressure ideal gas while that in cases 22 and 23 are supercritical fluid. However, the initial state of the fluid in case 23 (ρ = 361.03 kg/m^3) is closer to the corresponding pseudo-critical state (ρ_c = 467.6 kg/m^3) than that in case 22 (ρ = 348.89 kg/m^3). Due to a relatively higher thermal diffusivity in ideal gas (CO_2), the thermoacoustic waves in ideal gas can deliver the thermal energy to the right wall more efficiently than that with supercritical fluids at the very early time. On the other hand, in the near-critical region (Case 22 and 23), the diverging compressibility and small viscosity of the fluid allows the thermoacoustic waves to reflect within the enclosure for a relatively longer period of time while in ideal gas conditions (Case 21) the waves damp out within several acoustic times (t/τ) and thereby reducing the rate of increase in heat flux at the right wall to a great extent.

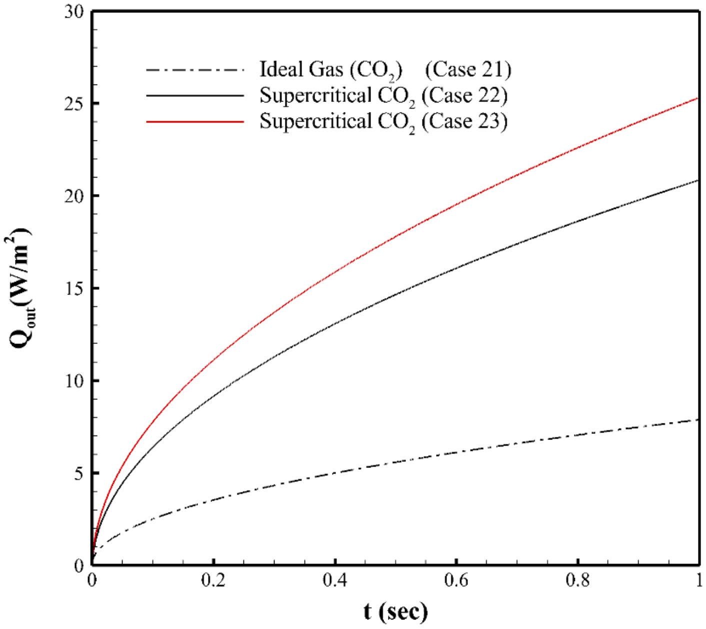

Figure 3.21: Temporal variation (long time) of heat flux (Q_{out}) at the right (cold) wall of the enclosure for carbon dioxide at both ideal and supercritical phases after a constant heat flux (100 W/m^2) is applied at the left wall.

The long time evolution of the heat flux at the right wall (Q_{out}) of the enclosure is shown in figure 3.21. It is observed that, for a relatively longer time period (1 sec) the heat transfer performance with supercritical fluid is superior to that with ideal gas. Both figures 3.20 and 3.21 also shows that, the fluid with a relatively close proximity (Case 23) to the corresponding pseudo-critical state delivers more thermal energy than the fluid whose initial state is relatively far (Case 22) from the corresponding pseudo-critical state.

It is evident from the above results that, the thermoacoustic waves in a near-critical fluid carry thermal energy from the boundary to deep inside the fluid due to the piston effect. After the rapid initial rise at the early time, the transport is mainly is governed by diffusion in the fluid. It is also observed from the result (figure 3.21) that, for supercritical carbon dioxide as the working fluid, almost 25% (Case 23) of the total energy supplied is delivered very quickly (within 1 sec). During the transient stage, the rest of the energy is consumed to increase the temperature of the fluid. Also the thermal transport performance (Q_{out}/Q_{in}) is found to be highly associated to the initial state of the supercritical fluid.

3.7 Summary and conclusions

The generation and propagation of thermally induced acoustic waves in supercritical carbon dioxide are investigated by numerically solving a fully compressible form of the Navier-Stokes equations. The NIST Standard Reference Database 23 [3] is used to generate two-dimensional look-up tables to represent the equation of state and other thermodynamic properties for supercritical carbon dioxide. Bulk viscosity calculated from the analytical equations developed by Onuki [56, 71] and Moldover [73] is also included in the numerical model. The novel contribution of the present study is the development and validation of a high fidelity predictive model based on an accurate equation of state for sub- and supercritical carbon dioxide and an in-depth analysis of the behavior of thermoacoustic transport phenomena in near-critical and near-pseudo-critical states. With the aid of the developed model, the transition of the thermoacoustic wave generation and propagation phenomena from a sub-critical to supercritical phase is investigated. The adiabatic piston effect phenomena in near-critical fluids are also investigated by systematically approaching the pseudo-critical states.

The results exhibit that rapid heating of the boundary emits strong compressive waves that carry energy and momentum from the heated boundary deep into the undisturbed regions of the fluid. The existence of the piston effect in supercritical fluid due to rapid heating of the boundary is also demonstrated. Two exciting phenomena are observed from the results presented. Firstly, as predicted by earlier studies [95, 159], the relative strength of the acoustic field ($\delta p/p_i$) as well as the corresponding change in bulk temperature (δT) certainly increases as the critical state of the fluid (CO_2) is approached. Secondly and most interestingly, change in these parameters ($\delta p/p_i$ and δT) are highly correlated with the pseudo-critical states. Near the pseudo-critical state ($\frac{\rho_i}{\rho_c} \rightarrow 1$), the acoustic field ($\delta p/p_i$) and the corresponding change in bulk temperature (δT) shows rapid increase while their magnitude decreases as the initial state is moved away from the pseudo-critical state. Proper inclusion of bulk viscosity in the model shows that, viscous resistance imposed on the expanding boundary layer by the high bulk viscosity fluid affects the thermoacoustic field both in the early and later times. A novel thermoacoustic wave driven thermal transport device using supercritical carbon dioxide as the working fluid is also proposed. From the study of this type of device, it is observed that a portion of the total energy supplied can be transmitted very quickly by the thermoacoustic waves. It is also observed that, the thermal transport performance (Q_{out}/Q_{in}) is mainly dependent on the initial state of the fluid and its proximity to the corresponding pseudo-critical state. Hence, the performance of the device can be adjusted easily and it can be used in conjunction with a traditional heat pipe where rapid transport of thermal energy is necessary.

CHAPTER 4: EXPERIMENTAL INVESTIGATION OF THERMALLY INDUCED ACOUSTIC WAVES IN SUPERCRITICAL FLUID[3]

4.1 Introduction

In this chapter, thermoacoustic waves in near-critical supercritical carbon dioxide are investigated experimentally on acoustic time scales using a fast electrical heating system along with high speed pressure measurements. In particular, the generation, propagation and decay of thermoacoustic waves in a cylinder filled with near-critical supercritical carbon dioxide at different initial states is studied experimentally. A thin nickel foil attached to one end of the cylinder is heated by a resistance-capacitance (*R*-*C*) circuit. The fast heating of the nickel foil generates a thermally induced acoustic wave in the closed cylinder which keeps traversing between the two ends and undergoes many reflections before it is fully damped out. The time-dependent pressure variations in the cylinder is measured by a microphone located at a specific point on the side of the cylinder with a fast-response data acquisition system (DAQ). The heating rate, at which the boundary temperature is raised, is a key factor in the generation of these acoustic waves. The effect of different rates of boundary heating on the acoustic wave formation mechanism near the critical point is also studied. Finally, thermoacoustic wave generation and propagation in near-critical supercritical fluid under the experimental conditions is also investigated numerically using the model described in the previous chapter and the results are compared with the experimental measurements.

---

[3] The results presented in this chapter can be found in, [173] N. Hasan and B. Farouk, "Fast Heating Induced Thermoacoustic Waves in Supercritical Fluids: Experimental and Numerical Studies," *Journal of Heat Transfer*, vol. 135, pp. 081701-081701, 2013.

4.2 Experimental apparatus

Achieving supercritical state safely is a key point for the success of measuring thermally induced acoustic pressure waves in supercritical carbon dioxide. The experimental setup is designed to ensure this. Figure 4.1 shows the details of the experimental setup.

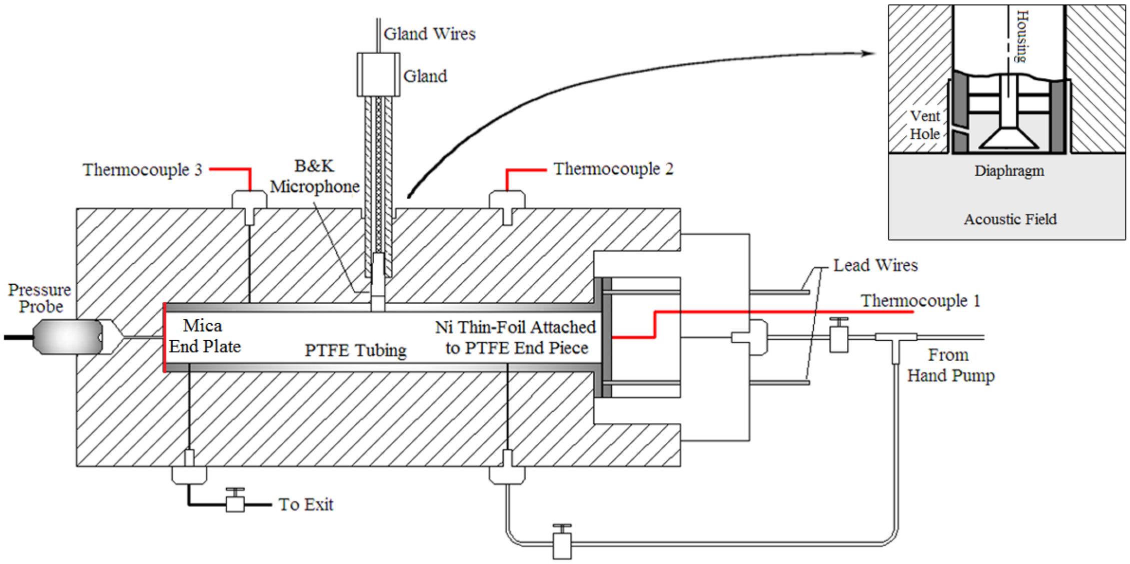

(a)

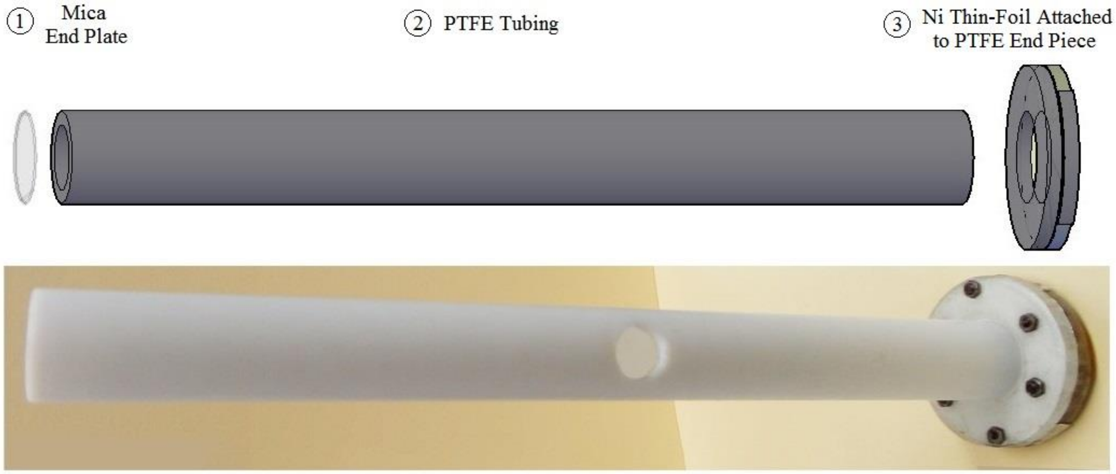

(b)

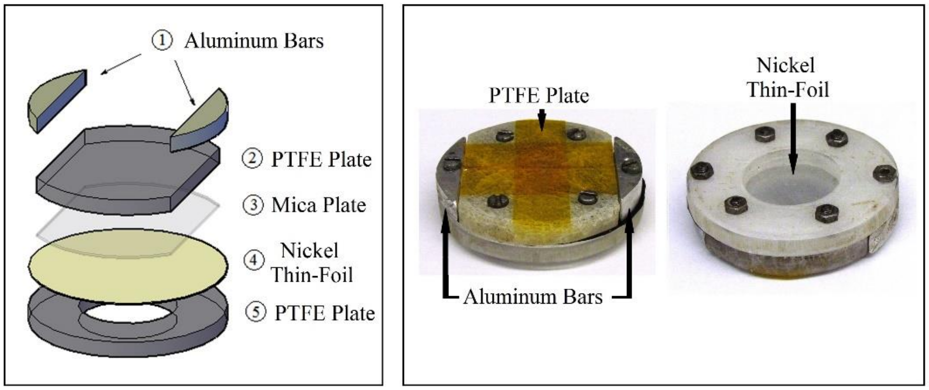

(c)

Figure 4.1: (a) Schematic diagram of the experimental setup. Inset: Detailed schematic of the B&K microphone. (b) PTFE tubing with end piece (c) Detailed view of the PTFE end piece with Ni thin-foil.

A supercritical fluid chamber (see figure 4.1a) is made from a block of 316 stainless steel and designed to withstand much higher pressure than the critical pressure of carbon dioxide (p_c = 7.3773 MPa). The supercritical chamber consists of gas inlet and outlet ports fitted with high pressure (103.4 MPa) ball valves and the chamber is connected to a carbon dioxide tank (p ~ 6.0 MPa). The thermoacoustic waves in supercritical carbon dioxide are studied in a PTFE (Polytetrafluoroethylene) tube (inside diameter 1.8 cm, length 25.0 cm, see fig. 4.1b) snugly fitted inside the supercritical chamber. A small hole in the PTFE tubing aligned with the gas inlet port provides flow path for the gas to and from the supercritical chamber. A very thin nickel foil (thickness 6.0 μm, electrical resistivity 6.84×10^{-8} ohm-m) completely covers one end of the tube and is attached with a mica end-piece. A similar mica plate is used at the other end of the tube. These mica plates ensure rigid reflecting surfaces for the pressure waves. In addition, thick PTFE plates are added at the back of the mica plate and anchored with the tube to ensure rigid support and a good seal for the tube (see figure 4.1c). The foil is anchored by two aluminum bars that serve as connection wires and supports for the foil. Lead wires from a foil heating circuit are introduced inside the supercritical chamber through compression fittings and are connected to the aluminum bars. A hand pump (HiP, 34.5 MPa, 60 mL/stroke) is used to raise the pressure of the carbon dioxide in the supercritical chamber from the tank pressure to a pressure above the critical point of carbon dioxide. Heating tape (Thermolyne, 0.5" x 4') wrapped around the supercritical chamber is used to raise the temperature of the carbon dioxide in the supercritical chamber from the room temperature (usually ~ 295 K) to a temperature above the critical point of carbon dioxide.

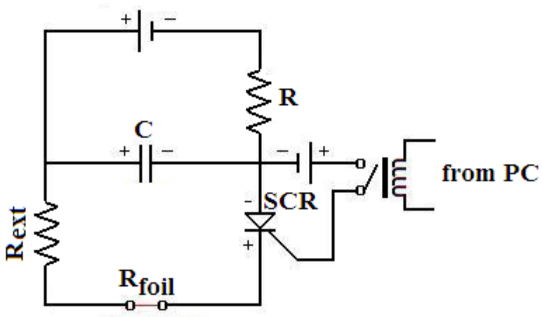

Figure 4.2: Electronic schematic of the foil heating circuit.

In order to generate thermally induced acoustic waves in the enclosure, rapidly increasing the boundary wall (nickel foil) temperature is of critical importance. The temperature rise rate at the boundary not only influences the character of thermally induced acoustic waves, but it also determines the strength of the waves, which determines whether the waves can be detected by a measurement device or not. With the knowledge gained from previous studies [74, 75], we utilize a direct-current heating of the nickel foil covered end-piece of the PTFE cylindrical enclosure by means of an *R*-*C* circuit. The electronic schematic of the foil heating circuit is shown in figure 4.2.

Table 4.1: Specifications of the experimental system for thermoacoustic transport studies

No.	**Part**	**Make and Model**	**Specification**
1	Capacitor	Cornell Dubilier CGS273U050V4C	27 mF 50 V
2	SCR	Littlefuse TO-218X	Max Trigger Time 2.5 μs
3	Foil	Alfa Aesar Nickel Thin-Foil	6 μm Thick Resistivity 6.84 x 10^{-8} Ω-m
4	Thermocouples	Omega CHCO-005 (Bare Wire) Omega EMTSS-125 (Probe Type)	Type E - 12.7 μm dia. Type E – 3.175 mm dia.
5	Pressure Probes	B&K 4193 with UC0211 Adapter Omega PX309-2KG5V	Sensitivity: 2 mV/Pa Pressure Rating: 13.8 MPa
6	Data Acquisition Board	NI 6052E	Sampling Rate: 333 kHz
7	Hand Pump	HiP 87-6-5	34.5 MPa 60 mL/stroke
8	Glands	Conax TG-24T(E)-A2-T	Pressure Rating: 22 MPa

Nickel foil is used in the present study for fast heating of a boundary wall. The dimensions of the foil (attached around a circular PTFE end-piece) are 5.0 cm x 3.6 cm x 6.0 μm and the electrical resistance of the foil is calculated to be 0.016 ohm. By carefully calculating every component in the *R-C* circuit, the circuit efficiency $\varepsilon = R_{foil} / R_{total}$ is found to be about 36%. A capacitor rated at 27 mF is used in the circuit. The circuit time constant (τ_{RC}) is hence 0.0012 sec. A silicon-control-rectifier (SCR), (Littelfuse, model: TO-218X) with a 2.5 μs triggering time is used to fully discharge the capacitor. This arrangement provides a rapid rise of the foil temperature for generating the acoustic waves in the surrounding gas along the tube. Some other advantages of the *R-C* heating system include good repeatability and easy control of heating rate and maximum temperature increase. The details of the apparatus and circuit elements are listed in table 4.1.

A condenser type microphone (12.7 mm Brüel & Kjær model 4193) is used to measure the thermally generated acoustic waves in the tube. The probe is mounted transversely on the plastic tube (see figure 4.1a), with the sensing surface flush with the inner wall of the tube. The probe is thus directly exposed to the gas and minimally interfered with the pressure wave propagation. For the experiments of thermally induced acoustic waves in supercritical carbon dioxide, the microphone probe is in a high pressure zone, while the data is transmitted to the DAQ card, which is in an atmospheric region. A multiple wire cable gland is employed to seal the connection port of the microphone cable. The Brüel & Kjær condenser microphone is chosen because of its high sensitivity, fast response, and wide frequency-response band. The probe instrumentation also includes a low-frequency adaptor (UC0211), a microphone preamplifier (model 2669) and a conditioning amplifier (ZN 2690). The Brüel & Kjær 4193 condenser microphone (see figure 4.1a Inset), consists of a metal housing, inside of which a delicate and highly tensioned diaphragm is placed ahead of a back-plate. The distance between the diaphragm and the back-plate changes if there is any pressure difference between the microphone housing and the tube volume exposed to the diaphragm. The corresponding capacitance variation is converted to pressure signal by the microphone cartridge (not shown). To eliminate the influence of static pressure variation and protect the diaphragm, the microphone housing is connected to the tube medium by a static pressure equalization vent hole (figure 4.1a Inset). The narrow vent hole ensures that the static pressure of the microphone housing follows the pressure variation in the tube. The vent hole is designed to equalize the static pressure variations without suppressing the low-frequency components of the dynamical acoustic pressure which are to be measured. The time constant of the microphone's pressure equalization system is about 0.1 s; therefore, frequencies below 10 Hz are affected by the vent hole. The Brüel & Kjær 4193 microphone is thus suitable for measuring the dynamic pressure variation when the static pressure in the tube remains constant or varies slowly.

Other than the pressure measurements, the temperature and voltage drop histories of the foil (after the capacitor is discharged) are also recorded in our experiments. Previous numerical studies [74, 75] of thermally generated acoustic waves by a rapidly heated surface show that the early temperature behavior of the heated surface (during the first several micro-seconds) has a significant influence on the behavior of the acoustic wave generated. Hence we pay special attention to the measurement of the foil temperature at early times after the capacitor is discharged. A Chromel-constantan type E thermocouple (Thermocouple 1, figure 4.1a) with a diameter of 12.7 μm is used for its fast response time. The attachment of thermocouple on the foil is also critical. Silver adhesive (503, Electron Microscope Science) is chosen after evaluating many other brands of adhesives, mainly for its high thermal conductivity and ease of applicability. Due to its heat capacitance, the adhesive slows down the response time of the thermocouple at very early times. The signals from the thermocouple probe are conditioned by an Omega Omni Amp IIB-E conditioning amplifier. The amplifier not only amplifies the weak signal from the thermocouple, but also isolates the high-frequency electrical disturbance by its interior signal conditioning circuit. Although the amplifier eliminates the electrical disturbance at early times, it does not accurately record the peak value of the temperature rise of the foil (due to signal conditioning by the Omega Omni Amp IIB-E amplifier). Two other type E thermocouples (Thermocouple 2 and 3, figure 4.1a) are used to measure the steady state initial temperature of the supercritical fluid. A high pressure transducer (Omega PX309) is used to measure and monitor the steady state pressure inside the supercritical chamber. The analog temperature, pressure and voltage measurements were recorded, digitized and saved through a National Instrument SCB-68 terminal block and a 6052E data acquisition (DAQ) board. High sample rate (333 kHz) of the 6052E DAQ board guarantees that the signals are recorded with high fidelity. The data acquisition system also provides a voltage output to a relay to control the triggering time of the SCR.

4.3 Experimental method

At the beginning of an experiment, the supercritical chamber is heated and pressurized to a specific initial temperature and pressure ($T_i > T_c$, $p_i > p_c$), where the experiment is to be performed and all measurement devices are powered up and run such that the warm-up time requirements are met. The capacitor is then charged up to a desired voltage V_0, which is measured by an HP 34401A multi-meter. The LabvVIEW 7.0 software is used to record the signals of temperature, voltage and pressure in the experiments, and to provide controlling signals. The SCR is triggered to initiate the experiment. At this point in the experiment, the capacitor is discharged causing fast heating of the foil. The foil temperature gradually falls after the initial rapid rise. After one experiment is carried out, the experimental conditions are initialized before the next set of measurements is made. Each experiment is repeated several times in order to confirm the measurements.

4.4 Estimation of experimental uncertainty

Several independent measurements are performed for the completion of the experimental study. These measurements are as follows: dynamic pressure in the tube (measured by the Brüel & Kjær 4193 microphone), foil temperature (measured by the Omega fine wire thermocouple), steady state pressure of the fluid (measured by Omega PX309 pressure probe), steady state temperature of the fluid (measured by Omega probe type thermocouples) and the voltage decay across the foil. All measurements are recorded by the NI 6052E DAQ board. The accuracy of the NI 6052E is ±4.747 mV for the range of voltage measurements made by the 4193 microphone and ±0.242 mV for the thermocouple measurements. There are two sources of fixed error in the Brüel & Kjær 4193 microphone system: ±0.2 dB from the 4193 microphone itself and ±0.1 dB from the 2690 signal conditioner. With the error introduced by the DAQ board, the total maximum error for the pressure measurements made by the Brüel & Kjær 4193 microphone is estimated to be ±0.15 Pa. The errors in the thermocouple measurements include ±0.045 ºC error from the cold junction compensation, 0.01%/ºC instability from the amplifier, ±0.02 ºC error from conversion of thermocouple voltage to temperature scale (ºC) and ±0.08 ºC DAQ board error. Consequently, the total temperature error is 0.145 ºC plus 0.01% of the reading value. The only error in the voltage measurement is from the DAQ board, which is ±7.47 mV. Apart from these fixed errors, high frequency micro-scale oscillations (noise) are also present in the system. The measured pressure trace is digitally filtered by using a third order Butterworth method. The fixed errors along with the inherent noise level of the experimental system during the measurements are used to calculate the total error of the acoustic pressure and foil temperature measurement. The total errors of the pressure and temperature measurement are presented as error bars in the filtered traces (pressure and temperature). The uncertainty associated with the experimental data is estimated by using the method recommended by Kline and McClintock [174]. Both the transient pressure measurements by the Brüel & Kjær 4193 microphone and voltage measurements exhibit very high degrees of consistency and very low uncertainties. For the 4193 microphone measurement, the uncertainty, with a 95% confidence level, is 0.85% for the experimental case with the lowest charging voltage and capacitance**.** The corresponding uncertainty is 0.1% for the voltage measurements. The maximum uncertainty is ±0.5% for the foil temperature measurements. The steady state initial temperature (T_i) for all the experiments is within ±0.05% of the measured value, and the steady state initial pressure (p_i) is within

±0.2% of the measurements. Hence, the error associated with the variation of the initial conditions is considered to be minor.

4.5 Measurement of thermoacoustic waves: Result and discussion

The behavior of thermally induced acoustic waves in supercritical carbon dioxide, generated by fast heating of a bounding solid wall in a closed cylindrical tube is investigated experimentally. The fast heating of the nickel foil generates a thermally induced acoustic wave in the closed cylinder, which keeps traversing between the two ends and undergoes many reflections before it is fully damped out. The time dependent gas pressure variation in the tube and the voltage and temperature histories of the foil are recorded by a fast-response measurement system. Experiments are first carried out in supercritical carbon dioxide relatively far from the critical point [p_i = 7.653 MPa (1110 psi), T_i = 315 K] with a capacitor charging voltage of V_0 = 30 V.

Figure 4.3a exhibits the transient voltage drop across the foil. The response shows a typical *R-C* circuit discharge behavior. The corresponding foil temperature (V_0 = 30 V) measured by the thermocouple is shown in figure 4.3b. At early times (for less than 0.04 s after the beginning of capacitor discharging) the foil temperature increase fast, but the increasing rate decreases gradually. The temperature rise in the foil depends on the heat gain and loss to the supercritical fluid. It should also be noted that during the capacitor discharge period, the electromagnetic disturbance is high, and the thermocouple cannot respond during the initial discharge period (for about t < 0.005 s).

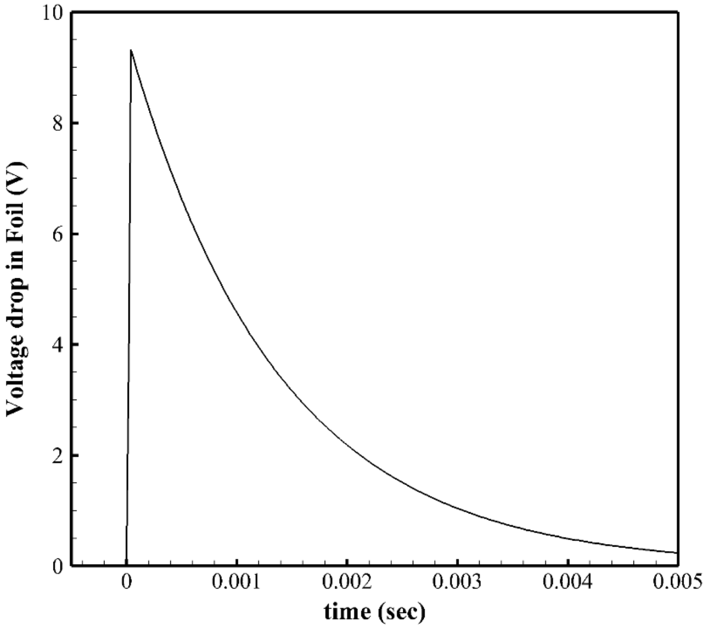

(a)

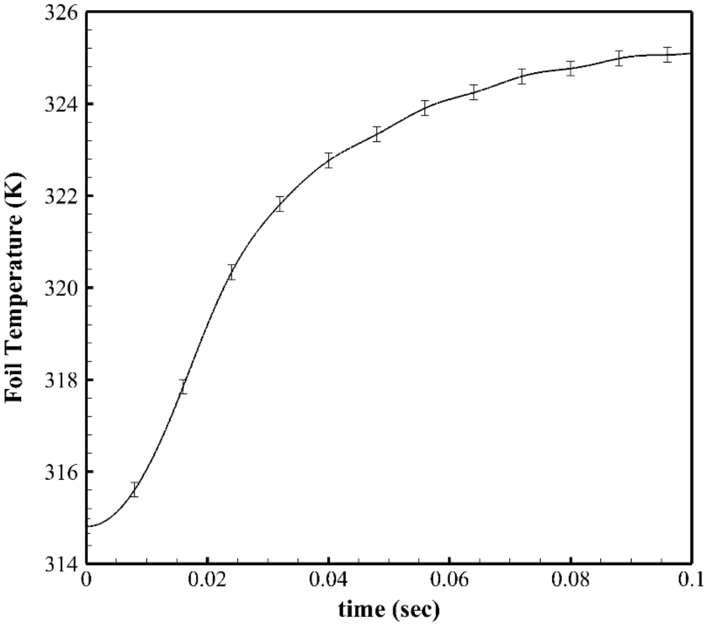

(b)

Figure 4.3: Temporal variation of (a) voltage drop across the foil and (b) corresponding foil temperature (measured) with p_i = 7.653 MPa (1110 psi), T_i = 315 K and V_0 = 30 V.

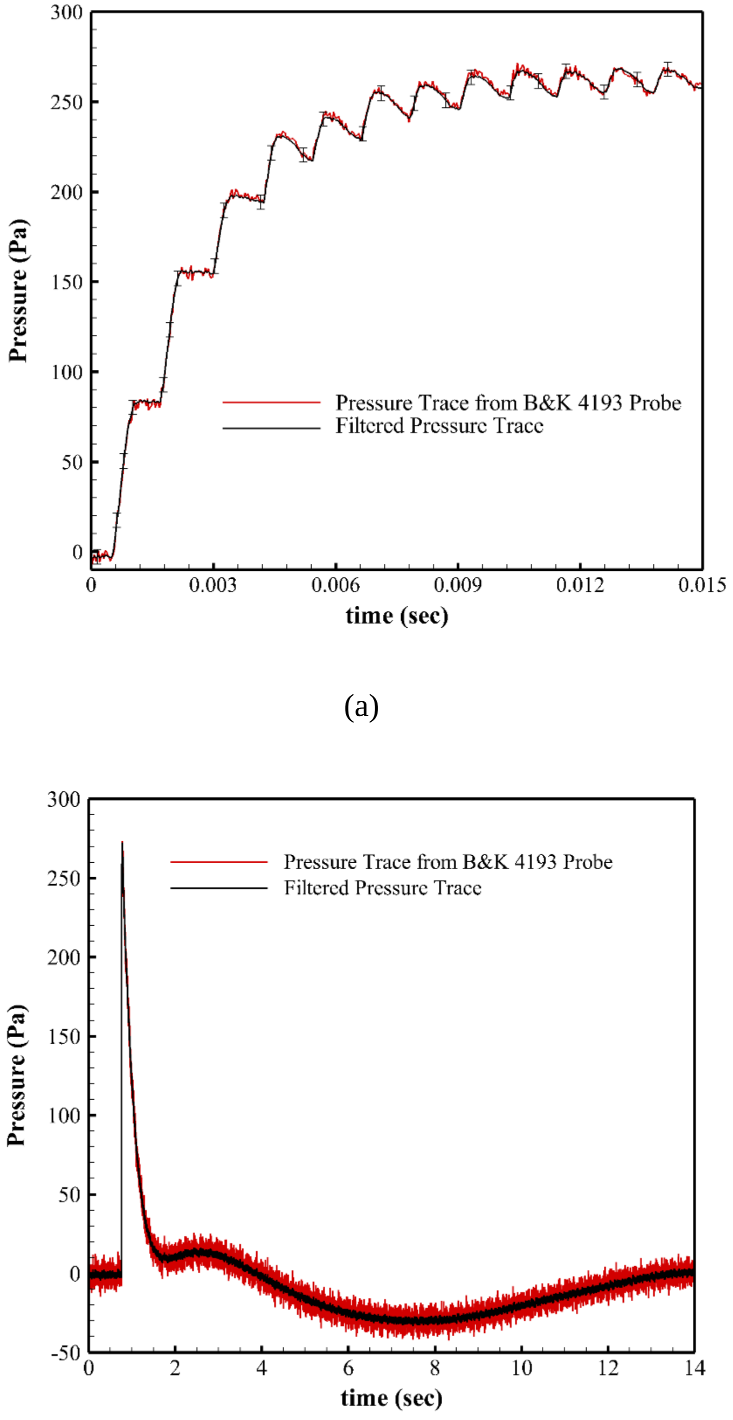

(a)

(b)

Figure 4.4: Temporal variation of pressure measured at the center of the cylinder by B&K microphone with p_i = 7.653 MPa (1110 psi), T_i = 315 K and V_0 = 30 V at (a) early time and (b) long time.

Figures 4.4a and 4.4b show the trace of the pressure wave measured by the Brüel & Kjær microphone with a capacitor charging voltage of V_0 = 30 V at early and long time scales respectively. The probe records a peak when the acoustic wave sweeps past the probe diaphragm during its motion from the heated side to the unheated side. The next peak indicates the reflected acoustic wave that now travels from the unheated side to the heated side. During the first several acoustic cycles (figure 4.4a) the wave shape shows sharp step like profiles. This is consistent with the previous studies [103, 169]. Due to viscous dissipation and energy losses, the characteristic acoustic wave profile gradually disappears. The measured Mach number (M) of the acoustic wave is about 1.0. High frequency disturbances in both early and long time scales are observed from the measurements (figure 4.4a and 4.4b). Similar disturbances were also reported in the experimental study by Miura *et al.* [103]. These are caused mainly by the fluid flow within the supercritical chamber induced by imperfections in foil and tube surface and non-uniform heating of the supercritical chamber. The high frequency noise is digitally filtered from the measured data and used to calculate the total error of the actual measurements. The pressure variations measured by the Brüel & Kjær 4193 microphone over a longer period of time (about 14.0 s) is presented in figure 4.4b. It is interesting to observe that the probe records pressure values lower than the ambient value (non-physical) beginning at about t = 3.0 s. This is due to the inherent construction and operational features of the Brüel & Kjær condenser microphone [75]. The existence of the narrow vent hole (see figure 4.1a inset) causes the non-physical results at longer times. The Brüel & Kjær microphone is suitable for the measurement of dynamic pressure where static pressure remains constant. It is not designed for the measurement with varying static pressure in the longer time scale [175].

In the experiment, as the Nickel thin-foil is suddenly heated, the fluid inside the tube also heats up and the static pressure starts increasing. The static pressure inside the tube increases to a maximum value, then decreases to the initial value in several seconds as the applied heat is lost to the ambient from the wall. Since, the diameter of the vent hole connecting the microphone housing to the pressure field in the tube is very small, the static pressure inside the microphone housing varies more slowly than that in the enclosed flow field. Within some time period, the static pressure inside the microphone housing becomes greater than that of the fluid in the tube, causing the pressure readings to fall below zero (from t = 3.0 s to t < 14.0 s in figure 4.4b). Finally, as the static pressure difference between the microphone housing and the tube is eliminated (due to the cooling of the system), the pressure measurement eventually become equal to zero in the longer time scale (t ≈ 14.0 s). This behavior of the Brüel & Kjær 4193 microphone, however, does not affect the thermoacoustic pressure measurements in the early time scale. Based on the observations discussed above, a series of experiments are performed in near-critical states. Effect of the near-critical property variations and the boundary heat rate on the generation of thermoacoustic waves are investigated in detail. The results obtained from these experiments are discussed in detail in the following sub-sections.

4.5.1 Effect of critically diverging thermo-physical properties

To observe the effect of the critical point (diverging thermo-physical properties) on the generation and propagation of thermoacoustic waves, two different sets of experiments are carried out with the same capacitor charging voltage V_0 = 30 V. The operating parameters for the two sets of experiments are shown in table 4.2.

Table 4.2: Operating parameters for the experiments performed

Experiment Set #	Capacitor Charging Voltage (V_0)	Initial Pressure (p_i)	Initial Temperature (T_i)
1	30 V	7.653 MPa (1110 psi)	315 K
	30 V	7.584 MPa (1100 psi)	315 K
	30 V	7.515 MPa (1090 psi)	315 K
2	30 V	7.515 MPa (1090 psi)	315 K
	30 V	7.515 MPa (1090 psi)	310 K
	30 V	7.515 MPa (1090 psi)	308 K
	30 V	7.515 MPa (1090 psi)	306 K

The first set of experiments (set #1) are performed at the same initial temperature (T_i = 315 K), but different initial pressures of supercritical carbon dioxide ranging from 7.515 MPa to 7.653 MPa (1090 psi to 1110 psi). Figure 4.5a shows the measured (filtered) pressure trace at the early time for the first set of experiments. It is observed that, as the initial pressure of the fluid approaches the critical pressure (p_c = 7.3773 MPa), relatively stronger acoustic fields are generated for the same capacitor charging voltage (*i.e.* same temperature perturbation (ΔT) in the fluid).

Accordingly, the strongest waves are generated (in figure 4.5a) for p_i = 7.515 MPa, which has the initial pressure closest to the critical pressure. However, the variation of the strength of the acoustic field is not significantly different since the initial state for all of the experiments performed in set #1 are relatively far from the critical point. The long time behavior of the pressure traces for set #1 is shown in figure 4.5b. The measured pressure values are again lower than the ambient value (non-physical) at longer times and are similar to the trends shown in Figure 4.4b. The reasons for the behavior are already explained.

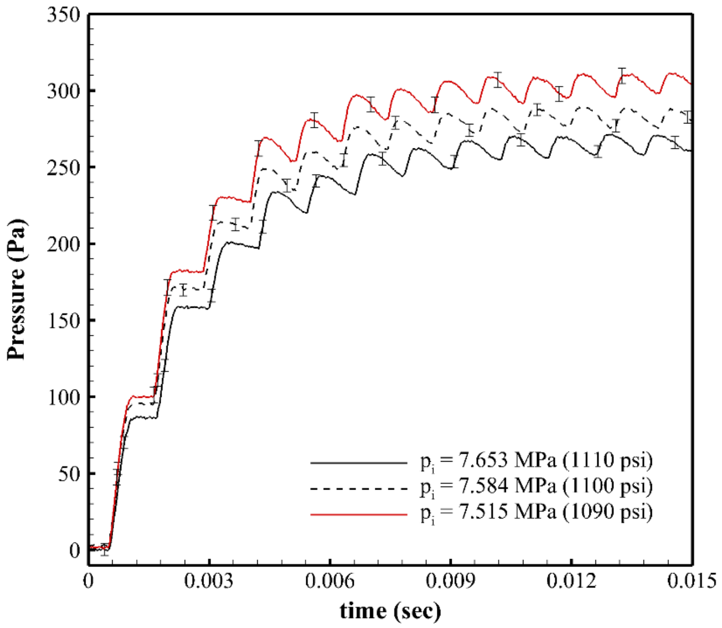

(a)

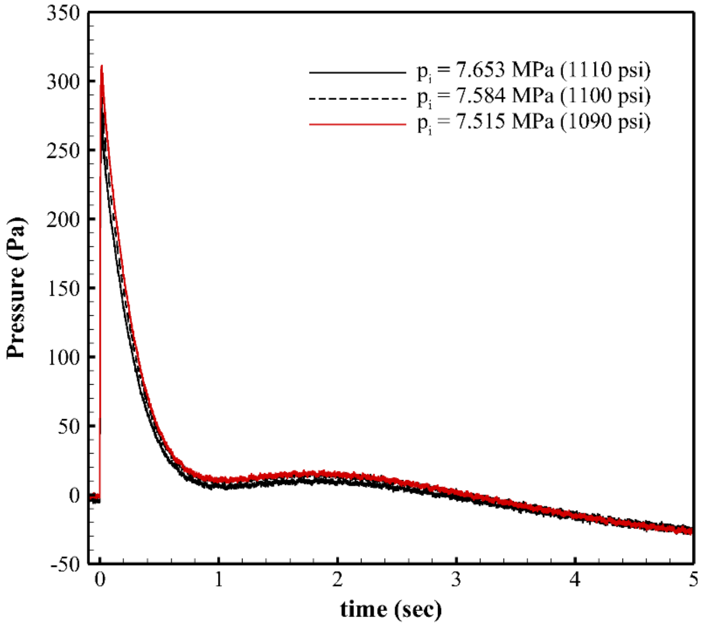

(b)

Figure 4.5: Temporal variation of pressure measured at the center of the cylinder by B&K microphone (filtered) with T_i = 315 K, V_0 = 30 K and at various initial pressures at (a) early time and (b) long time.

The second set of experiments (set #2) are performed at the same initial pressure (p_i = 7.515 MPa) with changing initial temperatures (T_i) ranging from 315 K to 306 K. The measured (filtered) pressure traces at both early and long time scales are shown in figure 4.6a and 4.6b respectively. The measured pressure values (in figure 4.6b) are again lower than the ambient value at longer times and are similar to the trends shown in figure 4.4b. The reasons for the behavior are already explained. Similar to the phenomena observed for the experiments performed in set #1, the strength of the generated acoustic fields for these experiments (set #2) also increased as the critical state is approached. It is also observed that, as the initial state of the fluid approaches the critical point, the variation of the strength of the acoustic field becomes significantly different.

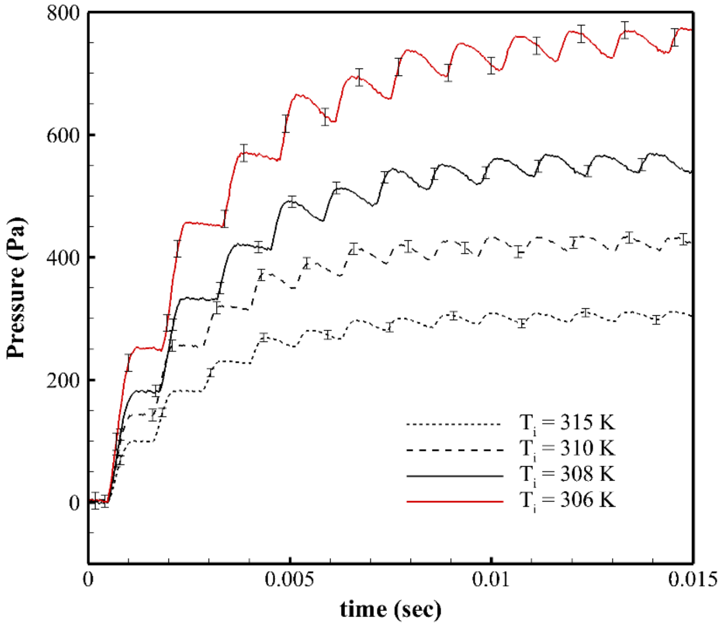

(a)

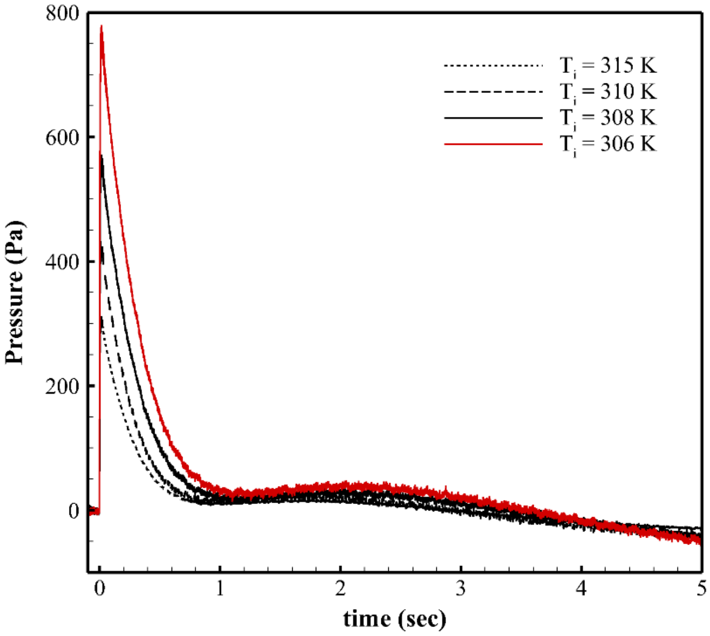

(b)

Figure 4.6: Temporal variation of pressure measured at the center of the cylinder by B&K microphone (filtered) with p_i = 7.515 MPa (1090 psi), V_0 = 30 K and at various initial temperatures at (a) early time and (b) long time.

From previous analysis [88], it was found that decreasing the thermal diffusivity (α) weakens the acoustic field, while both increasing $\left(\frac{\partial p}{\partial T}\right)_\rho$ and isothermal compressibility (β) enhances the acoustic field. In the above experiments, an increase in strength of the acoustic field is observed mainly due to the constructive combination of the increasing isothermal compressibility (β) and decreasing thermal diffusivity (α) near the critical point. The experiment performed in supercritical carbon dioxide with initial state p_i = 7.515 MPa (1090 psi) and T_i = 306 K hence exhibits the strongest acoustic field (figure 4.6a). Due to the same reason, it is also observed that the small scale disturbance in the pressure trace (indicated by the error bars in the figures) increases in magnitude as the critical point is approached. However, the measured acoustic speeds for all the experiments are in good agreement with the numerical value predicted by the NIST Standard Reference Database 23 [3].

4.5.2 Effect of charging voltage

Several experiments are carried out with different capacitor charging voltage (V_0) and keeping the initial state of the supercritical carbon dioxide fixed (p_i = 7.515 MPa, T_i = 306 K). Figure 4.7a shows the effects of the charging voltage on the temporal decay of voltage across the foil. The corresponding foil temperature measurements are given in figure 4.7b. Any change of the charging voltage of the capacitor only changes the total electrical energy stored in the capacitor; it does not affect the characteristics of the circuit. As it is observed from figure 4.7a and 4.7b, an increase in the charging voltage of the capacitor directly affects the temperature of the foil and hence the rate of increase of the foil temperature.

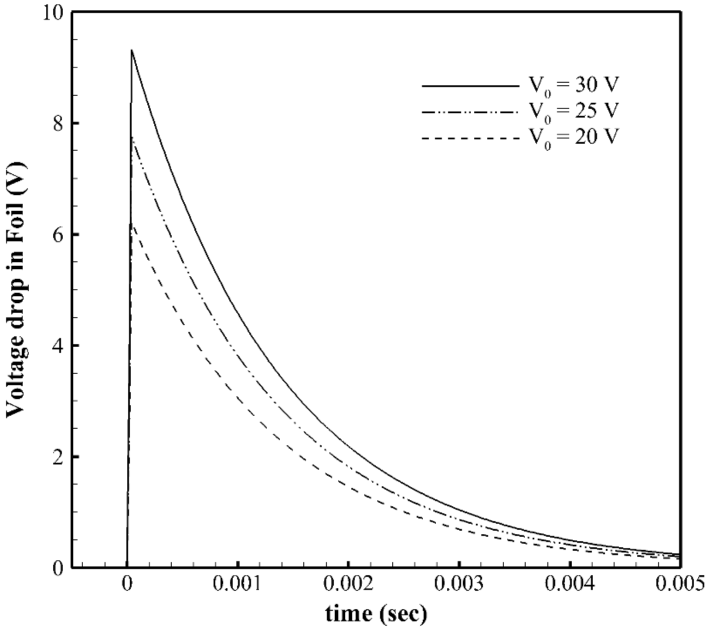

(a)

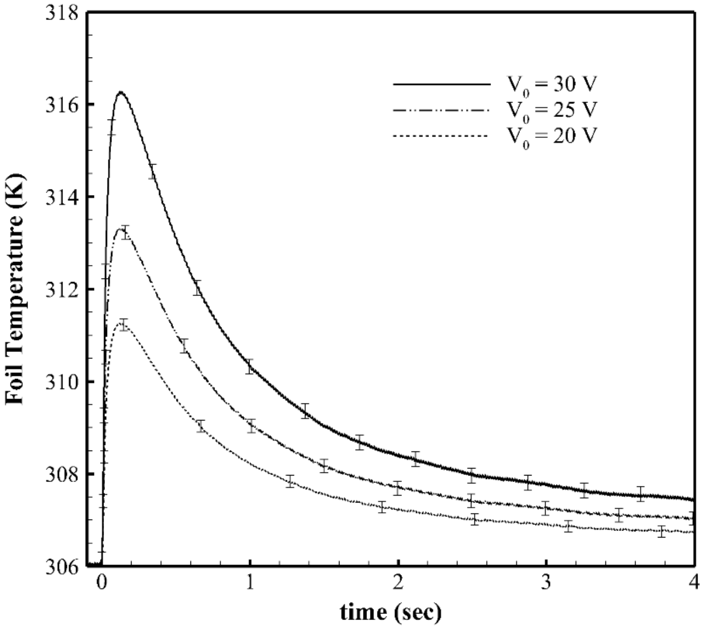

(b)

Figure 4.7: Temporal variation of (a) voltage drops across the foil and (b) foil temperatures for different charging voltages.

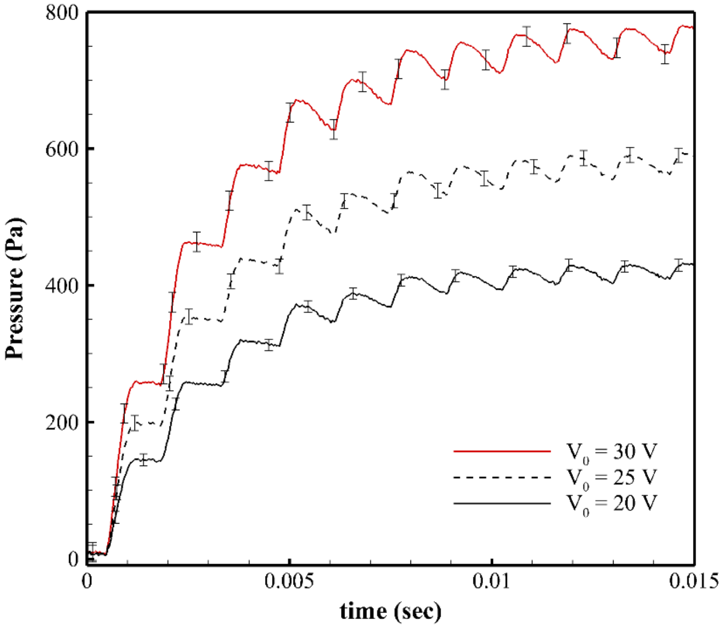

(a)

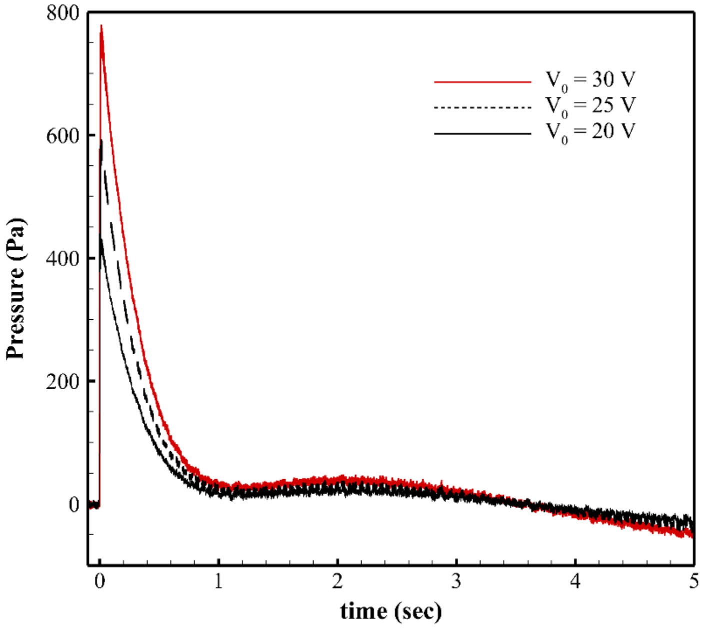

(b)

Figure 4.8: Temporal variation of pressure measured at the center of the cylinder by B&K microphone (filtered) with p_i = 7.515 MPa (1090 psi), T_i = 306 K and at various charging voltages at (a) early time and (b) long time.

Figure 4.8a shows the effects of the charging voltage (V_0) of the capacitor on the acoustic wave (early time) as measured by the Brüel & Kjær microphone under the same initial conditions of the supercritical fluid. It is observed that, relatively stronger acoustic waves are generated for higher charging voltages, because of the greater temperature rise rate of the boundary (foil). Physically, the acoustic wave originates from the local pressure disturbance near the wall introduced by sudden gas temperature increase. The sudden gas temperature increase is due to the heat conduction from the foil that is rapidly heated. Therefore, the strength of the generated acoustic wave is found to vary almost linearly with the charging voltage. The long time evolution of the measured pressure trace is shown in figure 4.8b. The measured pressure values (see figure 4.8a) are again lower than the ambient value (non-physical) at longer times and are similar to the trends shown in figure 4.4b. The reasons for the behavior are already explained.

4.6 Comparison of experimental and numerical results

Following the numerical model described in chapter 3, the thermoacoustic waves in supercritical carbon dioxide are also numerically simulated and compared with the experimental measurements. A confined layer of thermally quiescent and motion-free supercritical carbon dioxide inside a one dimensional layer of length, L is considered. A schematic of the computational domain is shown in figure 4.9. At $t > 0$, a prescribed time dependent thermal load (T_L) is applied at the left boundary.

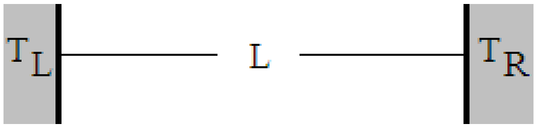

Figure 4.9: Schematic diagram of the computational domain.

The right wall temperature (T_R) is held at the initial bulk fluid temperature (T_i). The thermally induced acoustic waves generated are studied as a function of space and time. We consider one-dimensional continuity, compressible form of the Navier-Stokes equations and total energy equation to describe the generation and propagation of thermally induced acoustic waves in supercritical carbon dioxide (Equations 3.1-3.3). For speeding-up the numerical calculations carried out in the experimental geometry, non-dimensional form of these governing equations with appropriate scaling rules are used. The following non-dimensional variables are defined:

$$\hat{x} = \frac{x}{L} \qquad \hat{t} = \frac{c_{si}t}{L} \qquad \hat{u} = \frac{u}{c_{si}} \qquad \hat{p} = \frac{p}{\rho_i {c_{si}}^2} \qquad \hat{T} = \frac{k_i T}{\mu_i {c_{si}}^2}$$

$$\hat{\rho} = \frac{\rho}{\rho_i} \qquad \hat{\mu} = \frac{\mu}{\mu_i} \qquad \hat{\mu}_b = \frac{\mu_b}{\mu_i} \qquad \hat{k} = \frac{k}{k_i} \qquad \hat{h} = \frac{h}{{c_{si}}^2}$$

Here t is time, x is a cartesian coordinate, ρ is density, u is the velocity component in x direction, μ is the shear viscosity, μ_b is the bulk viscosity, h is the total enthalpy given by $e+\frac{p}{\rho}+\frac{1}{2}u^2$ (where e is the specific internal energy), k is the thermal conductivity, T is the temperature and p is pressure. The non-dimensional governing equations of the problem are then:

$$\frac{\partial\hat{\rho}}{\partial\hat{t}}+\frac{\partial}{\partial\hat{x}}\left(\hat{\rho}\hat{u}\right)=0 \tag{4.1}$$

$$\frac{\partial}{\partial\hat{t}}(\hat{\rho}\hat{u})+\hat{u}\frac{\partial}{\partial\hat{x}}(\hat{\rho}\hat{u})=-\frac{\partial\hat{p}}{\partial\hat{x}}+\left(\Pr_i.\frac{\tau_a}{\tau_d}\right)\left[\frac{4}{3}\frac{\partial}{\partial\hat{x}}\left(\hat{\mu}\frac{\partial\hat{u}}{\partial\hat{x}}\right)+\frac{\partial}{\partial\hat{x}}\left(\hat{\mu}_b\frac{\partial\hat{u}}{\partial\hat{x}}\right)\right] \tag{4.2}$$

$$\frac{\partial}{\partial\hat{t}}(\hat{\rho}\hat{h})+\hat{u}\frac{\partial}{\partial\hat{x}}(\hat{\rho}\hat{h})=\frac{\partial\hat{p}}{\partial\hat{t}}+\left(\Pr_i.\frac{\tau_a}{\tau_d}\right)\left[\frac{\partial}{\partial\hat{x}}\left(\hat{k}\frac{\partial\hat{T}}{\partial\hat{x}}\right)+\frac{4}{3}\hat{\mu}\left(\frac{\partial\hat{u}}{\partial\hat{x}}\right)^2+\hat{\mu}_b\left(\frac{\partial\hat{u}}{\partial\hat{x}}\right)^2\right] \tag{4.3}$$

Here, the subscript '*i*' refers to the conditions at the initial state. c_s is the local acoustic speed. Pr_i is the Prandtl number at the initial state (*i.e.* at $p = p_i$, $T = T_i$) of the fluid. τ_a and τ_d are the acoustic and diffusion time scales of the problem respectively, where $\tau_a = L/C$ and $\tau_d = L^2/\alpha$ (α is the thermal diffusivity).

Although the experiments are performed in a 25.0 cm long tube, the long time numerical simulation is carried out in one dimensional domains of length L = 1.0 cm and 25.0 cm. For the L = 1.0 cm case, the left wall thermal boundary condition is scaled using a temporal scaling factor of $L_{\mathrm{exp}eriment} / L_{computation} = 25$. Within the piston effect time scale $\tau_{PE} = \tau_d / (\gamma - 1)^2$, where γ is the ratio of specific heats) in near-critical fluid, the acoustic field is mainly one dimensional in nature [96, 176]. Also, an order of magnitude analysis of the non-dimensional form of the governing equations reveals that, the coefficient $\left(\mathrm{Pr}_i \cdot \tau_a / \tau_d\right)$ of the viscous terms in equations 4.2 and 4.3 is very small compared to the other terms of the equations within the piston effect time scale. Due to this reason, the non-linear viscous terms has a very small effect on the generation and propagation of the thermoacoustic waves in this time scale (τ_{PE}) except for the case where the initial state of the supercritical fluid is very close to the pseudo-critical state [169]. Hence scaling down the problem with the characteristic length scale should not significantly change the characteristics (amplitude and profile) of the acoustic wave at the very early time period. The thermal boundary conditions of the problem are given by:

$$\hat{T}_L = f(\hat{t}) \tag{4.4}$$

$$\hat{T}_R = \frac{T_i k_i}{\mu_i C_i^2} \tag{4.5}$$

The governing equations (equations 4.1~4.3) are solved by finite volume method using central difference scheme for the spatial discretization and a Crank-Nicolson scheme for time discretization. Details of the mathematical modeling and numerical scheme used are already discussed in chapter 3. Development of the time dependent thermal boundary condition and the comparison of the numerical result with the experimental measurements are discussed in the following sub-sections.

4.6.1 Development of time dependent thermal boundary condition

The experimental measurements of both the voltage drop and temperature decay of the foil are used to develop the thermal boundary condition of the heated wall for the numerical simulations. Limited by the properties of the Omega fine wire thermocouple, its contact with the foil and the electrical noise of the discharging circuit, the thermocouple (Thermocouple 1 in figure 4.1a) in our experiments can not accurately measure the foil temperature at very early times (temperature rise time). Hence, the foil voltage measurements and the electrical energy input into the foil are used to develop the transient change in foil temperature at very early times.

Figure 4.10 gives the foil voltage measurements and the foil temperatures calculated from the foil voltage measurements for V_0 = 30 V. In the calculation of foil temperature (from the voltage measurements), an energy balance equation for the foil is considered:

$$\rho c_P \delta A \frac{\partial T}{\partial t} = \frac{[V(t)]^2}{R_{total}} - q_{loss} \tag{4.6}$$

Here, ρ is the density of the foil, c_p is the specific heat of the foil, δ is the foil thickness, A is the foil surface area, q_{loss} is the total heat loss of the foil to the surrounding and $V(t)$ is the transient voltage response of the foil. At the early time, the heat loss to the surrounding is modeled by radiation loss and is given by $q_{loss} = \epsilon\sigma A\,(T^4 - T_i^4)$. Here ϵ is the emissivity of the foil and σ is the Stefan-Boltzmann constant. The above equation is numerically solved by an explicit scheme. From the calculated temperature profile, it was observed that the heat loss term has only a slight effect on the foil temperature during the temperature rise time (within the initial 0.005 s).

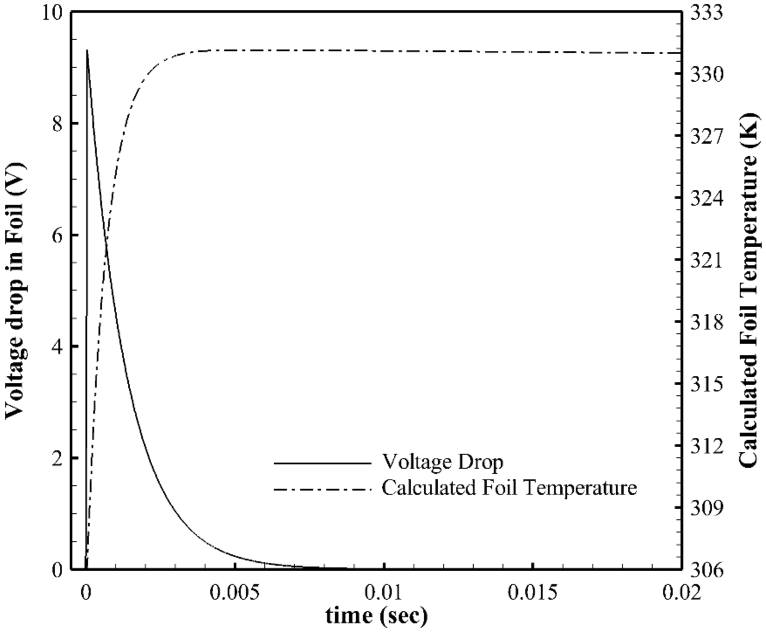

Figure 4.10: Measured foil voltage and calculated foil temperature at early times with V_0 = 30 V

Figure 4.11 shows the comparison of the calculated foil temperature (with radiation heat loss) from the voltage measurements and the thermocouple temperature measurements. The thermocouple data is conditioned by an Omega Omni Amp IIB-E conditioning amplifier. The signal conditioning circuit along with the adhesive used to attach the thermocouple with the foil slows down the overall response of the thermocouple. These effects perhaps cause the measured temperature data at early times to be under-predicted. In longer time scale, somewhat different reasons cause the discrepancy between the measured and predicted values of the temperature. There are several sources of heat loss, such as convective heat loss to air and conduction losses to the aluminum bars and the mica plate, that were not considered in equation 4.6. A polynomial fit of the measured data is obtained for $t > 0.15$ s and is extended from $t = 0.15$ s to $t = 0.0001$ s, as shown in figure 4.11.

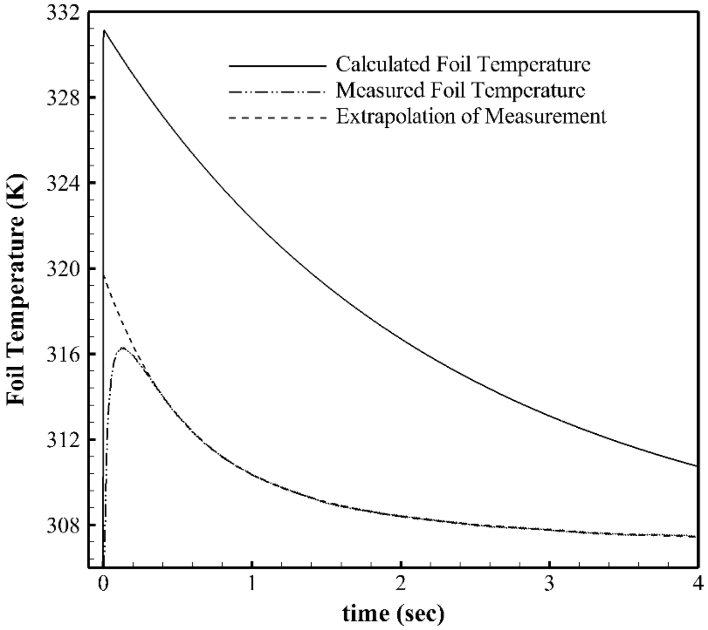

Figure 4.11: Measured, calculated and extrapolation of measured foil temperature with $V_0 = 30$ V

For the experiments, the foil temperature increases rapidly and then gradually decays. The predicted temperature increase of the foil (from the voltage measurement) meets the extrapolated curve of the temperature decay at about t = 0.0009 s. This is close to the calculated circuit time constant, $\tau_{RC} = R_{total}C$ = 0.0012 s for C = 27.0 mF as (section 4.2). The corrected temperature history of the foil (as shown in figure 4.11) is used as the temperature input (as high resolution look-up table) in our numerical simulations for the experimental case where V_0 = 30 V and p_i = 7.515 MPa (1090 psi), T_i = 306 K.

4.6.2 Numerical predictions

The generation of acoustic waves in supercritical carbon dioxide (p_i = 7.515 MPa, T_i = 306 K) in an enclosure by rapidly heating a boundary wall is simulated by numerically solving the compressible form of the Navier-Stokes equations. As observed from our numerical investigation of thermoacoustic transport (discussed in chapter 3), the behavior of the acoustic waves produced in supercritical fluid is strongly dependent on the rate of increase of the heated boundary and its subsequent cooling. Hence, it is of critical importance to apply the accurate boundary conditions in the numerical simulations. In section 4.6.1, the procedure to develop the temporal boundary condition for the heated foil (T_L) is discussed. The numerical simulations for the first several acoustic cycles are calculated for the scaled domain (L = 1.0 cm) and a domain with the exact length of the test section (L = 25.0 cm). The numerical model is used to obtain the predictions of the flow and acoustic fields in the experimental tube driven by fast heating of the foil. The temporal evolution of the pressure (experimental and numerical) is represented using a non-dimensionalized time scale (t/τ_a) for the sake of comparison.

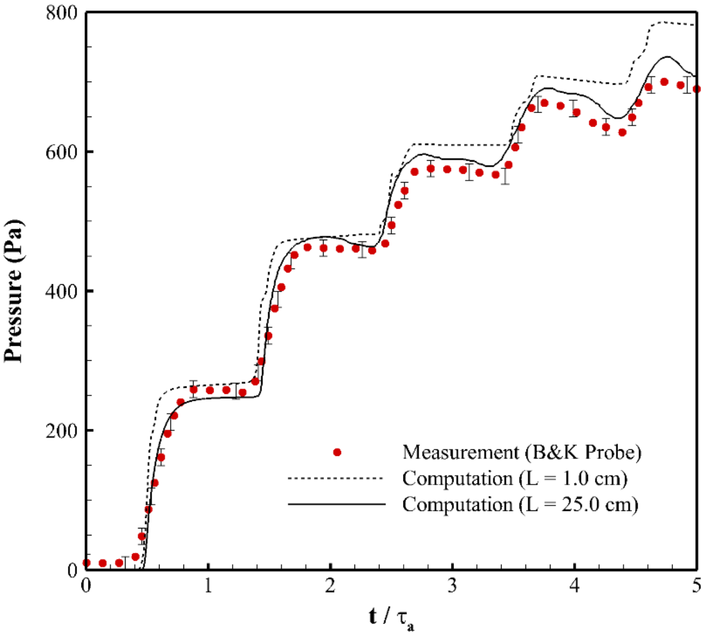

Figure 4.12: Temporal variation of measured and calculated pressure at the center of the cylinder with p_i = 7.515 MPa (1090 psi) and T_i = 306 K at early time.

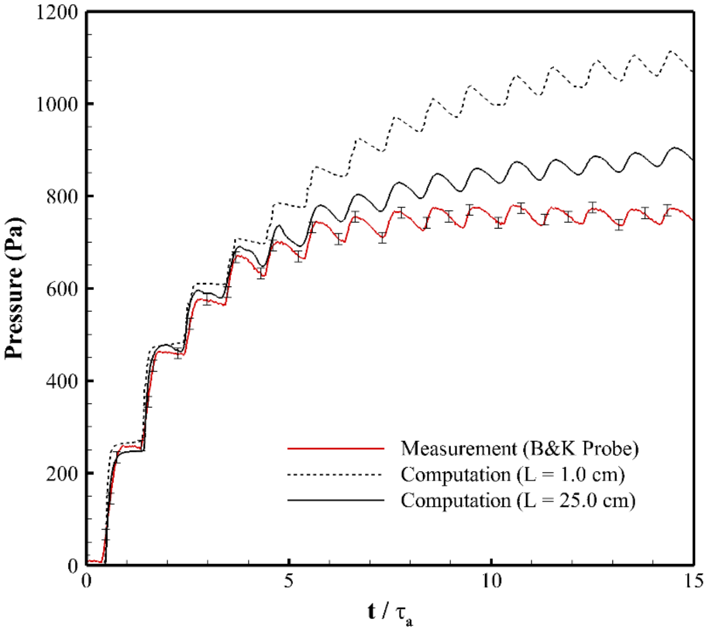

Figure 4.13: Temporal variation of measured and calculated pressure at the center of the cylinder with p_i = 7.515 MPa (1090 psi) and T_i = 306 K at long time.

For the pressure at the mid-point of the cylindrical tube, the comparison of the numerical and experimental results at the very early time is given in figure 4.12, with V_0 = 30 V. It is observed that, in the first several acoustic cycles ($t/\tau_a < 5$) the numerical and experimental results are in good agreement. The computational results for both the cases (L = 1.0 cm and L = 25.0 cm) compares well with the experimental pressure trace. No significant differences between the computational results are observed within this time period. This is also in accordance with the scaling analysis. However, the computational results are always found to slightly over-predict the experimental result. The reason the computational results are always a little bit higher than the experimental results may be that the parameters that used in the numerical model are slightly different from the real value. For example, the thickness of the metal foil plays a significant role in the numerical model. But, the value given by manufacturer (6.0 μm) has ±10% toleration level. There is also an error level associated with the measurement of the initial state of the supercritical carbon dioxide in the experimental system. So, it is possible that the initial state considered in our numerical model is not exactly same as that in the experiments. The overall good comparison between the computational and experimental pressure results at the very early time demonstrates that the method for reconstructing the transient foil temperature is reasonable.

Calculations with both the scaled and exact domains (L = 1.0 cm and 25.0 cm) are carried out for a longer period of time. The comparison of the experimental and the numerical evolution of pressure at a longer time scale are shown in figure 4.13. While the numerical results correctly predict the acoustic wave speed and amplitude of dynamic pressure fluctuations, a significant deviation of the computed pressure evolution from the measurement is noticed from the figure. Obviously, the case with the exact length (*L* = 25.0 cm) of the experimental system compares relatively well with the experimental measurement. This is mainly due to acoustic attenuation affecting the pressure wave as it propagates through longer distances. But it is also noticed that, there is still a significant amount of discrepancy existing between the calculated (*L* = 25.0 cm) and the measured pressure amplitude (~ 15% maximum). In the numerical model, both of the walls are considered smooth and rigid, and also the system is assumed to be sealed perfectly. However, in the experiments, the acoustic energy is partially absorbed by the walls when the wave hits one. In the longer time scale, the acoustic wave in the experimental system is also dissipated due to viscous damping introduced by the side walls. There is also the possibility of the existence of leakage flow through the crevices of the inlet port (figure 4.1a) in the experimental setup.

4.7 Summary and conclusions

Experimental measurements are performed to characterize the generation, propagation and dissipation of thermally induced acoustic waves in supercritical carbon dioxide near its critical point. Fast heating of a thin nickel foil along the boundary of the enclosure produces strong compressive waves that carry energy and momentum from the heated boundary deep into the undisturbed regions of the fluid. The behavior of the generated acoustic waves is studied as functions of the initial state of the supercritical fluid and the boundary heating rate. The thermally induced acoustic waves in supercritical carbon dioxide are also investigated by numerically solving a fully compressible form of the Navier-Stokes equations. The NIST Standard Reference Database 23 [3] is used to generate two-dimensional look-up tables to represent the equation of state and other thermodynamic properties for supercritical carbon dioxide. The results from the numerical simulations are compared with the experimental measurements with accurately developed boundary conditions.

Two interesting and significant phenomena are observed from the results presented. First, as predicted by the numerical studies described in chapter 3 and earlier studies [95, 159], the strength of the generated acoustic wave is found to be correlated with the initial state (p_i, T_i) of the supercritical fluid. It is observed that the relative strength of the heating induced acoustic wave increases as the critical state of the fluid (CO_2) is approached. Secondly, the strength of the generated acoustic field is also dependent on the rate of boundary heating (temperature rise rate). At early times, the computational and experimental results show an excellent match. But the experimental measurements and numerical results (L = 25.0 cm) for the pressure evolution at longer time scales do not compare well quantitatively. This deviation is explained by the presence of leakage flow in the experimental tube and viscous dissipation due to the side walls (simulations are considered one dimensional). The physical features of the computational and experimental results are also found to be in good agreement.

CHAPTER 5: NUMERICAL INVESTIGATION OF BUOYANCY INDUCED THERMAL TRANSPORT IN NEAR-CRITICAL SUPERCRITICAL FLUID[4]

5.1 Introduction

Supercritical fluids are characterized by high densities, high thermal conductivities (compared to gases) and low viscosities, but low thermal diffusivities (compared to liquids). Due to the high compressibility of supercritical fluids, very strong thermoacoustic waves are generated due to temperature relaxation at a boundary. In the long time scale under terrestrial gravity, the thermoacoustic waves are attenuated due to viscous dissipation and buoyancy driven flows. The interaction of thermoacoustic transport with buoyancy driven flows in near-critical supercritical carbon dioxide is investigated numerically in this chapter. Buoyancy driven thermal transport in supercritical carbon dioxide is studied numerically by employing a high-fidelity CFD model. Thermally quiescent and motion free supercritical carbon dioxide in a two-dimensional square enclosure confined by rigid walls is considered. The NIST Standard Reference database 23 [3] is used to obtain the ρ-p-T relations for supercritical carbon dioxide, along with the static enthalpy $h_0 = f(p, T)$, thermal conductivity $k = f(p, T)$, viscosity $\mu = f(p, T)$ and specific heat $c_p = f(p, T)$ relations. Different features regarding the flow field and thermal transport induced by natural convection near the critical point are revealed by the simulations. Correlations are developed to predict the heat transfer coefficient during buoyancy driven convection at both supercritical and near-critical conditions in the form $Nu = f(Ra, p', T', T'_{pc})$ where,

---

[4] The results presented in this chapter can be found in, [177] N. Hasan and B. Farouk, "Buoyancy driven convection in near-critical and supercritical fluids," *International Journal of Heat and Mass Transfer,* vol. 55, pp. 4207-4216, 2012.

$p' = (p_i - p_c)/p_c$ is the dimensionless pressure, $T' = (T_m - T_c)/T_c$ is the dimensionless temperature, $T_m = (T_i + T_{L\infty})/2$ and $T'_{pc} = (T_{pc} - T_c)/T_c$ is the dimensionless pseudo-critical temperature. The subscripts '*i*', '*m*', '*c*', and '*pc*' refer to the initial, mean, critical, and pseudo-critical conditions respectively. The subscript '$L\infty$' refers to final value of the left (heated) wall temperature. The effect of critically diverging bulk viscosity on buoyancy driven transport is also investigated.

5.2 Problem description

Thermally quiescent and motion-free supercritical carbon dioxide inside a square cavity (L = 10.0 mm) is considered. The initial state of the fluid is described as, T_i and p_i with $T_i > T_c$ and $p_i > p_c$ for all cases considered. Figure 5.1 shows the schematic diagram of the computational domain.

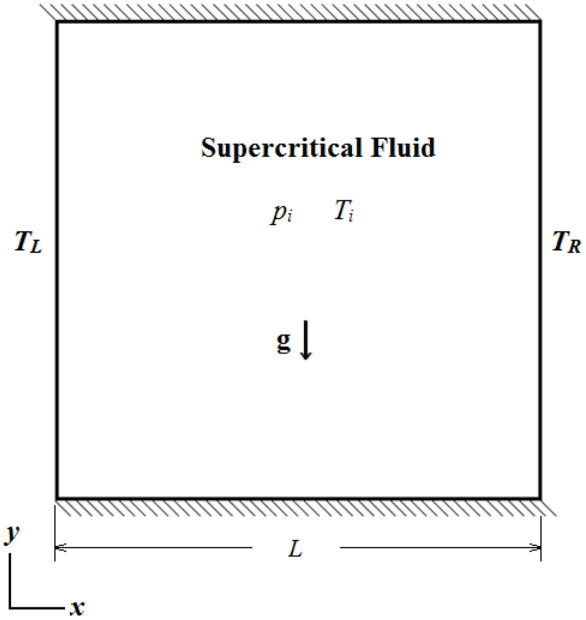

Figure 5.1: Schematic Diagram of the computational domain.

At $t > 0$, a prescribed thermal load is applied at the left boundary ($X/L = 0.0$) in the form of:

$$T_L(t) = f(t) = T_i + \Delta T(1 - e^{-At/\tau}) \tag{5.1}$$

Such that, at steady state, $T_L(t)\big|_{t\to\infty} = T_i + \Delta T$. Here, ΔT is the target temperature rise and A is the heating parameter (as discussed in chapter 3). The acoustic time, $\tau = L/C$ is defined as the flight time for an acoustic wave to traverse the slab. The left wall temperature (equation 5.1) is a sigmoid function of time which is characterized by a faster change in temperature at the early time and by a slower change as the target temperature is approached. The rate of the boundary heating is dependent on the combination of target temperature rise (ΔT) and the heating parameter (A).

5.3 Mathematical modeling

Natural convection in supercritical and near-critical fluids can be modeled by the complete hydrodynamic description for an isotropic, Newtonian, compressible, and dissipative (viscous and heat-conducting) fluid [76, 114]. Although there have been reasonable concerns over the legitimacy of applying continuum physics at the vicinity of the critical point, according to Stanley[57] the hydrodynamic limit is located around $\left(T - T_c\right)/T_c \approx 10^{-5}$ (for CO_2, $T - T_c \approx 3\,\text{mK}$) on the critical isobar ($p = p_c$). The physical conditions we consider here are relatively far from the hydrodynamic limit, and as a result they fall safely into the realm of continuum mechanics. The following two-dimensional continuity and the compressible form of the Navier-Stokes equations are used to describe the buoyancy driven flow in supercritical and near-critical carbon dioxide:

$$\frac{\partial \rho}{\partial t}+\nabla\cdot\left(\rho\overline{V}\right)=0 \tag{5.2}$$

$$\frac{\partial(\rho u)}{\partial t}+\nabla\cdot\left(\rho\overline{V}u\right)=-\frac{\partial p}{\partial x}+\nabla\cdot\left(\mu\nabla u\right)+\frac{\partial}{\partial x}\left[\mu_b\left(\frac{\partial u}{\partial x}+\frac{\partial v}{\partial y}\right)\right]+\rho g_x \tag{5.3}$$

$$\frac{\partial(\rho v)}{\partial t}+\nabla\cdot\left(\rho\overline{V}v\right)=-\frac{\partial p}{\partial y}+\nabla\cdot\left(\mu\nabla v\right)+\frac{\partial}{\partial y}\left[\mu_b\left(\frac{\partial u}{\partial x}+\frac{\partial v}{\partial y}\right)\right]+\rho g_y \tag{5.4}$$

$$\frac{D(\rho h)}{Dt}=\frac{\partial p}{\partial t}+\nabla\cdot\left(k\nabla T\right)+\mu\Phi+\mu_b\Psi \tag{5.5}$$

Here, Φ and Ψ are the viscous dissipation functions given by –

$$\Phi=2\left[\left(\frac{\partial u}{\partial x}\right)^2+\left(\frac{\partial v}{\partial y}\right)^2\right]+\left[\left(\frac{\partial v}{\partial x}\right)+\left(\frac{\partial u}{\partial y}\right)\right]^2-\frac{2}{3}\left(\nabla\cdot\overline{V}\right)^2 \tag{5.6}$$

$$\Psi=\left(\nabla\cdot\overline{V}\right)^2 \tag{5.7}$$

Here, x and y are the cartesian coordinates, t is time, ρ is density, $\vec{V}$ is the velocity vector given by $\overline{V}=u\hat{i}+v\hat{j}$, where, u and v are the velocities in x and y direction respectively, h is the total enthalpy, T is the temperature and p is pressure. The property shear viscosity (μ) is a measure of the resistance of a fluid which is being deformed by a shear stress while bulk viscosity (μ_b) is the measure of the resistance to a normal stress. The equation of state describing the ρ-p-T relation of supercritical fluids (including the near-critical states) is not well-described. It has been shown earlier [39] that the van der Waals equation of state does not represent the properties of supercritical carbon dioxide accurately near the critical point. In this study, we used the NIST Standard Reference Database 23 [3] for the $\rho = f(p, T)$ relations and for evaluation of other thermodynamic properties of supercritical and near-critical carbon dioxide. The NIST23 [3] equation of state describing the ρ-p-T relation of carbon dioxide is based on the equation of state proposed by Span and Wagner [65], which is mainly empirical in nature and includes special non-analytic terms to predict the correct behavior of the fluid to the immediate vicinity of the critical point. Two dimensional look-up tables are developed in the present study to represent the $\rho = f\,(p, T)$, $k = f\,(p, T)$, $\mu = f\,(p, T)$, $h_0 = f(p, T)$ and $c_p = f\,(p, T)$ data provided by the NIST Standard Reference Database 23. Bulk viscosity (μ_b) of near-critical CO_2 is calculated using the set of equations proposed by Onuki [56] and is given as a function of pressure and temperature. The temperature range considered for the look-up tables is 300K - 350K and the pressure range is 7.38 MPa – 12.0 MPa.

5.3.1 Boundary conditions

The thermal boundary conditions for the wall heating (left wall, T_L) has been given earlier in equation (5.1). The right wall is maintained at a constant temperature ($T_R = T_i$) while the top and bottom walls of the enclosure are insulated ($\frac{\partial T}{\partial n} = 0$, where n is the direction normal to the wall). No slip conditions are used for all four walls. Zero gradient boundary condition ($\frac{\partial \rho}{\partial n} = 0$) for fluid density at the walls is applied and the wall pressure is updated using the equation of state for supercritical carbon dioxide as a function of wall temperature and wall density.

5.3.2 Numerical method

The governing equations are solved by a finite volume method using a central difference scheme for the spatial discretization and a Crank-Nicolson scheme for time discretization. Throughout the simulations, a non-uniform grid spacing (Δx_{max} / Δx_{min} =

Δy_{max} / Δy_{min} = 5) with relatively finer mesh near the walls is considered to generate sufficiently high spatial resolution. For the early time calculations, a Courant number ($c_s\Delta t/\Delta x$) of 0.4 is set to assure proper numerical convergence of the solution. Here Δt is the time step, Δx is the grid spacing and c_s is the local acoustic speed. All computations were carried out on a Dell Precision T7500n computer.

5.4 Buoyancy driven thermal transport: Result and discussion

Numerical simulations for buoyancy driven flow in supercritical carbon dioxide are carried out for a number of cases in the near-critical region as well as far from the critical point and for different Rayleigh numbers ranging from 10^6 to 10^9. The Rayleigh number for the problem is defined as, $Ra = Gr.\mathrm{Pr}$. Here, Gr is the Grashof number and Pr is the Prandtl number. Grashoff number is given by $Gr = \frac{g\beta L^3 \Delta T}{\nu^2}$. Here, β is the volumetric thermal expansion coefficient, ν is the kinematic viscosity, L is the characteristic length of the computational domain and ΔT is the temperature difference between the hot and cold wall at the steady state. The spatially averaged steady state Nusselt number is calculated as $Nu = \frac{q'' L}{k\Delta T}$. Here, L is the characteristic length; k is the thermal conductivity of the fluid and q'' is the spatially averaged heat flux along the vertical walls calculated using the following equation:

$$q'' = \frac{1}{L}\int_0^L q_x dx \tag{5.8}$$

q_x is the local heat flux along the vertical walls. All fluid properties are evaluated at the bulk mean temperature ($T_m = \left(T_i + T_{L\infty}\right)/2$) and pressure. The results presented are for the transient as well as the steady state behavior of the convective flow field and thermal transport in supercritical carbon dioxide. The steady state solutions are obtained by directly solving the steady state form of the governing equations (equations 5.2 – 5.5).

5.4.1 Buoyancy driven flows in supercritical fluids

Buoyancy driven convection in a side heated enclosure filled with supercritical carbon dioxide is investigated here. For variation of the governing parameters, namely, the Rayleigh number and the temperature and pressure deviation from the critical point, the intensity and structure of the steady-state convective heat transfer are observed. Steady state temperature contours due to free convective flow (Ra = 10^8) in supercritical carbon dioxide both near ($p' = 3.66 \times 10^{-4}$, $T' = 2.9 \times 10^{-3}$ and $T_{pc}' = 3.88 \times 10^{-5}$) and far ($p' = 6.26 \times 10^{-1}$, $T' = 6.86 \times 10^{-2}$ and $T_{pc}' = 8.71 \times 10^{-2}$) from the critical point, is shown in figures 5.2 and 5.3 respectively. At this high Rayleigh number at early time (t = 1 sec), both figures 5.2a and 5.3a shows formation of thin thermal boundary layers along the vertical walls while the central region of the enclosure remains isothermal. As a result of the buoyancy effect, the upstream flow rises near the left warm surface and downstream flow moves near the cool right surface. Due to the vanishing thermal diffusivity near the critical point, diffusion is much slower in the near critical supercritical fluid (figure 5.2a) than in supercritical fluid far from the critical point (figure 5.3a). However, as the conditions inside the enclosure approaches steady state, the center of the enclosure becomes thermally stratified due to the large density variations present in the supercritical fluid and the temperature contours for cases both near and far from the critical point become almost identical (figures 5.2b and 5.3b).

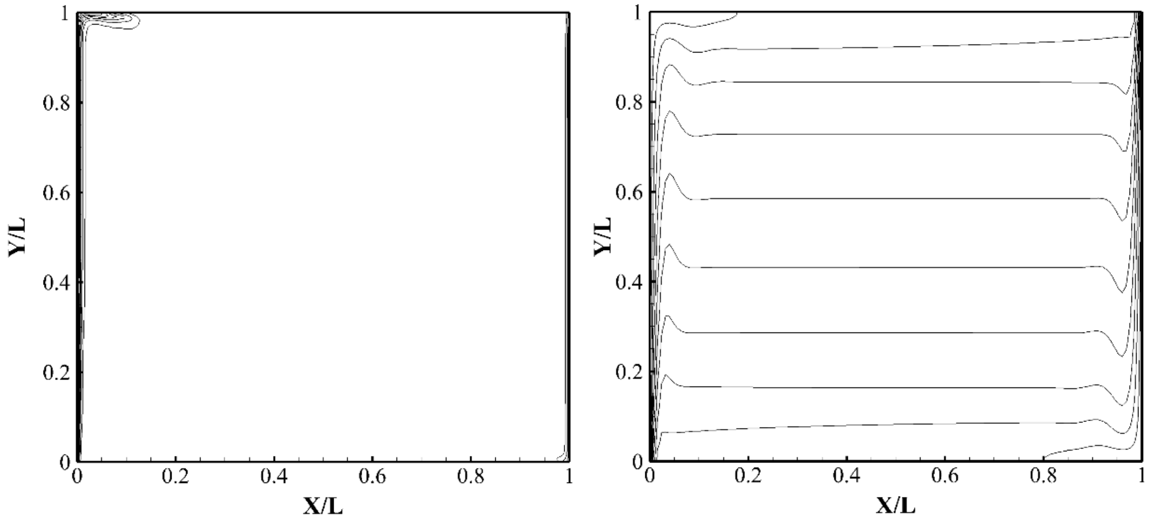

(a) (b)

Figure 5.2: Contours of steady state temperature inside the side heated enclosure filled with supercritical carbon dioxide near the critical point (p_i = 7.38 MPa, T_m = 305.0 K) with Ra = 10^8, p' = $3.66\text{x}10^{-4}$, T' = $2.9\text{x}10^{-3}$ and T_{pc}' = $3.88\text{x}10^{-5}$ at (a) t = 1.0 sec and (b) steady state [T_{max} = 305.05 K (left wall), T_{min} = 304.95 K (right wall), δT = 10 mK].

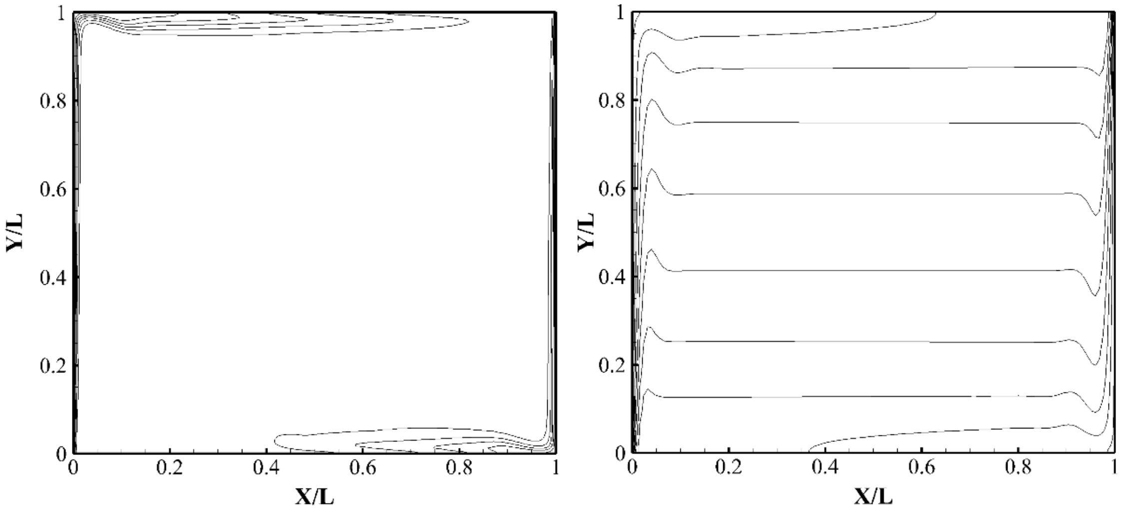

(a) (b)

Figure 5.3: Contours of steady state temperature inside the side heated enclosure filled with supercritical carbon dioxide far from the critical point (p_i = 12.0 MPa, T_m = 325.0 K) with Ra = 10^8, p' = $6.26\text{x}10^{-1}$, T' = $6.86\text{x}10^{-2}$ and T_{pc}' = $8.71\text{x}10^{-2}$; at (a) t = 1.0 sec and (b) steady state [T_{max} = 325.3 K (left wall), T_{min} = 324.7 K (right wall), δT = 60 mK].

The corresponding steady state velocity fields are shown in figures 5.4a and 5.4b respectively. Although the temperature contours and the flow field appear to be similar for supercritical fluids near and far from the critical point, it is observed that the thermal transport behavior in these two zones (near and far from the critical point) is unlike. The transport phenomena in supercritical fluid as observed from the present study are discussed in the following sections.

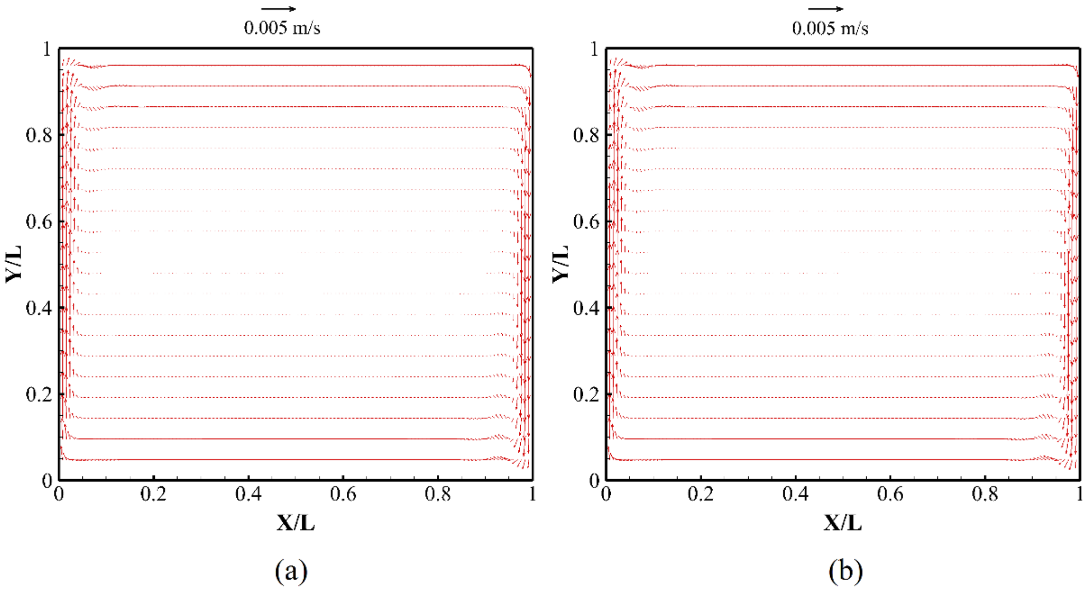

(a) (b)

Figure 5.4: Velocity vectors (Ra = 10^8) inside the side heated enclosure filled with supercritical carbon dioxide (a) near the critical point (p_i = 7.38 MPa, T_m = 305.0 K, p' = $3.66\text{x}10^{-4}$, T' = $2.9\text{x}10^{-3}$ and T_{pc}' = $3.88\text{x}10^{-5}$) and (b) far from the critical point (p_i = 12.0 MPa, T_m = 325.0 K, p' = $6.26\text{x}10^{-1}$, T' = $6.86\text{x}10^{-2}$ and T_{pc}' = $8.71\text{x}10^{-2}$) at steady state.

5.4.2 Nusselt number correlation for supercritical fluids far from the critical point

In a supercritical carbon dioxide far from the critical point (p > 10 MPa, T > 320 K), *i.e.* where $p' > 3.56\times10^{-1}, T' > 5.22\times10^{-2}$, the thermo-physical property variations are monotonic and the effect of the critical divergence is not felt. To study the thermal transport behavior in this region, a number of cases are calculated with different Rayleigh numbers (Ra) by changing the bulk pressure and temperature. Calculations for cases far from the critical point $(p > 10\text{MPa}, T > 320\text{K})$ *i.e.* $p' > 3.56\times10^{-1}, T' > 5.22\times10^{-2}$ reveal that, similar to convection in ideal gases, the Nusselt number (Nu) for free convective flow in supercritical fluids (far from the critical point) is a function of Rayleigh number (Ra) only.

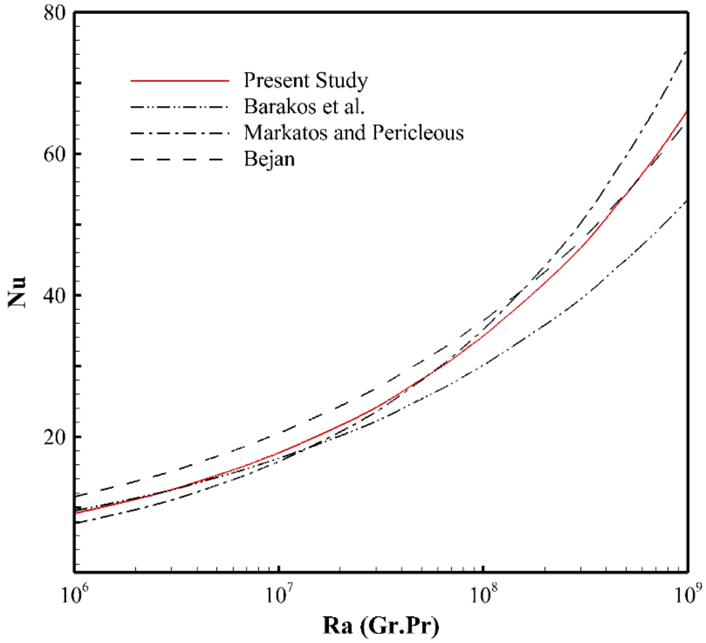

Figure 5.5: Variation of steady state spatially averaged Nusselt (Nu) number along the vertical walls as a function of Rayleigh (Ra) number for supercritical carbon dioxide far from the critical point.

A correlation for steady state spatially averaged Nusselt number for the buoyancy driven flow in supercritical carbon dioxide far from its critical point is obtained from the calculations, which is in the form:

$$Nu = 0.1754Ra^{0.2863} \tag{5.9}$$

This correlation covers a range of $10^6 < \mathrm{Ra} < 10^9$ and can be applied to calculate the free convective heat transfer coefficient in supercritical CO_2, far from its critical point. The correlation obtained from the present study (equation 5.9) is compared in figure 5.5 with Nusselt number (Nu) correlations for free convective flow in high density and high Prandtl number ($\mathrm{Pr} \gg 1$) fluids given by Barakos *et al.* [178], Markatos and Pericleous [179] and Bejan [180]. It is observed that, in the absence of critical divergence (far from the critical point), thermal transport behavior of supercritical fluids compares reasonably well to that for a high density and high Prandtl number gas.

5.4.3 Nusselt number correlation for supercritical fluids near the critical point

Near the critical point $\left(p < 10\mathrm{MPa},\ T < 320\mathrm{K},\ p' < 3.56\times10^{-1}, T' < 5.22\times10^{-2} \right)$, supercritical fluid properties are characterized by strong critical divergence as discussed in chapter 2. Usually for ideal gases and supercritical fluids far from the critical point (where thermo-physical property variations are monotonic), Nusselt number, which characterizes convective thermal transport, is a function of the Rayleigh number only. However, it was observed that, in the near critical supercritical region, transport of thermal energy varies not only as a function of Rayleigh number (Ra) but also as a function of the dimensionless pressure, $p' = \dfrac{\left(p_i - p_c\right)}{p_c}$ and temperatures $T' = \dfrac{\left(T_m - T_c\right)}{T_c}$, $T'_{pc} = \dfrac{\left(T_{pc} - T_c\right)}{T_c}$ where $T_m = \dfrac{(T_i + T_{L\infty})}{2}$. The subscripts '*i*', '*m*', '*c*' and '*pc*' refer to the initial, mean, critical, and pseudo-critical conditions.

Figure 5.6 shows the Nusselt number (Nu) variation in near critical carbon dioxide for different Rayleigh numbers, as a function of the dimensionless pressure (p') and temperature (T'). It is observed that, similar to the thermo-physical property variations near the critical point, the Nusselt number is also maximized along the pseudo-critical states (*i.e.* where $\rho = \rho_c$). The variation of Nusselt number (Nu) along the pseudo-critical states is explained as a complex combination of the divergence of the specific heat (c_p), thermal conductivity (k) and the shear viscosity (μ) around the near-critical supercritical zone. It is also observed that, for a fixed Rayleigh number (Ra) as the bulk pressure and temperature is moved away from the pseudo-critical state, the Nusselt number (Nu) eventually converges to a value given by the correlation (equation 5.9) in section 5.4.2.

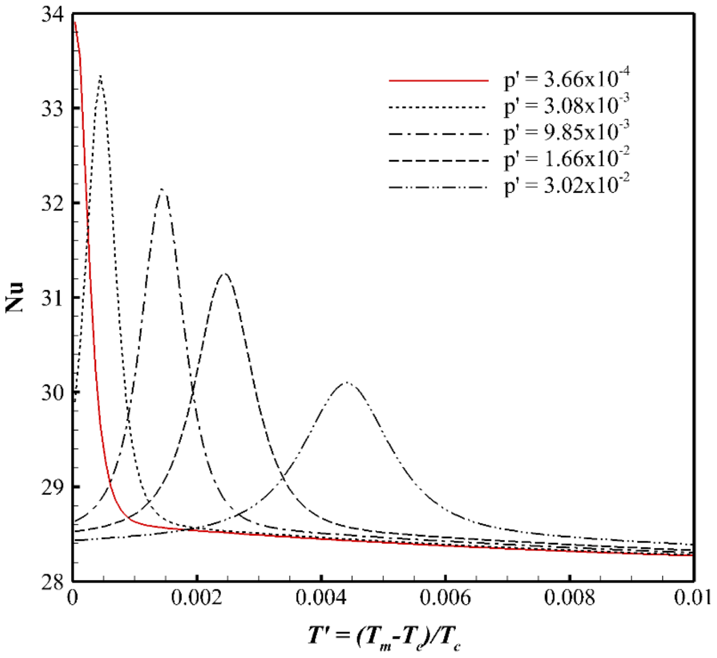

(a)

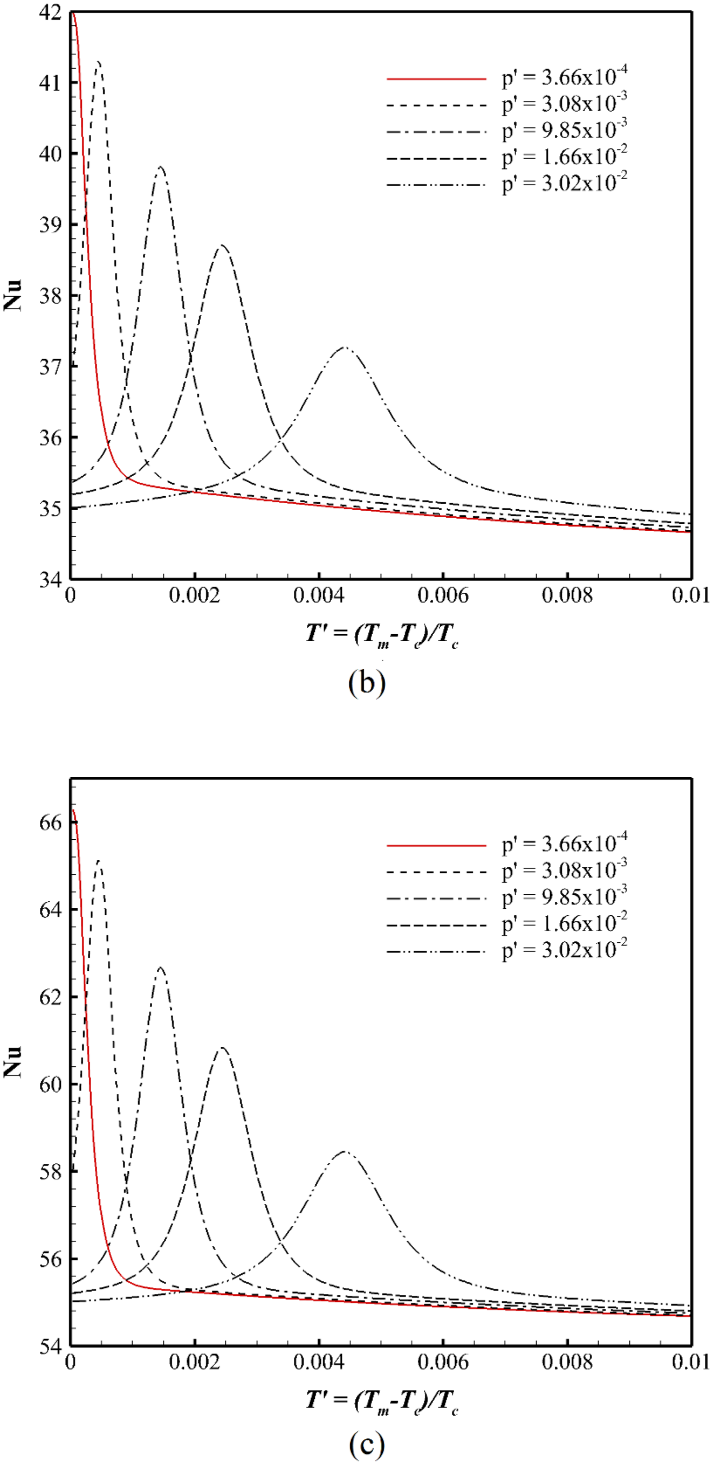

Figure 5.6: Variation of steady state spatially averaged Nusselt number as a function of $T' = \left(T_m - T_c\right)/T_c$ for different $p' = \left(p_i - p_c\right)/p_c$ for near-critical carbon dioxide with (a) Ra = 5x10^8 (b) Ra = 1x10^8 and (c) Ra = 5x10^8

A surface map for the Nusselt number variation near the critical point of carbon dioxide for Ra = $1\text{x}10^8$ is shown in figure 5.7. The point $p' = (p_i - p_c)/p_c = 0$, $T' = (T_m - T_c)/T_c = 0$ refers to the critical point. A strong divergence of the Nusselt number (Nu) at the critical point is observed. It is also observed that, for the same Rayleigh number (Ra), the Nusselt number (Nu) becomes a strong function of the dimensionless temperature (T') and pressure (p') and is maximized along the line where $\rho = \rho_c$ (pseudo-critical states). The divergence of the Nusselt number (Nu) along the pseudo-critical states is continuously diminishing as the dimensionless pressure (p') and temperature (T') moves away from the critical point ($p' = 0, T' = 0$).

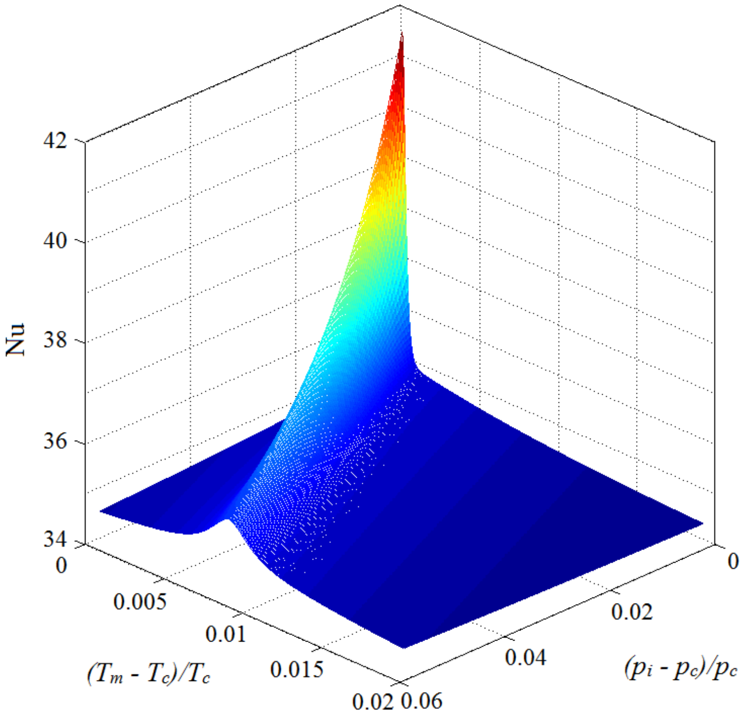

Figure 5.7: Steady state spatially averaged Nusselt number (Nu) surface map as a function of the dimensionless temperature $T' = (T_m - T_c)/T_c$ and pressure $p' = (p_i - p_c)/p_c$ for near-critical carbon dioxide at Ra = 10^8.

A correlation for Nusselt number (Nu) to fit the calculated data for different Rayleigh numbers (Ra) and the dimensionless pressure (p') and temperature (T') near the critical point of carbon dioxide is obtained which is in the form of:

$$Nu = 0.1754Ra^{0.2863} + 0.02267Ra^{0.3132} f \tag{5.10}$$

Where, $f = \left(\frac{0.6648}{(p'+T')^{0.0627}} e^{-43.21p'} \sec h \left[\frac{6024.62\left|T'-T'_{pc}\right|}{86.74p'+1} \right] + 0.0983e^{-105.21\left|T'-T'_{pc}\right|} \right)$ and

$p' = \frac{p_i - p_c}{p_c}$, $T' = \frac{T_m - T_c}{T_c}$ and $T'_{pc} = \frac{T_{pc} - T_c}{T_c}$. The above correlation is valid for the Rayleigh number range $10^6 < Ra < 10^9$ and the near critical range where, $0 < p' < 3.56\times10^{-1}$, $0 < T' < 5.22\times10^{-2}$ and $0 < T'_{pc} < 4.97\times10^{-2}$. The parameter $T'_{pc} = \frac{T_{pc} - T_c}{T_c}$ refers to the dimensionless pseudo-critical state temperature and the parameter '*f*' is defined to characterize the effect of pressure and temperature on the Nusselt number (Nu) variation. The parametric value $f = \infty$ indicates the critical point, where it decreases as the bulk mean pressure and temperature are moved away from the critical point. A parametric value of $f = 0$ indicates the point ($0 < p' < 3.56\times10^{-1}$, $0 < T' < 5.22\times10^{-2}$) where Nusselt number variation is insignificant with changing pressure and temperature.

Figure 5.8 shows the variation of Nusselt number as a function of Rayleigh number with changing values of the '*f*' parameter. The curve referring *f* = 0 is the same one obtained from equation 5.9 and shown in figure 5.5. It is observed that as critical point is approached

($f \rightarrow \infty$), Nusselt number (Nu) increases for the same Rayleigh number (Ra). However, this divergence is stronger in the high Rayleigh number region (10^8 ~ 10^9) than in lower Rayleigh number region (10^6). This behavior is mainly due to the transition to turbulence at the higher Rayleigh number flow regimes.

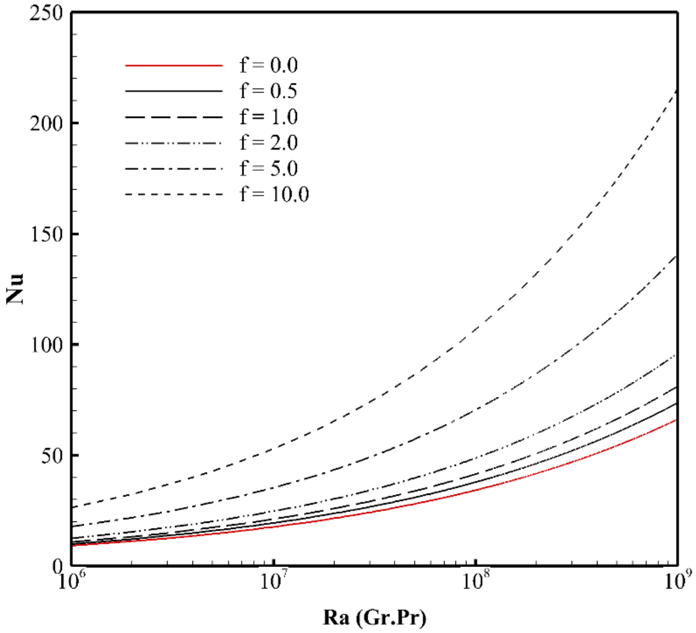

Figure 5.8: Variation of steady state spatially averaged Nusselt (Nu) number as a function of Rayleigh (Ra) number for supercritical carbon dioxide with different values of the parameter '*f*'

5.4.4 Effect of critically diverging bulk viscosity on buoyancy driven convection

To investigate the effect of critically diverging bulk viscosity on the buoyancy driven flow in supercritical fluids, a different problem geometry is employed. A two dimensional square cavity of height L = 10 mm, which is filled with supercritical carbon dioxide near its critical point is considered. The fluid is initially at rest, in thermodynamic equilibrium at a uniform temperature T_i = 304.3 K and pressure, p_i = 7.38 MPa (

$p' = 3.66\times10^{-4}$, $T' = 5.65\times10^{-4}$ and $T'_{pc} = 3.88\times10^{-5}$). Temperature of the bottom wall is raised to 304.4 K according to equation 5.1, whereas the top wall is kept at the initial temperature and the lateral walls are adiabatic. In the convective regime, the heat flow which is obtained on relatively longer time scales, exhibits some characteristics of that observed in turbulent convection in normally compressible fluids: it is composed of plumes in thermal boundary layers and jets on lateral walls. The results presented below describe the system evolution just after the beginning of bottom wall heating and after the convection onset.

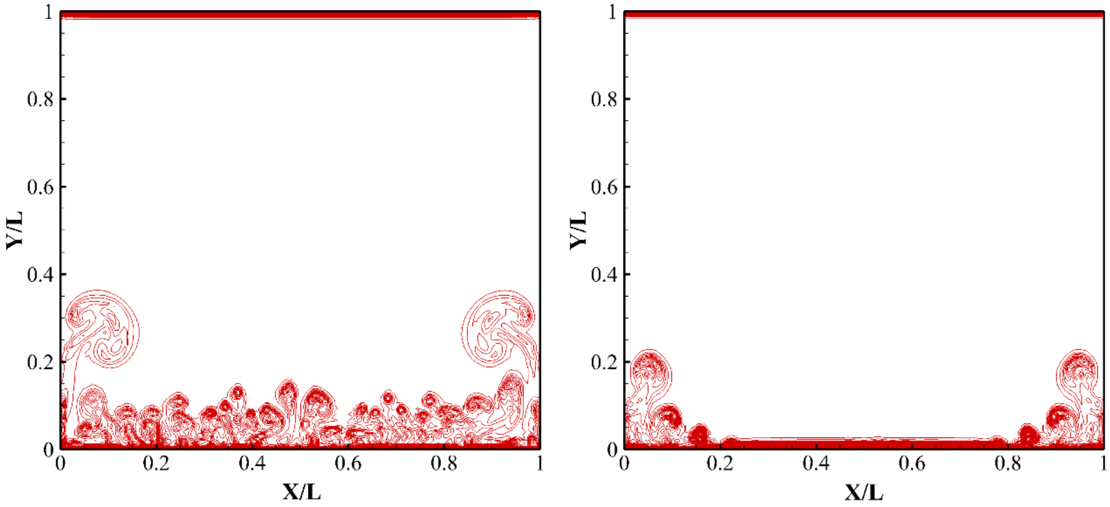

(a) (b)

Figure 5.9: Contours of temperatures inside a bottom heated enclosure at t = 1.5 sec for near critical carbon dioxide (p_i = 7.38 MPa, T_i = 304.3 K, p' = 3.66x10^{-4}, T' = 5.65x10^{-4} and T'_{pc} = 3.88x10^{-5}) and Ra = 7.35x10^{8} (a) without and (b) with the inclusion of bulk viscosity [T_{max} = 304.4 K (bottom wall), T_{min} = 304.3 K (top wall), δT = 1.0 mK].

Figure 5.9a and 5.9b shows the contours of temperature inside the enclosure with and without the effect of bulk viscosity respectively. It was observed that, at the very early stage, due to the high compressibility and the very small thermal diffusivity of the supercritical fluid, the heating of the bottom wall induces the appearance of three distinct zones in the fluid layer: two very thin thermal boundary layers near the bottom and top walls, in which diffusion realizes heat transfer, and the bulk of the cavity which temperature is homogeneously increased by thermoacoustic effects and bulk viscosity shows no effect at this time. However, in the convective flow regime, plumes developed along the heated boundary at a relatively earlier time (t = 1.5 sec) when the bulk viscosity was absent in the model. With the inclusion of the bulk viscosity, the boundary layers appear more stable at this time.

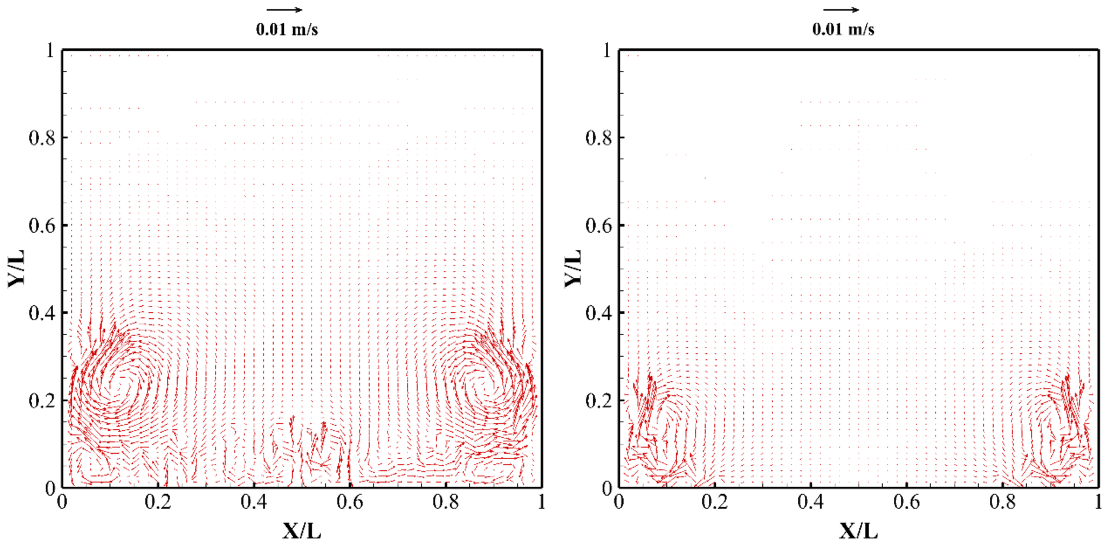

(a) (b)

Figure 5.10: Velocity Vectors inside a bottom heated enclosure at t = 1.5 sec for near-critical carbon dioxide (p_i = 7.38 MPa, T_i = 304.3 K, p' = 3.66x10^{-4}, T' = 5.65x10^{-4} and T_{pc}' = 3.88x10^{-5}) and Ra = 7.35x10^{8} (a) without and (b) with the inclusion of bulk viscosity.

The corresponding velocity fields are shown in figure 5.10a and 5.10b respectively. The velocity fields at the earlier time (t = 1.5 sec) are mainly characterized by two large upward rising plumes located at the bottom corners of the cavity and the rest of the cavity is almost undisturbed. However, for the case without considering the bulk viscosity (see figure 5.10a), several smaller convection rolls are also visible near the bottom (heated) wall while they are completely absent for the case considering bulk viscosity (see figure 5.10b).

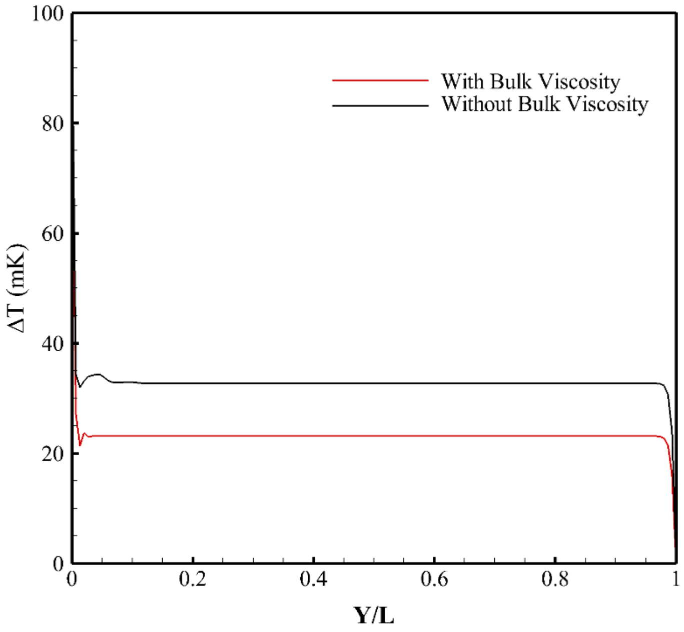

Figure 5.11: Spatial variation of temperature inside the enclosure at mid-plane (X/L = 0.5) at t = 1.5 sec for near-critical carbon dioxide (p_i = 7.38 MPa, T_i = 304.3 K, p' = 3.66×10^{-4}, T' = 5.65×10^{-4} and T_{pc}' = 3.88×10^{-5}) and Ra = 7.35×10^{8} with and without the effect of bulk viscosity.

Figure 5.11 shows the spatial variation of the bulk fluid temperature inside the enclosure at midplane (X/L = 0.5) and at t = 1.5 sec for the two cases. In both the cases, the uniform rise of the bulk due to *piston effect* can be observed from this figure. It is observed that, without the inclusion of the bulk viscosity, the temperature in the bulk of the fluid increases relatively faster. This is mainly due to two factors – first, inclusion of bulk viscosity in the thermoacoustic time scale attenuates the induced acoustic waves quickly which affects the thermoacoustic mode of transport and second, stability of the thermal boundary layer in the diffusion timescale affects the convective mode of transport.

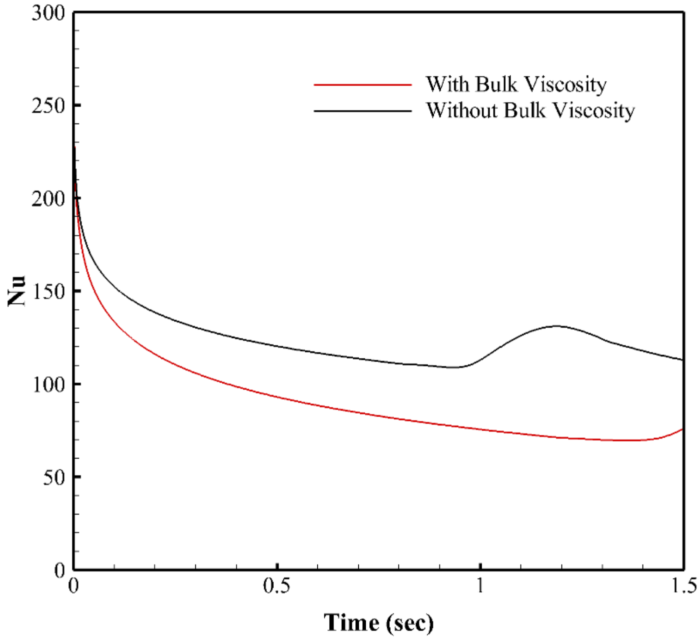

Figure 5.12: Temporal variation of spatially averaged Nusselt number (Nu) at the left wall ($X/L = 0.0$) of the enclosure at $t = 1.5$ sec for near-critical carbon dioxide ($p_i = 7.38$ MPa, $T_i = 304.3$ K, $p' = 3.66\text{x}10^{-4}$, $T' = 5.65\text{x}10^{-4}$ and $T_{pc}' = 3.88\text{x}10^{-5}$) and Ra = $7.35\text{x}10^{8}$ with and without the effect of bulk viscosity.

The temporal variation of spatially averaged Nusselt number at the left (heated) wall of the enclosure is shown in figure 5.12. At the beginning, the temporal heat transfer rate at the left wall is very high due to the heating. The value decreases as the system approaches thermal equilibrium. It is observed that the case including the bulk viscosity effects exhibits a relatively smaller Nusselt number compared to that without the effect of bulk viscosity. This is mainly due to the larger effective viscosity in the system. For the case without the inclusion of bulk viscosity, the rapid increase and decrease in temporal

Nusselt number around 1.0~1.3 sec indicates the collapse of the bottom boundary layer and release of thermal plumes from the heated surface. A similar pattern is also expected for the case including bulk viscosity, but at a later time. On a longer time period, the flow field is characterized by large-scale flow reversals by the occurrence of a large plume moving through the cavity and suppressing the preexisting primary convection cell [113, 115], and the system never reaches a steady-state. However, it is observed that, the temporal Nusselt number for the case including bulk viscosity is comparable to that given by equation 5.10 for near-critical carbon dioxide.

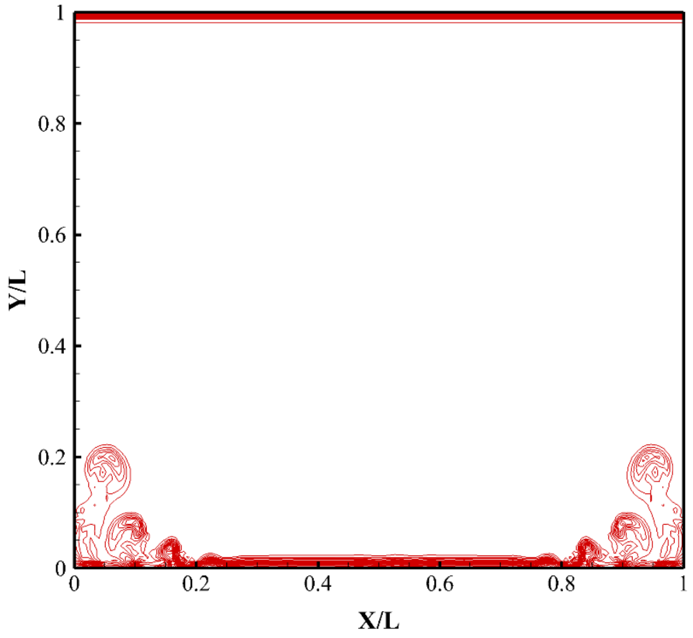

Figure 5.13: Contours of viscosity ratio (μ_b/μ) inside a bottom heated enclosure at t = 1.5 sec for near-critical carbon dioxide (p_i = 7.38 MPa, T_i = 304.3 K, p' = 3.66x10^{-4}, T' = 5.65x10^{-4} and T_{pc}' = 3.88x10^{-5}) and Ra = 7.35x10^{8}
[$(\mu_b/\mu)_{\max}$ = 1200 (top wall), $(\mu_b/\mu)_{\min}$ = 50 (bottom wall), $\delta(\mu_b/\mu)$ = 50]

Figure 5.13 shows the contours of viscosity ratio (μ_b/μ) inside the enclosure. At the initial stage, the viscosity ratio is around 1200 which indicates a relatively higher effective viscosity in the bulk of the fluid. As the bottom boundary is heated, the bulk viscosity effects become negligible ($\mu_b/\mu \sim 0$) along the hot boundary layer while the bulk of the fluid remains highly viscous ($\mu_b/\mu \sim 250$). Hence the process becomes analogous to one with diffusion of the less viscous fluid to a more viscous fluid. This whole phenomena is absent in the case where bulk viscosity is not considered, mainly due to negligible difference in viscosities between the boundary layer and the bulk of the fluid.

5.5 Summary and conclusion

Buoyancy driven flow induced thermal transport in supercritical carbon dioxide is investigated by numerically solving a fully compressible form of the Navier-Stokes equations. The NIST Standard Reference Database 23 [3] is used to generate two-dimensional look-up tables to represent the equation of state and other thermodynamic properties for supercritical carbon dioxide. With the aid of the developed model, thermal transport phenomena in supercritical carbon dioxide in the near-critical as well as far from the critical point are investigated.

The novel contribution of the present study is to demonstrate the effect of the pseudo-critical states (*i.e.* where $\rho = \rho_c$) on thermal transport as well as the development of a correlation to predict the thermal transport behavior of supercritical carbon dioxide both near and far from the critical point. The effect of critically diverging bulk viscosity on the buoyancy driven flow is also investigated. The results exhibit that in the absence of critical divergence far from the critical point $\left(p > 10\text{MPa}, T > 320\text{K} \right)$ thermal transport behavior of supercritical fluids is reasonably comparable to that for a high density and high

Prandtl number ($\mathrm{Pr} >> 1$) gas and depends on the Rayleigh number (Ra) of the flow only, while in the near critical region $\left(p_c < p < 10\text{MPa}, T_c < T < 320\text{K}\right)$, transport of thermal energy varies not only as a function of Rayleigh number (Ra) but also as a function of the pressure and temperature. It was also observed that, similar to the thermo-physical property variations near the critical point, the Nusselt number (Nu) maximizes along the pseudo-critical states. Correlations for Nusselt number was proposed for both of these regions as a function of the Rayleigh number of the flow and the dimensionless pressure $p' = \left(\frac{p_i - p_c}{p_c}\right)$ and temperatures $T' = \left(\frac{T_m - T_c}{T_c}\right)$, $T'_{pc} = \left(\frac{T_{pc} - T_c}{T_c}\right)$. It was found that, in the near-critical region, critically diverging bulk viscosity plays a major role on the development of boundary layer and thermal equilibration in the flow domain. These effects are only significant when the bulk viscosity has values higher than the shear viscosity and the bulk viscosity shows strong variation in the flow domain.

CHAPTER 6: FUNDAMENTAL STUDIES OF ACOUSTICALLY DRIVEN TRANSPORT IN NEAR-CRITICAL SUPERCRITICAL FLUID

6.1 Introduction

Interaction of acoustic waves in compressible fluids (*e.g.* supercritical fluids) and solid boundaries produces a non-linear phenomenon known as *acoustic streaming*. Acoustic streaming can enhance certain kinds of rate processes and has applications in localized micro-mixing and convective transport in reduced gravity environment. Application of mechanically driven acoustic waves coupled with acoustic streaming represents a potential efficient way of enhancing transport processes in the near critical region. This enhancement is mainly due to the augmented convective effects produced by compressions and decompressions of the acoustic waves as well as the formation of the secondary flow-field (acoustic streaming).

In this chapter, the generation and propagation of mechanically driven acoustic waves in sub- and supercritical carbon dioxide are experimentally studied and numerically simulated. A cylindrical shaped resonator filled with carbon dioxide (sub- and supercritical states) is considered for this problem. The oscillatory flow field in the enclosure is created by the vibration of one of the end walls of the resonator. The driving frequencies of the vibrating wall are chosen such that the lowest acoustic mode propagates along the resonator and a standing wave field is produced. The amplitude of the generated acoustic waves are measured at the pressure anti-node (end wall) by a piezo-resistive pressure transducer. The variations in acoustic and flow fields are also studied as a function of space and time.

Formation of the standing wave and acoustic streaming are numerically simulated by directly solving the full compressible form of the Navier-Stokes equations. The NIST Standard Reference Database 23 [3] is used to obtain the ρ-p-T relations for supercritical carbon dioxide as well as the different thermo-physical and transport properties of the fluid. With the developed model, physical processes including the interaction of the wave field with viscous effects and formation of streaming structures are simulated. The effects of near-critical property variations and fluid pressure on the formation process of the streaming structures are also investigated in detail.

6.2 Problem description

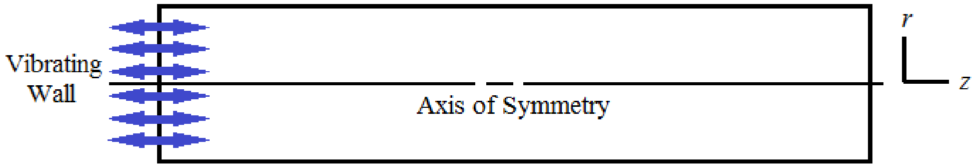

Figure 6.1: Schematic diagram of the problem geometry.

A cylindrical resonator with a length (L) of 25.0 cm is considered. The aspect ratio (L/D) of the resonator is around 12.5. The schematic of the geometry considered is shown in figure 6.1. One of the end walls (see figure 6.1) of the resonator is vibrated at a specific frequency. The frequency of vibration is chosen such that the lowest acoustic mode propagates through the fluid medium (*i.e.* $f = c_{si} / 2L$; where c_{si} is the acoustic speed at the initial state of the fluid). The axial symmetry of the problem geometry is utilized and only the top half of the domain is considered for the numerical calculations to simplify the computational efforts. Details regarding the experimental setup used for the measurement of the acoustic waves in sub- and supercritical carbon dioxide are discussed in the following section.

6.3 Experimental setup

For the investigation of mechanically driven acoustic waves in sub- and supercritical carbon dioxide, an experimental setup is designed and built following setup discussed in chapter 4. Figure 6.2 shows a schematic illustration of the experimental setup.

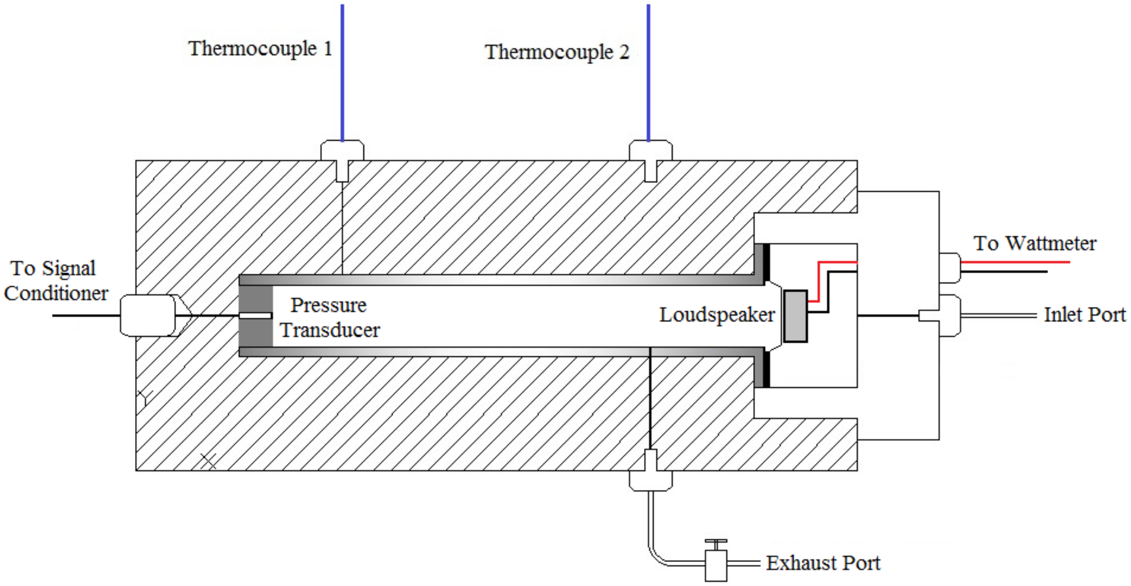

Figure 6.2: Schematic diagram of the experimental setup.

The supercritical chamber consists of gas inlet and outlet ports fitted with high pressure (103.4 MPa) ball valves and the chamber is connected to a carbon dioxide tank (p ~ 6.0 MPa). A hand pump (HiP, 34.5 MPa, 60 mL/stroke) is used to raise the pressure of the carbon dioxide in the supercritical chamber from the tank pressure to a pressure above the critical point of carbon dioxide. Heating tape (Thermolyne, 0.5” x 4’) wrapped around the supercritical chamber is used to raise the temperature of the carbon dioxide in the supercritical chamber from the room temperature (usually ~ 295 K) to the operating temperature. The mechanically driven acoustic waves in supercritical carbon dioxide are studied in a PTFE (Polytetrafluoroethylene) tube (inside diameter 2.0 cm, length 25.0 cm) snugly fitted inside the supercritical chamber. A small hole in the PTFE tubing aligned with the gas inlet port provides flow path for the gas to and from the supercritical chamber. The resonator is mounted horizontally with the acoustic driver on the right end (see figure 6.2) and a plug made of polyoxymethylene (Delrin) is used to close the opposite end. Delrin is a hard, high stiffness thermoplastic that prevents any absorption / attenuation of the acoustic waves during reflection from the end wall.

The acoustic driver in this system is an electro-mechanical driver type loudspeaker (CUI CMS0401KL-3X). The sinusoidal driving signal of the acoustic driver is generated by a function generator (BK Precision 4011A) and amplified by a Crown CE1000 type power amplifier. The signal generator is capable of providing ± 5.0 V sine waves up to a frequency of 5.0 MHz. A wattmeter (Powertek, ISW 8000) was connected between the amplifier and the loudspeaker to measure the RMS values of the delivered input power, the applied voltage, the applied current and the phase angle between the voltage and the current. An Endevco 8507C-1 series piezoresistive pressure transducer is used to detect and quantify the acoustic field. The transducer is installed in the delrin plug located at one end of the resonator. The cross-sectional area of the microphone is approximately one percent of the resonator area, therefore the error introduced by the presence of the probe in the sound field is assumed negligible. Lead wires from the loudspeaker and the pressure transducer are introduced inside the supercritical chamber through compression fittings. An Endevco 4428A pressure signal conditioner is used to process the signal from the transducer and provide excited voltage.

Table 6.1: Specifications of the experimental system for acoustically driven transport studies

No.	**Part**	**Make and Model**	**Specification**
1	Hand Pump	HiP 87-6-5	34.5 MPa 60 mL/stroke
2	Glands	Conax TG-24T(E)-A2-T	Pressure Rating: 22 MPa
3	Thermocouples	Omega EMTSS-125 (Probe Type)	Type E – 3.175 mm dia.
4	Pressure Transducers	Endevco 8507C-1	Sensitivity: 200 mV/psi Pressure Rating: 1 psi
		Omega PX309-2KG5V	Pressure Rating: 13.8 MPa
5	Acoustic Driver	CUI CMS0401KL-3X	Rated Power: 10 W Impedance: 8 Ω
6	Data Acquisition Board	NI 6052E	Sampling Rate: 333 kHz

Two type E thermocouples (Thermocouple 1 and 2, figure 6.2) are used to measure the steady state initial temperature of the supercritical fluid. A high pressure transducer (Omega PX309) is used to measure and monitor the steady state pressure inside the supercritical chamber. The analog temperature and pressure measurements are recorded, digitized and saved through a National Instrument SCB-68 terminal block and a 6052E data acquisition (DAQ) board. High sample rate (333 kHz) of the 6052E DAQ board guarantees that the signals are recorded with high fidelity. Details of the experimental setup are summarized in table 6.1.

6.4 Mathematical modeling

The numerical model of the acoustic resonator is described here. Specific details about the governing equations solved, the initial and boundary conditions and the numerical scheme used are also provided.

6.4.1 Governing equations

The transport processes in supercritical and near-critical fluids can be modeled by the hydrodynamic description for an isotropic, Newtonian, compressible, and dissipative (viscous and heat-conducting) fluid [76, 110, 167, 168]. The governing equations corresponding to mass, momentum and energy balances are as follows –

$$\frac{\partial \rho}{\partial t} + \nabla \cdot (\rho \vec{u}) = 0 \tag{6.1}$$

$$\frac{\partial (\rho \vec{u})}{\partial t} + \nabla \cdot (\rho \vec{u}\vec{u}) = -\nabla p + \nabla \cdot \tau_{ij} \tag{6.2}$$

$$\frac{\partial \left(\rho h_0\right)}{\partial t} + \nabla \cdot (\rho \vec{u} h_0) = \nabla \cdot (k \nabla T) + \nabla (\vec{u} \tau_{ij}) + \frac{\partial p}{\partial t} \tag{6.3}$$

Here, ρ is the density, $\boldsymbol{u}$ is the $(r - x)$ velocity vector, p is the pressure, T is the fluid temperature, k is the thermal conductivity of the fluid and the total enthalpy is h_0 given by

$$h_0 = i + \frac{p}{\rho} + \frac{1}{2}\left(\vec{u}\right)^2 \tag{6.4}$$

Here, i is the internal energy of the fluid. The equation of state describing the ρ-p-T relation of supercritical fluids (including the near-critical states) is not well-represented by the van der Waals equation of state [39]. In this study, we used the NIST Standard Reference Database 23 [181] for the $\rho = f(p, T)$ relations and for evaluation of other thermodynamic properties of supercritical and near-critical carbon dioxide. The NIST23 [181] equation of state describing the ρ-p-T relation of carbon dioxide is based on the equation of state proposed by Span and Wagner [65], which is mainly empirical in nature and includes special non-analytic terms to predict the correct behavior of the fluid to the immediate vicinity of the critical point. Two dimensional look-up tables are developed in the present study to represent the $\rho = f(p, T)$, $k_f = f(p, T)$, $\mu = f(p, T)$, $h_0 = f(p, T)$ and $c_p = f(p, T)$ data provided by the NIST Standard Reference Database 23.

6.4.2 Initial and boundary conditions

Initially thermally quiescent and motion-free sub-/supercritical carbon dioxide inside the domain is considered for the calculations. The initial state of the fluid is described as, T_i and p_i. The wall boundaries at the rigid end are maintained constant at the initial temperature of the fluid (isothermal). The isothermal boundary condition is the closest approximation to an experiment and has been shown in past studies to have the best agreement with experimental results [182, 183]. The vibrating wall and the wall along the length of the resonator are maintained adiabatic. For generating the acoustic waves, the vibrating wall is harmonically oscillated to model the motion of the speaker. The moving wall is vibrated according to the following equation:

$$x_{wall}(t) = x_{max} \sin(2\pi f t) \tag{6.5}$$

Here, x_{max} is the amplitude of vibration and f is the frequency of oscillation. The frequency of oscillation of the vibrating wall is chosen such that the lowest acoustic mode propagates through the fluid medium (*i.e.* $f = c_i / 2L$, where c_i is the acoustic speed at the initial state). For the numerical simulations, the amplitude of vibration of the moving wall is calculated from the power consumption of the electro-mechanical speaker using the model developed by Beranek [184].

6.4.3 Numerical scheme

The numerical scheme for solving the governing equations is based on the finite volume approach. The continuity, momentum and energy equations are solved for the fluid using the central difference scheme. The motion of the vibrating wall is captured by a moving grid scheme near the piston wall. The re-meshing scheme used in the simulations is the Transfinite Interpolation scheme [185]. A 2nd order Crank-Nicholson scheme (with a blending factor of 0.7) is used for the time derivatives in the continuity, momentum and energy equations. The time-step (Δt) for the simulations is dependent on the driving frequency. Around 850 time-steps per cycle is sufficient to accurately predict the motion of the piston and the pressure waves generated. For the range of frequencies considered in the present study, the time-step obeys the CFL condition with a Courant number ($C = c_s \times \Delta t / \Delta x$, where c_s is the acoustic speed for the given conditions) between 0.3 and 0.4. An overall convergence criterion is set for all the variables at 10^{-4} in the iterative implicit numerical solver. Due to the symmetry of the problem geometry, only one-half of the resonators' geometry (see figure 6.1) is considered for the simulations. The problem geometry is studied with non-uniform structured grid and fine grid is used in vicinity of the wall boundaries to provide adequate spatial resolution and capture the oscillating boundary layer (δ_v).

6.5 Results and discussions

Numerical simulations and experimental measurements of mechanically driven acoustic waves in sub- and supercritical carbon dioxide in a cylindrical resonator is performed for wide range of operating pressure and temperature of the supercritical fluid. The generated acoustic field and its interaction with the viscous effects leading to the formation of acoustic streaming structures in the fluid is studied as a function of space and time. The numerical model is validated first with results from past studies. The validation of the numerical model as well as the numerical and experimental results obtained from the present study is discussed in the following sub-sections.

6.5.1 Model validation

The numerical prediction of mechanically driven acoustic waves with the present model is compared with a previous numerical study by Aktas and Farouk [11]. Aktas and Farouk numerically investigated mechanically driven acoustic waves in atmospheric pressure nitrogen at 300 K in a two dimensional rectangular enclosure of length, $L = 8.825$ mm and varying width. The frequency and amplitude of the vibrating wall is always kept at 20 kHz and 10 μm respectively. The length of the enclosure is chosen such that $L = \lambda/2$ (λ is the wavelength calculated from $c_s = f\lambda$) and the lowest acoustic mode propagates through the fluid medium. For the case considered for validation of our present model, the width of the rectangular enclosure is $20\delta_v$. Here, δ_v is the viscous penetration depth given by:

$$\delta_v = \sqrt{\frac{2\mu}{\rho\omega}},\ \omega = 2\pi f \tag{6.6}$$

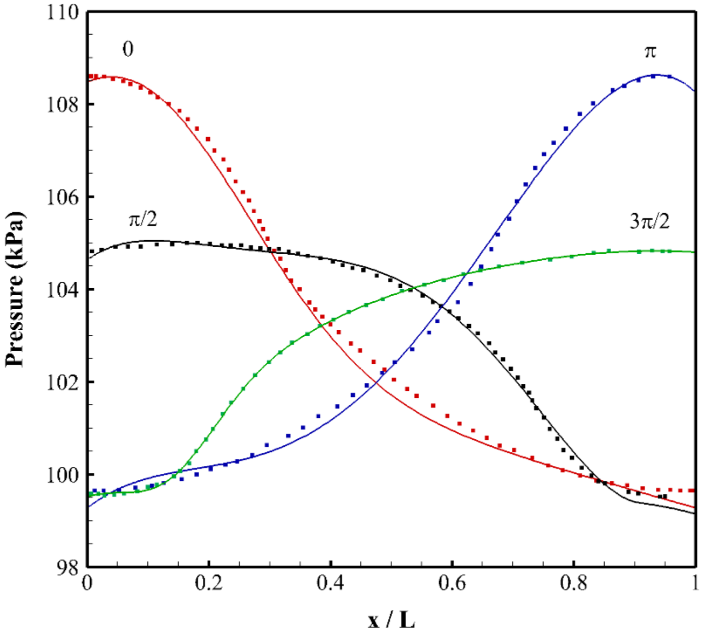

Figure 6.3: Spatial variation of pressure along the symmetry axis at four different instants ($\omega t = 0, \pi/2, 3\pi/2$ and π) during the 100th acoustic cycle as calculated using the present model (solid lines) and obtained by Aktas and Farouk [11] (solid squares).

Figure 6.3 shows the comparison of the predictions of the spatial variations of the pressure (absolute) along the symmetry axis at four different times ($\omega t = 0, \pi/2, 3\pi/2$ and π) in the 100th cycle as calculated using the present model with those obtained by Aktas and Farouk [11]. Here, x = 0 represents the vibrating wall. Pressure distribution for $\omega t = 2\pi$ (not shown here) is identical to the curve given for $\omega t = 0$. The perfectly sinusoidal profile of the emitted wave by the oscillating wall is weakly distorted due to viscous and nonlinear effects. At $\omega t = 0$ and $\omega t = \pi$, the amplitude of the pressure waves reach a maximum value in the enclosure. At the beginning of the cycle ($\omega t = 0$), the pressure is maximum on the vibrating wall of the enclosure and decreases with distance from the wall and reaches a minimum at the opposite wall ($x = L$). In the middle of the cycle ($\omega t = \pi$) the pressure profile is fairly symmetric with respect to the vertical midplane ($x = L/2$) to the profile given for ωt = 0, and reaches a maximum at the right wall. The pressure profiles given for different time levels intersect at approximately $x = L/2$ and creates a pressure node. For all the time instances considered in figure 6.3, the calculated pressure with the present model matches fairly well with that given by Aktas and Farouk. Due to attenuation caused by viscous and nonlinear effects, both pressure and velocity profiles slightly differ from a perfect sinusoidal wave field.

The streaming velocities in the enclosure are calculated using the following formula:

$$u_{st} = \frac{\langle \rho u \rangle}{\langle \rho \rangle}; v_{st} = \frac{\langle \rho v \rangle}{\langle \rho \rangle} \tag{6.7}$$

Here, u_{st} and v_{st} describes the x and y components of the streaming velocities, respectively. The ‹ › sign indicates the time-averaged quantities. The time averaging is performed during the 100th vibration cycle (between cycle #99 and #100). The streaming velocities calculated based on the time averaging during 80th and 100th cycles do not differ significantly. Hence, the average mass transport velocities are assumed to be cycle independent by this time (cycle # 100).

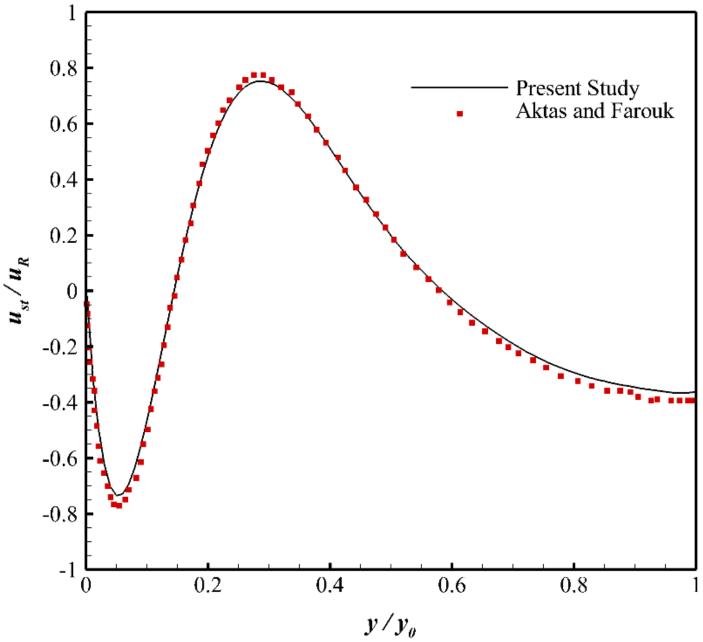

(a)

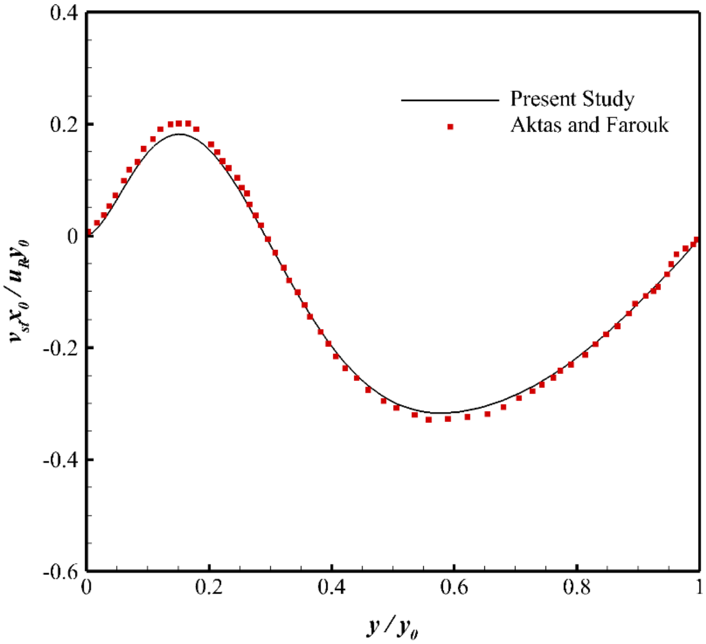

(b)

Figure 6.4: Variation of the (a) x component of the streaming velocity at $x = 3L/4$ and (b) y component of the streaming velocity at $x = L/2$ compared with Aktas and Farouk [11].

Spatial variation of the x component of streaming velocity at x = 3L/4 for the validation case is shown in figure 6.4a. In this figure, the vertical axis is the x component of the dimensionless streaming velocity (u_{st} / u_R) and u_R is given by $u_R = 3u_0^2/16c_s$. Here, u_0 is the maximum oscillatory velocity. This reference velocity value represents the maximum streaming velocity in case of a perfect sinusoidal wave form obtained by Rayleigh. Figure 6.4b shows the variation of the y component of streaming velocity along the enclosure semi-height at $x = L/2$. The vertical axis represents the y component of the non-dimensional streaming velocity ($v_{st}x_0 / u_R y_0$). Here x_0 is the length of the enclosure and y_0 is the semi-height of the enclosure. It is observed that, the dimensionless streaming velocities calculated from the present model are in good agreement with that predicted by Aktas and Farouk [11]. Figure 6.4a indicates the existence of two different vortical structures at $x = 3L/4$; one formed at the vicinity of the side wall (*inner streaming*) while the other is formed in the bulk fluid (*outer streaming*). The height of the circulatory flow structures (inner streaming) observed in the vicinity of the horizontal walls is characterized by the thickness of the acoustic boundary layer. The streaming structures seen in the middle section of the enclosure (outer streaming) have larger sizes. These predicted streaming structures are also in good agreement with the results reported by earlier studies [11, 186]. On an absolute scale, Aktas and Farouk [11] reported a maximum streaming velocity of approximately 0.06 m/s with a maximum instantaneous velocity of 12 m/s in the primary oscillatory flow field in the enclosure, while the present model slightly under predicts these velocities. The maximum streaming velocity and the instantaneous velocity calculated from the present model are 0.057 m/s and 11.2 m/s respectively. This deviation is mainly due to the implicit nature of the present numerical model (the model used by Aktas and Farouk [11] is explicit in nature and have less numerical diffusion).

6.5.2 Acoustic streaming in sub- and supercritical fluids

To investigate the formation of streaming structures in sub- and supercritical carbon dioxide in a cylindrical resonator, four cases are studied (cases 1 – 4). These four cases correspond to carbon dioxide at two different thermodynamic states (sub- and supercritical) excited at their resonant frequencies and at various amplitudes of vibration. At this stage the initial temperature of the fluid is kept constant (T_i = 308 K) and the pressure is varied. Table 6.2 below lists the cases studied.

Table 6.2: List of cases simulated for investigation of acoustic streaming formation in sub- and supercritical fluids

Case #	T_i (K)	p_i (MPa)	ρ / ρ_c	f (Hz)	x_{max} (μm)	δ_v (μm)
1	308	0.1	0.0037	545.3	346.7	72.2
2	308	2.0	0.0812	517.6	17.5	15.9
3	308	4.0	0.1854	484.2	8.8	11.1
4	308	7.6	0.6224	391.0	4.0	8.0

Here, the fluid in case 4 is in the supercritical state and this case is considered as the base case. In our experiments, acoustic waves are generated inside the cylindrical shaped resonator filled with supercritical carbon dioxide at this state (7.6 MPa and 308 K) with a speaker power of 10.0 W. The vibrational amplitude (x_{max}) of the moving wall corresponding to the acoustic impedance (ρc_s) of the fluid and the input power at case 4 is 4.0 μm (calculated using the model developed by Beranek [184]). For the acoustic wave measurements in cases 1-3, the input power is kept constant (10.0 W) and the vibrational amplitude is calculated using the same model [184]. For the same electro-mechanical variables of the speaker and input power, these amplitudes can also be approximated using the amplitude for case 4 and the following equation:

$$x_{\mathrm{max,n}} = x_{\mathrm{max,i}} \left(\frac{\rho_i}{\rho_n}\right)\left(\frac{f_i}{f_n}\right)^2 \tag{6.8}$$

Equation 8 is based on a simple force balance on the vibrating wall where the subscript 'i' refers to the values corresponding to the base case and the subscript '*n*' refers to the values corresponding to the n^{th} case.

Transient variation of the pressure (gage) at the mid-point of the end wall (pressure anti-node) of the cylindrical resonator at a pseudo-steady state for cases 1-4 are shown in figure 6.5. Both the computed and measured pressure transients are shown in this figure. A monotonic increase of the maximum pressure amplitude is observed with the increase in operating pressure. The maximum pressure amplitude reaches approximately 5.0 kPa at supercritical state (case 4), while it is around 0.6 kPa at atmospheric pressure (case 1). This monotonic increase is mainly due to the increase in density of the fluid with pressure. Also at atmospheric pressure (case 1), the pressure wave form is much sharper and shock wave-type profile is observed (figure 6.5a), while at higher sub-critical pressures (cases 2-3), the pressure profile is near-sinusoidal (figures 6.5b and 6.5c). At the supercritical state (case 4), the pressure profile again becomes sharper and shock-wave type (figure 6.5d). This behavior can be explained by the isothermal compressibility, $\beta = \frac{1}{\rho}\left(\frac{\partial \rho}{\partial p}\right)_T$ of the fluid. At atmospheric pressure the isothermal compressibility is high. However the compressibility quickly decreases with the increase of operating pressure until the supercritical state is reached, where the compressibility starts to increase again.

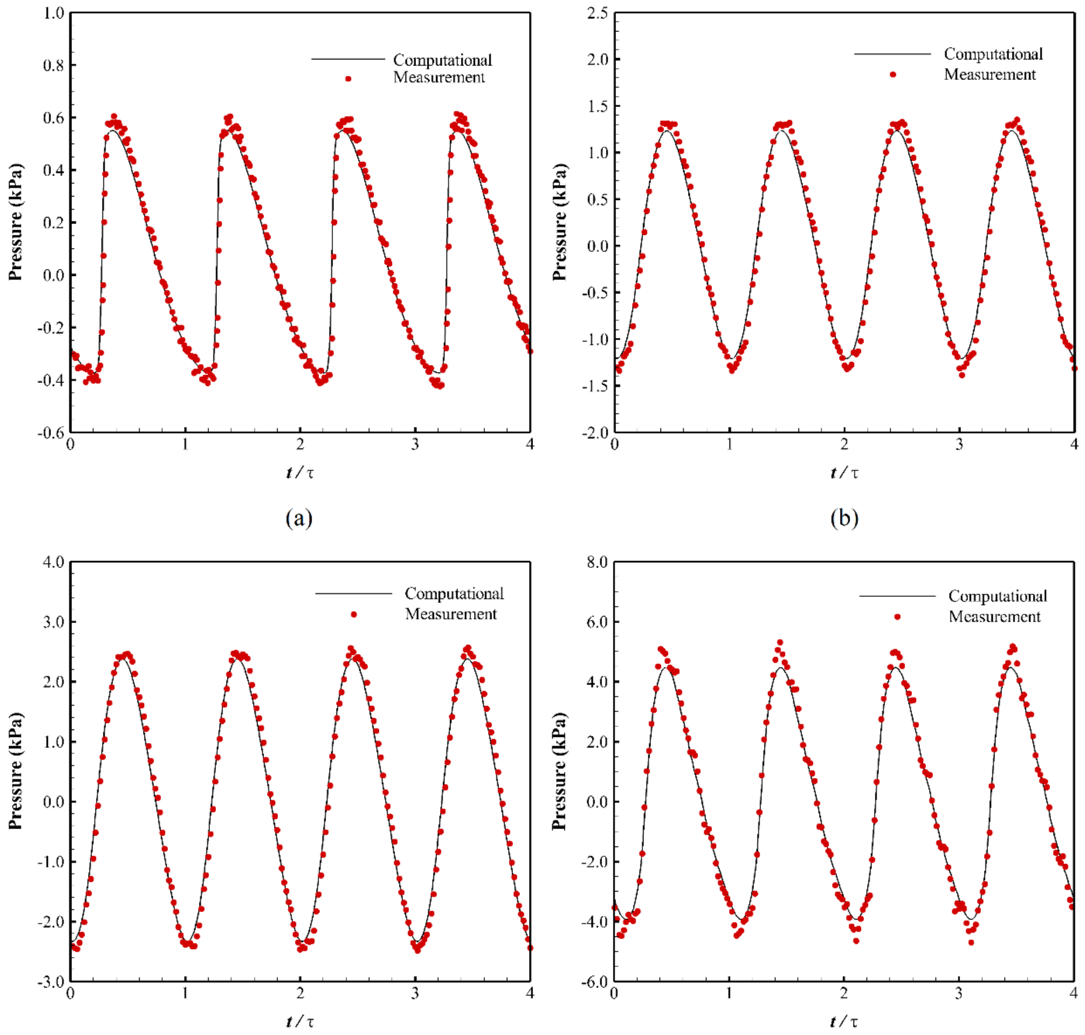

(a) (b)

(c) (d)

Figure 6.5: Transient variation of computed and measured pressure (gage) at the end wall of the cylindrical resonator at a pseudo-steady state for (a) p = 0.1 MPa, (b) p = 2.0 MPa, (c) p = 4.0 MPa and (d) p = 7.6 MPa and for four acoustic cycles.

For all the cases discussed (cases 1-4), the computed and the measured transient pressure distribution compares well. For the cases showing shock wave-type profiles (cases 1 and 4), existence of a slight variation between the measured and computed pressure amplitude is observed at the peaks and troughs of the wave-form. This is mainly due to the high experimental noise in the system when the temporal pressure gradient is high (*i.e.* at peak and troughs of the wave-form).

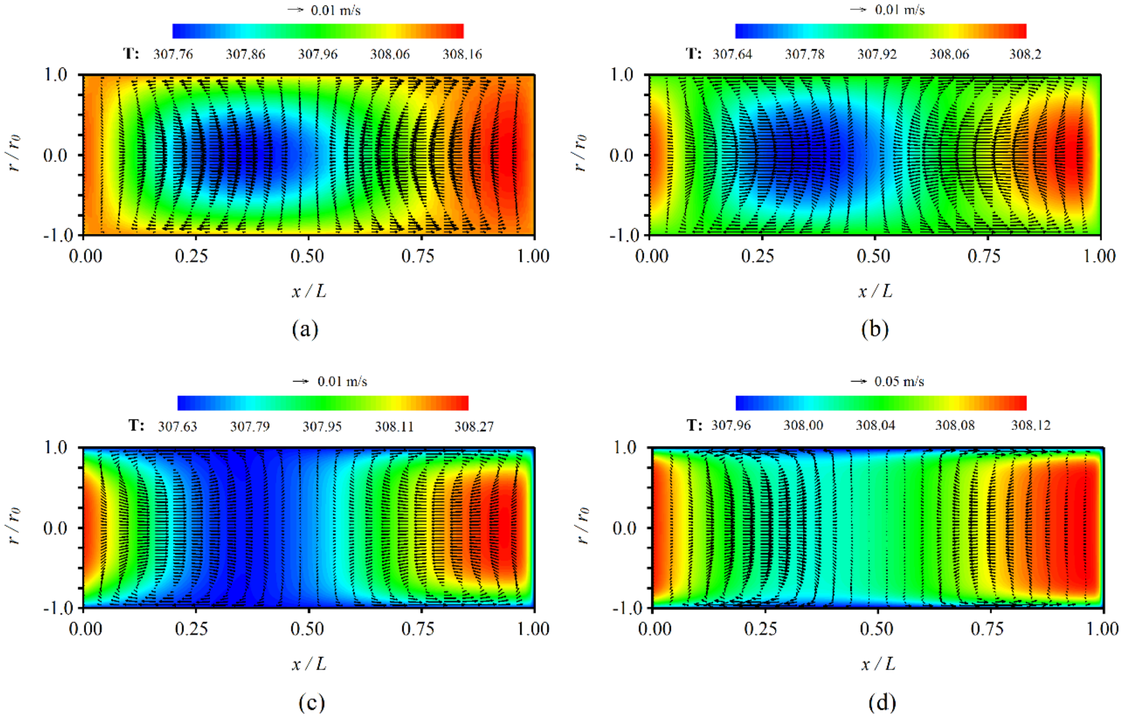

Figure 6.6: Cycle averaged temperature contours and flow-field (acoustic streaming) in the cylindrical resonator at a pseudo-steady state for (a) p = 0.1 MPa, (b) p = 2.0 MPa, (c) p = 4.0 MPa and (d) p = 7.6 MPa.

The quasi-steady (time-averaged) temperature contours and flow-fields in the resonator corresponding to cases 1-4 are shown in figure 6.6. For all these cases (cases 1-4), the flow patterns are observed in the shape of regular structures. Two outer steaming structures are observed in all these cases. At supercritical state (case 4), the maximum primary oscillatory flow velocity is computed as 8 m/s while the maximum flow speed is 0.041 m/s in the secondary steady streaming flow field (figure 6.6d). At atmospheric pressure (case 1), these velocities are 3 m/s and 0.009 m/s respectively (figure 6.6a).

Although the observed streaming structures are very similar for all these cases, the quasi-steady temperature contours are different. At sub-critical pressures (case 1-3), a cold zone is observed in the temperature contours roughly at the location of the pressure node (x/L = 0.5), while two hot zones are observed at the pressure anti-nodes (x/L = 0, 1). The cold zone expands in size as the pressure is increased (figures 6.6a-c). However, as soon as the supercritical state is reached, the cold zone almost disappears (figure 6.6d). The phenomena observed in the sub-critical regime has been reported in earlier studies [187] and is utilized in the development of thermoacoustic refrigerators [188]. The disappearance of the cold zone in the supercritical state is due to the high thermal conductivity (k) and Prandtl number (Pr) coupled with the high isothermal compressibility of the fluid at this state.

Variation of axial component of the non-dimensional streaming velocity at $x = 3L/4$ for cases 1-4 is shown in figure 6.7a. Similar to the maximum pressure amplitude, a monotonic increase in the streaming velocities with increasing pressure is observed in this figure. The difference in the streaming structures are also noticed from this figure. At atmospheric pressure (case 2), existence of the anti-clockwise rotating inner streaming structure gives rise to the negative velocity near the wall (x/L = 1). However, with the increase of operating pressure, the inner streaming structures are dissolved while the outer streaming structures expand and cover the entire domain. At supercritical state (case 4), streaming structures are characterized by relatively high streaming velocity (axial) near the wall and a flat plug-flow like profile in the rest of the domain as compared to a parabolic velocity profile at the atmospheric pressure (case 1).

Variation of the radial component of the non-dimensional streaming velocity at $x = L/2$ for cases 1-4 is shown in figure 6.7b. A strong radial velocity from the bulk fluid to the wall in the supercritical state (case 4) is observed from this figure. This strong velocity corresponds to a jet like flow at $x = L/2$ which is also observed from figure 6.6d. This behavior is highly desired for mixing applications, where the '*jet*' can efficiently carry the bulk fluid to the wall boundary layer.

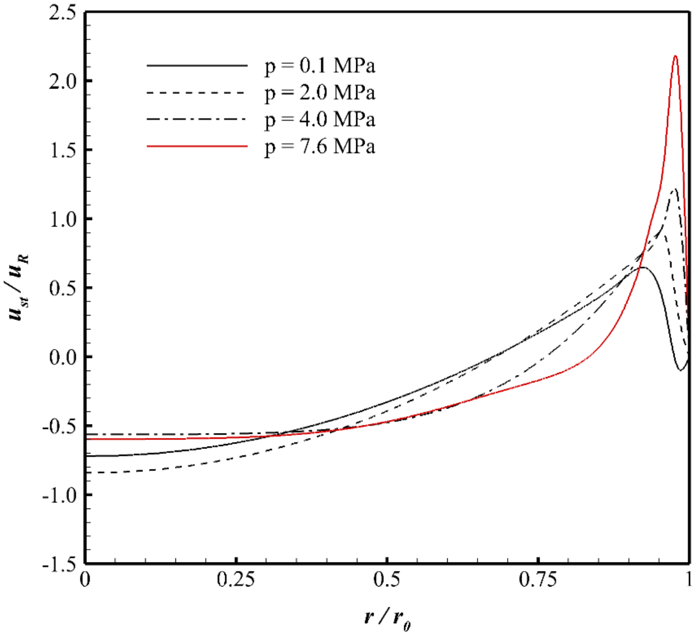

(a)

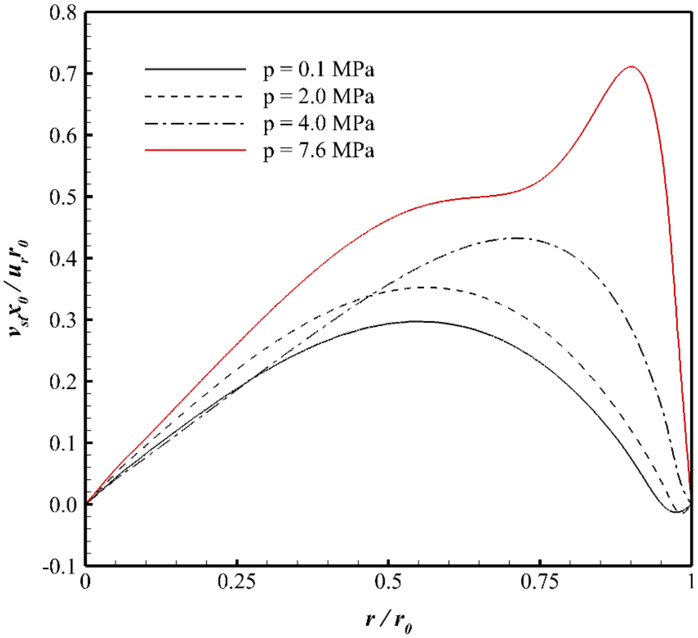

(b)

Figure 6.7: Spatial variation of the (a) axial component of the streaming velocity at *x* = 3*L*/4 and (b) radial component of the streaming velocity at *x* = *L*/2 for different operating pressures (cases 1-4).

6.5.3 Effect of pseudo-critical state

Effect of the pseudo-critical thermo-physical property variations on the mechanically driven acoustic waves and acoustic streaming formation is investigated in this section. Three additional cases (cases 5-7) along with case 4 is considered for this study. For these four cases, the operating pressure is supercritical and is kept constant at *p* = 7.6 MPa. The pseudo-critical state (*i.e.* where $\rho/\rho_c = 1$) corresponding to this pressure is at 305.43 K. Hence, the pseudo-critical state is approached by reducing the operating temperature. The four cases corresponds to fluids ranging from gas-like (*i.e.* $\rho/\rho_c < 1.0$) to liquid-like (*i.e.* $\rho/\rho_c > 1.0$) properties. Table 6.3 below lists the details of the cases studied. Here, the fluid corresponding to cases 4 and 5 are gas-like with relatively low density, thermal conductivity and acoustic speed, while that corresponding to case 7 is liquid-like with higher density, thermal conductivity and acoustic speed. The fluid corresponding to case 6 is very close to the pseudo-critical state.

Table 6.3: List of cases simulated for investigation of the effect of pseudo-critical states on acoustic streaming

Case #	T_i (K)	p_i (MPa)	ρ / ρ_c	f (Hz)	x_{max} (μm)	δ_v (μm)
4	308	7.6	0.6224	391.0	4.0	8.0
5	305.8	7.6	0.8	352.6	3.81	8.1
6	305.5	7.6	0.937	325.6	3.83	8.3
7	305.1	7.6	1.2	373.1	2.26	7.9

Temporal variation of the computed and measured pressures (gage) at the end wall (pressure anti-node) of the cylindrical resonator for cases 4-7 are shown in figure 6.8. Two specific phenomena are observed – first, the pseudo-critical state has a strong effect on the maximum pressure amplitude. It is observed that, as the pseudo-critical state (*i.e.* T = 305.43 K at p = 7.6 MPa) is approached, the maximum pressure amplitude increases. For the cases studied (cases 4-7), the maximum pressure amplitude is observed for the case (case 6, T = 305.5 K) closest to the pseudo-critical state. This is due to the high compressibility and density of the fluid as it approaches the pseudo-critical state. The maximum pressure amplitude decreases as the thermodynamic state of the fluid moves away from the pseudo-critical state (case 7, T = 305.1 K). At this state, density of the fluid is very high, but the compressibility is low. The second phenomena observed from the transient pressure is related to the pressure wave form. The pressure wave form corresponding to all these cases (cases 4-7) show shock wave-type profile with a sharp rise and long tail in general. However, the pressure wave form corresponding to the case closest to the pseudo-critical state (case 6, T = 305.5 K) exhibits a slightly different profile with a non-linear '*distortion*'. This '*distortion*' of the pressure transient is mainly due to the strong variation of acoustic speed of the near-pseudo-critical fluid at this case (case 6). At near-pseudo-critical states close to the critical point, the acoustic speed of the fluid exhibits relatively large variations with changing pressure and temperature. Hence, in an oscillating pressure (and hence temperature) field such as this, the acoustic speed of the fluid also oscillates to a great extent which in turn affects resonance and hence the standing wave field.

The measured pressure (see figure 6.8 - symbols) also shows similar '*distortion*' of the wave form discussed above. High frequency disturbances are observed from the measurements in the supercritical state (cases 4-7). Similar disturbances were also reported in earlier experimental studies in supercritical fluids [103, 173]. These are caused mainly due to the high compressibility of the medium and non-uniform heating of the supercritical chamber.

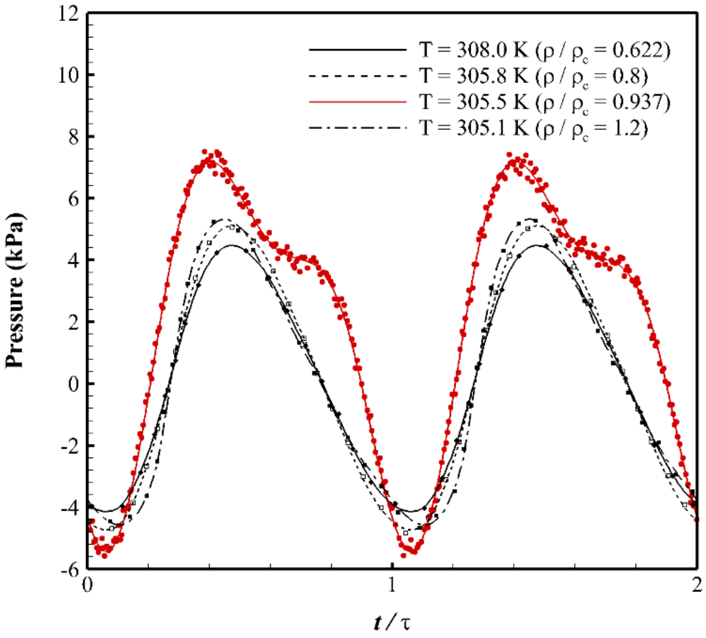

Figure 6.8: Transient variation of computed and measured pressure (gage) at the end wall of the cylindrical resonator at a pseudo-steady state for different operating temperatures at p = 7.6 MPa (cases 4-7). [Measured Pressures are shown with symbols: ◆ T = 308.0 K; ▫ T = 305.8 K; • T = 305.5 K and ▪ T = 305.1 K]

The quasi-steady (time-averaged) temperature contours and flow-fields in the resonator corresponding to cases 4-7 are shown in figure 6.9. Acoustic streaming structures are observed for all these cases (cases 4-7). For the cases relatively far from the pseudo-critical state (*i.e.* cases 4, 5 and 7), four outer steaming structures are observed. This behavior is in accordance with that observed in the previous section. However, at the near-pseudo-critical state (case 6), the streaming structures do not exhibit the regular pattern. It is observed that the existence of the '*distorted*' pressure field gives rise to eight outer streaming cells in the system instead of four (figure 6.9c). Out of these eight, four of the cells are large and prominent in shape. While, the other four are relatively small in size and are derived from the variation of the thermo-physical properties (e.g. acoustic speed of the medium) due to the wave field '*distortion*'. The strong thermo-physical property variation also affects the temperature field of the resonator. For the cases with gas-like properties (*i.e.* $\rho / \rho_c < 1.0$), a strong temperature gradient is observed in the resonator – with hot zones near the pressure anti-nodes and a cold zone near the pressure node. This temperature gradient is rather weak for the near-pseudo-critical state (case 6) due to very high specific heat of the fluid. The temperature gradient becomes practically non-existent in the case with liquid-like properties (*i.e.* $\rho / \rho_c > 1.0$). This is due to the relatively high thermal conductivity of the fluid at this state.

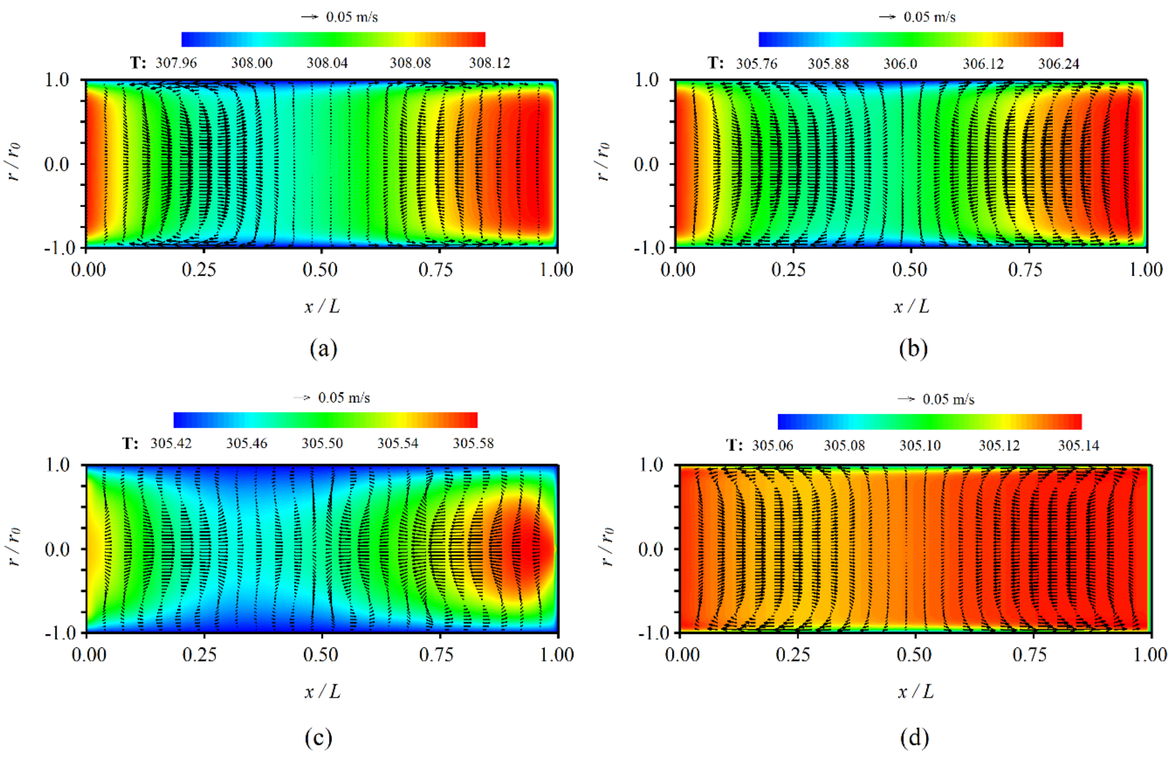

Figure 6.9: Cycle averaged temperature contours and flow-field (acoustic streaming) in the cylindrical resonator at a pseudo-steady state for (a) T = 308.0 K (case 4), (b) T = 305.8 K (case 5), (c) T = 305.5 K (case 6) and (d) T = 305.1 K (case 7) for an operating pressure of 7.6 MPa.

Variation of axial component of the non-dimensional streaming velocity at $x = 3L/4$ for cases 4-7 is shown in figure 6.10a. For the cases relatively far from the pseudo-critical state (*i.e.* cases 4, 5 and 7), similar to the maximum pressure amplitude the streaming velocities also increase monotonically as the corresponding pseudo-critical is approached. The streaming velocity distribution at these states show a flat plug-like profile in the bulk fluid with a sharp gradient near the wall. But for the near-pseudo-critical state (case 6, T = 305.5 K), the streaming velocity is not very high near the wall. The streaming velocity distribution in this state exhibits a parabolic profile (similar to the profile at atmospheric pressure, case 1). In this case, the streaming velocity is comparatively high in the bulk fluid (along the axis of the resonator) rather than the wall. Variation of the radial component of the non-dimensional streaming velocity at $x = L/2$ for cases 4-7 is shown in figure 6.10b. Similar to case 4 (section 6.5.2), a strong radial velocity from the bulk fluid to the wall in the supercritical states (cases 4-7) is observed.

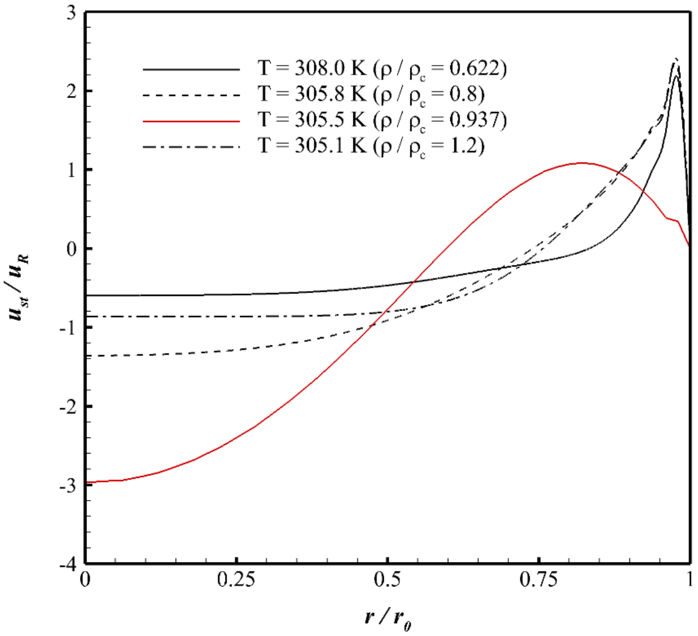

(a)

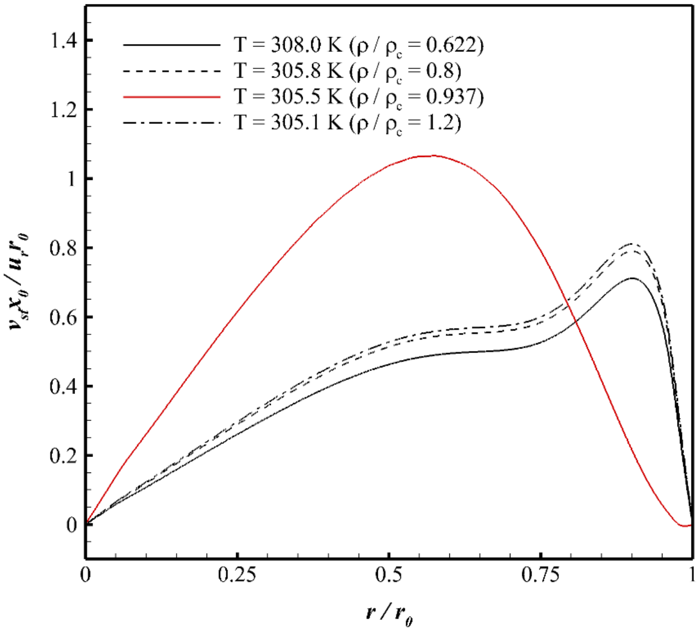

(b)

Figure 6.10: Spatial variation of the (a) axial component of the streaming velocity at $x = 3L/4$ and (b) radial component of the streaming velocity at $x = L/2$ for different operating temperatures at p = 7.6 MPa (cases 4-7).

6.5.4 Effect of operating pressure

The effect of operating pressure on the mechanically driven acoustic wave and acoustic streaming in the supercritical state is investigated and discussed here. Two different operating pressures (8.0 MPa and 8.5 MPa) are considered for this study. To understand the effect of operating pressure on the near-pseudo-critical acoustic streaming formation, three cases ($\rho / \rho_c < 1.0$, $\rho / \rho_c \sim 1.0$ and $\rho / \rho_c > 1.0$) are considered for each of these pressures. Table 6.4 below lists the details of the cases studied.

Table 6.4: List of cases simulated for investigation of the effect of operating pressure on acoustic streaming

Case #	T_i (K)	p_i (MPa)	ρ / ρ_c	f (Hz)	x_{max} (μm)	δ_v (μm)
8	307	8	1.2	401.1	1.97	7.6
9	308	8	0.933	360.9	3.13	7.9
10	308.75	8	0.8	373.0	3.42	7.8
11	309.3	8.5	1.2	422.8	1.78	7.4
12	311.1	8.5	0.936	384.1	2.76	7.7
13	312.5	8.5	0.8	392.5	3.10	7.7

Temporal variation of the computed and measured pressures (gage) at the end wall (pressure anti-node) of the cylindrical resonator for cases 8-10 (p = 8.0 MPa) are shown in figure 6.11. The same features of the pressure wave form (monotonic increase as pseudo-critical state is approached, sharp and shock wave-type profile etc.) are also observed in this pressure. However, for the near-pseudo-critical state (case 9, T = 308.0 K), the non-linear variation in the pressure wave form is not as prominent as observed for p = 7.6 MPa (case 6). The experimental measurements for this case also confirms this observation. Temporal variation of the computed and measured pressures (gage) at the end wall (pressure anti-node) of the cylindrical resonator for cases 11-13 (p = 8.5 MPa) are shown in figure 6.12. It is observed that, the near-pseudo-critical effect on the pressure wave form (*i.e.* the non-linear variation) is further relaxed at this pressure.

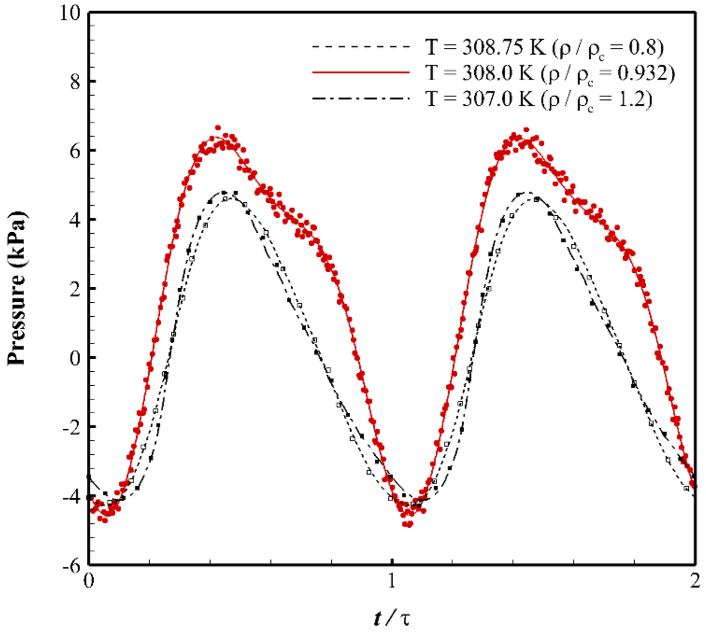

Figure 6.11: Transient variation of computed and measured pressure (gage) at the end wall of the cylindrical resonator at a pseudo-steady state for different operating temperatures at p = 8.0 MPa (cases 8-10). [Measured Pressures are shown with symbols: ▫ T = 308.75 K; • T = 308.0 K and ▪ T = 307.0 K]

This behavior of the pressure (acoustic) wave can be explained by the near-critical thermo-physical property variations. As the operating pressure is increased, the thermodynamic state of the fluid is moved far away from the critical point and the thermo-physical property variations (including the acoustic speed) at these higher pressures (*e.g.* p = 8.0 MPa and 8.5 MPa) are not very strong. Hence, the acoustic speed variation of the fluid (as discussed in section 6.5.3) in the resonator at the near-pseudo-critical state becomes very small / negligible and as a consequence of that the pressure wave form becomes similar to that observed at the cases far from the pseudo-critical states.

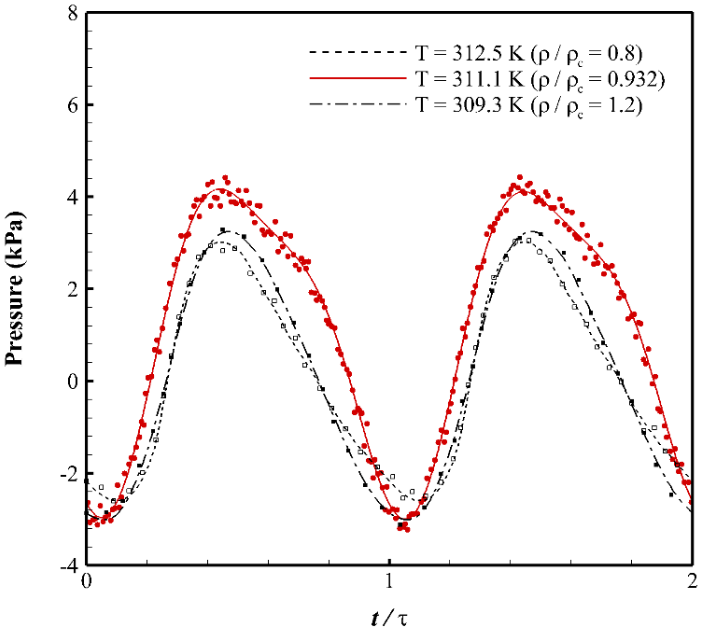

Figure 6.12: Transient variation of computed and measured pressure (gage) at the end wall of the cylindrical resonator at a pseudo-steady state for different operating temperatures at p = 8.5 MPa (cases 11-13). [Measured Pressures are shown with symbols: ▫ T = 312. 5 K; • T = 311.1 K and ▪ T = 309.3 K]

The quasi-steady (time-averaged) temperature contours and flow-fields in the resonator corresponding to the cases at two different operating pressures (cases 8-13) are shown in figure 6.13. It is observed that for the cases far from the corresponding pseudo-critical states (*i.e.* cases 8, 10, 11 and 13) the operating pressure has a negligible effect on the streaming structures. The regular outer streaming structures are observed for these cases (figures 6.13a, 6.13c, 6.13d and 6.13f respectively). However, for the near-pseudo-critical states (case 9 and 12), the additional streaming cells (corresponding to the '*distortion*' of the standing wave field) are not significant at this elevated pressures. At p = 8.0 MPa, the additional streaming cell can be noticed and is almost merged with the regular outer streaming structure (figure 6.13b). At p = 8.5 MPa, the additional structure is not noticed at all.

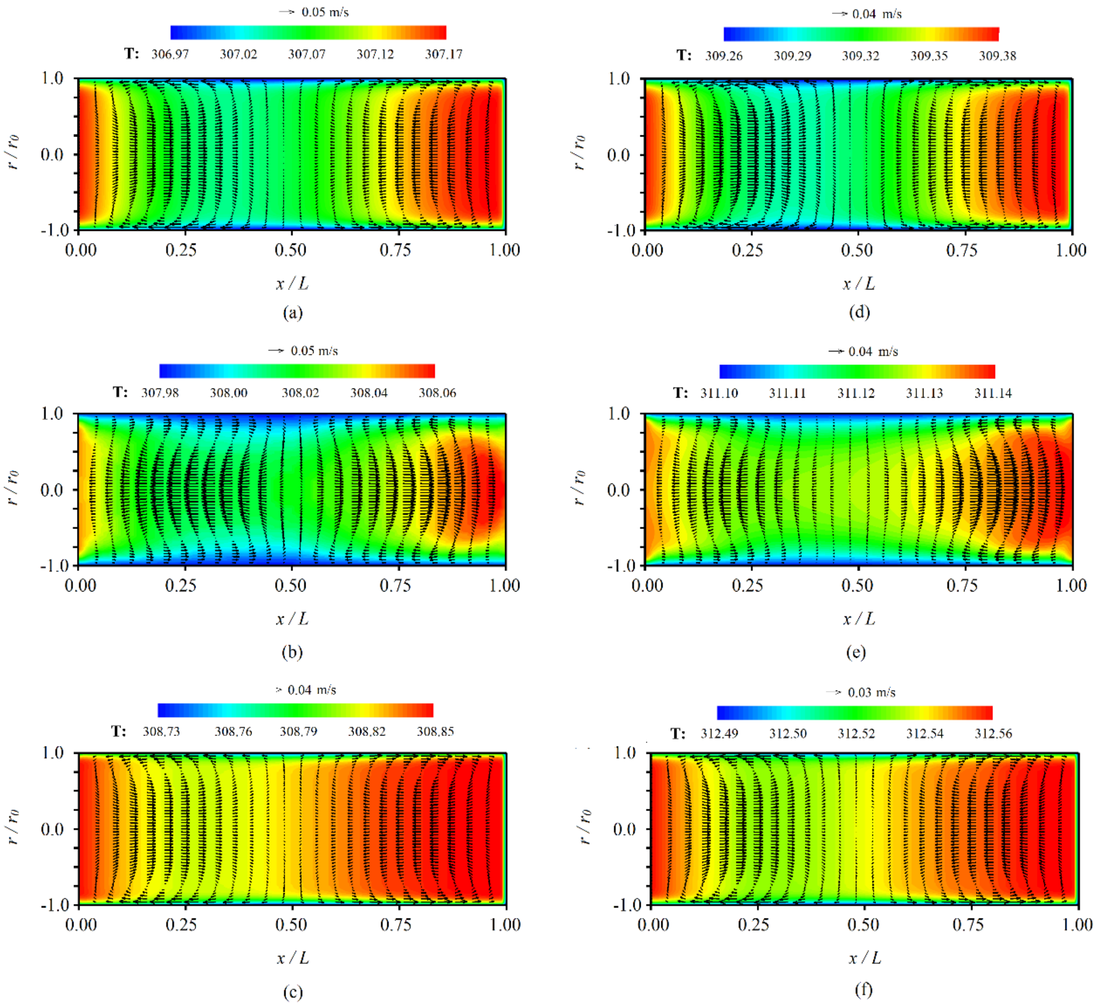

Figure 6.13: Cycle averaged temperature contours and flow-field (acoustic streaming) in the cylindrical resonator at a pseudo-steady state for (a) p = 8.0 MPa, T = 307.0 K (case 8), (b) p = 8.0 MPa, T = 308.0 K (case 9), (c) p = 8.0 MPa, T = 308.75 K (case 10), (d) p = 8.5 MPa, T = 309.3 K K (case 11), (e) p = 8.5 MPa, T = 311.1 K (case 12) and (f) p = 8.5 MPa, T = 312.5 K (case 13).

The temperature contours for these cases (case 8-13) also show similar trends as discussed in the previous section (section 6.5.3). This include a strong temperature gradient for the cases with gas-like properties (case 8 and 11, figures 6.13a and 6.13d respectively)

– with hot zones near the pressure anti-nodes and a cold zone near the pressure node, a rather weak for the near-pseudo-critical state (case 9 and 12, figures 6.13b and 6.13e respectively) and a very small gradient in the case with liquid-like properties (case 10 and 13, figures 6.13c and 6.13f respectively). But this trend is relaxed as the operating pressure is increased. At the highest operating pressure (p = 8.5 MPa), the temperature gradient is almost the same for the three cases studied.

Variation of axial component of the non-dimensional streaming velocity at $x = 3L/4$ corresponding to the cases at two different operating pressures (cases 8-13) are shown in figure 6.14. It is observed that, the operating pressure has a negative effect on the streaming velocity. The maximum amplitude of the non-dimensional streaming velocity decreases with increasing pressure.

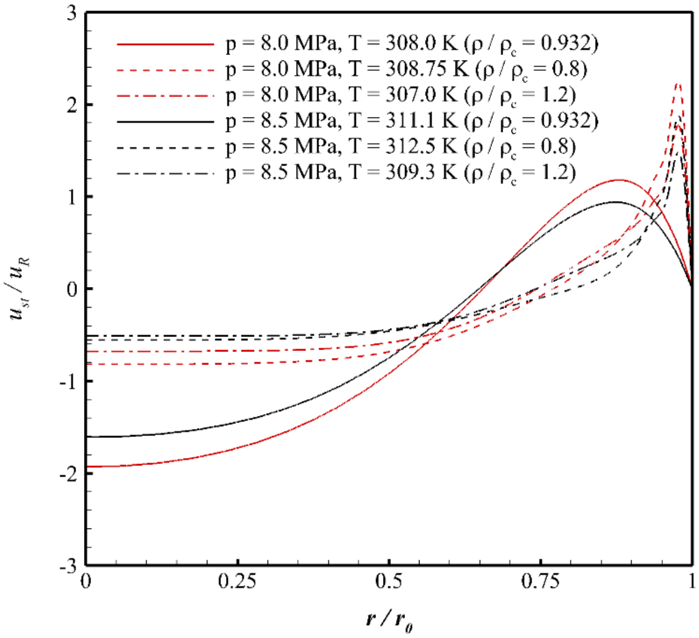

Figure 6.14: Spatial variation of the axial component of the streaming velocity at $x = 3L/4$ for different operating temperatures at p = 8.0 MPa (cases 8-10) and p = 8.5 MPa (cases 11-13).

Although the additional streaming structures are not observed in the near-pseudo-critical states (case 9 and 12), the distribution of the axial streaming velocity remains parabolic. A slight difference between the axial streaming velocities in the bulk fluid (along the axis of the resonator) for the cases in the gas-like ($\rho / \rho_c < 1.0$) and liquid-like ($\rho / \rho_c < 1.0$) property regimes are observed at relatively low pressures (figure 6.10a and 6.14a). With the increase in operating pressure, this difference is minimized.

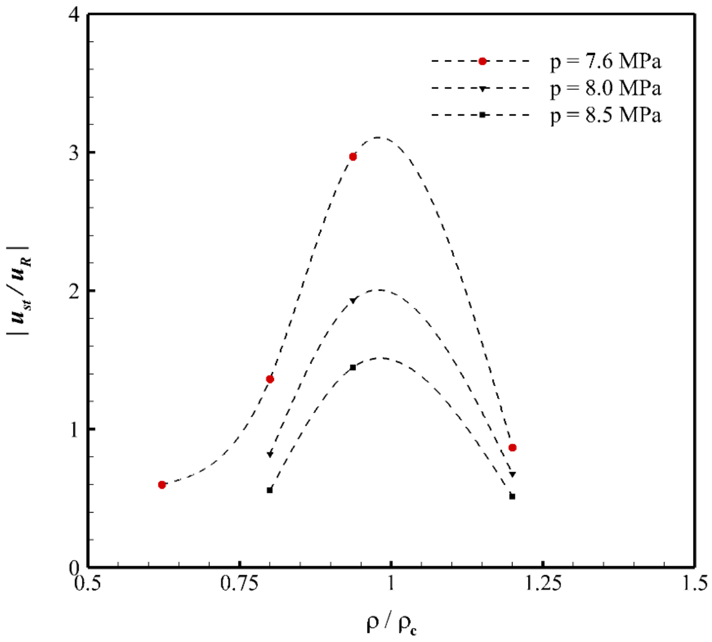

Figure 6.15: Variation of non-dimensional axial streaming velocity in the bulk fluid (along the resonator axis) with reduced density (ρ / ρ_c) at different isobars.

The observations from figures 6.10a and 6.14 are summarized and shown in figure 6.15. Figure 6.15 shows the variation of the axial streaming velocity (non-dimensional) along the axis of the resonator with reduced density for the three different operating pressures studied (p = 7.6 MPa, 8.0 MPa and 8.5 MPa). The reduced density axis represents the proximity of the thermodynamic state to the pseudo-critical state ($\rho / \rho_c = 1.0$). It is observed that, the streaming velocity in the bulk fluid (*i.e.* along the axis of the resonator) is maximized at the pseudo-critical point. At pressures close to the critical pressure (*e.g.* p = 7.6 MPa), the axial streaming velocity is slightly higher in the gas-like property regime ($\rho / \rho_c < 1.0$) than that in the liquid-like property regime ($\rho / \rho_c > 1.0$). This variation is mainly due to the reduced viscosity and higher compressibility of the gas-like fluid. With the increase in pressure, the thermo-physical property variations become weak and this trend is barely noticed.

6.6 Summary and conclusions

Mechanically driven resonant acoustic waves in near-critical supercritical carbon dioxide is investigated in this chapter. The formation of acoustic (pressure) waves, acoustic-viscous boundary layer interactions, and associated flows in a cylindrical resonator are numerically studied by solving the unsteady, compressible Navier–Stokes equations in an axisymmetric *x-r* coordinate system. The acoustic field in the enclosure is created due to the harmonic vibration of the end wall. The effects of pseudo-critical state ($\rho / \rho_c \sim 1.0$) and operating pressure on the acoustic field and the formed flow structures are determined by utilizing a highly accurate numerical scheme. The computations are accompanied by appropriate experimentations on acoustically driven transport. Acoustic waves generated by an electro-mechanical driver in a cylindrical resonator filled with supercritical carbon dioxide are measured using a fast-response pressure field microphone. The results from the numerical simulations are compared with the experimental measurements with accurately developed boundary conditions.

Several interesting and significant phenomena are observed from the numerical simulations and confirmed by the experimental measurements. The observed primary oscillatory and secondary steady flow fields in the supercritical fluid medium demonstrate significant effects of the thermodynamic state (sub-critical / supercritical / pseudo-critical) as well as the operating pressure. The strength of the acoustic wave field was found to be in direct relation with the thermodynamic state (near-pseudo-critical / far from the pseudo-critical state). It is observed that due to the strong thermo-physical property variations, amplitude of the maximum pressure increases as the thermodynamic state of the fluid approaches the corresponding pseudo-critical state. In the near-pseudo-critical state, the pressure wave form exhibits a non-linear and '*distorted*' profile due to the large variation of acoustic speed of the supercritical fluid in the resonator. This phenomena also affects the formation of acoustic streaming structures in the near-pseudo-critical state. Far from the pseudo-critical state, the streaming structure consists of four counter rotating cells with a '*jet*' like flow-field along the semi-length of the resonator (at the pressure node). While near the pseudo-critical state, irregular streaming structures consisting of eight outer streaming cells in the resonator are observed. The evolved flow structures are also dependent on the operating pressure. The irregular streaming patterns are observed mainly for near-pseudo-critical states at operating pressures close to the critical pressure (p_c = 7.377 MPa). However, these structures quickly re-orients to the regular streaming patterns (four outer streaming cells) with the increase operating pressure. The phenomena observed both numerically and experimentally in this study can be utilized for mixing applications in supercritical fluid medium, especially for enhancing the transport characteristics in supercritical fluid extraction processes.

CHAPTER 7: NUMERICAL INVESTIGATION OF MASS TRANSFER ENHANCEMENT IN SUPERCRITICAL FLUID EXTRACTION PROCESS USING ACOUSTIC WAVES[5]

7.1 Introduction

The supercritical fluid extraction (SFE) process has attracted increasing interest over the past few years [13, 14]. This is particularly motivated by concerns about environmental effects. Conventional separation techniques such as solvent extraction, partitioning (also known as *liquid–liquid extraction*; a method to separate compounds based on their relative solubility in two different immiscible liquids) and distillation usually have the drawback of leaving trace amounts of inorganic (potentially toxic) solvents or to cause thermal degradation [15]. Some supercritical fluids have the potential to replace these toxic industrial solvents. There are also possibilities of tuning the supercritical solvent characteristics for highly specific reactions or separations. Supercritical fluids are now being used in several applications (lab-scale or industrial) associated with the development of sustainable chemistry and engineering.

Although, supercritical fluid is widely used in process industries and in power generation, the transport dynamics is relatively slow near the critical point and therefore improvements in convective transport (both thermal and mass) are required [157]. The use of acoustic excitation represents a potential efficient way of enhancing transport processes in the near critical region [13, 46]. In the present chapter, computational fluid dynamics

---

[5] The results presented in this chapter can be found in, [189] N. Hasan and B. Farouk, "Mass transfer enhancement in supercritical fluid extraction by acoustic waves," *Journal of Supercritical Fluids*, vol. 80, pp. 60-70, 2013.

models of supercritical fluid extraction process is developed. The spatio-temporal simulation results are used to predict and explain the transport processes associated in supercritical fluid extraction. As discussed in chapter 2, supercritical fluid extraction (SFE) from solid phase is usually carried out in fixed bed extractors (*i.e.* packed extraction columns), while that from fluid phase is carried out using a membrane contactor. Both of these systems are numerically investigated with the developed computational fluid dynamics model. Supercritical fluid extraction of caffeine from a solid matrix of coffee beans in a fixed bed extractor is considered. Ethanol recovery from an aqueous feed using supercritical carbon dioxide in a membrane contactor is also simulated. The models are developed considering diffusion-controlled regime in the process. Convective-diffusive transport of the bulk fluid phase at dynamic conditions is considered along with accurate representation of the thermo-physical properties of supercritical carbon dioxide. The NIST Standard Reference Database 23 [3] is used to obtain the ρ–p–T relation as well as the thermo-physical properties of supercritical carbon dioxide. Correlations developed by Catchpole and King [67] are used to obtain the binary diffusion coefficient (D_{12}) of the solute (caffeine and ethanol in these cases) in supercritical carbon dioxide. The solubility of the solute in supercritical carbon dioxide is obtained using the correlation developed by Gurdial *et al.* [69]. Henry's law is used to describe the equilibrium state of solid and fluid phases. Different features regarding the flow field and species transport induced by mixed convection in the supercritical fluid extraction system are revealed by the simulations. Novel applications of the acoustically augmented supercritical fluid (CO_2) extraction in fixed bed extractor (caffeine extraction) and membrane contactor (ethanol recovery) are demonstrated numerically. Due to the selective and non-toxic extraction properties, supercritical fluids (supercritical CO_2 in this case) are a good candidate for recovering chemicals from aqueous feed using the membrane contactors. The low binary diffusivity and solubility of the solvent makes the dynamics of the process slow. Hence, acoustically excited waves can be used in these systems to enhance the transport dynamics.

7.2 Problem description

To numerically investigate the flow and transport in supercritical fluid extraction systems, two different problem geometries are studied. The first problem investigates the supercritical fluid extraction of caffeine in a fixed bed extractor, while the second problem investigates the recovery of ethanol using supercritical fluid in a membrane contactor. The problems are described in detail in the following sections.

7.2.1 Supercritical fluid extraction: Fixed bed extractor

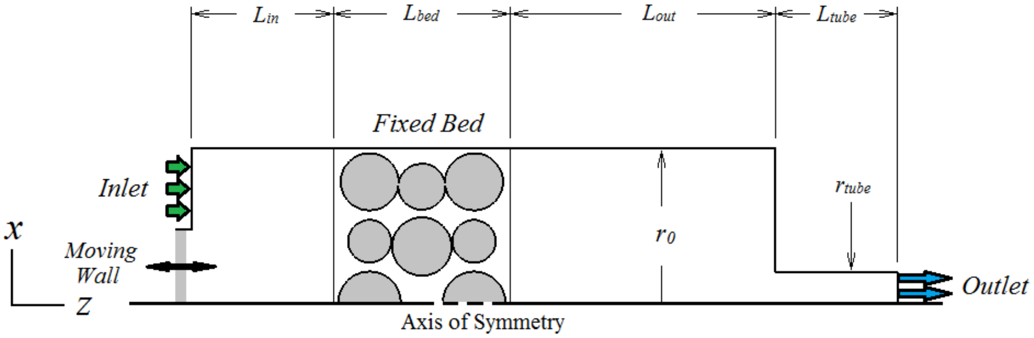

Figure 7.1: Schematic diagram of the fixed bed extraction column

A circular cylindrical shell (extraction column) with a fixed bed of solute particles (coffee beans) and an inlet for introducing supercritical carbon dioxide and outlet tubing for allowing the discharge flow of the extracts is considered (figure 7.1). The geometrical model for the present study is developed following the experimental investigations by Riera *et al.* [48, 49].

The inlet section of the model also consists of an annular opening and a flat circular vibrating plate. The vibrating plate is introduced at the inlet section to model a piezoelectric (acoustic) transducer used to generate the acoustic waves in the fluid. A piezoelectric power transducer in similar orientation inside the extraction column has also been used by Riera *et al.* [48, 49]. The fixed bed consisting of coffee beans are modeled as porous spherical particles. A mono-sized sphere stack [190] is selected for this study. A three-layer arrangement (total of 56 spheres) is chosen as the geometrical model for CFD simulations. A two-dimensional approach to circle packing theory [191] is used to build a unit stack and then it is extrapolated to build a three-dimensional geometry. The origin is placed at the inlet of the extraction column. The geometrical parameters of the model are listed in table 7.1.

Table 7.1: Geometrical parameters of the fixed bed extractor

Parameter	**Value**
Height of the inlet section, L_{in}	2.0 cm
Height of the Fixed Bed, L_{bed}	2.7 cm
Height of the outlet section, L_{out}	4.0 cm
Length of the discharge tubing, L_{tube}	2.0 cm
Radius of the Extractor, r_o	2.5 cm
Radius of the discharge tubing, r_{tube}	0.5 cm

7.2.2 Supercritical fluid extraction: Membrane contactor

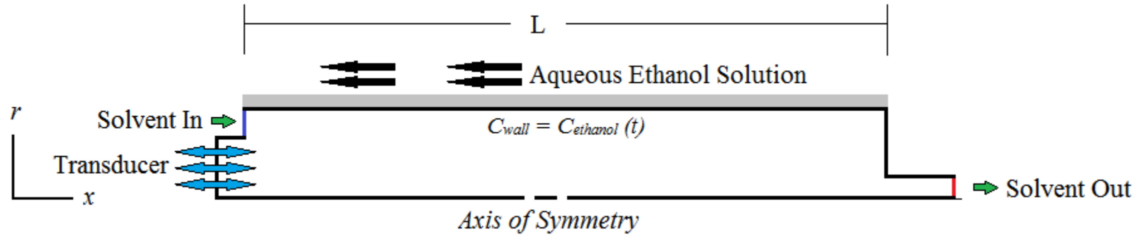

Figure 7.2: Schematic diagram of the membrane contactor.

A membrane contactor for the recovery (*i.e.* extraction) of ethanol from a 10% w/w aqueous solution using supercritical carbon dioxide is considered. The schematic diagram of the system considered is shown in figure 7.2. The system consists of a single hollow fiber membrane housed in stainless steel tubing. The liquid feed (aqueous solution of ethanol) flows around the fiber membrane and the solvent fluid (supercritical carbon dioxide) flows in countercurrent flow inside the fiber membrane. For simplifying the problem only the supercritical carbon dioxide flow in the hollow fiber membrane is simulated with an ethanol concentration boundary condition for the side walls. Details regarding the boundary conditions are discussed later in this chapter. The total length of the membrane contactor is 2.5 cm with an aspect ratio (*L/D*) of 12.5. For generating the acoustic waves inside the fiber membrane, a concentric vibrating wall (motion along the *x*-axis) is considered as a piston to model an electro-mechanical transducer whose front surface vibrates harmonically; generating longitudinal waves which propagate through the fluid. Similar to the cylindrical resonator problem in the previous chapter (chapter 6), the moving wall is vibrated at the resonant frequency of the supercritical solvent.

7.3 Mathematical modeling

Due to the different problem geometry and flow physics of the two problems studied in this chapter, mathematical modeling of the supercritical fluid extraction processes in the fixed bed extractor and in the membrane contactor is slightly different. The models are discussed in details in the following sub-sections.

7.3.1 Fixed bed extractor

When a fixed bed of solid (coffee beans) is contacted with a flowing solvent (carbon dioxide) at a selected supercritical condition, the mass transport mechanism involves diffusion and adsorption of supercritical fluid solvent followed by solute desorption, diffusion through pores, and the convective transport along with the flowing supercritical fluid solvent across the bed height. Based on the different transport mechanisms involved in the supercritical fluid extraction process, the following assumptions are considered –

a) The fixed bed consisting of dry coffee beans are modeled as porous spherical particles (diameter ~ 0.8 cm, porosity 0.515 and permeability 10~11 Darcy [136]) arranged in a staggered pattern in three layers.

b) A single pseudo-component (caffeine) is considered in the model.

c) Caffeine ($C_8H_{10}N_4O_2$) is assumed to be uniformly distributed in the untreated porous solid particles (dry coffee beans).

d) The volume fraction of porous particles in the fixed bed (see figure 7.1) is not influenced by the change in caffeine concentration during the extraction.

e) Transport properties (dynamic viscosity) of the supercritical solvent/caffeine mixture are equal to that of the supercritical solvent.

f) Thermal equilibrium is considered between the flowing solvent (supercritical carbon dioxide) and the porous fixed bed of solids (dry coffee beans).

The geometrical shape of coffee beans from different cultivars varies from non-uniform ellipsoids to spheres. For the sake of simplicity, the coffee beans are approximated as uniform spheres with an equivalent surface area (obtained from Peker *et al.* [136]). Since the inlet flow rate considered in the study is very low and the corresponding Reynolds number is very small (10~15), the transport of caffeine is mainly dependent on the surface area of the spherical particles (coffee beans). The irregularities of the particle geometry would have negligible effect on the overall caffeine yield. Hence, a porous spherical particle to model coffee beans should be a good approximation. The transport processes in supercritical fluid extraction in a fixed bed extractor can be modeled by the complete hydrodynamic description for an isotropic, Newtonian, compressible, and dissipative (viscous and heat-conducting) fluid [167, 168]. Since the extraction process considered is essentially isothermal, the energy equation is not considered in the problem formulation. The governing equations corresponding to mass, momentum and species balances are listed below:

For the supercritical fluid/caffeine mixture (in bulk fluid):

$$\frac{\partial \rho}{\partial t} + \nabla \cdot \left(\rho \bar{u} \right) = 0 \tag{7.1}$$

$$\frac{\partial (\rho \bar{u})}{\partial t} + \nabla \cdot \left(\rho \bar{u}\bar{u} \right) = -\nabla p + \nabla \cdot \bar{\bar{\tau}} + \rho \bar{g} \tag{7.2}$$

$$\frac{\partial C_f}{\partial t} + \nabla \cdot \left(\bar{u} C_f \right) = D_{AB} \nabla^2 C_f \tag{7.3}$$

For the supercritical fluid/caffeine mixture in porous-solid medium (packed bed):

$$\frac{\partial\left(\varepsilon\rho\right)}{\partial t}+\nabla\cdot\left(\varepsilon\rho\bar{u}\right)=0 \tag{7.4}$$

$$\frac{\partial(\varepsilon\rho\bar{u})}{\partial t}+\nabla\cdot\left(\varepsilon\rho\bar{u}\bar{u}\right)=-\nabla p+\nabla\cdot\left(\varepsilon\bar{\bar{\tau}}\right)-\frac{\varepsilon^2\mu}{\kappa}\bar{u}+\rho\bar{g} \tag{7.5}$$

$$\frac{\partial\left(\varepsilon C_S\right)}{\partial t}+\nabla\cdot\left(\varepsilon\bar{u}C_S\right)=D_{eff}\nabla^2 C_S \tag{7.6}$$

Here, t is time, ρ is density of the mixture, $\bar{u}$ is the mixture velocity vector given by $\bar{u}=u\hat{i}+v\hat{j}+wk$, where, u, v and w are the velocities in x, y and z directions respectively, and p is pressure. The concentrations of the solute (caffeine) in the gaseous and porous-solid phases are given by C_f and C_S respectively. The porosity and permeability of the porous-solid phase are given by ε and κ respectively.

7.3.2 Membrane contactor

Similar to the fixed bed extractor problem, the transport processes in a membrane contactor is modeled by solving the mass, momentum, energy and species balance equation. The governing equations for the problem is listed below –

$$\frac{\partial\rho}{\partial t}+\nabla\cdot\left(\rho\bar{u}\right)=0 \tag{7.7}$$

$$\frac{\partial(\rho\bar{u})}{\partial t}+\nabla\cdot\left(\rho\bar{u}\bar{u}\right)=-\nabla p+\nabla\cdot\bar{\bar{\tau}} \tag{7.8}$$

$$\frac{D(\rho h_0)}{Dt}=\frac{\partial p}{\partial t}+\nabla\cdot\left(k_f\nabla T\right)+\nabla\left(\bar{u}\bar{\bar{\tau}}\right) \tag{7.9}$$

$$\frac{\partial C_f}{\partial t}+\nabla\cdot\left(\bar{u}C_f\right)=D_{AB}\nabla^2 C_f \tag{7.10}$$

Here, t is time, ρ is density, $\bar{u}$ is the velocity vector given by $\bar{u} = u_x \hat{i}_x + u_r \hat{i}_r$, where, u_x and u_r are the velocities in the axial and radial directions respectively, h_0 is the total enthalpy, T is the temperature, p is pressure and C_f is the concentration of the solute (ethanol).

7.3.3 Equation of state and thermo-physical properties

The equation of state describing the ρ-p-T relation of supercritical carbon dioxide (including the near-critical states) is not well-represented by the van der Waals equation of state [39]. In this study, we used the NIST Standard Reference Database 23 [3] for the $\rho_{CO2} = f(p, T)$ relations and for evaluation of other thermo-physical properties of supercritical and near-critical carbon dioxide. As discussed in previous chapters, the NIST23 equation of state describing the ρ-p-T relation of supercritical carbon dioxide is based on the equation of state proposed by Span and Wagner [65], which is mainly empirical in nature and includes special non-analytic terms to predict the correct behavior of the fluid to the immediate vicinity of the critical point. The density of the supercritical solvent/solute mixture is given by $\rho = \left({x_{CO_2}}/{\rho_{CO_2}} + {x_{solute}}/{\rho_{solute}} \right)^{-1}$ where x is the species mass fraction and the subscripts 'CO_2' and 'solute' refers to the supercritical solvent (carbon dioxide) and the solute (caffeine / ethanol) respectively. Transport properties of the supercritical carbon dioxide/solute mixture are practically independent of the solute (*i.e.* caffeine or ethanol) mass fraction due to very small saturation concentration of solute in supercritical carbon dioxide. Hence, the mixture transport properties (*e.g.* dynamic viscosity) are considered to be equal to that of the solvent. Two dimensional look-up tables are developed in the present study to represent the $\rho_{CO2} = f(p, T)$, $\mu = f(p, T)$ etc. data provided by the NIST Standard Reference Database 23. The binary diffusion coefficient of the solutes (D_{12}) in supercritical carbon dioxide is calculated using the correlations proposed by Catchpole and King [67] and is given as a function of pressure and temperature. For the fixed bed extractor problem, the effective diffusivity of caffeine in the porous solids is calculated using $D_{eff} = \varepsilon^2 D_{12}$. The temperature range considered for the look-up tables is 304K - 325K and the pressure range is 7.4 MPa – 12 MPa. With the developed computational fluid dynamics model, the transport characteristics of supercritical fluid extraction process and the output (%) of the extraction process is investigated. The extraction output is presented in terms of yield of the supercritical fluid extraction process. The percentage yield of the process is defined as –

$$\%\ \text{yield} = \frac{\text{mass of solute extracted}}{\text{initial mass of solute in the system}} \times 100\% \tag{7.11}$$

7.3.4 Initial and boundary conditions

Initially thermally quiescent and motion-free supercritical carbon dioxide inside the computational domain is considered in the problems (described in section 7.2.1 and 7.2.2). The initial state of the fluid is described as, T_i and p_i. For generating the acoustic waves, the moving wall is harmonically oscillated to model an electro-mechanical transducer. The moving wall is vibrated according to the following equation –

$$x_{wall}(t) = x_{max} \sin(2\pi f t) \tag{7.12}$$

Here, x_{max} is the maximum wall displacement and f is the frequency of oscillation. The frequency of oscillation of the moving wall is chosen such that the lowest acoustic mode propagates through the fluid medium (*i.e.* $f = c_i / 2L$, where c_i is the acoustic speed at the initial state). The different initial and boundary condition parameters used to simulate the supercritical fluid extraction (SFE) process in the fixed bed extractor and the membrane contactor are given in sections 7.4 and 7.5 respectively.

For the solution of solid-fluid (*i.e.* from wall to bulk fluid) interfacial mass transport equations (Eqn. 7.3 and 7.6) in the fixed bed extractor (described in section 7.2.1), two interfacial boundary conditions have to be fulfilled. First, the interfacial concentration jump is defined by the thermodynamic equilibrium assumption $C_f \big|_{solvent} = H\, C_f \big|_{wall}$, and second, the interfacial fluxes obey the continuity condition $D_{eff} \nabla C_f \big|_{wall} = D_{AB} \nabla C_f \big|_{solvent}$. Here, H is the Henry coefficient and $H = \frac{C_{sat.}}{C_0}$ [192-194]. $C_{sat.}$ is the saturation concentration of the solute (*i.e.* caffeine) in supercritical carbon dioxide. A zero gradient boundary condition for solute concentration (C_f) is applied at the outlets.

The solution of solid-fluid interfacial mass transport equations (Eqn. 7.10) in the membrane contactor (described in section 7.2.2) is much more simplified as the porous solid wall of the membrane contactor is not modeled here. Instead, a time dependent boundary condition at the side wall (see figure 7.2) is considered. The time dependent aqueous feed concentration (C_{feed}) is calculated according to the following equation –

$$C_{feed}(t) = C_o - \frac{1}{V} \int_0^t \dot{v} \overline{C_f}\, dt \qquad (7.13)$$

Here, C_o is the initial ethanol concentration, V is the volume of the recirculation tank (considered as 1.0 m^3), $\dot{v}$ is the volumetric flow rate and $\overline{C_f}$ is the average ethanol concentration at the outlet of the membrane contactor. The ethanol concentration at the side wall (C_{wall}) is set as per the following conditions –

$$C_{wall} = \begin{cases} C_{sat}\text{, when } C_{feed} > C_{sat} \\ C_{feed}\text{, Otherwise} \end{cases} \tag{7.14}$$

7.3.5 Numerical scheme

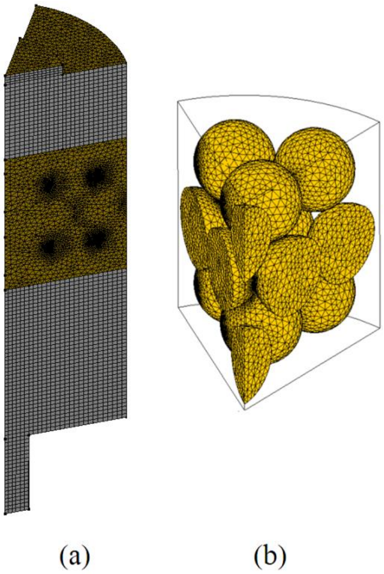

Figure 7.3: Generated geometric model of (a) supercritical fluid extraction column and (b) fixed bed consisting of porous spherical particles.

For the fixed bed extractor problem (section 7.2.1), only one-sixth (a 60^o pie-section about the z-axis) of the problem domain is modeled for the simulations considering the symmetry of the geometric model. This significantly reduces the total time of the numerical calculations. Figure 7.3 shows the generated geometry and mesh of the supercritical fluid extractor and the fixed bed. The construction of particle-to-particle contact points is an important issue in model generation. To include real contact points, the spheres are modeled overlapping by 2.5% of their diameters with the adjacent surfaces in the geometric model.

The membrane contactor problem is solved considering axial symmetry of the geometry. For both the problems, the governing equations are solved by a finite volume method using a central difference scheme for the spatial discretization and a Crank-Nicolson scheme for time discretization. Non-uniform grid spacing with relatively finer mesh near the walls and particle-to particle contact points is considered. The fixed bed extractor model consists of tetrahedral elements in the particle and fixed bed region and hexahedral elements in all other regions. A total of 309972 elements are used for the calculations (fixed bed extractor). Trans-Finite Interpolation (TFI) scheme is used to re-mesh problem domain for cases with acoustic waves. All computations were carried out on a Dell Precision T7500n workstation.

7.4 Results and discussions: Fixed bed extractor

The transport processes in caffeine extraction from dry coffee beans is simulated with a computational fluid dynamics model. The prediction of the extraction yield of the supercritical fluid extraction process with the described numerical method is first compared with a previous experimental study [136]. The discussions on the model validation is described in the following sub-section.

7.4.1 Model Validation

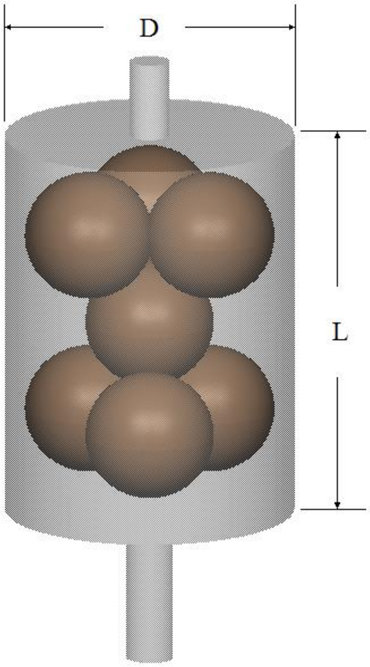

Figure 7.4: Schematic diagram of the extraction column used by Peker *et al.* [136]

Peker *et al.* [136] presented an experimental study of the extraction of caffeine from whole coffee beans with supercritical carbon dioxide in a continuous-flow extraction apparatus. In their experimental investigation, 7 coffee beans (diameter ~ 0.8 cm) in an extraction column of length L = 1.27 cm and diameter, D = 1.73 cm was used. A schematic diagram of the extraction column used by Peker *et al.* [136] is shown in figure 7.4. The extraction yields are determined as functions of the solvent (supercritical carbon dioxide) flow rate and initial states (pressure and temperature). The simulation with the present numerical model for the comparison is carried out at an intermediate solvent flow rate (2.46 ml/min) and initial state (13.8 MPa and 323 K) based on the conditions as specified in Ref. [136]. The spherical particles are arranged in a staggered pattern in three layers. The Henry coefficient for the initial state considered, is provided (H = 0.0036) in the investigation by

Peker *et al.* [136] and this same value is used in the simulations. The simulations are carried out for 200 min and the calculated extraction yield is compared to that obtained experimentally.

The contours of caffeine concentration in the bulk fluid (C_f) and in the porous solid phase (C_s) at three different times of the process are shown in figure 7.5. The extraction process is mainly diffusion controlled at the very early time (figure 7.5a) and convection controlled at the longer time scale (figures 7.5b and 7.5c). It is also observed that the dynamics of the process is very slow. After 200 minutes of extraction, a considerable amount of caffeine is still trapped inside the porous solid phase (figure 7.5c).

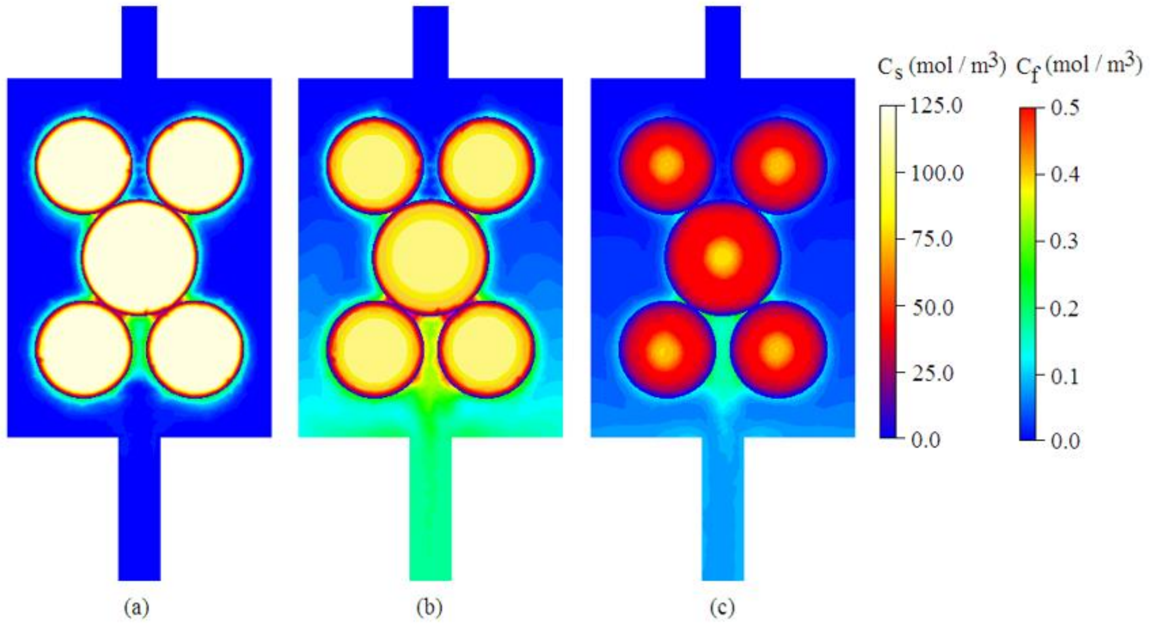

Figure 7.5: Contours of caffeine concentration in the fluid phase (C_f) and in the porous-solid phase (C_s) inside the extraction column at (a) t = 5 min, (b) t = 100 min and (c) t = 200 min.

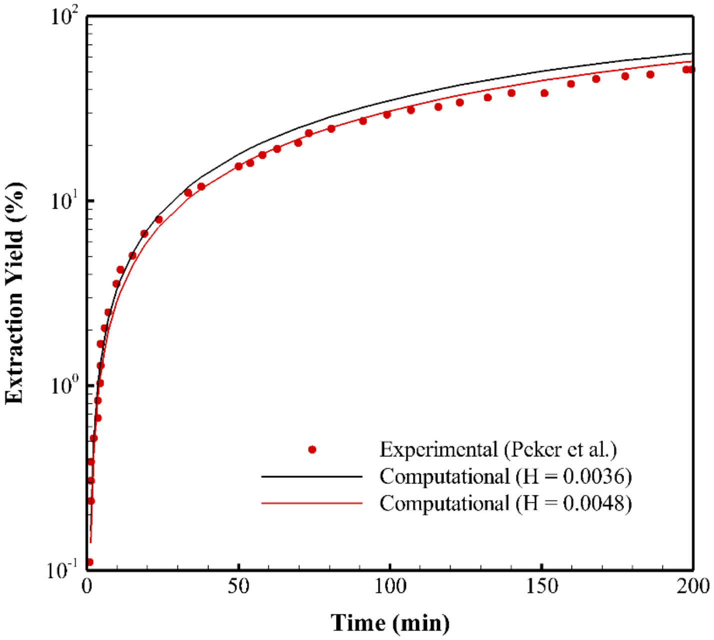

Figure 7.6: Comparison of temporal evolution of calculated caffeine yield (%) at the extraction column outlet with experimental data provided by Peker *et al.* [136]

Figure 7.6 shows the comparison of the transient variation of the extraction yield by the present numerical method with that obtained experimentally by Peker *et al.* [136]. It is observed that, the computational results (H = 0.0036) under predicts the extraction yield at the early time and over predicts it at the longer time scale. This behavior of the numerical model is explained by the variations in equilibrium saturation concentration of caffeine (C_{sat}) calculated from the Henry coefficient (H). The correlations developed by Gurdial *et al.* [69] gives a value of 0.0048 for the Henry coefficient at the considered initial state (13.8 MPa, 323 K). This value is considerably different from the value used in the simulations (H = 0.0036, as provided by Peker *et al.* [136]). Using a relatively lower equilibrium saturation concentration (H = 0.0036) of caffeine resulted in a smaller extraction yield at the early time and greater yield at the longer time scale. However, the calculated extraction yield is always within 8% of the experimental value. A second case is also simulated with the Henry coefficient value provided by the correlations developed by Gurdial *et al.* [69] ($H = 0.0048$). It is observed that, the case corresponding to $H = 0.0048$ provides a better approximation for the measurements (within 5% of the reported value).

7.4.2 Supercritical fluid extraction of caffeine

A total of eight cases are simulated with the developed computational fluid dynamics model to investigate the transport characteristics of supercritical fluid extraction process and the effect of acoustic waves on the yield (%) of caffeine extraction from a fixed bed extractor. Details regarding the simulated cases are presented in table 7.2. A solvent flow rate of 2.5 ml/min is considered for all the cases.

Table 7.2: List of calculated cases for supercritical fluid extraction of caffeine in fixed bed extractor.

Case No.	p_i (MPa)	T_i (K)	Henry Coefficient $\times 10^3$	Frequency of Vibration (Hz)	Amplitude of Vibration (μm)
1	10.0	307	6.5	-	-
2	10.0	315	2.4	-	-
3	8.0	307	0.71	-	-
4	8.0	315	0.0041	-	-
5	10.0	307	6.5	1855	25
6	10.0	315	2.4	1356	25
7	8.0	307	0.71	1090	25
8	8.0	315	0.0041	1142	25

Extraction of caffeine from porous solid spheres (modeled as coffee beans) using supercritical carbon dioxide as the solvent is considered first. The initial states of the supercritical solvent are near-critical and the fluid properties vary from liquid-like ($\rho/\rho_{cr} > 1$, case 1-3) to gas-like ($\rho/\rho_{cr} < 1$, case 4) regions. The binary diffusion coefficient of caffeine at the corresponding states of carbon dioxide is very small (in the order of 10^{-7} m^2/sec) and is of comparable magnitude. Lab-scale supercritical fluid extractors are usually operated at very low flow rates, usually in the range of 0.5~4 ml/min [49, 135, 136, 166]. In accordance to that, a volumetric flow rate of 2.5 ml/min is applied at the inlet section (see figure 7.1). Figure 7.7a shows the contours of bulk fluid pressure inside the supercritical fluid extractor at pseudo-steady state (t = 5 min) for case 1. The velocity contours and streamlines of the flow field in the extraction column at the pseudo-steady state for case 1 are shown in figure 7.7b.

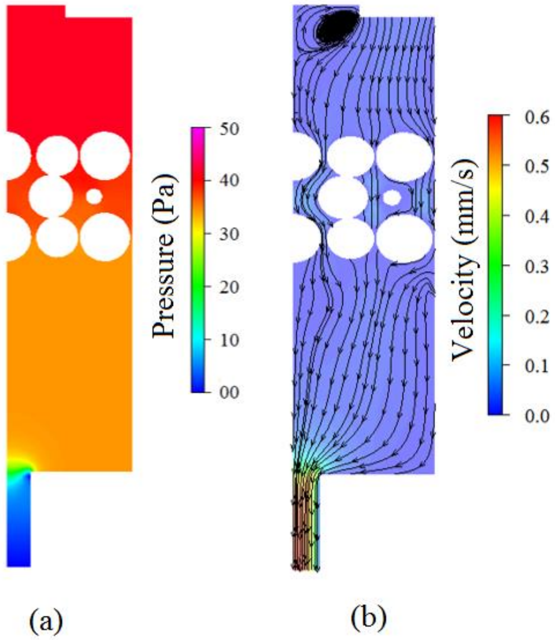

Figure 7.7: (a) Contours of bulk fluid pressure and (b) velocity with streamlines of flow field inside the extraction column at *t* = 5 min for case 1.

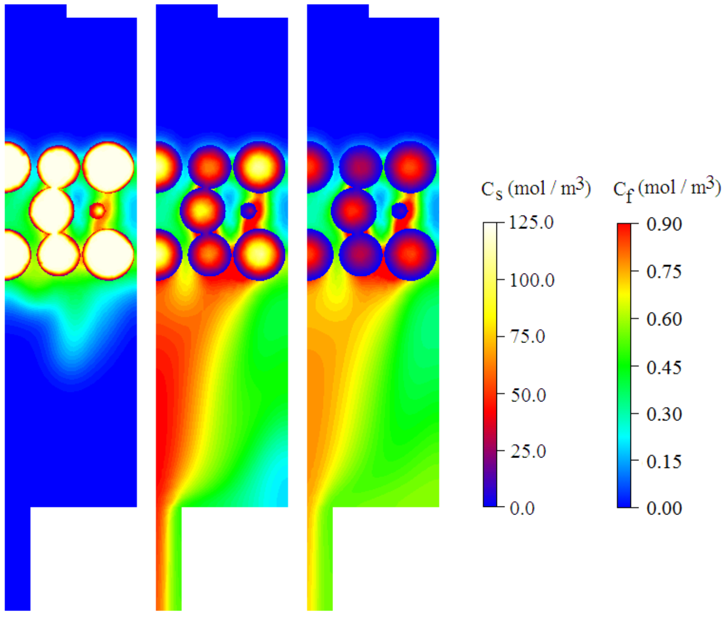

(a) (b) (c)

Figure 7.8: Contours of caffeine concentration in the fluid phase (*C_f*) and in the porous-solid phase (*C_s*) inside the extraction column at (a) *t* = 5 min, (b) *t* = 60 min and (c) *t* = 120 min for case 1.

The contours of caffeine concentration in the supercritical fluid extractor at different times ranging from 5 to 120 minutes for cases 1 (maximum solubility of caffeine) and 4 (minimum solubility of caffeine) are shown in figures 7.8 and 7.9 respectively. It is observed that, for the both cases the extraction process is mainly diffusion controlled at the very early time (up to ~ 5 minute). While at the longer time scale it is controlled by convection. However, due to the small porosity and permeability of the spherical particles, there is hardly any convection of solute species (*i.e.* caffeine) within the porous solid particles. The relatively small solvent flow rate in the extraction column makes the overall kinetics of the extraction process very slow. Also, the process is strongly dependent on the equilibrium saturation concentration of caffeine (C_{sat}). The equilibrium saturation concentration of caffeine for case 1 is about three orders of magnitude higher than that in case 4. This makes the process very slow in case 4. Due to this reason, extraction is never carried out in the gas-like ($\rho/\rho_{cr} < 1$) regions of the supercritical solvent.

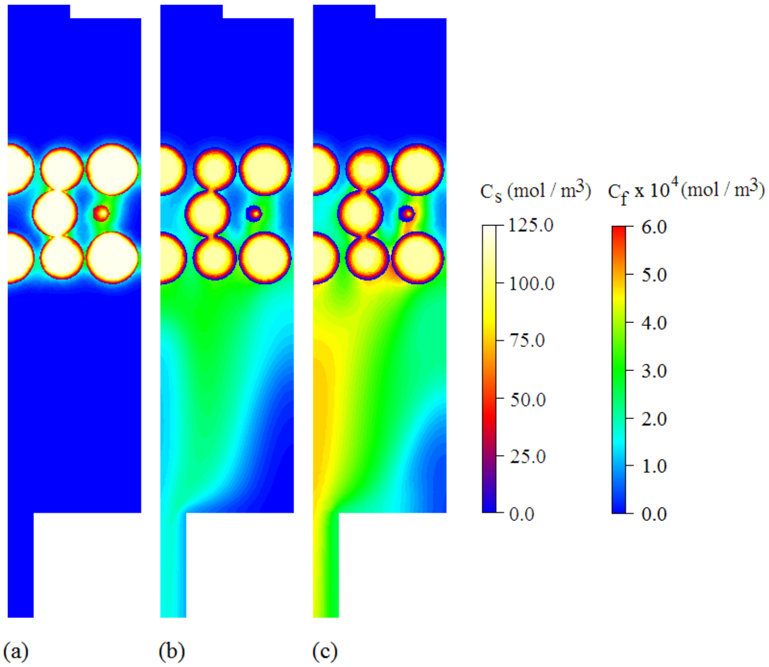

Figure 7.9: Contours of caffeine concentration in the fluid phase (C_f) and in the porous-solid phase (C_s) inside the extraction column at (a) t = 5 min, (b) t = 60 min and (c) t = 120 min for case 4.

Figure 7.10 shows the percentage yield of the caffeine at the outlet of the extraction column for cases 1-4. A sharp variation of the yield is observed in all the cases; at the initial period of extraction. At the static condition, some solute is extracted from the solid matrix by pure diffusion and is gathered at the outer surface of the particles (figures 7.8a and 7.9a). In the beginning of the convection regime, these solutes from the surface of the particles are carried to the outlet giving a sharp rise in extraction yield (figure 7.8b). It is observed that, solutes in the outer parts of particles are extracted much faster than the solutes in the inner parts of particles at the beginning of the dynamic extraction. This observation is in accordance with the study by Roy *et al.* [137]. As the extraction time proceeds, the diffusion of solutes from inner parts to the bulk phase becomes more difficult due to the decrease in driving force between the solid and fluid phases leading to the reduction of extraction rate (figure 7.8c).

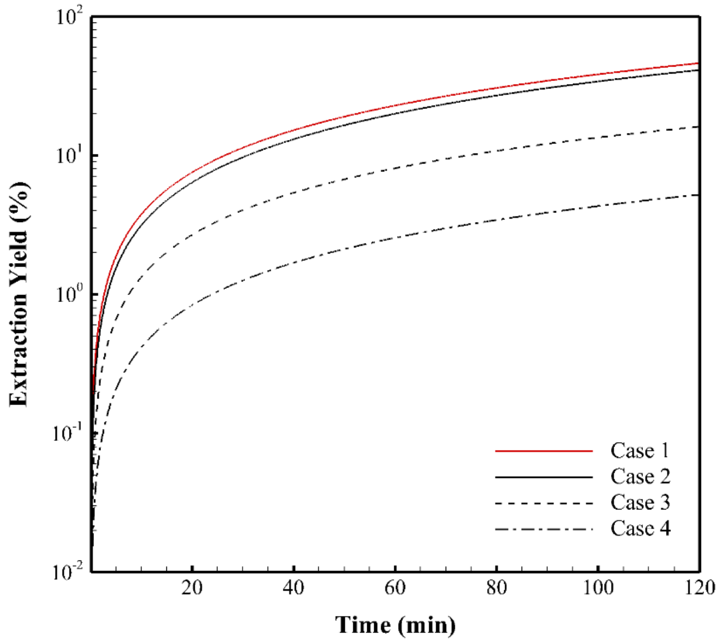

Figure 7.10: Temporal evolution of caffeine yield (%) at the outlet of the extraction column for cases 1-4.

7.4.3 Effect of acoustic waves on supercritical fluid extraction in fixed bed extractor

Acoustic waves are introduced to the same cases (cases 1-4) discussed in the previous section (section 7.4.2). Perturbation at the inlet end wall generates relatively high amplitude (around 0.5-1.0 kPa) pressure waves in the compressible solvent (carbon dioxide). These waves propagate through the fixed bed and reflect back from the bottom end wall (z = +8.7 cm). The frequencies of the moving wall for the cases simulated (case 5-8) are chosen such that the lowest acoustic mode propagates through the compressible fluid (*i.e.* at resonant frequency of the fluid medium based on the length of the extraction column, $f_{resonant} = c_{fluid} / 2L$). The instantaneous and cycle averaged flow fields inside the extraction column for case 5 (at t = 5 min) are shown in figure 7.11. It is observed that, the pressure waves induce relatively large scale (almost two times larger than the steady flow case 1) oscillating convective motion inside the extraction column; especially in the fixed bed region (figure 7.11a). The perturbation of the inlet wall and the reflections from the bottom wall also results in some irregularities in the flow as observed in figure 7.11a. These irregular flow patterns (instantaneous) facilitate the convection from the fixed bed and mixing. The cycle averaged flow field at *t* = 5 min is shown in Figure 7.11b. However, no streaming patterns [186] are observed in the cycle averaged flow field. This is mainly due to the effect of the steady flow coming from the inlet; superimposed on the generated oscillating flow field.

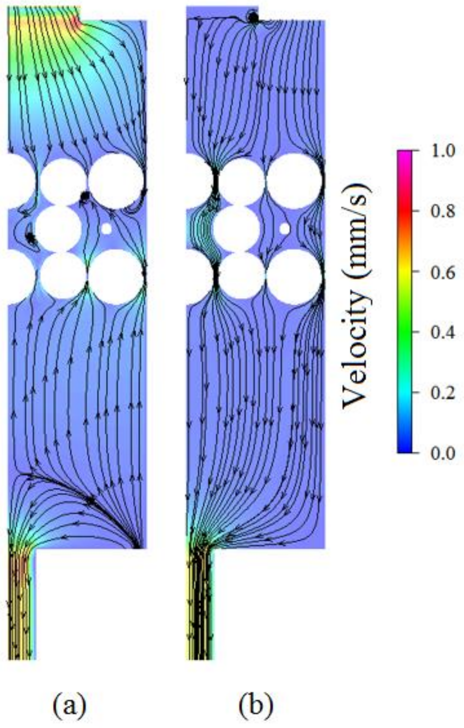

Figure 7.11: Velocity contours and streamlines of (a) instantaneous and (b) cycle averaged flow field inside the extraction column at *t* = 5 min for case 5.

Figure 7.12 shows the temporal pressure distribution at the bottom wall (z = +8.7 cm) for cases 5-8. The time period shown in the figure is around five cycles. Due to a large aspect ratio of the extraction column (L/D ~ 1.8), the wall has very small effect on the bulk flow. This leads to less attenuation and relatively high amplitude (around 0.5-1.0 kPa) of the pressure waves. It is also observed that, due to relatively high compressibility and small dynamic viscosity of the near-critical fluid (case 7 and 8); high amplitude pressure waves are generated in the bulk fluid for the same acoustic perturbation. The amplitude of the generated pressure waves are found to be in direct correlation with the proximity of the initial state of the solvent to the corresponding pseudo-critical state ($\rho / \rho_c = 1.0$), as well as the dynamic viscosity of the supercritical solvent.

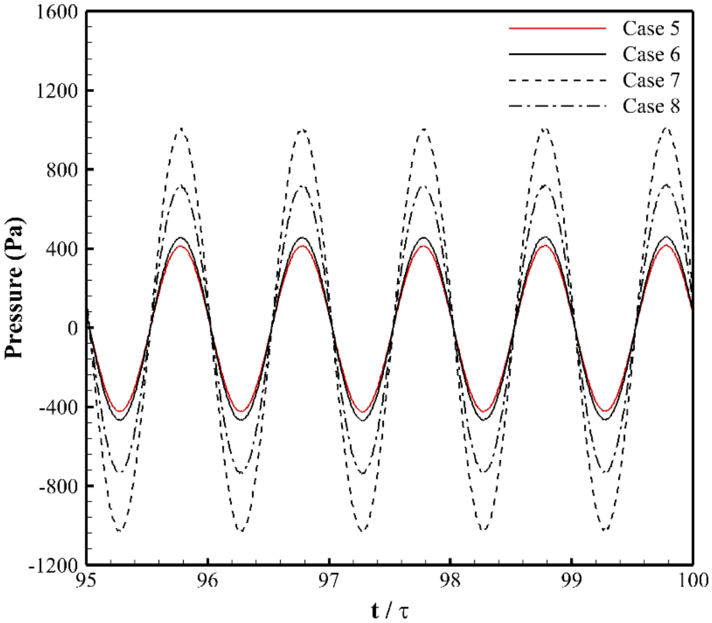

Figure 7.12: Temporal evolution of pressure at the bottom wall (z = +8.7 cm) of the extraction column for cases 5-8.

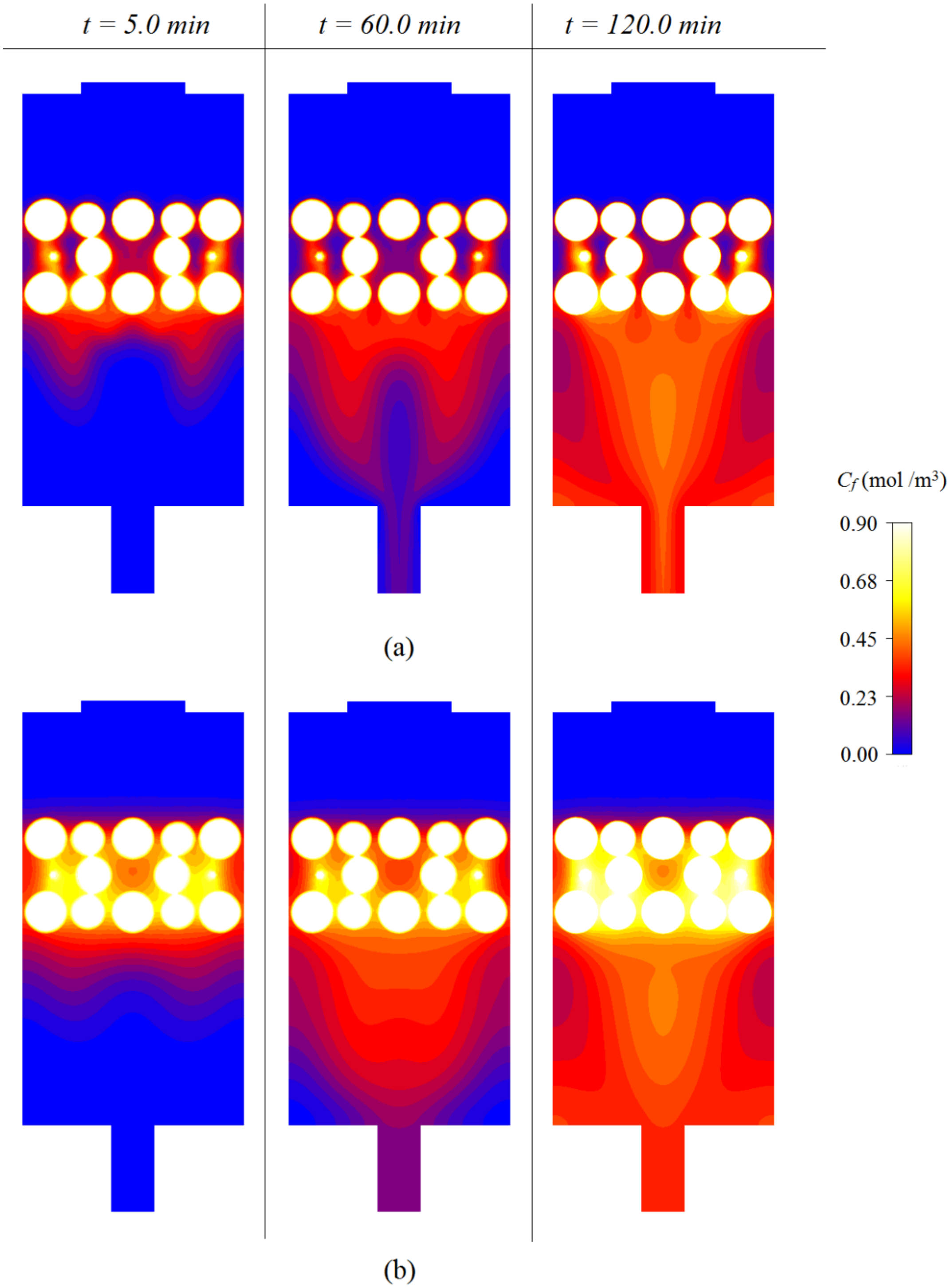

Figure 7.13: Contours of caffeine concentration (C_f) in the fixed bed extractor at three different times (a) without [case 1] and (b) with [case 5] the application of acoustic waves.

The contours of caffeine concentration in the supercritical fluid fixed bed extractor at different times ranging from 5 to 120 minutes for the cases with and without acoustic wave excitations at p = 10.0 MPa (case 1 and 5) are shown in figure 7.13. It is observed that, for the both cases the extraction process is mainly diffusion controlled at the early time (up to ~ 5 minute). While at the longer time scale it is controlled by convection. However, due to the small porosity and permeability of the spherical particles, there is hardly any convection of solute species (*i.e.* caffeine) within the porous solid particles. The relatively small solvent flow rate in the extraction column makes the overall kinetics of the extraction process slow. For the case without acoustic waves (case 1, figure 7.13a), a concentration gradient in the fixed bed from upstream to the downstream of the flow is observed. This is due to the downward direction of the solvent flow inside the extraction column. Also, there are localized concentration gradients present in the fixed bed extractor due to the particle-to particle contact and wall effect. However, this concentration gradient is not distinct for the case with acoustic waves (case 5, figure 7.13b). Also, due to the presence of higher convective mass transfer in the system, relatively higher concentration of caffeine in the extractor is observed for the case with acoustic waves.

The solute concentrations at the particle surface in the convective regime (t = 120 min) for case 1 (without acoustic waves) and case 5 (with acoustic waves) are shown in figure 7.14. For the case without acoustic waves, a concentration gradient in the fixed bed from upstream to the downstream of the flow is observed. This is due to the downward direction of the solvent flow inside the extraction column. Also, there are localized concentration gradients present in the extractor due to the particle-to particle contact and wall effect. However, this concentration gradient is not very distinct for the case with acoustic waves (case 5). Also, due to the presence of higher convective mass transfer in the system, relatively smaller average surface concentration of the particles in all the three layers is observed for the case with acoustic waves.

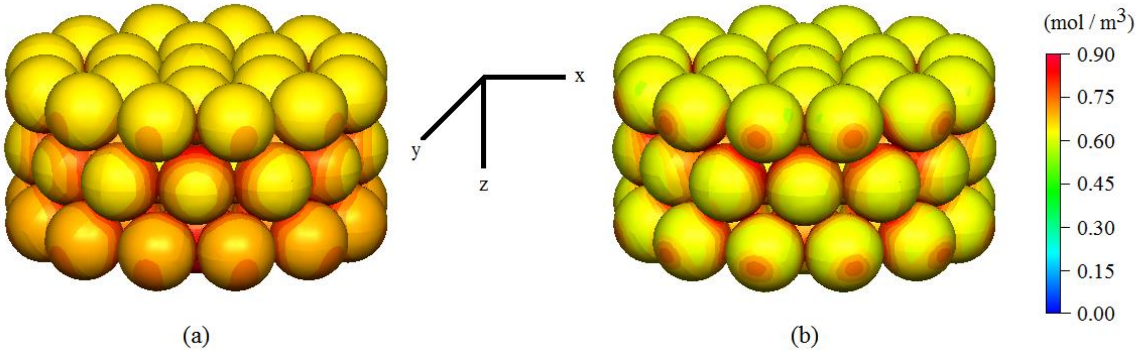

Figure 7.14: Contours of caffeine concentration (C_f) at the surface of the spherical particles at t = 120 min (a) without [case 1] and (b) with the effect of acoustic waves [case 5].

The temporal evolution of the percentage yield of caffeine for the cases with acoustic waves (case 5-8) is compared to the cases without acoustic waves (cases 1-4) in figure 7.15. It is observed that, the relatively high convective velocities induced by the pressure waves increased the yield of the solute (caffeine) in all the cases. It is also observed that due to the absence of caffeine on the surface of the spherical particles, the yield of caffeine at the outlet is not at all affected by the acoustic waves at the very early time (diffusion controlled regime). In the longer time period, acoustic excitation increased the extraction yield at different rates depending on the initial state of the supercritical solvent. The inlet end wall perturbations in case 7 produce the largest pressure oscillation in the extraction column (figure 7.12) and hence the rate of increase of the extraction yield is maximum for this case. Cases 5, 6 and 8 also exhibit a similar phenomenon but relatively smaller rates of increase due to acoustic waves. Due to the large-scale pressure oscillations in the bulk fluid, the extraction yield for case 7 increased from 16% (case 3) to 25% after the end of 120 min. However, since the solubility (*i.e.* saturation concentration) of caffeine is relatively lower in case 7, the net extraction yield is still smaller than some of the other cases (case 5 and 6) calculated in this study. Case 5 and 6 shows relatively better yield of extraction (~ 55%) with the application of acoustic waves.

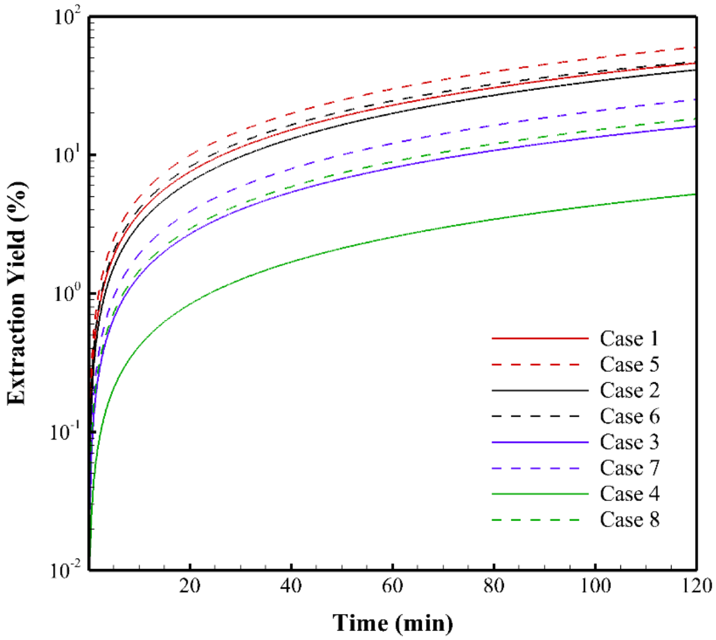

Figure 7.15: Temporal evolution of caffeine yield (%) at the outlet of the extraction column with the effect of acoustic waves.

7.5 Results and discussions: Membrane contactor

A membrane contactor (figure 7.2) used for extracting ethanol from an aqueous feed is considered for this study. Two cases (with and without the application of acoustic waves) are simulated to investigate the effect of acoustically augmented transport on the recovery yield. The initial state of the supercritical solvent (CO_2) is considered near-critical (p_i = 7.6 MPa, T_i = 306 K). The initial and boundary conditions for the simulations are listed in table 7.3. Transient simulations are carried out to a pseudo-steady state (t = 15 min) for both the cases. The recovery output is presented in terms of yield of the supercritical fluid extraction process.

Table 7.3: Initial and boundary conditions for the membrane contactor simulations

Parameter	**Membrane Contactor**
Solvent-Solute	CO_2 - Ethanol
Initial pressure, p_i	7.6 MPa
Initial temperature, T_i	306 K
Initial Solute Concentration, C_o	2.0 kmol/m^3
Henry Coefficient, H	0.00127
Solvent (CO_2) flow rate, F	5.0 ml/min
Frequency of Oscillation, f	3.307 kHz
Maximum Wall Displacement, x_{max}	10.0 µm

Contours of ethanol concentration in the membrane contactor at t = 15 min for the two cases are shown in figures 7.16a and 7.16b. A scaling factor of 2.0 is applied in the radial direction to clearly show the contours. Two different features of the concentration contour are noticed from these figures. The case with acoustic wave produces two regular streaming structures as discussed in chapter 6. Similar to the near-critical streaming structures, these structures are also centered near the end walls (*i.e.* not at x / L = 0.75). The streaming structures serves as feeding channels carrying ethanol from the side wall to the bulk flow. As a result, the much higher concentration of ethanol in the solvent flow is observed in this case (figure 7.16a) as compared to the case without acoustic waves (figure 7.16b). For the case without acoustic waves, a concentration boundary layer is visible near the side wall. The boundary layer thickness near the end (right) wall increases suddenly. This is mainly due to the change in direction of the velocity at the end wall.

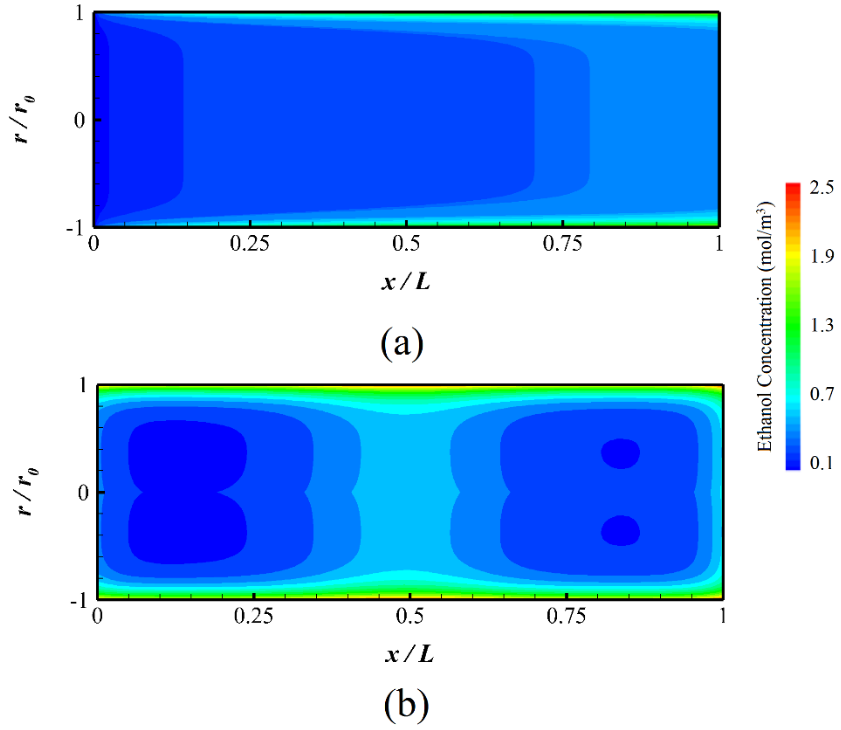

Figure 7.16: Contours of ethanol concentration in the membrane contactor (a) with acoustic waves (x_{max} = 10.0 µm and *f* = 3.307 kHz) and (b) without acoustic waves at *t* = 15 min.

Figure 7.17 shows the temporal evolution of the normalized pressure at the end (right) wall of the membrane contactor for the case with the application of acoustic waves. The time period shown in the figure is around four cycles. As discussed in chapter 6, the high compressibility and small dynamic viscosity of the near-critical fluid induces relatively high amplitude pressure waves in the bulk fluid for a small acoustic perturbation (x_{max} = 10 µm). For comparison, temporal evolution of the normalized pressure at the end (right) wall of a cylindrical shape resonator with same length (*L*) and aspect ratio (*L*/*D*) of the membrane contactor is also shown in figure 7.17. It is observed that, there is a small drop in the oscillatory pressure amplitude due to the through flow from inlet to outlet. The acoustic wave profile in the membrane contactor and the cylindrical shaped resonator are 'saw-tooth' like with sharp rise and a gradual fall.

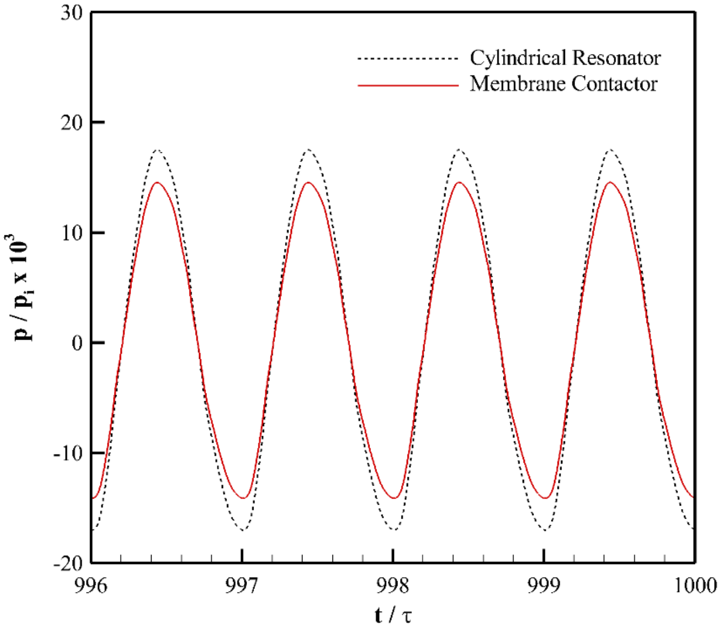

Figure 7.17: Temporal evolution of pressure at the end (right) wall of the membrane contactor (x_{max} = 10.0 µm and *f* = 3.307 kHz).

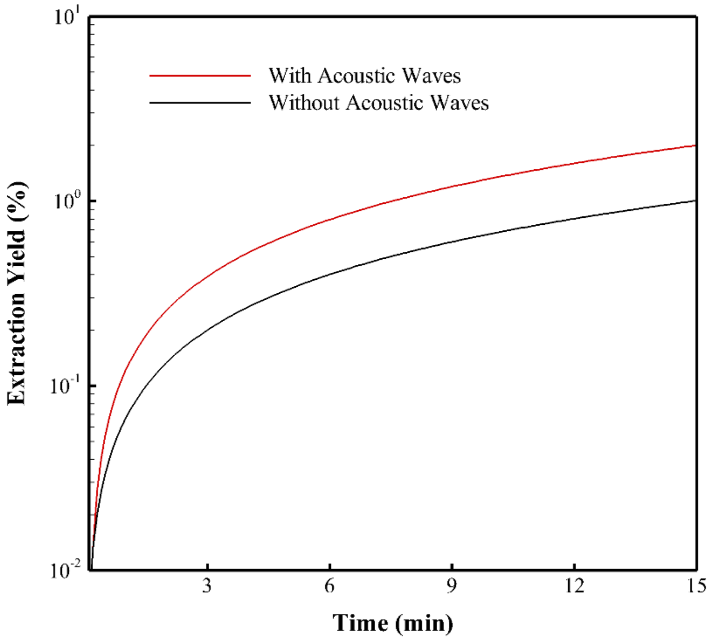

Figure 7.18: Temporal evolution of ethanol recovery yield (%) at the outlet of the membrane contactor with and without the effect of acoustic waves.

The cumulative recovery yield of ethanol from the aqueous feed up to t = 15 min for the calculated cases is shown in figure 7.18. It is observed that, the relatively high convective velocities induced by the pressure waves as well as the streaming structures significantly increase the yield of the ethanol recovery process. The extraction dynamics is slow with supercritical solvents. For the case without acoustic waves, the recovery yield of ethanol is only around 1.1% after 15 minutes of operation. The application of acoustic waves increased the recovery yield by a factor of ~ 2. However, the slope of the recovery yield curve for the case with acoustic waves is relatively higher than that without the acoustic waves. Hence, a higher enhancement is recovery yield may be expected at longer times.

7.6 Summary and conclusions

Mass transfer enhancement in supercritical fluid extraction processes using high amplitude resonant acoustic waves is investigated. Two different supercritical fluid extraction processes are simulated –the extraction of caffeine from a porous solid matrix (fixed bed) of spherical particles using supercritical carbon dioxide flow is considered first. Two levels of porosity are considered for the fixed bed of spherical particles – the bed porosity and the particle porosity. The bed porosity is modeled geometrically while the individual particle porosity is modeled by employing volume averaged porous media models. The convective mass transfer in supercritical fluid extraction process is simulated with the aid of a computational fluid dynamics model. A direct quantitative comparison of the caffeine extraction yield from coffee beans with a previous experimental investigation [18] shows a good match in the time-scale of the process. With the aid of the developed model, the influence of acoustically excited flows on supercritical extraction is investigated. Recovery of ethanol from an aqueous feed using supercritical carbon dioxide in a membrane contactor is also simulated and the effect of acoustic waves and streaming structures on the extraction yield is investigated in detail.

Enhancement in extraction yield is observed for both the systems with the application of acoustic waves. The enhancement is mainly due to the cumulative effect of increased localized convection (due to perturbation) and formation of streaming structures in the extraction systems. The numerical results also show that, the effect of acoustic waves can be enhanced in the near-critical regime. The highly compressible and less viscous near-critical solvent (carbon dioxide) generates large-scale oscillations in the flow-field which results in relatively higher enhancement in process yield. In case of a fixed bed extractor, the enhancement is mainly due to localized convection. The positioning of the porous fixed bed in the extraction column attenuates the acoustic waves to a greater extent and hinders the formation of streaming structures. Application of acoustic waves enhances the yield of caffeine extraction by around 15-25%, with trends of even greater improvements towards the end of the extraction process. While in the membrane contactor, higher streaming velocities near the wall increases the concentration boundary layer thickness and there-by increases mixing of the solute (ethanol) with the solvent.

The observations confirm that acoustic waves significantly accelerate the kinetics of the supercritical extraction process and improve the final extraction yield. These improvements are attributed to an increase in the overall mass transfer coefficient. Such promising result supports the need for further experimental research in this field, especially with near-critical solvents.

CHAPTER 8: SUMMARY AND CONCLUSIONS

8.1 Overall summary

Considering the major goals introduced in chapter 1, the research reported in the subsequent chapters show that supercritical fluids exhibit complex and non-linear transport phenomena near the critical point which can be utilized to enhance the performance of different thermal and chemical process systems that uses these fluids. Based on the motivations of the research work, the objectives set were divided into two main areas:

(a) To gain a better understanding of thermoacoustic transport in near-critical fluids.

(b) To investigate the acoustically driven transport phenomena in near-critical fluids.

In keeping with these objectives, this dissertation reports research that was completed in order to meet the set goals. Chapter 3 reports the development and validation of the numerical model for investigating thermoacoustic transport phenomena in near-critical supercritical fluids. Investigation of a novel fast response heat transfer device based on the near-critical thermoacoustic phenomena is also reported in this chapter. Experimental measurements of thermoacoustic waves in near-critical supercritical fluid as well as a comparison of the experimental measurements with the computational results (reported in chapter 3) are reported in chapter 4. The reported studies discuss the experiments conducted and the corresponding results from the characterization of the thermoacoustic waves under a variety of operating conditions (thermodynamic state of the fluid, boundary heating rate etc.). Chapter 5 discusses the interaction of thermoacoustic transport with developing natural convection in the fluid as well as the effect of diverging bulk viscosity of the near-critical fluid on the thermal transport. Development of a correlation to predict the thermal transport induced by buoyancy driven flow in supercritical fluids is reported in this chapter. Acoustically augmented flow and transport in near-critical fluids are reported in chapter 6 and 7. The experimental and numerical studies to investigate the mechanically driven acoustic waves in near-critical fluids as well as the development of computational fluid dynamic (CFD) models of different supercritical fluid extraction systems are discussed in these chapters. The specific conclusions of each of the above studies are presented in the next section of this chapter and the impact of the research is discussed. Based on that discussion, ideas for continuing and future work are presented in the section following the conclusions.

8.2 Specific conclusions and impact of findings

The conclusions are divided into four sub-sections as follows:

(a) Characterization of thermoacoustic transport in near-critical fluids.
(b) Interaction of thermoacoustic transport with natural convection.
(c) Characterization of acoustically augmented transport in near-critical fluids and
(d) Enhancement of supercritical fluid extraction using acoustic waves.

Details of the specific conclusions and impacts of the findings for the above four areas (a) - (d) are given in the following four sub-sections 8.2.1 - 8.2.4.

8.2.1 Characterization of thermoacoustic transport in near-critical fluids

Thermally induced acoustic waves are much stronger in supercritical fluids than in ideal gases under the same temperature increase and the rate of increase [91]. Thermoacoustic waves in a confined layer of near-critical fluid induce an adiabatic compression of the bulk fluid which results in a homogeneous temperature increase of the bulk known as '*piston effect*'. There are numerous analytical and numerical models available in the literature to predict supercritical fluid transport. However, most of these models do not consider the highly complex equation of state and non-linear thermo-physical property variations of the near-critical fluids. Experimental studies on the behavior of the thermoacoustic phenomena in the near-critical supercritical region detailing the temperature and pressure measurements were also not reported in the literature. In this study, generation and propagation of thermoacoustic wave and associated transport phenomena in near-critical supercritical fluids were investigated both experimentally and numerically.

The novel contribution of this study is the development and validation of a high fidelity predictive models based on an accurate equation of state for sub- and supercritical carbon dioxide and an in-depth analysis of the behavior of thermoacoustic transport phenomena in near-critical and near-pseudo-critical states. With the aid of the developed model, the transition of the thermoacoustic wave generation and propagation phenomena from a sub-critical to supercritical phase were investigated. Experimental measurements were also performed to characterize the generation, propagation and dissipation of thermally induced acoustic waves in supercritical carbon dioxide near its critical point. The adiabatic piston effect phenomena in near-critical fluids were also investigated by systematically approaching the pseudo-critical states. The results exhibit that rapid heating of the boundary emits strong compressive waves that carry energy and momentum from the heated boundary deep into the undisturbed regions of the fluid. The existence of the piston effect in supercritical fluid due to rapid heating of the boundary were also demonstrated numerically. Two exciting phenomena were observed from the numerical investigations. Firstly, as predicted by earlier studies [95, 159], the relative strength of the acoustic field ($\delta p/p_i$) as well as the corresponding change in bulk temperature (δT) certainly increases as the critical state of the fluid (CO_2) is approached. Secondly and most interestingly, change in these parameters ($\delta p/p_i$ and δT) are highly correlated with the pseudo-critical states. Near the pseudo-critical state ($\frac{\rho_i}{\rho_c} \to 1$), the acoustic field ($\delta p/p_i$) and the corresponding change in bulk temperature (δT) shows rapid increase while their magnitude decreases as the initial state is moved away from the pseudo-critical state. Proper inclusion of bulk viscosity in the model shows that, viscous resistance imposed on the expanding boundary layer by the high bulk viscosity fluid affects the thermoacoustic field both in the early and later times. A novel thermoacoustic wave driven thermal transport device using supercritical carbon dioxide as the working fluid was also proposed. From the study of this type of device, it was observed that a portion of the total energy supplied can be transmitted very quickly by the thermoacoustic waves. It was also observed that, the thermal transport performance (Q_{out}/Q_{in}) is mainly dependent on the initial state of the fluid and its proximity to the corresponding pseudo-critical state. Hence, the performance of the device can be adjusted easily and it can be used in conjunction with a traditional heat pipe where rapid transport of thermal energy is necessary.

The specific impact of this study on the thermoacoustics and supercritical fluids community can be summarized in the following points:

- This study reports one of the first experimental investigations of thermoacoustic wave generation and propagation in the near-critical supercritical region with detailed temperature and pressure measurements.
- A highly efficient and high-fidelity one-dimensional computational fluid dynamic model consisting of accurately represented equation of state and near-critical thermo-physical property variations is presented and validated with experimental measurements. Given the lack of numerical models with accurately represented equation of state and thermo-physical properties of near-critical fluids, this is a significant impact.
- The study also reports for the first time the effect of pseudo-critical states and bulk viscosity on the thermoacoustic wave generation and transport.

8.2.2 Interaction of thermoacoustic transport with natural convection

In the long time scale under the action of gravity, the thermoacoustic convection mode of transport interacts with the buoyancy driven convection. Buoyancy driven convection in supercritical fluids has been investigated in the past. However, convection of a pure fluid near the critical point is difficult to study both experimentally and theoretically due to the critical divergence of the thermo-physical properties. As a result, no satisfactory correlations were available to predict the convective heat transfer in near-critical fluids. In this study, thermal transport phenomena in supercritical fluids (carbon dioxide) in the near-critical as well as far from the critical point were investigated numerically with the aid of a computational fluid dynamic model.

The novel contribution of the this study is to demonstrate the effect of the pseudo-critical states (*i.e.* where $\rho = \rho_c$) on buoyancy driven thermal transport (*i.e.* transport phenomena in longer time scale) as well as the development of a correlation to predict the thermal transport behavior of supercritical carbon dioxide both near and far from the critical point. The effect of critically diverging bulk viscosity on the buoyancy driven flow was also investigated. The results exhibit that in the absence of critical divergence far from the critical point $\left(p > 10\text{MPa},\ T > 320\text{K} \right)$ thermal transport behavior of supercritical fluids is reasonably comparable to that for a high density and high Prandtl number ($\Pr \gg 1$) gas and depends on the Rayleigh number (Ra) of the flow only, while in the near critical region $\left(p_c < p < 10\text{MPa},\ T_c < T < 320\text{K} \right)$, transport of thermal energy varies not only as a function of Rayleigh number (Ra) but also as a function of the pressure and temperature. It was also observed that, similar to the thermo-physical property variations near the critical point, the Nusselt number (Nu) maximizes along the pseudo-critical states. Correlations for Nusselt number was proposed for both of these regions as a function of the Rayleigh number of the flow and the dimensionless pressure $p' = \left(\frac{p_i - p_c}{p_c} \right)$ and temperatures $T' = \left(\frac{T_m - T_c}{T_c} \right)$, $T'_{pc} = \left(\frac{T_{pc} - T_c}{T_c} \right)$. It was found that, in the near-critical region, critically diverging bulk viscosity plays a major role on the development of boundary layer and thermal equilibration in the flow domain. These effects are only significant when the bulk viscosity has values higher than the shear viscosity and the bulk viscosity shows strong variation in the flow domain. The specific impact of this study can be summarized in the following points:

- Correlations to predict the thermal transport behavior in the near-critical as well as far from the critical point of the fluid is developed. This is a significant impact on the field of supercritical fluid heat transfer due to the lack to information regarding heat transfer phenomena in the near-critical regime.
- The study reports one of the first investigations of effect of critically diverging bulk viscosity on natural convection and flow stability.

8.2.3 Characterization of acoustically augmented transport in near-critical fluids

Finite amplitude resonant acoustic waves in an enclosure induces a secondary flow field known as 'acoustic streaming'. This secondary flow field may be effective in accelerating certain kinds of rate processes, especially to enhance mixing processes and to augment heat and mass transfer through resonator walls. Studies on acoustic wave induced convective transport inside an enclosure have been conducted by several researchers [11, 50, 51, 195-197] in the past. However, most of these studies were limited to ideal gases at near atmospheric pressures. Mechanically driven resonant acoustic waves in near-critical supercritical carbon dioxide was investigated in this study. The formation of acoustic (pressure) waves, acoustic-viscous boundary layer interactions, and associated flows in a cylindrical resonator were numerically studied by solving the unsteady, compressible Navier–Stokes equations in an axisymmetric *x-r* coordinate system. The acoustic field in the enclosure was generated due to the harmonic vibration of the end wall. The effects of pseudo-critical state ($\rho / \rho_c \sim 1.0$) and operating pressure on the acoustic field and the formed flow structures were determined by utilizing a highly accurate numerical scheme. The computations were accompanied by appropriate experimentations on acoustically driven transport. Acoustic waves generated by an electro-mechanical driver in a cylindrical resonator filled with supercritical carbon dioxide were measured using a fast-response pressure field microphone. The results from the numerical simulations were then compared with the experimental measurements with accurately developed boundary conditions.

Several interesting and significant phenomena were observed from the numerical simulations and confirmed by the experimental measurements. The observed primary oscillatory and secondary steady flow fields in the supercritical fluid medium demonstrate significant effects of the thermodynamic state (sub-critical / supercritical / pseudo-critical) as well as the operating pressure. The strength of the acoustic wave field was found to be in direct relation with the thermodynamic state (near-pseudo-critical / far from the pseudo-critical state). It was observed that due to the strong thermo-physical property variations, amplitude of the maximum pressure increases as the thermodynamic state of the fluid approaches the corresponding pseudo-critical state. In the near-pseudo-critical state, the pressure wave form exhibits an irregular, non-linear profile due to the existence of a secondary resonant frequency in the system. This phenomena also affects the formation of acoustic streaming structures in the near-pseudo-critical state. Far from the pseudo-critical state, the streaming structure consists of two counter rotating cells with a '*jet*' like flow-field along the semi-length of the resonator (at the pressure node). While near the pseudo-critical state, irregular streaming structures consisting of four outer streaming cells in the top half of the resonator were observed. The evolved flow structures are also dependent on the operating pressure. The irregular streaming patterns were observed mainly for near-pseudo-critical states at operating pressures close to the critical pressure (p_c = 7.377 MPa). However, these structures quickly re-orients to the regular streaming patterns (two outer streaming cells) with the increase operating pressure. The phenomena observed both numerically and experimentally in this study can be utilized for mixing applications in supercritical fluid medium, especially for enhancing the transport characteristics in supercritical fluid extraction processes. The specific impact of this study can be summarized in the following points:

- Acoustic streaming in near-critical supercritical fluids was reported for the first time. This was enabled by the multi-dimensional nature of the developed computational model. Acoustic streaming was shown to be dependent on the thermodynamic state of the fluids.
- The numerical model was used to investigate the formation and structure of acoustic streaming in near-critical fluids. This can be used as an effective tool for designing acoustically driven processes in near-critical fluids.

8.2.4 Enhancement of supercritical fluid extraction using acoustic waves

Mass transfer enhancement in supercritical fluid extraction systems using acoustic waves in a relatively recent concept. Proper implementation of an actual prototype system requires a lot of design and testing. Numerical modeling and simulation is an efficient tool for this purpose. Transport processes in supercritical fluid extraction systems are generally modeled using the species (mass) conservation equation with a constant flow-field [124, 141, 142, 145, 166]. However, numerical models solely based on the differential mass balance integration are unable to predict the yield of the extraction process under an oscillating flow field or in complex geometries. A reliable and validated CFD model of the supercritical fluid extraction process for understanding the near-critical transport phenomena in supercritical fluid extraction systems is not available in the literature. In this study, computational fluid dynamics models to simulate the supercritical fluid extraction processes were developed. Mass transfer enhancement in supercritical fluid extraction processes using high amplitude resonant acoustic waves was investigated with the developed models. Two different supercritical fluid extraction processes were simulated – the extraction of caffeine from a porous solid matrix (fixed bed) of spherical particles using supercritical carbon dioxide flow was considered first. The influence of acoustically excited flows on supercritical extraction was investigated. Recovery of ethanol from an aqueous feed using supercritical carbon dioxide in a membrane contactor was also simulated and the effect of acoustic waves and streaming structures on the extraction yield was investigated in detail.

Enhancement in extraction yield was observed for both the systems with the application of acoustic waves. The enhancement was mainly due to the cumulative effect of increased localized convection (due to perturbation) and formation of streaming structures in the extraction systems. The numerical results also showed that, the effect of acoustic waves can be enhanced in the near-critical regime. The highly compressible and less viscous near-critical solvent (carbon dioxide) generates large-scale oscillations in the flow-field which results in relatively higher enhancement in process yield. In case of a fixed bed extractor, the enhancement is mainly due to localized convection. The positioning of the porous fixed bed in the extraction column attenuates the acoustic waves to a greater extent and hinders the formation of streaming structures. Application of acoustic waves enhanced the yield of caffeine extraction by around 15-25%, with trends of even greater improvements towards the end of the extraction process. While in the membrane contactor, higher streaming velocities near the wall increased the concentration boundary layer thickness and there-by increased mixing of the solute (ethanol) with the solvent. The specific impact of this study on the chemical process industry can be summarized in the following points:

- This study reports the first experimentally validated computational fluid dynamic model of a supercritical fluid extraction system. The multi-dimensional computational model can be an effective tool for designing supercritical fluid extraction processes.
- The novel concept of acoustically enhanced mass transfer in supercritical fluid extraction systems was demonstrated in this study. The results presented can be used as a guideline to set the operating conditions for these systems.

8.3 Future work and recommendations for continuing research

Significant progress was made in the area of supercritical fluid transport with the research reported in this dissertation. These significant contributions include the development of experimentally validated numerical models for thermoacoustic convection in near-critical fluids and supercritical fluid extraction systems. However, there is always room for improvement. Acoustic-fluid dynamic interactions in near-critical supercritical fluids have applications in a wide range of industrial processes and create challenging problems. Several research problems in this area remain which require further investigation to fully explore the nature of their underlying physical processes. To further advance the knowledge and understanding of near-critical transport phenomena in engineering systems, the following research tasks are recommended.

8.3.1 Supercritical fluids in thermoacoustic devices

The knowledge gathered from the fundamental studies on near-critical thermoacoustic transport carried out in this research project can be utilized in designing thermoacoustic devices. Thermoacoustic devices are used to pump heat from one place to another (in case of a refrigerator), utilizing high amplitude acoustic waves, or conversely to induce high amplitude acoustic waves (in case of an engine) using a heat difference. An ideal working gas for a thermoacoustic device (*i.e.* engine or refrigerator) should have the following thermo-physical properties – high acoustic speed [198, 199] as the power density of the device is proportional to the speed of sound. It should have a low thermal conductivity to reduce the heat transfer from the hot side to the cold side across the working gas [200]. It should have a specific heat ratio (γ) close to one and a relatively high Prandtl number, which leads to a minimum onset temperature [201, 202]. A low viscosity and high density of the fluid is also desirable to minimize viscous losses and leakage while operating at high pressures. These contradicting requirements indicate that the optimum thermodynamic state of the working fluid in a thermoacoustic engine should be selected according to the particular design objective with careful consideration of the temperature of the available heat source. From these perspectives, supercritical fluids (especially supercritical carbon dioxide) have the potential to be used as working fluids in thermoacoustic devices. Near the critical point, thermo-physical properties of supercritical fluids exhibit large deviations for small change in temperature and pressure and hence they can be ‘tuned’ for highly specific applications. Near-critical fluid is somewhat compressible, has a large thermal expansion coefficient (comparable to or larger than that of an ideal gas), and has other attractive thermo-physical properties (such as – relatively low viscosity and very high specific heat).

Near-critical fluids have been considered as working fluids for thermoacoustic devices in the past. Gu *et al*. [203] utilized supercritical heat recovery process in the stack (regenerator) section of a traditional thermoacoustic stirling engine to enhance the efficiency of the device. Haberbusch *et al.* [204] reported development of a thermoacoustic Stirling heat engine (TASHE) to drive a pulse tube refrigerator (PTR) and electrical linear alternator for instrument cooling and power generation for space applications. Three different working fluids – namely hydrogen, helium and supercritical carbon dioxide were investigated in their study using a DeltaEC [205] model. It was reported that supercritical carbon dioxide shows promising benefits and competitive thermal efficiency that is worthy to conduct design in parallel with traditionally used working fluids (*e.g.* helium). Our fundamental studies on thermoacoustic wave generation and transport in near-critical fluids showed that, relatively high amplitude acoustic waves can be generated in supercritical fluids even for a small temperature change. This is mainly due to the large thermal expansion coefficient (a desired property for conversion of heat to work) of these fluids. Thermoacoustic devices using near-critical working fluids are potentially important in applications involving large amounts of heat transfer across small temperature differences (in the order of 30^{o}C). It is expected such devices to be highly efficient and to have compact, inexpensive heat exchangers [206, 207].

Considering the potential of a supercritical fluid thermoacoustic engine discussed above, one interesting research direction would be to develop a multi-dimensional computational fluid dynamic (CFD) model that can be used to accurately predict the behavior and performance of a supercritical fluid thermoacoustic engine. This involves addressing the presence of heat-exchanger material in the system and how it affects the flow fields, accounting for heat transfer between the operating fluid (preferably supercritical carbon dioxide) and the solid surfaces including the heat-exchanger material and the walls of the components and accurately predicting the acoustic nature of the system.

8.3.2 Effect of higher harmonics on acoustic streaming in supercritical fluids

The numerical model developed to simulate acoustically augmented flow and transport in supercritical fluids has provided important insight into the thermal-fluid interactions inside the supercritical fluid resonators. However, the model can be used to further investigate the acoustically driven transport phenomena in supercritical fluids.

One interesting and important study would be to investigate the effect of the driving frequency on the formation of streaming structures. Investigation of the mechanically driven acoustic waves reported in chapter 6 was mainly focused on resonant (first harmonic) standing waves in the resonator. However, the effect of using higher harmonics ($f = nf_1$) on acoustic streaming structures generated in supercritical fluids as well as in atmospheric pressure gases is an open field of study. Intuitively, it can be assumed that higher harmonic frequencies will generate more streaming cells in the resonator (due to greater number of pressure nodes in the system); however variation of the driving frequency might also lead to the variation of the streaming velocities. The developed model can be utilized to investigate the optimal driving frequency that will provide efficient mixing of the fluid in the system.

Visualization of the flow structures inside a cylindrical resonator have been performed by numerous researchers in the past. But, most of these earlier studies are limited to atmospheric pressure gases / liquids. Flow visualization studies in supercritical fluid resonators will improve the understanding of acoustic streaming driven convective transport in these fluids. This can further validate the proposed application of using mechanically driven acoustic waves in supercritical fluid extraction to enhance mixing. The challenge of such a study lies in the development of an experimental system that will allow flow visualization studies in high pressures. In addition to flow visualization, velocity measurements of the generated oscillatory field will also improve our understanding of acoustically driven transport in high pressure / near-critical fluids. The best method of attempting velocity measurements would be with constant temperature anemometers given the visualization challenges posed in these high pressure systems (with regards to PIV methods).

8.3.3 Supercritical fluid extraction systems

Two different types of supercritical fluid extraction systems – fixed bed extractor and membrane contactor were modeled and simulated in the present research. They provided important insight on the underlying mechanisms of solvent extraction process using supercritical fluids. These models can be further improved to more accurately simulate the diffusion-convection processes in supercritical fluid extraction systems.

One important and significant improvement of the membrane contactor model would be to include the feed flow physics and the species transport in the membrane. The model developed in the present research do not consider the feed flow through the membrane contactor annulus as well as the porous membrane wall (section 7.3.3). The concentration boundary condition was calculated using a volume average model (Eqn. 7.13). Investigation of the effect of feed flow rate and membrane transport on the overall extraction yield would be a significant contribution in this area.

Another important research task in the field of mass transfer enhancement in supercritical fluid extraction using acoustic waves, is the experimental validation of the numerical results obtained from the present research. Developing an economical, lab-scale supercritical fluid flow reactor that would continuously pressurize and supply supercritical fluids for this experimentation is a major challenge. One concept idea is to use a high pressure liquid chromatography pump (HPLC) for this purpose. Saturated liquid carbon dioxide (at room temperature) flowing from a siphon tube fitted tank will be further cooled using a cold heat-exchanger (driven by peltier coolers). The sub-cooled liquid will then be pressurized above the supercritical pressure by the HPLC pump. The pressurized liquid will be heated by a hot heat exchanger to the operating temperature (> critical temperature in this case) and will flow through a test section where the experiments will be carried out. The same electro-mechanical transducers can be used the experiments to generated acoustic waves in the extraction system.

BIBLIOGRAPHY

[1] P. Atkins and J. de-Paula, *Physical chemistry*. New York: W. H. Freeman and Co., 2010.

[2] W. J. Leitner, Philip G. (1999). *Chemical synthesis using supercritical fluids*.

[3] NIST, "Reference Fluid Thermodynamic and Transport Properties Database," in *NIST23* vol. Version 9.0, ed. Gaithersburg, MD: NIST, 2010.

[4] A. Baiker, "Supercritical fluids in heterogeneous catalysis," *Chemical Reviews,* vol. 99, pp. 453-474, 1999.

[5] G. W. Swift, *Thermoacoustics : a unifying perspective for some engines and refrigerators*. Melville, NY: Acoustical Society of America through the American Institute of Physics, 2002.

[6] D. R. Kassoy, "The Response of a Confined Gas to a Thermal Disturbance. I: Slow Transients," *SIAM Journal on Applied Mathematics,* vol. 36, pp. 624-634, 1979.

[7] B. Farouk, E. S. Oran, and T. Fusegi, "Numerical study of thermoacoustic waves in an enclosure," *Physics of Fluids,* vol. 12, pp. 1052-1061, 2000.

[8] W. L. Nyborg, "Acoustic Streaming near a Boundary," *The Journal of the Acoustical Society of America,* vol. 30, pp. 329-339, 04/00/ 1958.

[9] M. Tatsuno, "Secondary streaming induced by an oscillating cylinder," ed, 1982.

[10] M. Campbell, J. Cosgrove, C. Greated, S. Jack, and D. Rockliff, "Review of LDA and PIV applied to the measurement of sound and acoustic streaming," *Optics and Laser Technology,* vol. 32, pp. 629-639, 2000.

[11] M. K. Aktas and B. Farouk, "Numerical simulation of acoustic streaming generated by finite-amplitude resonant oscillations in an enclosure," *The Journal of the Acoustical Society of America*, vol. 116, pp. 2822-2831, 11/00/ 2004.

[12] E. A. Brignole, "Supercritical fluid extraction," *Fluid Phase Equilibria*, vol. 29, pp. 133-144, 1986.

[13] J. A. Cárcel, J. V. García-Pérez, J. Benedito, and A. Mulet, "Food process innovation through new technologies: Use of ultrasound," *Journal of Food Engineering,* vol. 110, pp. 200-207, 2012.

[14] M. Herrero, J. A. Mendiola, A. Cifuentes, and E. Ibáñez, "Supercritical fluid extraction: Recent advances and applications," *Journal of Chromatography A*, vol. 1217, pp. 2495-2511, 2010.

[15] A. Bertucco and G. Vetter, *High Pressure Process Technology: Fundamentals and Applications*. Amsterdam: Elsevier Science, 2001.

[16] G. Brunner, *Gas extraction : an introduction to fundamentals of supercritical fluids and the application to separation processes*. Darmstadt; New York: Steinkopff ; Springer, 1994.

[17] B. Widom, "Equation of State in the Neighborhood of the Critical Point," *The Journal of Chemical Physics,* vol. 43, pp. 3898-3905, 1965.

[18] L. Kadanoff, "Spin-spin correlations in the two-dimensional ising model," *Il Nuovo Cimento B (1965-1970),* vol. 44, pp. 276-305, 1966.

[19] K. G. Wilson, "Renormalization Group and Critical Phenomena. I. Renormalization Group and the Kadanoff Scaling Picture," *Physical Review B,* vol. 4, pp. 3174-3183, 1971.

[20] K. K. Knapp and R. H. Sabersky, "Free convection heat transfer to carbon dioxide near the critical point," *International Journal of Heat and Mass Transfer,* vol. 9, pp. 41-51, 1966.

[21] R. H. Sabersky and E. G. Hauptmann, "Forced Convection Heat Transfer to Carbon Dioxide near the Critical Point," *International Journal of Heat and Mass Transfer,* vol. 10, pp. 1499-1508, 1967.

[22] R. J. Neumann and E. W. P. Hahne, "Free convective heat transfer to supercritical carbon dioxide," *International Journal of Heat and Mass Transfer,* vol. 23, pp. 1643-1652, 1980.

[23] W. Gang, Q. Bi, H. Wang, Z. Yang, X. Zhu, and Z. Hu, "Forced Convection Heat Transfer Using High Temperature and Pressure Water in an Upward-Inclined Tube," *Journal of Heat Transfer,* vol. 134, pp. 020905-8, 2012.

[24] M. Haghshenas Fard, "CFD modeling of heat transfer of CO2 at supercritical pressures flowing vertically in porous tubes," *International Communications in Heat and Mass Transfer,* vol. 37, pp. 98-102, 2010.

[25] P.-X. Jiang, Y.-J. Xu, J. Lv, R.-F. Shi, S. He, and J. D. Jackson, "Experimental investigation of convection heat transfer of CO2 at super-critical pressures in vertical mini-tubes and in porous media," *Applied Thermal Engineering,* vol. 24, pp. 1255-1270, 2004.

[26] S. M. Liao and T. S. Zhao, "An experimental investigation of convection heat transfer to supercritical carbon dioxide in miniature tubes," *International Journal of Heat and Mass Transfer,* vol. 45, pp. 5025-5034, 2002.

[27] M. Mohseni and M. Bazargan, "Effect of Turbulent Prandtl Number on Convective Heat Transfer to Turbulent Flow of a Supercritical Fluid in a Vertical Round Tube," *Journal of Heat Transfer,* vol. 133, pp. 071701-10, 2011.

[28] H. Tokanai, Y. Ohtomo, H. Horiguchi, E. Harada, and M. Kuriyama, "Heat Transfer of Supercritical CO2 Flow in Natural Convection Circulation System," *Heat Transfer Engineering,* vol. 31, pp. 750-756, 2010/08/01 2010.

[29] X.-R. Zhang, L. Chen, and H. Yamaguchi, "Natural convective flow and heat transfer of supercritical CO2 in a rectangular circulation loop," *International Journal of Heat and Mass Transfer,* vol. 53, pp. 4112-4122, 2010.

[30] A. Bruch, A. Bontemps, and S. Colasson, "Experimental investigation of heat transfer of supercritical carbon dioxide flowing in a cooled vertical tube," *International Journal of Heat and Mass Transfer,* vol. 52, pp. 2589-2598, 2009.

[31] E. W. P. Hahne, "Natural convection heat transfer through an enclosed horizontal layer of supercritical carbon dioxide," *Heat and Mass Transfer,* vol. 1, pp. 190-196, 1968.

[32] S. M. Liao and T. S. Zhao, "Measurements of Heat Transfer Coefficients From Supercritical Carbon Dioxide Flowing in Horizontal Mini/Micro Channels," *Journal of Heat Transfer,* vol. 124, pp. 413-420, 2002.

[33] D. A. Olson, *Heat transfer of supercritical carbon dioxide flowing in a cooled horizontal tube*. Gaithersburg, MD :: U.S. Dept. of Commerce, Technology Administration, National Institute of Standards and Technology, 2000.

[34] S. S. Pitla, D. M. Robinson, E. A. Groll, and S. Ramadhyani, "Heat Transfer from Supercritical Carbon Dioxide in Tube Flow: A Critical Review," *HVAC&R Research,* vol. 4, pp. 281-301, 1998/07/01 1998.

[35] M. Bazargan and D. Fraser, "Heat Transfer to Supercritical Water in a Horizontal Pipe: Modeling, New Empirical Correlation, and Comparison Against Experimental Data," *Journal of Heat Transfer,* vol. 131, pp. 061702-9, 2009.

[36] J. Licht, "Heat transfer to water at supercritical pressures in a circular and square annular flow geometry," *International journal of heat and fluid flow,* vol. 29, p. 156, 2008.

[37] J. Licht, M. Anderson, and M. Corradini, "Heat Transfer and Fluid Flow Characteristics in Supercritical Pressure Water," *Journal of Heat Transfer,* vol. 131, pp. 072502-14, 2009.

[38] J. Wang, H. Li, S. Yu, and T. Chen, "Investigation on the characteristics and mechanisms of unusual heat transfer of supercritical pressure water in vertically-upward tubes," *International Journal of Heat and Mass Transfer,* vol. 54, pp. 1950-1958, 2011.

[39] K. A. Gillis, I. I. Shinder, and M. R. Moldover, "Thermoacoustic boundary layers near the liquid-vapor critical point," *Physical Review E,* vol. 70, p. 021201, 2004.

[40] Z. Lei, "Thermoacoustic Convection and Transport in Supercritical Fluids under Normal and Micro-gravity Conditions," PhD, Mechanical Engineering & Mechanics, Drexel University, Phiadelphia, PA, 2010.

[41] A. Onuki, "Thermoacoustic effects in supercritical fluids near the critical point: Resonance, piston effect, and acoustic emission and reflection," *Physical Review E,* vol. 76, p. 061126, 2007.

[42] B. Shen and P. Zhang, "Thermoacoustic waves along the critical isochore," *Physical Review E,* vol. 83, p. 011115, 2011.

[43] P. Zhang and B. Shen, "Thermoacoustic wave propagation and reflection near the liquid-gas critical point," *Physical Review E,* vol. 79, p. 060103, 2009.

[44] T. Wang and M. X. B. S. Z. Yang, "Investigation on the elimination of organic substances in urine by supercritical water oxidation," *Space Medicine and Medical Engineering,* vol. 10, pp. 370-2, 1997.

[45] V. M. B. King and T. R. Bott., "Extraction of Natural Products Using Near-Critical Solvents.," *Chemie Ingenieur Technik,* vol. 65, pp. 1516-1516, 1993.

[46] S. Balachandran, S. E. Kentish, R. Mawson, and M. Ashokkumar, "Ultrasonic enhancement of the supercritical extraction from ginger," *Ultrasonics Sonochemistry,* vol. 13, pp. 471-479, 2006.

[47] U. Ender and S. Peter, "Enhancement of the efficiency of countercurrent near-critical fluid extraction by pressure pulsation," *Chemical Engineering and Processing: Process Intensification,* vol. 26, pp. 207-213, 1989.

[48] E. Riera, A. Blanco, J. García, J. Benedito, A. Mulet, J. A. Gallego-Juárez, *et al.*, "High-power ultrasonic system for the enhancement of mass transfer in supercritical CO2 extraction processes," *Physics Procedia,* vol. 3, pp. 141-146, 2010.

[49] E. Riera, Y. Golás, A. Blanco, J. A. Gallego, M. Blasco, and A. Mulet, "Mass transfer enhancement in supercritical fluids extraction by means of power ultrasound," *Ultrasonics Sonochemistry,* vol. 11, pp. 241-244, 2004.

[50] A. Gopinath and A. F. Mills, "Convective heat transfer from a sphere due to acoustic streaming," *The Journal of the Acoustical Society of America,* vol. 94, pp. 1773-1774, 09/00/ 1993.

[51] M. F. Hamilton, Y. A. Ilinskii, and E. A. Zabolotskaya, "Thermal effects on acoustic streaming in standing waves," *The Journal of the Acoustical Society of America,* vol. 114, pp. 3092-3101, 12/00/ 2003.

[52] G. Hang and S. Hongming, "Theoretical study of acoustic streaming induced cooling effect in the microscale," in *Ultrasonics Symposium, 2008. IUS 2008. IEEE*, 2008, pp. 934-937.

[53] Q. Wan and A. V. Kuznetsov, "Numerical Study of the Efficiency of Acoustic Streaming for Enhancing Heat Transfer between Two Parallel Beams," *Flow, Turbulence and Combustion,* vol. 70, pp. 89-114, 2003/01/01 2003.

[54] I. L. Pioro, *Heat Transfer and Hydraulic Resistance at Supercritical Pressure in Power-Engineering Applications*. New York: ASME, 2006.

[55] I. L. Pioro, H. F. Khartabil, and R. B. Duffey, "Heat transfer to supercritical fluids flowing in channels—empirical correlations (survey)," *Nuclear Engineering and Design,* vol. 230, pp. 69-91, 2004.

[56] A. Onuki, "Dynamics in fluids," in *Phase Transition Dynamics*, ed: Cambridge University Press, 2002, p. 728.

[57] H. E. Stanley, *Introduction to Phase Transitions and Critical Phenomena*. New York: Oxford University Press, 1971.

[58] C. M. Rayner, "Transition of carbon dioxide vapor-liquid equilibrium to supercritical phase," ed: University of Leeds.

[59] C. Domb, *The critical point : a historical introduction to the modern theory of critical phenomena*. London; Bristol, PA: Taylor & Francis, 1996.

[60] S. Li, G. S. Varadarajan, and S. Hartland, "Solubilities of theobromine and caffeine in supercritical carbon dioxide: correlation with density-based models," *Fluid Phase Equilibria,* vol. 68, pp. 263-280, 1991.

[61] J. Hegseth, Beysens D., Perrot F., Nikolayev V., "Growth and morphology of phase separating supercritical fluids," in *Fourth Microgravity Fluid Physics and Transport Phenomena Conference,* Cleveland, OH, 1998, pp. 184-189.

[62] J. C. Nieuwoudt and J. V. Sengers, "Frequency dependence of transport properties of fluids near the critical point," *Physica A: Statistical Mechanics and its Applications,* vol. 147, pp. 368-386, 1987.

[63] R. F. Berg, M. R. Moldover, and G. A. Zimmerli, "Frequency-dependent viscosity of xenon near the critical point," *Physical Review E,* vol. 60, pp. 4079-4098, 1999.

[64] K. A. Gillis, I. I. Shinder, and M. R. Moldover, "Bulk Viscosity, Thermoacoustic Boundary Layers, and Adsorption near the Critical Point of Xenon," *Physical Review Letters,* vol. 97, p. 104502, 2006.

[65] R. Span and W. Wagner, "A New Equation of State for Carbon Dioxide Covering the Fluid Region from the Triple-Point Temperature to 1100 K at Pressures up to

800 MPa," *Journal of Physical and Chemical Reference Data*, vol. 25, pp. 1509-1596, 1996.

[66] R. H. Sabersky and E. G. Hauptmanni, "Forced Convective Heat Transfer to Carbon Dioxide Near the Critical Point," *International Journal of Heat and Mass Transfer,* vol. 10, pp. 1499-1508, 1967.

[67] O. J. Catchpole and M. B. King, "Measurement and Correlation of Binary Diffusion Coefficients in Near Critical Fluids," *Industrial & Engineering Chemistry Research*, vol. 33, pp. 1828-1837, 1994/07/01 1994.

[68] M. B. King and O. J. Catchpole, "Physico-chemical data required for the design of near-critical fluid extraction process.," in *Extraction of Natural products using near-critical solvents*, M. B. King and T. R. Bott, Eds., ed London: Blackie Academic & Professional, 1993, pp. 184–231.

[69] G. S. Gurdial, P. A. Wells, N. R. Foster, and R. P. Chaplin, "The role of polarity in correlations of solid-supercritical fluid phase systems," *The Journal of Supercritical Fluids,* vol. 2, pp. 85-96, 1989.

[70] G. G. Stokes, "On the Theories of the Internal Friction of Fluids in Motion, and of the Equilibrium and Motion of Elastic Solids," *Transactions of the Cambridge Philosophical Society,* vol. 8, pp. 287-342, 1845.

[71] A. Onuki, "Dynamic equations and bulk viscosity near the gas-liquid critical point," *Physical Review E,* vol. 55, pp. 403-420, 1997.

[72] A. Onuki, "Thermoacoustic effects in supercritical fluids near the critical point: Resonance, piston effect, and acoustic emission and reflection," *Physical Review E*, vol. 76, Dec 2007.

[73] M. R. Moldover, J. V. Sengers, R. W. Gammon, and R. J. Hocken, "Gravity effects in fluids near the gas-liquid critical point," *Reviews of Modern Physics,* vol. 51, p. 79, 1979.

[74] M. A. Brown and S. W. Churchill, "Experimental measurements of pressure waves generated by impulsive heating of a surface," *AIChE Journal*, vol. 41, pp. 205-213, 1995.

[75] Y. Lin and B. Farouk, "Experimental and numerical studies of thermally induced acoustic waves in an enclosure," *Journal of Thermophysics and Heat Transfer (AIAA),* vol. 22, pp. 105-114, 2008.

[76] B. Zappoli, S. Amiroudine, P. Carles, and J. Ouazzani, "Thermoacoustic and buoyancy-driven transport in a square side-heated cavity filled with a near-critical fluid. ," *Journal of Fluid Mechanics,* vol. 316, pp. 53-72, 1996.

[77] M. A. Brown and S. W. Churchill, "Finite-difference computation of the wave motion generated in a gas by a rapid increase in the bounding temperature," *Computers & Chemical Engineering,* vol. 23, pp. 357–376, 1999.

[78] L. Rayleigh, "On the conduction of heat in a spherical mass of air confined by walls at a constant temperature," *Philosophical Magazine,* vol. XLVII, pp. 314-325, 1899.

[79] L. Trilling, "On Thermally Induced Sound Fields," *The Journal of the Acoustical Society of America,* vol. 27, pp. 425-431, 1955.

[80] B. Larkin, "Heat flow to a confined fluid in zero gravity," in *2nd Thermophysics Specialist Conference,* ed: American Institute of Aeronautics and Astronautics, 1967.

[81] A. M. Radhwan and D. R. Kassoy, "The response of a confined gas to a thermal disturbance: rapid boundary heating," *Journal of Engineering Mathematics,* vol. 18, pp. 133-156, 1984/06/01 1984.

[82] H. Ozoe, N. Sato, and S. W. Churchill, "The effect of various parameters on thermoacoustic convection," *Chemical Engineering Communications,* vol. 5, pp. 203 - 221, 1980.

[83] H. Ozoe, N. Sato, and S. W. Churchill, "Numerical analyses of two- and thee-dimensional thermoacoustic convection generated by a transient step in the temperature of one wall," *Numerical Heat Transfer, Part A: Applications,* vol. 18, pp. 1-15, 1990/07/01 1990.

[84] S. W. Churchill and M. A. Brown, "Thermoacoustic convection and the hyperbolic equation of conduction," *International Communications in Heat and Mass Transfer,* vol. 14, pp. 647-655, 11// 1987.

[85] Y. Huang and H. H. Bau, "Thermoacoustic waves in a semi-infinite medium," *International Journal of Heat and Mass Transfer,* vol. 38, pp. 1329-1345, 1995.

[86] Y. Huang and H. H. Bau, "Thermoacoustic waves in a confined medium," *International Journal of Heat and Mass Transfer,* vol. 40, pp. 407-419, 1997.

[87] M. K. Aktas and B. Farouk, "Numerical simulation of developing natural convection in an enclosure due to rapid heating," *International Journal of Heat and Mass Transfer,* vol. 46, pp. 2253-2261, 2003.

[88] Y. Lin, "Acoustic Wave Induced Convection and Transport in Gases under Normal and Micro-gravity Conditions," PhD, Mechanical Engineering and Mechanics, Drexel University, Philadelphia, 2007.

[89] Y. Lin, B. Farouk, and E. S. Oran, "Interactions of thermally induced acoustic waves with buoyancy induced flows in rectangular enclosures," *International Journal of Heat and Mass Transfer*, vol. 51, pp. 1665-1674, 2008.

[90] M. Parang and A. Salah-Eddine, "Thermoacoustic convection heat-transfer phenomenon," *AIAA Journal*, vol. 22, pp. 1020-1022, 1984/07/01 1984.

[91] G. Seibert, B. Fitton, and B. Battrick, *A world without gravity*. Noordwijk, the Netherlands: ESA Publications Division, 2001.

[92] P. Carles, "A brief review of the thermophysical properties of supercritical fluids," *Journal of Supercritical Fluids*, vol. 53, pp. 2-11, Jun 2010.

[93] Y. Garrabos, M. Bonetti, D. Beysens, F. Perrot, T. Fröhlich, P. Carlès*, et al.*, "Relaxation of a supercritical fluid after a heat pulse in the absence of gravity effects: Theory and experiments," *Physical Review E*, vol. 57, pp. 5665-5681, 1998.

[94] H. Boukari, J. N. Shaumeyer, M. E. Briggs, and R. W. Gammon, "Critical speeding up in pure fluids," *Physical Review A*, vol. 41, pp. 2260-2263, 1990.

[95] A. Onuki and R. A. Ferrell, "Adiabatic heating effect near the gas-liquid critical point," *Physica A: Statistical Mechanics and its Applications,* vol. 164, pp. 245-264, 1990.

[96] A. Onuki, H. Hao, and R. A. Ferrell, "Fast adiabatic equilibration in a single-component fluid near the liquid-vapor critical point," *Physical Review A*, vol. 41, pp. 2256-2259, 1990.

[97] B. Zappoli, D. Bailly, Y. Garrabos, B. Le Neindre, P. Guenoun, and D. Beysens, "Anomalous heat transport by the piston effect in supercritical fluids under zero gravity," *Physical Review A,* vol. 41, p. 2264, 1990.

[98] B. Zappoli, D. Beysens, P. Guenoun, B. Khalil, Y. Garrabos, and B. Le Neindre, "Anomalies of heat transport in near critical fluids under weightlessness," *Advances in Space Research*, vol. 11, pp. 269-276, 1991.

[99] H. Klein, G. Schmitz, and D. Woermann, "Temperature propagation in near-critical fluids prior to and during phase separation," *Physical Review A,* vol. 43, pp. 4562-4563, 04/15/ 1991.

[100] B. Zappoli and P. Carles, "Thermo-acoustic nature of the critical speeding up," *European Journal of Mechanics, B/Fluids,* vol. 14, pp. 41-65, 1995.

[101] M. Bonetti, F. Perrot, D. Beysens, and Y. Garrabos, "Fast thermalization in supercritical fluids," *Physical Review E*, vol. 49, pp. R4779-R4782, 06/01/ 1994.

[102] B. Shen and P. Zhang, "On the transition from thermoacoustic convection to diffusion in a near-critical fluid," *International Journal of Heat and Mass Transfer,* vol. 53, pp. 4832-4843, 10// 2010.

[103] Y. Miura, S. Yoshihara, M. Ohnishi, K. Honda, M. Matsumoto, J. Kawai*, et al.*, "High-speed observation of the piston effect near the gas-liquid critical point," *Physical Review E,* vol. 74, p. 010101R, 2006.

[104] A. Nakano and M. Shiraishi, "Piston effect in supercritical nitrogen around the pseudo-critical line," *International Communications in Heat and Mass Transfer,* vol. 32, pp. 1152-1164, Oct 2005.

[105] G. De Vahl Davis, "Natural convection of air in a square cavity: A bench mark numerical solution," *International Journal for Numerical Methods in Fluids,* vol. 3, pp. 249-264, 1983.

[106] S. Kimura and A. Bejan, "The Boundary Layer Natural Convection Regime in a Rectangular Cavity With Uniform Heat Flux From the Side," *Journal of Heat Transfer,* vol. 106, pp. 98-103, 1984.

[107] S. Ostrach, "Natural Convection in Enclosures," *Journal of Heat Transfer,* vol. 110, pp. 1175-1190, 1988.

[108] S. Yoshikawa, R. L. Smith Jr, H. Inomata, Y. Matsumura, and K. Arai, "Performance of a natural convection circulation system for supercritical fluids," *The Journal of Supercritical Fluids,* vol. 36, pp. 70-80, 2005.

[109] X. Y. Shan, D. P. Schmidt, and J. J. Watkins, "Study of natural convection in supercritical CO2 cold wall reactors: Simulations and experiments," *Journal of Supercritical Fluids,* vol. 40, pp. 84-92, Feb 2007.

[110] G. Accary, P. Bontoux, and B. Zappoli, "Convection in a supercritical fluid: A reduced model for geophysical flows," *Physics of Fluids,* vol. 19, pp. 014104-6, 2007.

[111] G. Accary, P. Bontoux, and B. Zappoli, "Turbulent Rayleigh–Bénard convection in a near-critical fluid by three-dimensional direct numerical simulation," *Journal of Fluid Mechanics,* vol. 619, pp. 127-145, 2009.

[112] K. Nishikawa, T. Ito, and H. Yamashita, "Free-Convective Heat Transfer to a Supercritical Fluid," *Journal of Heat Transfer,* vol. 95, pp. 187-191, 1973.

[113] I. Raspo, B. Zappoli, and P. Bontoux, "Unsteady two-dimensional convection in a bottom heated supercritical fluid," *Comptes Rendus Mécanique,* vol. 332, pp. 353-360, 2004.

[114] G. Accary and I. Raspo, "A 3D finite volume method for the prediction of a supercritical fluid buoyant flow in a differentially heated cavity," *Computers & Fluids,* vol. 35, pp. 1316-1331, 2006.

[115] A. Furukawa and A. Onuki, "Convective heat transport in compressible fluids," *Physical Review E,* vol. 66, p. 016302, 2002.

[116] G. Accary, I. Raspo, P. Bontoux, and B. Zappoli, "An adaptation of the low Mach number approximation for supercritical fluid buoyant flows," *Comptes Rendus Mécanique,* vol. 333, pp. 397-404, 2005.

[117] M. Varmazyar and M. Bazargan, "Modeling of Free Convection Heat Transfer to a Supercritical Fluid in a Square Enclosure by the Lattice Boltzmann Method," *Journal of Heat Transfer,* vol. 133, pp. 022501-5, 2011.

[118] L. K. McCune and R. H. Wilhelm, "Mass and Momentum Transfer in a Solid-Liquid System," *Industrial & Engineering Chemistry,* vol. 41, pp. 1124-1134, 1949/06/01 1949.

[119] J. E. Williamson, K. E. Bazaire, and C. J. Geankoplis, "Liquid-Phase Mass Transfer at Low Reynolds Numbers," *Industrial & Engineering Chemistry Fundamentals,* vol. 2, pp. 126-129, 1963/05/01 1963.

[120] E. J. Wilson and C. J. Geankoplis, "Liquid Mass Transfer at Very Low Reynolds Numbers in Packed Beds," *Industrial & Engineering Chemistry Fundamentals,* vol. 5, pp. 9-14, 1966/02/01 1966.

[121] S. N. Upadhyay and G. Tripathi, "Liquid-phase mass transfer in fixed and fluidized beds of large particles," *Journal of Chemical & Engineering Data,* vol. 20, pp. 20-26, 1975/01/01 1975.

[122] M. Paulaitis, V. Krukonis, R. Kurnik, and R. Reid, "Supercritical fluid extraction," *Reviews in Chemical Engineering,* vol. 1, pp. 179-250, 1983.

[123] N. Bulley, M. Fattori, A. Meisen, and L. Moyls, "Supercritical fluid extraction of vegetable oil seeds," *Journal of the American Oil Chemists' Society,* vol. 61, pp. 1362-1365, 1984.

[124] E. L. G. Oliveira, A. J. D. Silvestre, and C. M. Silva, "Review of kinetic models for supercritical fluid extraction," *Chemical Engineering Research and Design,* vol. 89, pp. 1104-1117, 2011.

[125] C. P. Passos, M. A. Coimbra, F. A. Da Silva, and C. M. Silva, "Modelling the supercritical fluid extraction of edible oils and analysis of the effect of enzymatic pre-treatments of seed upon model parameters," *Chemical Engineering Research and Design,* vol. 89, pp. 1118-1125, 2011.

[126] E. Reverchon and I. De Marco, "Supercritical fluid extraction and fractionation of natural matter," *The Journal of Supercritical Fluids,* vol. 38, pp. 146-166, 2006.

[127] E. Reverchon and C. Marrone, "Modeling and simulation of the supercritical CO2 extraction of vegetable oils," *The Journal of Supercritical Fluids,* vol. 19, pp. 161-175, 2001.

[128] J. O. Valderrama and R. F. Alarcón, "A novel hybrid numerical technique to determine mass transport properties in supercritical fluid extraction processes," *Communications in Numerical Methods in Engineering,* vol. 25, pp. 173-184, 2009.

[129] P. G. Debenedetti and R. C. Reid, "Diffusion and mass transfer in supercritical fluids," *AIChE Journal,* vol. 32, pp. 2034-2046, 1986.

[130] G. Knaff and E. U. Schlünder, "Diffusion coefficients of naphthalene and caffeine in supercritical carbon dioxide," *Chemical Engineering and Processing,* vol. 21, pp. 101-105, 1987/3// 1987.

[131] T. Gamse, "Industrial applications and current trends in supercritical fluid technologies," *Hemijska Industrija,* vol. 59, pp. 207-212, 2005.

[132] K. Zosel, "Process for recovering caffeine," 1974.

[133] M. A. McHugh and V. J. Krukonis, *Supercritical fluid extraction principles and practice*. Boston: Butterworth-Heinemann, 1994.

[134] G. Brunner, "Applications of Supercritical Fluids," *Annual Review of Chemical and Biomolecular Engineering,* vol. 1, pp. 321-342, 2010/06/15 2010.

[135] M. Fattori, N. Bulley, and A. Meisen, "Carbon dioxide extraction of canola seed: Oil solubility and effect of seed treatment," *Journal of the American Oil Chemists' Society,* vol. 65, pp. 968-974, 1988.

[136] H. Peker, M. P. Srinivasan, J. M. Smith, and B. J. McCoy, "Caffeine extraction rates from coffee beans with supercritical carbon dioxide," *AIChE Journal,* vol. 38, pp. 761-770, 1992.

[137] B. C. Roy, M. Goto, and T. Hirose, "Extraction of Ginger Oil with Supercritical Carbon Dioxide: Experiments and Modeling," *Industrial & Engineering Chemistry Research,* vol. 35, pp. 607-612, 1996/01/01 1996.

[138] M. Herrero, A. Cifuentes, and E. Ibañez, "Sub- and supercritical fluid extraction of functional ingredients from different natural sources: Plants, food-by-products, algae and microalgae: A review," *Food Chemistry,* vol. 98, pp. 136-148, 2006.

[139] W.-Q. Tang, D.-C. Li, Y.-X. Lv, and J.-G. Jiang, "Extraction and Removal of Caffeine from Green Tea by Ultrasonic-Enhanced Supercritical Fluid," *Journal of Food Science,* vol. 75, pp. C363-C368, 2010.

[140] S. Shirazian, A. Marjani, and F. Fadaei, "Supercritical extraction of organic solutes from aqueous solutions by means of membrane contactors: CFD simulation," *Desalination,* vol. 277, pp. 135-140, 2011.

[141] A. Lee, N. Bulley, M. Fattori, and A. Meisen, "Modelling of supercritical carbon dioxide extraction of canola oilseed in fixed beds," *Journal of the American Oil Chemists' Society,* vol. 63, pp. 921-925, 1986.

[142] J. D. Espinoza-Pérez, A. Vargas, V. J. Robles-Olvera, G. C. Rodrı´guez-Jimenes, and M. A. Garcı´a-Alvarado, "Mathematical modeling of caffeine kinetic during solid–liquid extraction of coffee beans," *Journal of Food Engineering,* vol. 81, pp. 72-78, 2007.

[143] J. Fernandes, P. F. Lisboa, P. C. Simões, J. P. B. Mota, and E. Saatdjian, "Application of CFD in the study of supercritical fluid extraction with structured packing: Wet pressure drop calculations," *The Journal of Supercritical Fluids,* vol. 50, pp. 61-68, 2009.

[144] S. Machmudah, A. Martin, M. Sasaki, and M. Goto, "Mathematical modeling for simultaneous extraction and fractionation process of coffee beans with supercritical CO2 and water," *The Journal of Supercritical Fluids,* vol. 66, pp. 111-119, 2012.

[145] H. Z. Nei, S. Fatemi, M. R. Mehrnia, and A. Salimi, "Mathematical modeling and study of mass transfer parameters in supercritical fluid extraction of fatty acids from Trout powder," *Biochemical Engineering Journal,* vol. 40, pp. 72-78, 2008.

[146] G. Afrane and E. H. Chimowitz, "Experimental investigation of a new supercritical fluid-inorganic membrane separation process," *Journal of Membrane Science,* vol. 116, pp. 293-299, 8/7/ 1996.

[147] S. Sarrade, C. Guizard, and G. M. Rios, "Membrane technology and supercritical fluids: chemical engineering for coupled processes," *Desalination,* vol. 144, pp. 137-142, 9/10/ 2002.

[148] S. I. Semenova, H. Ohya, T. Higashijima, and Y. Negishi, "Separation of supercritical CO2 and ethanol mixtures with an asymmetric polyimide membrane," *Journal of Membrane Science,* vol. 74, pp. 131-139, 10/28/ 1992.

[149] H. Ohya, T. Higashijima, Y. Tsuchiya, H. Tokunaga, and Y. Negishi, "Separation of supercritical CO2 and iso-octane mixtures with an asymmetric polyimide membrane," *Journal of Membrane Science,* vol. 84, pp. 185-189, 9/23/ 1993.

[150] L. Sartorelli and G. Brunner, "Separation of Extracts From Supercritical Carbon Dioxide by Means of Membranes," *Chemie Ingenieur Technik,* vol. 73, pp. 712-713, 2001.

[151] Y.-W. Chiu and C.-S. Tan, "Regeneration of supercritical carbon dioxide by membrane at near critical conditions," *The Journal of Supercritical Fluids,* vol. 21, pp. 81-89, 9// 2001.

[152] L. H. C. Carlson, A. Bolzan, R. Machado, and F. Antonio, "Separation of d-limonene from supercritical CO2 by means of membranes," *Journal of supercritical fluids.,* vol. 34, p. 143, 2005.

[153] J. R. Robinson and M. J. Sims, "Method and system for extracting a solute from a fluid using dense gas and a porous membrane," ed: Google Patents, 1996.

[154] G. D. Bothun, B. L. Knutson, H. J. Strobel, and S. E. Nokes, "Mass transfer in hollow fiber membrane contactor extraction using compressed solvents," *Journal of Membrane Science*, vol. 227, pp. 183-196, 2003.

[155] A. Gabelman, S. T. Hwang, and W. B. Krantz, "Dense gas extraction using a hollow fiber membrane contactor: experimental results versus model predictions," *Journal of Membrane Science,* vol. 257, pp. 11-36, 2005.

[156] S. J. Sarrade, G. M. Rios, and M. Carles, "Supercritical CO2 extraction coupled with nano-filtration separation: Applications to natural products," *Separation and Purifcation Technology,* vol. 14, pp. 19-26, 1998.

[157] H. Sovová, "Rate of the vegetable oil extraction with supercritical CO2—I. Modelling of extraction curves," *Chemical Engineering Science,* vol. 49, pp. 409-414, 1994.

[158] N. Djennaoui, F. Heraudeau, P. Guenoun, D. Beysens, and B. Zappoli, "Thermal transport in a pure fluid near the critical point," *Acta Astronautica,* vol. 29, pp. 189-193, 1993.

[159] B. Zappoli, "The response of a nearly supercritical pure fluid to a thermal disturbance," *Physics of Fluids A: Fluid Dynamics,* vol. 4, pp. 1040-1048, 1992.

[160] A. Nakano and M. Shiraishi, "Numerical simulation for the Piston effect and thermal diffusion observed in supercritical nitrogen," *Cryogenics,* vol. 44, pp. 867-873, Dec 2004.

[161] P. Carles, "The effect of bulk viscosity on temperature relaxation near the critical point," *Physics of Fluids,* vol. 10, pp. 2164-2176, 1998.

[162] B. Zappoli and A. Durand-Daubin, "Direct numerical modelling of heat and mass transport in a near supercritical fluid," *Acta Astronautica,* vol. 29, pp. 847-859, 1993.

[163] B. Zappoli, S. Amiroudine, P. Carles, and J. Ouazzani, "Inversion of acoustic waves reflection rules in near critical pure fluids," *Physics of Fluids,* vol. 7, pp. 2283-2287, 1995.

[164] B. Zappoli and P. Charles, "Acoustic saturation of the critical speeding up," *Physica D: Nonlinear Phenomena,* vol. 89, pp. 381-394, 1996.

[165] B. Zappoli, "Influence of convection on the piston effect," *International Journal of Thermophysics,* vol. 19, pp. 803-815, May 1998.

[166] M. S. Diaz and E. A. Brignole, "Modeling and optimization of supercritical fluid processes," *The Journal of Supercritical Fluids,* vol. 47, pp. 611-618, 2009.

[167] A. Guardo, M. Casanovas, E. Ramírez, F. Recasens, I. Magaña, D. Martínez, *et al.*, "CFD modeling on external mass transfer and intra-particle diffusional effects on the supercritical hydrogenation of sunflower oil," *Chemical Engineering Science,* vol. 62, pp. 5054-5061, 2007.

[168] A. Guardo, M. Coussirat, F. Recasens, M. A. Larrayoz, and X. Escaler, "CFD studies on particle-to-fluid mass and heat transfer in packed beds: Free convection effects in supercritical fluids," *Chemical Engineering Science,* vol. 62, pp. 5503-5511, 2007.

[169] N. Hasan and B. Farouk, "Thermoacoustic Transport in Supercritical Fluids at Near-critical and Near-pseudo-critical States," *The Journal of Supercritical Fluids,* vol. 68, pp. 13-24, 2012.

[170] H. Boukari, M. E. Briggs, J. N. Shaumeyer, and R. W. Gammon, "Critical speeding up observed," *Physical Review Letters,* vol. 65, pp. 2654-2657, 1990.

[171] J. P. van Doormaal and G. D. Raithby, "Enhancements of the SIMPLE method for predicting incompressible fluid flows," *Numerical Heat Transfer,* vol. 7, pp. 147-163, 1984/04/01 1984.

[172] D. Beysens, D. Chatain, V. S. Nikolayev, J. Ouazzani, and Y. Garrabos, "Possibility of long-distance heat transport in weightlessness using supercritical fluids," *Physical Review E,* vol. 82, Dec 2010.

[173] N. Hasan and B. Farouk, "Fast Heating Induced Thermoacoustic Waves in Supercritical Fluids: Experimental and Numerical Studies," *Journal of Heat Transfer,* vol. 135, pp. 081701-081701, 2013.

[174] S. J. Kline and F. A. McClintock, "Describing Uncertainties in Single-Sample Experiments," *Mechanical Engineering,* vol. 53, pp. 3-8, 1953.

[175] Brüel&Kjær, "Product Catalogue - Microphones & Conditioning," ed, 2009, pp. 2-7.

[176] P. Carlès and K. Dadzie, "Two typical time scales of the piston effect," *Physical Review E,* vol. 71, p. 066310, 2005.

[177] N. Hasan and B. Farouk, "Buoyancy driven convection in near-critical and supercritical fluids," *International Journal of Heat and Mass Transfer,* vol. 55, pp. 4207-4216, 2012.

[178] G. Barakos, E. Mitsoulis, and D. Assimacopoulos, "Natural convection flow in a square cavity revisited: Laminar and turbulent models with wall functions," *International Journal for Numerical Methods in Fluids,* vol. 18, pp. 695-719, 1994.

[179] N. C. Markatos and K. A. Pericleous, "Laminar and turbulent natural convection in an enclosed cavity," *International Journal of Heat and Mass Transfer,* vol. 27, pp. 755-772, 1984.

[180] A. Bejan, "Note on Gill's solution for free convection in a vertical enclosure," *Journal of Fluid Mechanics,* vol. 90, pp. 561-568, 1979.

[181] E. Lemmon, M. Huber, and M. McLinden, "NIST Standard Reference Database 23," vol. Version 9.0, ed. Gaithersburg, MD: NIST, 2010.

[182] A. Alexeev, A. Goldshtein, and C. Gutfinger, "Heat interaction in a resonance tube," *Physics of Fluids,* vol. 14, pp. 1812-15, 2002.

[183] A. Alexeev and C. Gutfinger, "Resonance gas oscillations in closed tubes: Numerical study and experiments," *Physics of Fluids,* vol. 15, pp. 3397-3408, 2003.

[184] L. L. Beranek, *Acoustics,* 2nd ed. New York: Acoustical Society of America, 1986.

[185] C. Dyken and M. S. Floater, "Transfinite mean value interpolation," *Comput. Aided Geom. Des.,* vol. 26, pp. 117-134, 2009.

[186] M. F. Hamilton, Y. A. Ilinskii, and E. A. Zabolotskaya, "Acoustic streaming generated by standing waves in two-dimensional channels of arbitrary width," *The Journal of the Acoustical Society of America,* vol. 113, pp. 153-160, 01/00/ 2003.

[187] D. S. Antao and B. Farouk, "High amplitude nonlinear acoustic wave driven flow fields in cylindrical and conical resonators," *The Journal of the Acoustical Society of America,* vol. 134, pp. 917-932, 2013.

[188] D. S. Antao and B. Farouk, "Experimental and numerical investigations of an orifice type cryogenic pulse tube refrigerator," *Applied Thermal Engineering,* vol. 50, pp. 112-123, 1/10/ 2013.

[189] N. Hasan and B. Farouk, "Mass transfer enhancement in supercritical fluid extraction by acoustic waves," *Journal of Supercritical Fluids,* vol. 80, pp. 60-70, 2013.

[190] J. R. F. G. de Carvalho and J. M. P. Q. Delgado, "Lateral dispersion in liquid flow through packed beds at Pem < 1,400," *AIChE Journal,* vol. 46, pp. 1089-1095, 2000.

[191] R. L. Graham, B. D. Lubachevsky, and K. J. Nurmela, "Dense packings of congruent circles in a circle," *Discrete Math.,* vol. 181, pp. 139-154, 1998.

[192] R. Battino and H. L. Clever, "The Solubility of Gases in Liquids," *Chemical Reviews,* vol. 66, pp. 395-463, 1966/08/01 1966.

[193] J. J. Carroll. (1991) What is Henry's Law? *Chemical engineering progress*. 48-54.

[194] F. L. Smith and A. H. Harvey. (2007) Avoid Common Pitfalls When Using Henry's Law. *Chemical engineering progress*. 33-39.

[195] J. Cai, X. Huai, S. Liang, and X. Li, "Augmentation of natural convective heat transfer by acoustic cavitation," *Frontiers of Energy and Power Engineering in China,* vol. 4, pp. 313-318, 2010/09/01 2010.

[196] B.-G. Loh, S. Hyun, P. I. Ro, and C. Kleinstreuer, "Acoustic streaming induced by ultrasonic flexural vibrations and associated enhancement of convective heat transfer," *The Journal of the Acoustical Society of America,* vol. 111, pp. 875-883, 02/00/ 2002.

[197] B. Tajik, A. Abbassi, M. Saffar-Avval, A. Abdullah, and H. Mohammad-Abadi, "Heat transfer enhancement by acoustic streaming in a closed cylindrical enclosure filled with water," *International Journal of Heat and Mass Transfer,* vol. 60, pp. 230-235, 5// 2013.

[198] J. R. Olson and G. W. Swift, "Similitude in thermoacoustics," *The Journal of the Acoustical Society of America,* vol. 95, pp. 1405-1412, 1994.

[199] G. W. Swift, "Thermoacoustic engines," *The Journal of the Acoustical Society of America,* vol. 84, pp. 1145-1180, 1988.

[200] J. Wheatley, T. Hofler, G. W. Swift, and A. Migliori, "An intrinsically irreversible thermoacoustic heat engine," *The Journal of the Acoustical Society of America,* vol. 74, pp. 153-170, 1983.

[201] G. W. Swift, *Thermoacoustics: A unifying perspective for some engines and refrigerators*: Acoustical Society of America, 2001.

[202] J. R. Belcher, W. V. Slaton, R. Raspet, H. E. Bass, and J. Lightfoot, "Working gases in thermoacoustic engines," *The Journal of the Acoustical Society of America,* vol. 105, pp. 2677-2684, 1999.

[203] Z. Gu, H. Sato, and X. Feng, "Using supercritical heat recovery process in Stirling engines for high thermal efficiency," *Applied Thermal Engineering,* vol. 21, pp. 1621-1630, 11// 2001.

[204] M. Haberbusch, C. Nguyen, J. C. Ickes, and G. W. Swift, "High-Power Thermoacoustic Stirling Heat Engine Results," in *9th Annual International Energy*

Conversion Engineering Conference, ed: American Institute of Aeronautics and Astronautics, 2011.

[205] B. Ward, J. Clark, and G. Swift, "Design Environment for Low-amplitude ThermoAcoustic Energy Conversion.," ed, 2001.

[206] G. W. Swift, "A Stirling engine with a liquid working substance," *Journal of Applied Physics,* vol. 65, pp. 4157-4172, 1989.

[207] G. W. Swift, "Malone Refrigeration," presented at the The Sixth International Stirling Engine Conference and Exhibition, Rotterdam, Netherlands, 1993.

VITA

Nusair Mohammed Ibn Hasan was born in Dhaka, Bangladesh on July, 1985. He received his Bachelor’s in Mechanical Engineering from Bangladesh University of Engineering and Technology (BUET) in 2008 with concentrations on thermal-fluid science. He then joined BUET as a lecturer and worked in the department of Mechanical Engineering for more than two years. He received his Master’s of Science (M.Sc.) in Mechanical Engineering from the same university where his research work was related to variable valve timing in SI engines; supported by the Directorate of Advisory, Extension and Research Services (DAERS) of BUET. He joined the doctoral program in the department of Mechanical Engineering and Mechanics at Drexel University, Philadelphia, in September 2010. He has received the *George Hill Jr. Endowed Fellowship* and ‘*Highly Commended*’ citation for *Graduate Research Excellence Award*. He has also received several travel grant fellowships from National Science Foundation and Drexel’s Graduate Studies Office. He has worked both as a Research and Teaching Assistant throughout his years at Drexel University. His research interests include computational and experimental investigations of transport phenomena in industrial applications, thermoacoustics, non-thermal plasma discharges and reactive flow modeling.

Journal Publications:

1. Nusair Hasan and Bakhtier Farouk, “Transport and Dynamics of Trans-critical Carbon Dioxide Flow in a Tubular Heat Exchanger: Applications in Waste Heat Recovery”, 2014, *Applied Thermal Engineering* (In Preparation).

2. Nusair Hasan and Bakhtier Farouk, “Experimental and Numerical Investigations of Resonant Acoustic Waves in Near-Critical Supercritical Fluids”, 2014, *Journal of Acoustic Society of America* (Under Review).

3. Bakhtier Farouk and Nusair Hasan, “Acoustic Wave Generation in Near-Critical Supercritical Fluids: Effects on Mass Transfer and Extraction”, 2014, *The Journal of Supercritical Fluids* (Under Review).

4. Nusair Hasan, Dion Antao and Bakhtier Farouk, “DC Negative Corona Discharge in Atmospheric Pressure Helium: Transition from the Corona to the ‘Normal’ Glow Regime”, 2014, *Plasma Sources Science and Technology,* v. 23.

5. Nusair Hasan and Bakhtier Farouk, “Mass Transfer Enhancements in Supercritical Fluid Extraction Process”, 2013, *The Journal of Supercritical Fluids,* v. 80.

6. Nusair Hasan and Bakhtier Farouk, “Fast Heating Induced Thermoacoustic Waves in Supercritical Fluids: Experimental and Numerical Studies”, 2013, *Journal of Heat Transfer,* v.135-8.

7. Nusair Hasan and Bakhtier Farouk, “Buoyancy Driven Convection in Near-Critical and Supercritical Fluids”, 2012, *International Journal of Heat and Mass Transfer,* v. 55.

8. Nusair Hasan and Bakhtier Farouk, “Thermoacoustic Transport in Supercritical Fluids at Near-critical and Near-pseudo-critical States”, 2012, The Journal of Supercritical Fluids, v. 68.